Improved Measurements Of Hadronic-Mass Moments In Decays $\mathbf{B \to X_c \ell \nu}$ and Determination of $|V_{cb}|$

DISSERTATION

zur Erlangung des akademischen Grades
Doctor rerum naturalium
(Dr. rer. nat.)

vorgelegt
der Fakultät Mathematik und Naturwissenschaften
der Technischen Universität Dresden

von
Diplom-Physiker Jan Erik Sundermann
geboren am 20. November 1976 in Hamburg

Gutachter : Prof. Dr. Klaus R. Schubert
Prof. Dr. Michael Kobel
Dr. Oliver Buchmüller

Eingereicht am : aa. bb. 2006

Disputation am : aa. bb. 2006

Abstract

Kurzfassung

Contents

Chapter 1

Introduction

The *Standard Model of Particle Physics* comprises the current knowledge about the interactions between the smallest constituents of matter, the quarks and leptons. Even though the Standard Model is extremely succesfull in predicting physical observables with high accuracy it seems clear from a theoretical point of view that the Standard Model has to be extended to describe physics at higher energies. However, new physics effects that lie beyond the descriptiveness of the Standard Model might also be observable at energies in reach of today's accelerator experiments. For this reason the Standard Model is subject to several experimental high precision tests that try to verify the consistency of the theory and search for physical effects beyond that Standard Model. Several of those tests are directly related to the *Cabibbo-Kobayashi-Maskawa* (CKM) matrix that relates the quark's weak flavor eigenstates to their mass eigenstates.

The elements of the CKM matrix are free parameters in the Standard Model and have to be determined experimentally. A precise measurement of the individual CKM matrix elements will allow to test the unitarity of the quark mixing matrix that is an important property of the Standad Model. This thesis presents a work that allows the determination of the CKM matrix elements $|V_{cb}|$ together with other fundamental parameters of the Standard Model, the masses of the b and c quarks.

One of the most promising approaches for the determination of $|V_{cb}|$ utilizes effective field theories for the theoretical description of semileptonic B meson decays to hadronic final states containing a charm quark, $B \to X_c \ell \nu$. A theoretical approach that combines properties of the *Heavy Quark Effective Theory* (HQET) with an Operator Product Expansion called *Heavy Quark Expansion* (HQE) has already proven to be very successfull. The HQE provides reliable predictions of inclusive observables like the total semileptonic rate $\Gamma(B \to X_c \ell \nu)$ or the moments of the related invariant hadronic mass distribution $< m_X^n >$.

Measuring the moments of the invariant hadronic mass spectrum in semileptonic B meson decays requires the identification of all particles be-

longing to the hadronic system X_c. The presented work implements a technique that fully reconstructs one of the B meson decays in events $e^+e^- \to \Upsilon(4S) \to B\overline{B}$, thereby separating its decay products from the hadronic system of the semileptonic decays. A possible semileptonic decay of the remaining B meson is identified by its associated lepton. Experimentally the identification of leptons with low momenta is complicated. Thus, requiring a minimum lepton momentum is inevitable. This work presents measurements of the first to sixth invariant hadronic mass moments, $< m_X^n >$ with $n = 1 \ldots 6$, as functions of the minimum lepton momentum between $p_\ell^* \geq 0.8\,\mathrm{GeV}/c$ and $p_\ell^* \geq 1.9\,\mathrm{GeV}/c$ calculated in the restframe of the B meson. Measuring moments up to very high minimum lepton momenta, thereby entering the region near the kinematic endpoint in which the HQE is expected to break down, allows to evaluate the behavior of the theoretical prediction in the expected break-down region.

1.1 Outline

The presented work is organized as follows:

- Chapter 2 discusses the physics of B meson decays required for the motivation and interpretations of the presented measurement. After a brief introduction to the Standard Model of Particle Physics, electroweak interactions of elementary particles and the CKM quark mixing matrix will be discussed. The two consequent sections cover special topics concerning the decays of B mesons and inclusive semileptonic decays to hadronic final states containing a charm quark, $B \to X_c \ell \nu$. It concludes with a discussion of how moments of the invariant hadronic mass, $< m_X^n >$, can be used to extract the CKM matrix element $|V_{cb}|$.

- Chapter 3 gives an overview of the *BABAR* detector located at the PEP-II e^+e^- storage rings at the Stanford Linear Accelerator Center. We will give a short overview of the different *BABAR* subdetectors.

- Chapter 4 contains a brief overview of the applied method to measure the first to sixth hadronic mass moments as functions of the minimum lepton momentum in the semileptonic decay. In the employed technique one B meson in events $e^+e^- \to \Upsilon(4S) \to B\overline{B}$ is fully reconstructed in several hadronic modes, thereby separating its decay products from the hadronic system of the semileptonic decay. The semileptonic decay of the second B meson is identified by requiring a single detected electron. The resolution of the reconstructed hadronic system suffers from the limited acceptance and resolution of the detector. For the extraction of moments we utilize a method that "calibrates" the measured hadronic masses by applying correction factors on an event-by-event basis.

- CHAPTER 5 gives a detailed description of the performed measurement, therebye following the brief outline given in the previous chapter. It starts with an overview of the used data and MC simulation samples followed by a description of the semi-exclusive reconstruction method that is utilized for the full reconstruction of hadronic B meson decays. Then particle selection criteria will be outlined. The reconstruction of the hadronic system is described in the consequent section followed by a description of the background subtraction. Finally the extraction of moments $< m_X^n >$ from the reconstructed hadronic system will be discussed. The chapter concludes with a presentation of the obtained results.

- CHAPTER 6 discusses several potential sources of systematic uncertainties. Described are effects associated with the calibration procedure, background subtraction, effects stemming from mis modeling in MC simulations, and concludes with stability tests of the extracted results.

- CHAPTER 7 the obtained results are interpreted and compared to other measurements. We use our results together with other measured moments of the lepton energy spectrum in semileptonic B meson decays and moments of the photon energy spectrum in decays $B \to X_s\gamma$ to extract the CKM matrix element $|V_{cb}|$ in a combined fit to theoretically predicted moments.

Chapter 2

Inclusive Semileptonic B-Meson Decays and $|V_{cb}|$

The following chapter will give a brief introduction to theoretical concepts utilized to describe and interpret the decays of B mesons investigated in this work. Section 2.1 will give a brief introduction to the Standard Model of Particle Physics followed by a discussion of the weak interaction part of the Standard Model and the *Cabibbo-Kobayashi-Maskawa* quark mixing matrix in sections 2.2 and 2.3.

Theoretical concepts that are of special interest for the description of the physics of heavy mesons and inclusive measurements of semileptonic B meson decays $B \to X_c \ell \nu$ will be discussed in the sections 2.4 and 2.5. We will discuss basic aspects of the *Heavy Quark Effective Theory* and the *Heavy Quark Expansion*. There are several review articles covering this field of elementary particle physics which are among others [1,2,3].

2.1 The Standard Model of Particle Physics

The most comprehensive theoretical framework for the description of interactions between the smallest constituents of matter, the quarks and leptons, is the *Standard Model of Particle Physics*. The Standard Model represents the best current knowledge about strong, weak, and electromagnetic interactions of elementary particles. Interactions are described by a $SU(3)_C \otimes SU(2)_W \otimes U(1)_Y$ relativistic quantum field theory combining the $SU(3)_C$ color charge group, the $SU(2)_W$ weak isospin group, and the hypercharge symmetry group $U(1)_Y$.

In the current view all matter is made out of three kinds of elementary particles: leptons, quarks, and gauge bosons. There are six leptons arranged into three generations:

$$\begin{pmatrix}\nu_e\\ e\end{pmatrix}\begin{matrix}\text{electron-neutrino}\\ \text{electron}\end{matrix} \qquad \begin{pmatrix}\nu_\mu\\ \mu\end{pmatrix}\begin{matrix}\text{muon-neutr.}\\ \text{muon}\end{matrix} \qquad \begin{pmatrix}\nu_\tau\\ \tau\end{pmatrix}\begin{matrix}\text{tau-neutr.}\\ \text{tau}\end{matrix}$$

Similar, there are six "flavors" of quarks falling into three generations:

$$\begin{pmatrix} u \\ d \end{pmatrix} \begin{matrix} \text{up-quark} \\ \text{down-quark} \end{matrix} \qquad \begin{pmatrix} c \\ s \end{pmatrix} \begin{matrix} \text{charm-quark} \\ \text{strange-quark} \end{matrix} \qquad \begin{pmatrix} t \\ b \end{pmatrix} \begin{matrix} \text{top-quark} \\ \text{bottom-quark} \end{matrix}$$

Furthermore, for every elementary particle there exists a corresponding antiparticle. While the different quark and lepton generations are equal regarding their quantum numbers they differ in their masses increasing hierarchically from quark generation to quark generation and from lepton generation to lepton generation. Neutrinos are known to have masses since the observation of neutrino oscillations in 1998 by the Super-Kamiokande experiment [4]. Since the origin of neutrino masses has not been answered conclusively yet, that is for example if neutrinos are Majorana or Dirac particles, and the question of neutrino masses does not affect the theoretical interpretation of B meson decays under study in this work, we will consider neutrinos in the following discussion of electroweak interactions and heavy quark decays as massless.

Every interaction has its bosonic mediator. Electroweak interactions are mediated by the photon, W^+, W^-, and Z^0. Charged particles interact electromagnetically, i.e. all quarks and leptons except neutrinos. The weak interaction couples only to the left-handed quarks and leptons thereby maximally violating parity conservation. The strong interaction is mediated by eight gluons coupling to the so called color charge of the quarks. Leptons do not take part in the strong interaction.

2.2 Electroweak Interaction and Symmetry Breaking

Until now three generations of quarks and leptons were observed that can be arranged in three left-handed quark doublets, six right-handed quark singulets, three left-handed lepton doublets, and three right-handed lepton singulets:

$$\begin{aligned} &\text{quarks:} && Q_L^i = \begin{pmatrix} u_L^i \\ d_L^i \end{pmatrix},\ u_R^i,\ d_R^i \\ &\text{leptons:} && L_L^i = \begin{pmatrix} \nu_L^i \\ e_L^i \end{pmatrix},\ \ell_R^i \end{aligned} \qquad (i = 1 \ldots 3). \tag{2.1}$$

The electroweak interaction part of the standard model has the structure of a $SU(2)_W \otimes U(1)_Y$ group which is a combination of the weak $SU(2)_W$-symmetry group and the hypercharge group $U(1)_Y$. The weak interaction part of the theory couples to the left-handed doublet structure of the fermions, the weak isospin. The right-handed fermion singlets do not take part in the weak interaction. The weak interaction is mediated by the three

	I	I_3	Q	Y
$Q^i_L = \begin{pmatrix} u_i \\ d_i \end{pmatrix}_L$, $u_i = u, c, t$	$\frac{1}{2}$	$+\frac{1}{2}$	$+\frac{2}{3}$	$+\frac{1}{3}$
$d_i = d, s, b$	$\frac{1}{2}$	$-\frac{1}{2}$	$-\frac{1}{3}$	$+\frac{1}{3}$
$u^i_R = u_R, c_R, t_R$	0	0	$+\frac{2}{3}$	$+\frac{4}{3}$
$d^i_R = d_R, s_R, b_R$	0	0	$-\frac{1}{3}$	$-\frac{2}{3}$
$L^i_L = \begin{pmatrix} \nu_i \\ l_i \end{pmatrix}_L$, $\nu_i = \nu_e, \nu_\mu, \nu_\tau$	$\frac{1}{2}$	$+\frac{1}{2}$	0	-1
$l_i = e, \mu, \tau$	$\frac{1}{2}$	$-\frac{1}{2}$	-1	-1
$\ell^i_R = e_R, \mu_R, \tau_R$	0	0	-1	-2
$H = \begin{pmatrix} h^+ \\ h^0 \end{pmatrix}$	$\frac{1}{2}$	$+\frac{1}{2}$	$+1$	$+1$
	$\frac{1}{2}$	$-\frac{1}{2}$	0	$+1$

Table 2.1: Properties of quark, lepton, and Higgs fields in the electroweak interaction. The fields Q^i_L and L^i_L are the left-handed quark and lepton doublets, respectively. Right-handed fields are indicated by a subscript R. The fields H is the Higgs doublet. The given quantum numbers are the weak isospin (I), the third component of the weak isospin (I_3), the electric charge (Q), and weak hypercharge, $Y = 2(Q - I_3)$.

non-abelian gauge fields W^μ_1, W^μ_2, and W^μ_3. The $U(1)_Y$–interaction mediated by a single abelian gauge field B^μ couples to the weak hypercharge of the fermions. The hypercharge quantum number Y is related to the charge Q and the third component of the weak isospin I_3 by the Gell-Mann-Nishijima relation,

$$Y = 2\,(Q - I_3)\,. \tag{2.2}$$

Table 2.1 summarizes the mentioned quantum numbers of all appearing fields.

The Lagrangian density describing the dynamics and electroweak interactions of the quark and lepton fields is given by,

$$\mathcal{L} = \sum_{i=1\ldots3} \bar{\Psi}^i_L i \not{D}_L \Psi^i_L + \sum_{i=1\ldots3} \bar{\Psi}^i_R i \not{D}_R \Psi^i_R - \frac{1}{4} F^A_{\mu\nu} F^{A\mu\nu} - \frac{1}{4} f_{\mu\nu} f^{\mu\nu}, \tag{2.3}$$

where $\bar{\Psi}^i_L$ is either the left-handed quark doublet Q^i_L or the left-handed lepton doublet L^i_L. $\bar{\Psi}^i_R$ are the right-handed quark and lepton fields u^i_R, d^i_R, or ℓ^i_R. D^μ_L are D^μ_R are the covariant derivatives of the left- and right-handed fields,

$$\begin{aligned} D^\mu_L &= \partial^\mu + i g_1 T^A W^\mu_A + i g_2 Y B^\mu \\ D^\mu_R &= \partial^\mu + i g_2 Y B^\mu \end{aligned} \qquad (A = 1\ldots3), \tag{2.4}$$

with $T^A = \sigma^A/2$ the three generators of $SU(2)_W$ symmetry group proportional to the Pauli spin matrices σ^A. The generator of the $U(1)_Y$ symmetry

group is equal to one. The dynamics of the weak and hypercharge gauge fields are described by the field strength tensors $F^A_{\mu\nu}$ $(A = 1 \ldots 3)$ and $f_{\mu\nu}$, respectively. The gauge fields W^μ_A and B^μ are not the physical fields observed in nature. The physical fields $W^\pm$, Z^0, and A arise from the fields W_μ and B by performing a linear transformation,

$$\begin{aligned} W^\pm &= \frac{W^1 \mp iW^2}{\sqrt{2}}, \\ Z^0 &= \cos(\Theta_W)\, W^3 - \sin(\Theta_W)\, B, \\ A &= \sin(\Theta_W)\, W^3 + \sin(\Theta_W)\, B, \end{aligned} \tag{2.5}$$

and introducing the Weinberg mixing angle Θ_W.

Experimental observations show that the quarks, leptons, and the gauge bosons $W^\pm$ and Z^0 are massive particles. Up to this point all gauge and particle fields appearing in the electroweak Lagrangian (cf. equation 2.3) are massless, i.e. the Lagrangian contains no mass terms. Adding Dirac mass terms like $m^2 W^\mu_A W_{\mu A}$ would violate the invariance under local gauge transformation. In order to obtain gauge invariant mass terms Peter Higgs introduced in 1964 a doublet of complex scalar fields [5,6,7,8,9],

$$H = \begin{pmatrix} h^+ \\ h^0 \end{pmatrix}, \tag{2.6}$$

where h^+ and h^0 are its charged and neutral components, respectively. The $SU(2)_W \otimes U(1)_Y$ symmetry group is spontaneously broken by the specific structure of the vacuum with the Higgs potential,

$$V(H) = -\mu^2 H^\dagger H + \lambda^2 (H^\dagger H)^2. \tag{2.7}$$

The Higgs sector of the Standard Model Lagrangian,

$$\mathcal{L}_{Higgs} = (D_\mu H)^\dagger (D^\mu H) - V(H), \tag{2.8}$$

is invariant under local gauge transformation. Expanding H around its vacuum expectation value, $v^2 = \mu^2/2\lambda^2$, and eliminating h^+ and $\mathrm{Im}\, h^0$ by choosing a convenient gauge,

$$H = \begin{pmatrix} 0 \\ \frac{v}{\sqrt{2}} + \mathrm{Re}\, h^0 \end{pmatrix}, \tag{2.9}$$

leads to massive gauge bosons and a massive Higgs boson. Quarks and leptons get their masses because of their Yukawa coupling to the Higgs doublet,

$$\mathcal{L}_{Yuk} = g_u^{ij} \bar{u}^i_R H^T \epsilon Q^j_L - g_d^{ij} \bar{d}^i_R H^\dagger Q^j_L - g_\ell^{ij} \bar{\ell}^i_R H^\dagger L^j_L + \mathrm{h.c.} \tag{2.10}$$

In every term a right- and a left-handed field couples to the Higgs field. The matrices g^{ij} give the strength of the Higgs field coupling and ϵ is the

anti-symmetric matrix, $\epsilon = \left(\begin{smallmatrix} 0 & 1 \\ -1 & 0 \end{smallmatrix}\right)$. From equation 2.10 follows for the mass matrices of the quark- and lepton-fields,

$$M_u = \frac{v g_u}{\sqrt{2}}, \qquad M_d = \frac{v g_d}{\sqrt{2}}, \qquad M_e = \frac{v g_e}{\sqrt{2}}. \tag{2.11}$$

The matrices M are not necessarily diagonal. By multiplication with unitary matrices from the left and right they can be diagonalized. Since up- and down-type quarks are part of the same $SU(2)$ doublet it is not possible to diagonalize their mass matrices simultaneously. Therefore, transforming the flavor eigenstate fields into their mass eigenstate fields gives,

$$\begin{pmatrix} u_L \\ d_L \end{pmatrix} = \begin{pmatrix} \mathcal{U}(u,L) u'_L \\ \mathcal{U}(d,L) d'_L \end{pmatrix} = \mathcal{U}(u,L) \begin{pmatrix} u'_L \\ V d'_L \end{pmatrix}, \tag{2.12}$$

with the unitary transformation matrices $\mathcal{U}(u,L)$ and $\mathcal{U}(d,L)$ for the up-type and for the down-type fields, respectively. The u'_L and d'_L are the mass eigenstates of the up- and down-type quarks, respectively. The matrix V is the so called *Cabibbo-Kobayashi-Maskawa* (CKM) matrix.

2.3 The CKM Matrix and the Unitary Triangle

The unitary CKM matrix relates the weak flavor eigenstates of the quarks (d, s, b) to their mass eigenstates (d', s', b'),

$$\begin{pmatrix} d \\ s \\ b \end{pmatrix} = \begin{pmatrix} V_{ud} & V_{us} & V_{ub} \\ V_{cd} & V_{cs} & V_{cb} \\ V_{td} & V_{ts} & V_{tb} \end{pmatrix} \begin{pmatrix} d' \\ s' \\ b' \end{pmatrix}. \tag{2.13}$$

As a consequence flavor changing charged currents can occur at tree level with transition rates proportional to $|V_{ij}|^2$. The corresponding CKM matrix element denotes the relative strength of the coupling. Flavor changing neutral currents at tree level are forbidden in the Standard Model.

The CKM matrix has to be unitary in the standard model. It can be parameterized by three mixing angles and a CP-violating phase. Following the observation of a hierarchy between the different matrix elements Wolfenstein proposed an expansion of the CKM matrix in terms of the four parameters λ, A, ρ, and η, defined by the relations,

$$\begin{aligned} \lambda &= \frac{|V_{us}|}{\sqrt{|V_{ud}|^2 + |V_{us}|^2}} \sim 0.22, \\ A\lambda^2 &= \lambda \left| \frac{V_{cb}}{V_{us}} \right|, \\ A\lambda^2(\rho + i\eta) &= V^*_{ub}, \end{aligned} \tag{2.14}$$

and λ being the expansion parameter. The CKM matrix written in the Wolfenstein parameterization is,

$$V = \begin{pmatrix} 1-\frac{\lambda^2}{2} & \lambda & A\lambda^3(\rho - i\eta) \\ -\lambda & 1-\frac{\lambda^2}{2} & A\lambda^2 \\ A\lambda^3(1-\rho-i\eta) & -A\lambda^2 & 1 \end{pmatrix} + \mathcal{O}(\lambda^4). \tag{2.15}$$

The unitarity of the CKM matrix imposes the relation,

$$\frac{V_{ud}V_{ub}^*}{V_{cd}V_{cb}^*} + \frac{V_{cd}V_{cb}^*}{V_{cd}V_{cb}^*} + \frac{V_{td}V_{tb}^*}{V_{cd}V_{cb}^*} = 0, \tag{2.16}$$

that can be represented in the complex plane as a triangle. There are several experimental constraints on the parameters of this triangle which allow an overdetermination of the shape of the unitary triangle and thus test the consistency of the Standard Model. Figure 2.1 illustrates the unitary triangle in the $\bar{\rho}$–$\bar{\eta}$ plane obtained from a fit combining several observables [10]. Introducing the parameters $\bar{\rho}$ and $\bar{\eta}$ ensures that the apex of the unitary triangle, $\bar{\rho} + i\bar{\eta} = -V_{ud}V_{ub}^*/V_{cd}V_{cb}^*$, is phase-convention independent and the CKM matrix written in terms of λ, A, $\bar{\rho}$, and $\bar{\eta}$ is unitary to all orders in λ.

The CKM matrix element $|V_{cb}|$ which is of special interest for the presented measurement is currently known to be [11],

$$|V_{cb}| = (41.96 \pm 0.73) \times 10^{-3}, \tag{2.17}$$

with a relative uncertainty of 1.7%. It enters in the global CKM fit with the 4th power into the relation between CP violation parameter in the system of neutral kaons, ϵ_K, and ρ, η. Experimentally the CKM matrix element $|V_{cb}|$ can be determined through the study of semileptonic B meson decays $B \to X_c \ell \nu$. In the following an overview of the theory involved in the mathematical description of heavy mesons and inclusive semileptonic B meson decays will be given.

2.4 Heavy Quark Effective Theory

The *Heavy Quark Effective Theory* (HQET) is an effective field theory that can be derived from the theory of strong interaction *Quantum Chromo Dynamics* (QCD) in the limit of heavy quark masses, $m_Q \to \infty$. In this limit QCD has spin-flavor heavy quark symmetry, which has important implications for the properties of hadrons containing a single heavy quark. The effective field theory is constructed so that only inverse powers of m_Q appear in the effective Lagrangian, in contrast to the QCD Lagrangian that has positive powers of m_Q.

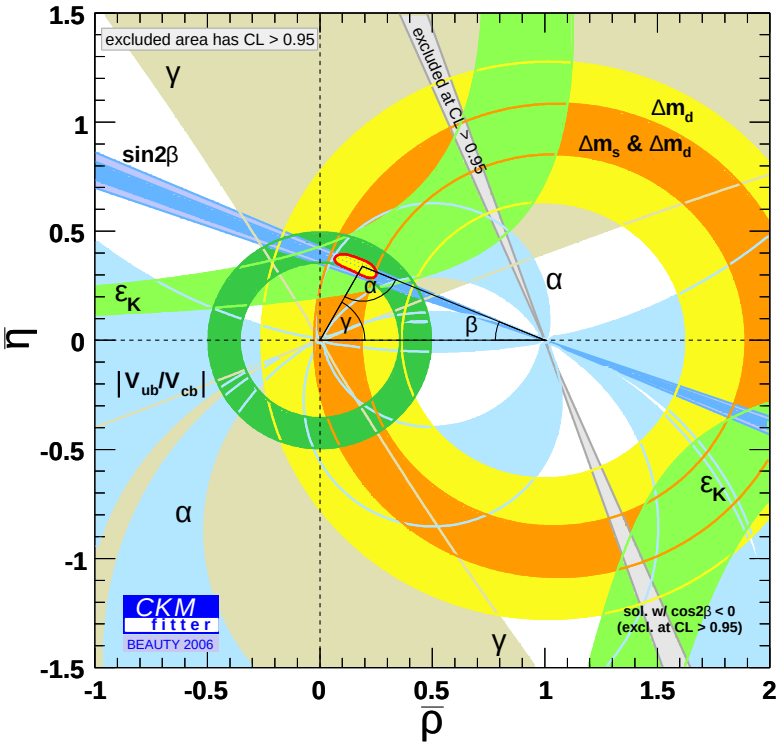

Figure 2.1: Global fit of the unitary triangle in the $\bar{\rho}$–$\bar{\eta}$ plane [10].

2.4.1 The Heavy Quark Limit of QCD

The QCD portion of the Standard Model that describes the strong interactions of quarks and gluons is characterized by a renormalized coupling that depends on the energy scale of the the interaction. While the mediators of the electromagnetic force carry no charge and thus do not interact with each other, the gauge fields of the strong interaction, the gluons, carry color charge and can interact with each other. The self-interaction of gluons leads to a modified behavior of the fine structure constant of the strong interaction as a function of the energy scale μ,

$$\alpha_s(\mu) = \frac{12\pi}{(33 - 2N_q)\ln\left(\mu^2/\Lambda^2_{QCD}\right)}. \tag{2.18}$$

If the number of accessible quark flavors N_q is less than 16, $\alpha_s(\mu)$ becomes weak at high energies or low distances. This phenomenon is called "asymptotic freedom". The strong interaction fine structure constant, as suggested in equation 2.18, diverges as $\mu \to \Lambda_{QCD}$. The parameter Λ_{QCD} is the scale at which the QCD becomes strongly coupled, perturbation theory breaks down, and non-perturbative effects become important. Experimentally, Λ_{QCD} is $\sim 200\,\mathrm{MeV}$, and it sets the scale for non-perturbative strong interaction effects.

Consider a hadron H_Q that is composed of a heavy quark Q and "light degrees of freedom", consisting of light quarks and gluons. The Compton wavelength of the heavy quark scales with its mass, $\lambda_Q \sim 1/m_Q$, and decreases with increasing quark mass. In contrast the light degrees of freedom are characterized by momenta of order Λ_{QCD} and large Compton wavelengths, $\lambda_l \sim 1/\Lambda_{QCD} \gg \lambda_Q$. Therefore, the light degrees of freedom cannot resolve properties of the heavy quark other than its conserved gauge quantum numbers. In particular this is the actual value of λ_Q which corresponds to the mass m_Q of the heavy quark.

The typical momenta p exchanged by the light degrees of freedom among each other and with the heavy quark are of order Λ_{QCD} and thus non-perturbative in their nature. For these momenta with $p \ll m_Q$ the heavy quark does not recoil and remains at rest in the rest frame of the hadron acting as a static source of electric and chromoelectric gauge field. In the heavy quark limit, $m_Q \to \infty$, the dynamics of the light degree of freedom depend only on the presence of the static gauge field and remain unchanged under the exchange of the heavy quark flavor or mass. This behavior is called *Heavy Quark Flavor Symmetry*. As a consequence the spectrum of excitations of heavy hadrons is independent of flavor and mass of the heavy quark as depicted in figure 2.2. Heavy quark flavor symmetry breaking effects of first order in $1/m_Q$ are proportional to $1/m_{Q_a} - 1/m_{Q_b}$.

The spin-dependent interactions are proportional to the chromomagnetic

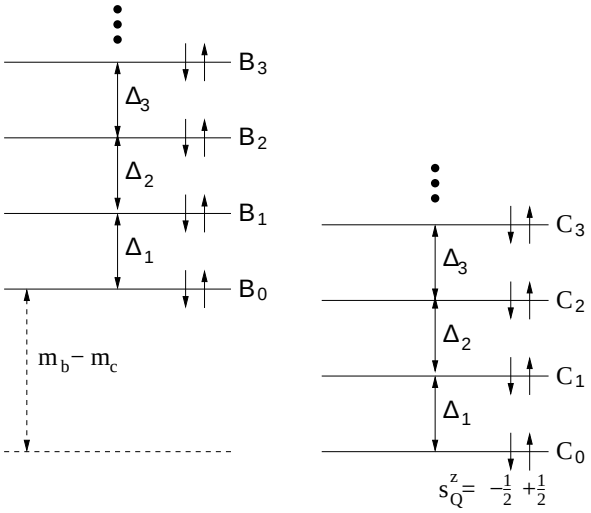

Figure 2.2: Spectroscopy of heavy mesons containing a bottom- or charm-quark in the heavy quark limit. The excitation energy Δ_i does not depend on the mass of the heavy quark. The offset in the energy of the two spectra is given by the difference of the two quark masses, $m_b - m_c$. The energies of two hadrons with different spin quantum numbers, $s_Q^z = \pm\frac{1}{2}$, is degenerated.

moment of the quark,

$$\mu_Q = \frac{g}{2m_Q}. \tag{2.19}$$

The heavy quark Q has the spin quantum numbers $s_Q = \frac{1}{2}$ and $s_Q^z = \pm\frac{1}{2}$. In the heavy quark limit, $m_Q \to \infty$, the light degrees of freedom get insensitive to s_Q and the energies of two hadrons with different s_Q^z are degenerated (see figure 2.2). This leads to the *Heavy Quark Spin Symmetry*. Heavy quark spin symmetry breaking does not have to be proportional to the difference of $1/m_Q$'s, since the spin symmetry is broken even for two hadrons containing heavy quarks with the same mass.

In the heavy quark limit of QCD spin and flavor symmetry can be summarized in a bigger heavy quark spin-flavor symmetry,

$$SU(2)_{\text{spin}} \otimes U(N_Q)_{\text{flavor}} \to U(2N_Q)_{\text{spin-flavor}}, \tag{2.20}$$

where N_Q is the number of heavy quarks. In this symmetry the total angular momentum $\hat{\mathbf{J}}$ and the spin of the heavy quark $\hat{\mathbf{S}}_Q$ are good quantum numbers. Therefore, the spin of the light degrees of freedom,

$$\hat{\mathbf{S}}_l \equiv \hat{\mathbf{J}} - \hat{\mathbf{S}}_Q \tag{2.21}$$

is also conserved.

	Quark Content	Mass [MeV/c^2]	Γ [MeV/c^2]	τ [fs]	$I(J^P)$	s_l
D^+	$c\overline{d}$	1869.3 ± 0.5		1040 ± 7	$\frac{1}{2}(0^-)$	$\frac{1}{2}$
D^{*+}		2010.0 ± 0.4	0.096 ± 0.022		$\frac{1}{2}(1^-)$	$\frac{1}{2}$
D_1^+		2423.4 ± 3.1	25 ± 6		$\frac{1}{2}(1^+)$	$\frac{3}{2}$
D_2^{*+}		2459 ± 4	29 ± 5		$\frac{1}{2}(2^+)$	$\frac{3}{2}$
D_0^{*+}		2403 ± 40	283 ± 40		$\frac{1}{2}(0^+)$	$\frac{1}{2}$
$D_1'^+$					$\frac{1}{2}(1^+)$	$\frac{1}{2}$
D^0	$c\overline{u}$	1864.5 ± 0.4		410.1 ± 1.5	$\frac{1}{2}(0^-)$	$\frac{1}{2}$
D^{*0}		2006.7 ± 0.4	< 2.1		$\frac{1}{2}(1^-)$	$\frac{1}{2}$
D_1^0		2422.3 ± 1.3	20.4 ± 1.7		$\frac{1}{2}(1^+)$	$\frac{3}{2}$
D_2^{*0}		2461.1 ± 1.6	43 ± 4		$\frac{1}{2}(2^+)$	$\frac{3}{2}$
D_0^{*0}		2352 ± 50	261 ± 50		$\frac{1}{2}(0^+)$	$\frac{1}{2}$
$D_1'^0$		2427 ± 40	384^{+130}_{-110}		$\frac{1}{2}(1^+)$	$\frac{1}{2}$

Table 2.2: Properties of heavy charmed mesons containing light $\overline{u}$ or $\overline{d}$ antiquarks [12]: total width (Γ), life time (τ), isospin (I), total angular momentum (J), parity (P), and the spin of the light degrees of freedom (s_l).

Heavy mesons are made up of a heavy b or c quark[1], carrying the spin quantum number $s_Q = \frac{1}{2}$, and a light antiquark $\overline{q}$, either $\overline{u}$, $\overline{d}$, or $\overline{s}$, with the spin $s_l = \frac{1}{2}$. The ground state mesons form a doublet with spin $j = \frac{1}{2} \otimes \frac{1}{2} = 0 \oplus 1$. If the light antiquark is either a $\overline{u}$ or $\overline{d}$, these mesons are called D and D^* if Q is a c quark, or B and B^* if Q is a b quark. Accordingly, we call mesons containing a light $\overline{s}$ antiquark D_s^+, D_s^{*+}, B_s, or B_s^*.

The lowest excited states of heavy mesons are those with a relative orbital angular momentum, $L = 1$, between the light antiquark and the heavy quark. It is called D^{**}. The the light degrees of freedom carry the spin quantum numbers $s_l = \frac{1}{2}$ or $\frac{3}{2}$. If Q is a c quark, mesons with $s_l = \frac{1}{2}$ are called D_0^* and D_1', and mesons with $s_l = \frac{3}{2}$ form a system of states called D_1 and D_2^*. The D_1 and D_2^* are narrow states while D_0^* and D_1' are wide resonances. Table 2.2 summarizes the properties of heavy charmed mesons that contain light $\overline{u}$ or $\overline{s}$ antiquarks.

2.4.2 Effective Lagrangian

The strong interaction of quarks and gluons is characterized in the Standard Model by a $SU(3)_C$ symmetry group with the Lagrangian density,

$$\mathcal{L}_{QCD} = \bar{\Psi}\left(i\gamma^\mu D_\mu - m\right)\Psi - \frac{1}{4}G^a_{\mu\nu}G^{\mu\nu}_a \quad (a = 1 \ldots 8), \tag{2.22}$$

[1] Top quarks decay too quickly to establish a static chromoelectric field.

where D_μ is the $SU(3)_C$ covariant derivative,

$$D_\mu = \partial_\mu + igA^a_\mu T_a \qquad a = 1 \ldots 8. \tag{2.23}$$

Here, the $T_a = \frac{1}{2}\lambda_a$ are the eight generators of the $SU(3)_C$ gauge group with λ_a the Gell-Mann-Matrices and A^a_μ the eight gauge fields of color. The $G^a_{\mu\nu}$ are the gluon field strength tensors.

As discussed above, properties of mesons containing a single heavy quark manifest heavy quark spin-flavor symmetry in the limit $m_Q \to \infty$. Since the QCD Lagrangian in equation 2.22 does not manifest the spin-flavor symmetry it is convenient to reformulate the QCD in an effective field theory that provides a controlled expansion about the limit $m_Q \to \infty$. This effective theory is called *Heavy Quark Effective Theory* (HQET).

The momentum exchange between the heavy quark Q and the light degrees of freedom is of order $\Lambda_{QCD} \ll m_Q$ taking Q never far away from its mass shell, $p^2_Q = m^2_Q$. Thus, the momentum p^μ_Q can be decomposed into two parts,

$$p^\mu = m_Q v^\mu + k^\mu, \tag{2.24}$$

where $m_Q v^\mu$ is the large on-shell part, with v^μ being the four-velocity of the heavy quark. The small fluctuation $k^\mu \sim \Lambda_{QCD}$ determines the amount by which the quark is off-shell because of its interactions. Since soft interactions can change k^μ but not v^μ in the heavy quark limit, v^μ acts as a good quantum number of the effective QCD Lagrangian.

It is convenient to reformulate the original quark field $Q(x)$ in terms "large" and "small" velocity dependent component fields,

$$Q_v(x) = e^{im_Q v\cdot x} P_+ Q(x), \qquad \mathfrak{Q}_v(x) = e^{im_Q v\cdot x} P_- Q(x), \tag{2.25}$$

such that,

$$Q(X) = e^{-im_Q v\cdot x} \left(Q_v(x) + \mathfrak{Q}_v(x)\right). \tag{2.26}$$

The operators $P_\pm$ are velocity dependent projection operators defined as,

$$P_\pm = \frac{1 \pm \not{v}}{2} \tag{2.27}$$

that become in the rest frame of heavy quark, $P_\pm = (1 \pm \gamma^0)/2$, projecting out the upper and lower two components of the heavy quark spinor. In the limit $m_Q \to \infty$ only the two upper spinor components propagate mixing with the two lower components. The mixing occurs with the amplitude $\sim 1/(2m_Q)$ and frequency $\sim 2m_Q$. Therefore, the lower two components of the spinor projected out by P_- are suppressed with $1/m_Q$,

$$P_+ Q(x) = Q(x) + \mathcal{O}\left(\frac{1}{m_Q}\right), \qquad P_- Q(x) = 0 + \mathcal{O}\left(\frac{1}{m_Q}\right). \tag{2.28}$$

While the field $Q_v(x)$ in equation 2.26 is mass independent and carries the heavy quark spin-flavor symmetry, the field $\mathfrak{Q}_v(x)$ vanishes in the heavy

quark limit. The exponential factor $e^{im_Q v\cdot x}$ in $Q_v(x)$ and $\mathfrak{Q}_v(x)$ removes the large on-shell component from the heavy quark momentum.

Starting from the original QCD Lagrangian density in equation 2.22 the effective HQET Lagrangian at tree level in leading order perturbation theory follows by substituting equation 2.26 with $\mathfrak{Q}_v(x) = 0$:

$$\mathcal{L}_{HQET} = \bar{Q}_v(x)\,(iv_\mu D^\mu)\,Q_v(x). \tag{2.29}$$

The effective Lagrangian in equation 2.29 does not depend on the mass or spin of the heavy quark and thus incorporates spin-flavor symmetry. Non-perturbative corrections proportional to Λ_{QCD}/m_Q that break the spin-flavor symmetry will be introduced in the next section.

2.4.3 Non-Perturbative Corrections

The HQET Lagrangian including $1/m_Q$ corrections can be derived from the QCD Lagrangian by substitution with the effective fields in equation 2.26,

$$\begin{aligned}\mathcal{L}_{HQET} = \bar{Q}_v(x)\,(iv\cdot D)\,Q_v(x) - \bar{\mathfrak{Q}}_v(x)\,(iv\cdot D + 2m_Q)\,\mathfrak{Q}_v(x)\\ +\bar{Q}_v(x) i\not{D}\mathfrak{Q}_v(x) + \bar{\mathfrak{Q}}_v(x) i\not{D} Q_v(x).\end{aligned} \tag{2.30}$$

The field $\mathfrak{Q}_v(x)$ corresponds to an excitation with the mass $2m_Q$ and can be integrated out of the theory by application of the classical equation of motion, $(i\not{D} - m_Q)Q(x)$:

$$(iv\cdot D + 2m_Q)\mathfrak{Q}_v(x) = i\not{D}_\perp Q_v(x), \tag{2.31}$$

where $D^\mu_\perp \equiv D^\mu - v\cdot D\, v^\mu$ is the perpendicular component of D^μ with respect to the velocity v^μ. Substituting equation 2.31 back into the effective Lagrangian in equation 2.30 and expanding in $1/m_Q$ gives,

$$\mathcal{L}_{HQET} = \mathcal{L}_0 + \mathcal{L}_1 + \mathcal{O}(1/m_b^2), \tag{2.32}$$

where $\mathcal{L}_0$ is the lowest order Lagrangian as defined in equation 2.29. The Lagrangian $\mathcal{L}_1$ is of first order in $1/m_Q$. It is given by,

$$\mathcal{L}_1 = -\bar{Q}_v(x)\frac{\not{D}^2_\perp}{2m_Q}Q_v(x) - g\bar{Q}_v(x)\frac{\sigma^{\mu\nu}G_{\mu\nu}}{4m_Q}Q_v(x), \tag{2.33}$$

using the identity $[D^\mu, D^\nu] = igG^{\mu\nu}$ and the definition $\sigma_{\mu\nu} = i[\gamma_\mu, \gamma_\nu]/2$. The first term in equation 2.33 is the nonrelativistic heavy quark kinetic energy. It breaks heavy quark flavor symmetry because of the explicit dependence on m_Q. The second term describes the magnetic moment interaction of the heavy quark. It breaks both heavy quark spin and flavor symmetry.

Both expressions in equation 2.33 contain operators whose matrix elements will play an important role in the Operator Product Expansion utilized for theoretical description of inclusive semileptonic B meson decays. This will be discussed in the next section.

2.5 Inclusive Semileptonic B-Meson Decays

In this section methods will be discussed that allow to extract the CKM matrix element $|V_{cb}|$ from the total semileptonic decay width $\Gamma(B \to X_c \ell\nu)$ calculated in the framework of the Heavy Quark Effective Theory utilizing an Operator Product Expansion approach.

Semileptonic B-meson decays to hadronic final states containing a charm quark, $B \to X_c \ell\nu$, arise from the matrix elements of the weak Hamiltonian density,

$$H_W = \frac{4G_F}{\sqrt{2}} V_{cb} \underbrace{\bar{c}\gamma^\mu P_L b}_{J^\mu_{(bc)}} \underbrace{\bar{\ell}\gamma_\mu P_L \nu_\ell}_{J_{(\ell\nu)\mu}}, \tag{2.34}$$

where G_F is the Fermi constant and $P_L = (1 - \gamma_5)/2$ is the operator projecting out the left-handed field. The weak Hamiltonian in equation 2.34 depends directly on the CKM matrix element V_{cb}. It can be factored into a leptonic, $J_{(\ell\nu)\mu}$, and hadronic, $J^\mu_{(bc)}$, current, since leptons do not have any strong interaction. In contrast to the matrix element of the leptonic current it is much more difficult to calculate the matrix element of the hadronic current since the quark level transition is dressed by non-perturbative QCD effects.

Figure 2.3 shows weak decay diagrams for the semileptonic b quark and B meson decays. The hadronic final state X_c could be for example a resonant state like a single D or D^* mesons or a multiparticle state comprising $D\pi$ or $D^*\pi$ mesons. When calculating observables of the inclusive semileptonic B decay like $\Gamma(B \to X_c \ell\nu)$ it is possible to revert to the formalism of HQET and perform a double expansion in powers of α_s and Λ_{QCD}/m_b therebye introducing non-perturbative matrix elements firstly appearing at order $1/m_b^2$. This procedure based on an Operator Product Expansion (OPE) approach and perturbative QCD is called *Heavy Quark Expansion* (HQE)

The predictions obtained from the HQE for the differential $B \to X_c \ell\nu$ semileptonic decay rate cannot be compared directly with experimental measurements in all regions of the phase space. The HQE provides a reliable prediction only when the hadronic final state smoothly averages over several final state hadronic masses m_X. Near the kinematic endpoint only lower-mass final hadronic states can contribute and the expansion breaks down. On the other hand the HQE approach provides reliable predictions of inclusive observables that integrate over a sufficient number of exclusive final states, like the total semileptonic rate $\Gamma(B \to X_c \ell\nu)$, the moments of the invariant hadronic mass spectrum $< m_X^n >$, or the moments of the lepton energy spectrum $< E_\ell^n >$. The HQE also allows the prediction of moments of the photon energy spectrum in rare decays $B \to X_s\gamma$. Even though the moments $< m_X^n >$ do not directly depend on $|V_{cb}|$ they allow to measure the dominant non-perturbative matrix elements that cannot be calculated reliably.

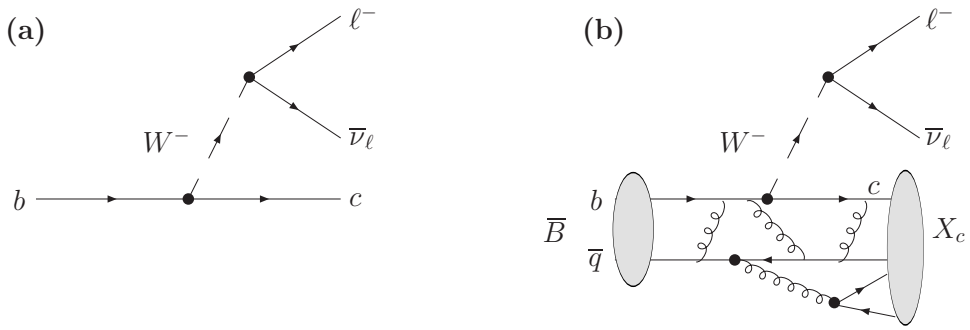

Figure 2.3: Weak decay diagrams for semileptonic b quark (a) and B meson (b) decays. The weak Hamiltonian of the heavy meson decay can be factored into a leptonic and hadronic current, since leptons do not have any strong interaction.

Perturbative corrections to the moments and total rate can be implemented in miscellaneous schemes using different normalization scales. Beside the so called *1S scheme* [13] the *kinetic scheme* [14, 15, 16] by Uraltsev et al. provides calculations of different moments and the total semileptonic rate. We will use these calculations in the final interpretation of the measured invariant hadronic mass moments and for the extraction of $|V_{cb}|$.

The next section 2.5.1 will give a short introduction to the HQE followed by a discussion of its implementation in the kinetic scheme in section 2.5.2.

2.5.1 The Heavy Quark Expansion

The differential decay rate of the inclusive semileptonic decay in the rest-frame of the B meson after integration over whole the phase space is given by,

$$\frac{\mathrm{d}\Gamma(B \to X_c \ell \nu)}{\mathrm{d}q^2 \mathrm{d}E_\ell \mathrm{d}E_\nu} = \frac{1}{4} \sum_{X_c} \sum_{\substack{\text{lepton} \\ \text{spins}}} \frac{|\langle X_c \ell \nu | H_W | B \rangle|^2}{2m_B} \delta^4[p_B - (p_\ell + p_\nu) - p_{X_c}], \tag{2.35}$$

where H_W is the weak Hamiltonian as defined in equation 2.34. The kinematic variables, $q^\mu = p_\ell^\mu + p_\nu^\mu$, define the momentum transfer of the W boson transferred to the leptons. The differential decay rate is calculated by summing over all lepton spin orientations and hadronic final states X_c. Since the leptonic final states do not interact strongly with the hadronic system, the matrix element can be decomposed into leptonic and hadronic matrix elements,

$$\frac{\mathrm{d}\Gamma(B \to X_c \ell \nu)}{\mathrm{d}q^2 \mathrm{d}E_\ell \mathrm{d}E_\nu} = 2G_F^2 |V_{cb}|^2 W_{\alpha\beta} L^{\alpha\beta}, \tag{2.36}$$

with $L^{\alpha\beta}$ the spin summed leptonic tensor and $W_{\alpha\beta}$ the hadronic tensor,

$$\begin{aligned} W_{\alpha\beta} = & \sum_{X_c} \frac{(2\pi)^3}{2m_B} \delta^4[p_B - q - p_{X_c}] \\ & \times \left\langle B(p_B)|J^{\dagger\alpha}_{(bc)}|X_c(p_{X_c})\right\rangle \left\langle X_c(p_{X_c})|J^{\beta}_{(bc)}|B(p_B)\right\rangle . \end{aligned} \tag{2.37}$$

Here $J^{\beta}_{(bc)}$ is the left-handed hadronic current as defined in equation 2.34. The optical theorem of QCD relates the hadronic matrix element to the imaginary part of the forward scattering amplitude,

$$W^{\alpha\beta} = -\frac{1}{\pi}\mathrm{Im}\, i \int \mathrm{d}^4x \frac{e^{-iq\cdot x}}{2m_B} \left\langle B|T\left[J^{\dagger\alpha}_{(bc)}(x)J^{\beta}_{(bc)}(0)\right]|B\right\rangle \tag{2.38}$$

$$\equiv -\frac{1}{\pi}\mathrm{Im}\, T^{\alpha\beta}, \tag{2.39}$$

where $T[J^{\dagger\alpha}_{(bc)}(x)J^{\beta}_{(bc)}(0)]$ is the time ordered product of the heavy quark currents.

The hadronic matrix $T^{\alpha\beta}$ can be calculated using the Operator Product Expansion formalism meaning that $T^{\alpha\beta}$ will be expanded in powers of $1/m_b$ as a series of local operators of the heavy quark field. The coefficients of the operators that occur in this expansion can be computed using QCD perturbation theory. The following section will discuss results for total semileptonic rate and for moments of the invariant hadronic mass distribution obtained in the kinetic scheme.

2.5.2 The Kinetic Scheme

For the interpretation of the measured invariant hadronic mass moments and final extraction of the CKM matrix element $|V_{cb}|$ we will use Heavy Quark Expansions calculated in the kinetic scheme. Following up the discussion in the previous section the total semileptonic rate is calculated up to order $1/m_b^3$ as [15],

$$\begin{aligned} \Gamma_{SL}(B \to X_c\ell\nu) = & \frac{G_F^2 m_b^5}{192\pi^3}|V_{cb}|^2(1+A_{ew})A_{pert}(r,\mu) \\ & \times \left[z_0(r)\left(1 - \frac{\mu_\pi^2(\mu) - \mu_G^2(\mu) + \frac{\rho_D^3(\mu)+\rho_{LS}^3(\mu)}{m_b(\mu)}}{2m_b^2(\mu)}\right)\right. \\ & \left. - 2(1-r)^4\frac{\mu_G^2(\mu) + \frac{\rho_D^3(\mu)+\rho_{LS}^3(\mu)}{m_b(\mu)}}{m_b^2(\mu)} + d(r)\frac{\rho_D^3(\mu)}{m_b^3(\mu)} + \mathcal{O}(1/m_b^4)\right], \end{aligned} \tag{2.40}$$

with $r = m_c^2(\mu)/m_b^2(\mu)$. The tree level phase space factor $z_0(r)$ is defined as,

$$z_0(r) = 1 - 8r + 8r^3 - r^4 - 12r^2\ln r, \tag{2.41}$$

and the expression $d(r)$ is given by,

$$d(r) = 8\ln r + \frac{34}{3} - \frac{32}{3}r - 8r^2 + \frac{32}{3}r^3 - \frac{10}{3}r^4. \tag{2.42}$$

The factor $1 + A_{ew}$ accounts for electroweak corrections. It is estimated to be approximately,

$$1 + A_{ew} \approx \left(1 + \frac{\alpha}{\pi}\ln\frac{M_Z}{m_b}\right)^2 \approx 1.014. \tag{2.43}$$

The quantity A_{pert} accounts for perturbative contributions and is estimated to be $A_{pert} \approx 0.908$. The parameter μ denotes the Wilson normalization scale that separates effects from long- and short-distance dynamics. It is chosen to be $\mu = 1\,\text{GeV}$.

The expression in equation 2.40 is in leading order equal to the decay to the free b quark. The leading non-perturbative corrections arise in order $1/m_b^2$. They are controlled by the matrix elements μ_π^2 and μ_G^2 of the kinetic and chromomagnetic operators respectively,

$$\mu_\pi^2(\mu) \equiv -\frac{< B|\bar{b}\vec{D}b|B >_\mu}{2m_B}, \qquad \mu_G^2(\mu) \equiv -\frac{< B|\bar{b}\sigma^{\mu\nu}G_{\mu\nu}b|B >_\mu}{4m_B}. \tag{2.44}$$

Both operators have already been derived as corrections of order $1/m_b$ in the effective Lagrangian of the HQET (cf. equation 2.33). Corrections of order $1/m_b^3$ are defined by the Darwin and "spin-orbital" LS terms,

$$\rho_D^3(\mu) \equiv -\frac{< B|\bar{b}\vec{D}\cdot\vec{E}b|B >_\mu}{4m_B}, \qquad \rho_{LS}^3(\mu) \equiv \frac{< B|\bar{b}(\vec{\sigma}\cdot\vec{E}\times i\vec{D})b|B >_\mu}{2m_B}. \tag{2.45}$$

HQE calculations for other inclusive variables of B meson decays rely on the same set of non-perturbative parameters as the total semileptonic rate. The moments of the invariant hadronic mass distribution in semileptonic decays $B \to X_c\ell\nu$, $< m_X^n >$, measured in this analysis, have been calculated in [14]. They are given by the expressions,

$$\begin{aligned} < m_X^n > (m_b(\mu), m_c(\mu), \mu_\pi^2(\mu), \mu_G^2(\mu), \rho_D^3(\mu), \rho_{LS}^3(\mu); \alpha_s) = \\ V + B(m_b - 4.6\,\text{GeV}) + C(mc - 1.2\,\text{GeV}) \\ + P(\mu_\pi^2 - 0.4\,\text{GeV}^2) + D(\rho_D^3 - 0.1\,\text{GeV}^3) \\ + G(\mu_G^2 - 0.35\,\text{GeV}^2) + L(\rho_{LS}^3 + 0.15\,\text{GeV}^3) \\ + S(\alpha_s - 0.22), \end{aligned} \tag{2.46}$$

where the dependence on the HQE parameters has been linearized relative to meaningful reference values. The coefficients V, B, C, P, D, G, L, and S are of the dimension of proper powers of GeV depending on the order n

of the calculated moment. Numerical values have been calculated in [14] as functions of the minimum lepton momentum p_ℓ^*.

Overall, the HQE in the kinetic scheme up to order $1/m_b^3$ has six free parameters:

- Leading order:
  - $m_b(\mu)$, b quark mass
  - $m_c(\mu)$, c quark mass
- Non-perturbative correction of order $1/m_b^2$:
  - $\mu_\pi^2(\mu)$, kinetic expectation value
  - $\mu_G^2(\mu)$, chromomagnetic expectation value
- Non-perturbative correction of order $1/m_b^3$:
  - $\rho_D^3(\mu)$, Darwin term
  - $\rho_{LS}^3(\mu)$, "spin-orbital" LS term

Furthermore, the theoretical calculation of the total semileptonic rate depends on the CKM matrix element $|V_{cb}|$ and will be used for its extraction in a global fit to hadronic mass moments measured in this analysis combined with other measured moments of the lepton energy spectrum in semileptonic B meson decays and moments of the photon energy spectrum in decay $B \to X_s\gamma$. See section 7 for a description of the applied fit procedure.

Chapter 3

The *BABAR* Experiment

3.1 Introduction

The *BABAR* experiment is located at the Stanford Linear Accelerator Center (SLAC) in California. Its primary physics goal is the precision measurement of the time dependent *CP*-violating asymmetries in the decay of neutral B^0-mesons. Further integral parts of the *BABAR* physics program are the precise measurement of standard model pareters like the angles of the Unitary Triangle α, β, and γ or the CKM matrix elements $|V_{ub}|$ and $|V_{cb}|$. Many of the the involved decays have low branching fractions, typically 10^{-4}. A high luminosity as well as high-performace tracking systems, calorimetry, and particle identification are prerequisite to achieve the formulated goals.

3.2 The PEP-II *B*-Meson Factory

The PEP-II B-meson factory [17] was designed to meet this requirements. As shown in figure 3.1 it consists of a high energy electron storage ring (HER) with a beam energy of 9.0 GeV and a low energy positron storage ring (LER) with a beam energy of 3.1 GeV resulting in an interaction energy in the center of mass frame of $10.58\,\mathrm{GeV}/c^2$ operating is the mass of the $\Upsilon(4S)$ resonance. The produced $\Upsilon(4S)$ resonance decays almost entirely into $\bar{B}^0 B^0$ or $B^+ B^-$ pairs. Due to the asymmetric configuration of the beam energies their decay products are boosted with $\beta\gamma = 0.55$ in the laboratory frame resulting in an average separation of the B-meson decay vertices of $\sim 240\mu$m. This feature allows to reconstruct the vertices of the two B-mesons, to determine their relative decay times, and to extract the time dependence of their decay rates.

Between May 1999 and August 2006 the PEP-II collidered delivered an integrated luminosity of $406.28\,\mathrm{fb}^{-1}$ corresponding to approximately 450×10^6 $B\overline{B}$ pairs. A peak luminosity of $12.069\,\mathrm{cm}^{-2}\mathrm{s}^{-1}$ was reached with 1722 buches and currents of 2900 mA in the LER as well as 1875 mA in the HER.

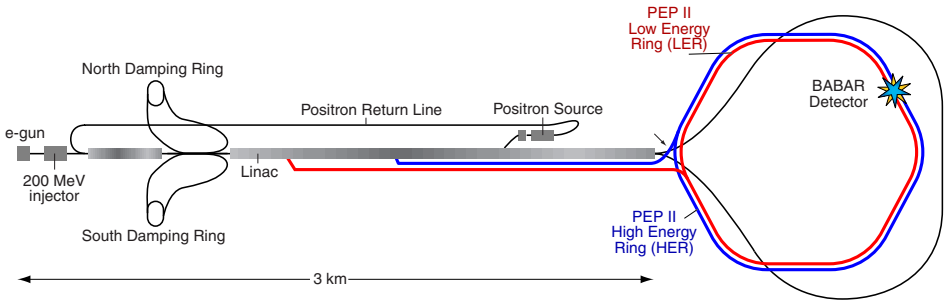

Figure 3.1: The Stanford Linear Collider and $PEP-II$ e^+e^- storage rings.

3.3 The *BABAR* Detector

The *BABAR* detector is a general-purpose megnetic spectrometer. The two primary objectives are

- a precise measurement of charged particle trajectories in order to reconstruct B meson decay vertices with a resolution of $80\,\mu\mathrm{m}^2$. Together with a precise measurement of photon energies B-meson decays to several final states can be reconstructed exclusively with low background and high efficiency.
- the excellent identification of electrons, muons, and kaons with high efficiency and low misidentification rate.

Fig. 3.2 illustrates the layout of the *BABAR* detector. It consists of five subcomponents. Charged particle tracks can be measured with the silicon vertex tracker and the drift chamber. The detector of internally reflected Čerenkov light serves especially for the discrimination of pion and kaon particle types. Electromagnetic showers of electrons and photons can be measured with the electromagnetic calorimeter. The *BABAR* detector is a magnetic spectrometer with a solenoidal superconducting coil operating at a field strength of 1.5 T. Outside of the solenoidal coil the muon and hadron identification system in form of the instrumented flux return is placed.

The *BABAR* coordinate system to be used throughout this document is defined as follows:

- the z axis points parallel to the magnetic field of the solenoid in the direction of the e^- beam.
- the y axis points vertical upwards
- the x axis points horizontally away from the center of the PEP-II rings
- the point of origineis defined as the nominal interaction points of the e^- and e^+ beams.

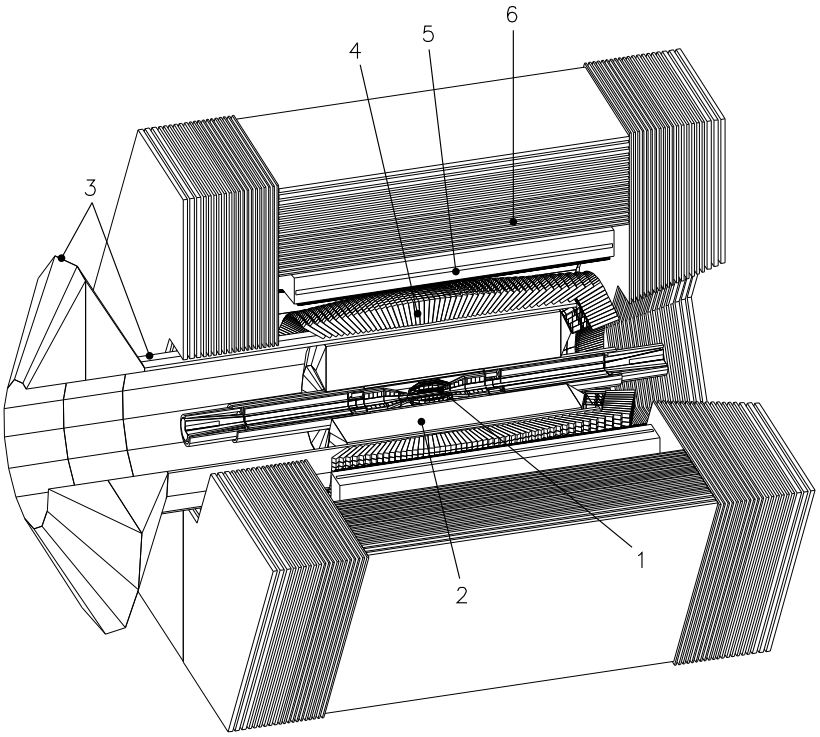

Figure 3.2: Layout of the *BABAR* detector with its sub-detectors: (**1**) Silicon Vertex Tracker (SVT), (**2**) Drift Chamber (DCH), (**3**) Detector of Internally Reflected Čerenkov Light (DIRC), (**4**) Electromagnetic Calorimeter (EMC, (**5**) Solenoid Coil, and (**6**) Instrumented Flux Return (IFR).

See [18] for a detailed description of the detector and its sub-systems. A short overview of the different components will be given in the following sections.

3.3.1 The Silicon Vertex Tracker

The Silicon Vertex Tracker (SVT) provides a tracking system close to the beam pipe which is appropriate to resolve the decay vertices of the two B-mesons. In combination with the drift chamber this allows the reconstruction of exclusive B- and D-meson with a high resolution and low background.

The SVT consists of five concentric layers of double-sided silicon strip sensors organized in 6, 6, 6, 16, and 18 modules, respectively. The silicon strips on the opposite sides of each layer are oriented orthogonally to each other, on one side parallel and on the other transverse to the beam. The innermost layer is located at a distance of 32 mm to the beam while the outermost layer has a distance of $114 - 144$ mm to the beam. The inner three layers give a spatial resolution of $10 - 15\,\mu$m. Layer four and five give a spatial resolution of $\approx 40\,\mu$m.

For low energetic charged particles, like pions from D^* decays, with transverse momenta below $p_t \sim 100\,\mathrm{MeV}/c$ the SVT is the only appropriate tracking device, since such "SVT-only" particles do not reach the drift chamber.

The SVT provides additional information about the ionization dE/dx with up to ten measurements for every track and a resolution of appoximate 14%. It can be utilized for particle identification purposes.

3.3.2 The Drift Chamber

For the detection of charged particles with transverse momenta greater than $p_t \sim 100\,\mathrm{MeV}/c$ and the measurment of their momenta and angles the multi-wire Drift Chamber (DCH) is the main detector. As depicted in figure 3.3 its shape is that of a cylinder with a length of 2764 mm, an inner radius of 236 mm, and an outer radius of 809 mm. The chamber center is offset by 370 mm from the interaction point in the direction of the boost along the z axis. Therefore, it has an asymmetric angular coverage of $17.2° \leq \theta \leq 152.6°$.

The DCH is filled with a 80 : 20 mixture of helium and isobutane and typically operating at 1960 V. It is composed of 7104 small hexagonal drift cells, 11.9 mm by approximately 19.0 mm along the radial and azimuthal directions, arranged in 40 cylindrical layers. Each drift cell is made up of one gold-coated tungsten-rhenium sense wire with a diameter of $20\,\mu$m surrounded by six aluminum field wires with diameters of $80 - 120\,\mu$m. The layers are grouped by four into ten superlayers, with the same wire orientation and equal numbers of cells in each layer of a superlayer. Spatial resolution along the beam line is provided by superlayers with different stereo angles varying between ± 45 mrad and ± 76 mrad. The stereo angles alternate between axial (A) and stereo pairs with positive (U) and negative (V) stereo

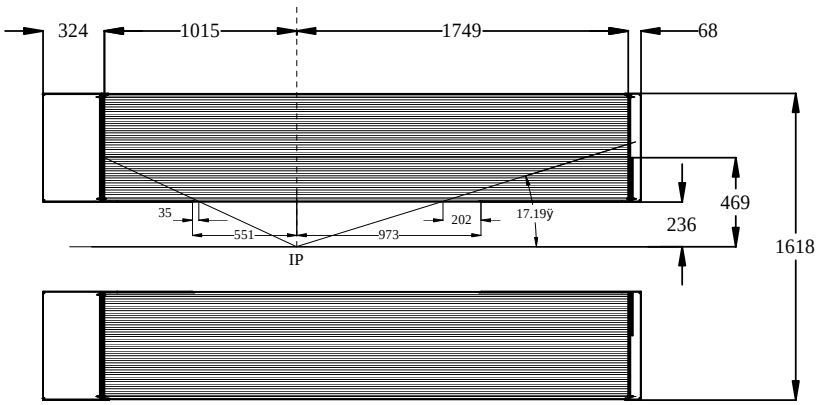

Figure 3.3: The multi-wire Drift Chamber.

angles, in the order AUVAUVAUVA.

The overall achieved resolution of measured charged track momenta is dominated by the DCH and followes the linear dependence,

$$\frac{\sigma_{p_t}}{p_t} = (0.13 \pm 0.01)\% \cdot p_t[\,\mathrm{GeV}/c] + (0.45 \pm 0.03)\%, \tag{3.1}$$

while the position and angular measurements near the interaction point are dominated by the SVT.

The measurement of the specific energy loss dE/dx can be used for particle identification purposes. The dE/dx is derived from the total charge deposited in every drift cell with an average resolution of 7.5%.

3.3.3 The Čerenkov Detector

The Detector of Internally Reflected Čerenkov light (DIRC) is a Čerenkov detector designed for charged particle identification. It consists of 144 bars made of fused silica each with a length of 4.9 m, a thickness of only 17.25 mm, and a width of 35 mm arranged in a 12-sided polygonal barrel. They lead into the instrumented imaging region as picture in figure 3.4.

Charged particles traversing the fused silica with a velocity v greater than the velocity of light c' within the radiator of refractive index $n = 1.473$, i.e. $v > c/n$, emit a cone of light under the Čerenkov angle,

$$\cos\Theta_c = \frac{1}{n\beta} = \frac{\sqrt{1 + \left(\frac{m}{p}\right)^2}}{n}, \tag{3.2}$$

with $\beta = v/c$, m the particle's mass, and p the particle's momentum.

The emitted photons are guided through multiple total internal reflection to the Standoff box. The standoff box contains about 6000 l of purified water

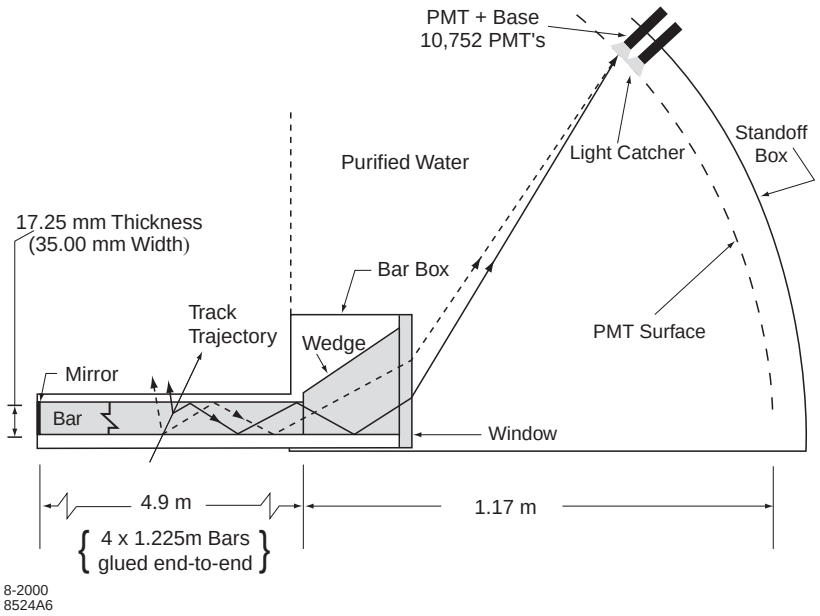

Figure 3.4: The detector of Internally Reflected Čerenkov light (DIRC).

with an index of refraction of $n \approx 1.346$ reasonably close to that of the fused silica and thus minimizing the total internal reflection at the silica-water interface. The Čerenkov light entering the imaging region is detected as cones by an array of 10572 closely packed photo multuplier tubes (PMTs) with 29 mm diameter mounted on the toroidal surface on the back.

Together with the momentum provided by the *BABAR* tracking system the angle Θ_c can be used for particle identification. With a single track resolution of $\Delta\Theta_c = 2.5$mrad for the Čerenkov angle, the DIRC achieves a pion–kaon separation of 4.2σ for particles with momenta of $p = 3\,\mathrm{GeV}/c$.

3.3.4 The Electromagnetic Calorimeter

The Electromagnetic Calorimeter (EMC) is designed to measure electromagnetic showers with a high efficiency, as well as angular and energy resolution over a wide energy range from 20 MeV to 9 GeV. It is the main detector component for the measurement of photons, for instance from π^0 or η decays, and for the identification of electrons with momenta above $700\,\mathrm{MeV}/c$. Its design is shown in figure 3.5.

The EMC consists of a cylindrical barrel and a conical forward endcap with an angular coverage of of $-0.775 \leq \cos\theta \leq 0.962$ and of $-0.916 \leq \cos\theta \leq 0.895$ in the center-of-mass frame.

The barrel consists of 5760 crystals arranged in 48 rings with 120 identical crystals in each ring. The endcap holds 820 crystals arranged in 8 rings. For

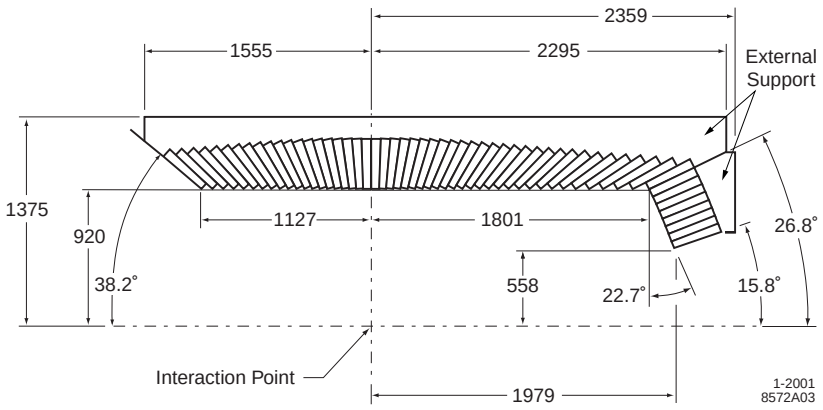

Figure 3.5: The Electromagnetic Calorimeter.

the crystal material thallium-doped CsI was chosen which is characterized by a short radiation length of $X_0 = 1.85\,\text{cm}$ and a Molière radius of $R_m = 3.8\,\text{cm}$. To account for the boost which leads to higher photon energies for smaller polar angles the crystal lengths increase starting from 29.6 cm in the backward to 32.4 cm in the forward direction, corresponding to $16X_0$ and $17.5X_0$, respectively. Their cross sectional area is chosen to be comparable to R_m. Photons from electromagnetic showers developing in the crystals are detected with two silicon photodiodes mounted at the rear of each crystal.

Typically an electromagnetic shower spreads over several adjacent crystals forming acluster of energy deposits. Thus, for the reconstruction of particles an efficient recognition of those clusters is important.

The cluster recognition algorithm starts from a seed crystal with an energy above 10 MeV. Surrounding crystals are considered to be part of the same cluster if their energies exceed a threshold of 1 MeV or if they are contiguous neighbors of crystals with at least 3 MeV. Clusters containing more than one local energy maximum are split into several so called bumps. Using tracking information obtained by the SVT and DCH, it is decided whether a cluster or bump is generated by a neutral or charged particle. If a bump cannot be associated to a charged particle a neutral candidate is created with the measured energy and shower shape, otherwise the EMC information is associated to a charged candidate measured in the tracking system.

Due to accumulating damage of beam-generated radiation a frequent calibration of each individual crystal and clusters has to be performed. At low energies this taks is performed using a radioactive photon source. Slow neutrons are used to irradiate Fluorinert resulting in the decay chain ${}^{19}F + n \rightarrow {}^{16}N + \alpha$, ${}^{16}N \rightarrow {}^{16}O^* + \beta$, ${}^{16}O^* \rightarrow {}^{16}O + \gamma$. The emitted photons have an energy of 6.13 MeV. They can be used for an absolute calibration at this energy scale. For high energies between 3 GeV and 9 GeV the energy calibration is performed with electrons from Bhabha scattering, $e^{\pm} \rightarrow e^{\pm}$.

Starting from a well defined initial state the kinematics of the final state depending on the polar angle is known. Calibration is done by comparison to Monte Carlo simulated Bhabha events. Both calibration methods are combined by a logarithmic interpolation. The overall energy resolution achieved is,

$$\frac{\sigma_E}{E} = \frac{(2.32 \pm 0.30)\%}{\sqrt[4]{E[\,\mathrm{GeV}]}} \oplus (1.85 \pm 0.12)\%. \tag{3.3}$$

The *BABAR* EMC has an angular resolution of,

$$\sigma_\theta = \sigma_\phi = \left(\frac{3.87 \pm 0.07}{\sqrt{E[\,\mathrm{GeV}]}} + 0.00 \pm 0.04 \right) \mathrm{mrad}, \tag{3.4}$$

corresponding to an angular resolution of approximately 12 mrad at low energies and an angular resolution of about 3 mrad at high photon energies.

3.3.5 The Instrumented Flux Return

The Instrumented Flux Return (IFR) is the main sub-system for the identification of muons and neutral hadrons, like K_L^0 and neutrons. It is located outside the solenoidal coil and uses its steel flux return as muon filter and hadron absorber. The IFR covers polar angles between 17° and 157°. Resistive Plate Chambers (RPCs) are installed as detectors between the segmented steel of the barrel and end door of the flux return (cf. figure 3.6). The steel is segmented into 18 plates with increasing thickness, from 2 cm for the inner nine plates to 10 cm for the outermost plate. The total thickness of the steel plates amounts to 65 cm in the barrel and 60 cm in the end door. The nominal gap between the steel plates is 3.5 cm in the inner layers of the barrel and 3.2 cm elsewhere. There are 19 RPC layers in the barrel and 18 in the endcaps. The RPCs are operated in limited streamer mode. Their active volumes are filled with a mixture of argon, freon ($C_2H_2F_4$) and a few percent of Isobutane.

Overall muon identification efficiencies between 65% and 80% with misidentification probabilities between 2% and 4% for pions and between 0.5% and 1% for kaons are achieved for momenta above $p = 1.5\,\mathrm{GeV}/c$.

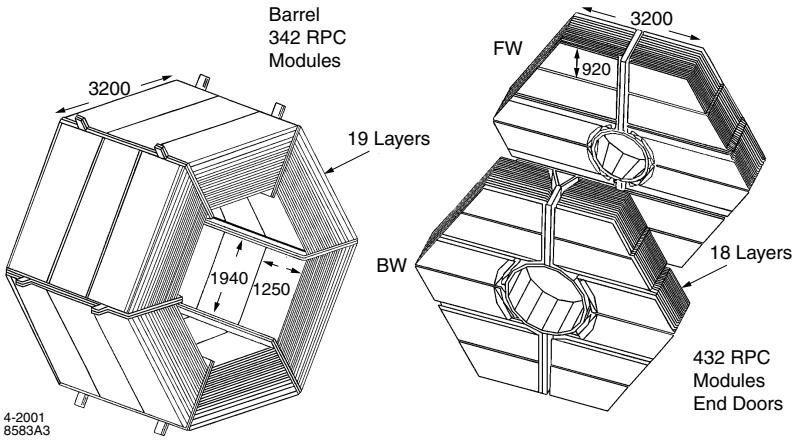

Figure 3.6: The Instrumented Flux Return is located outside the solenoidal coil and uses its steel flux return as muon filter and hadron absorber. Resistive Plate Chambers are installed as detectors between the segmented steel of the barrel (left) and end door (right) of the flux return.

Chapter 4

Outline of the Analysis

Measuring the moments of the invariant hadronic mass spectrum in semileptonic decays $B \to X_c \ell \nu$ requires the identification of all particles belonging to the hadronic system X_c. We employ a technique that fully reconstructs the second B meson in events $e^+e^- \to \Upsilon(4S) \to B\overline{B}$ in several hadronic decay modes, thereby separating its decay products from the hadronic system (see section 5.2 for details). Figure 4.1 illustrates the studied event structure schematically.

After a fully reconstructed B_{reco} candidate has been selected the semileptonic decay of the second B_{SL} meson in the event is identified by requiring one identified lepton among the tracks not assigned to the B_{reco} candidate. Afterwards, all remaining charged tracks and neutral candidates are assigned to the hadronic system X_c of the semileptonically decaying B_{SL}.

Even though it would be preferable for the theoretical interpretation to measure the moments of the invariant hadronic mass spectrum without restriction on the momentum of the lepton, the identification of leptons with low momenta is experimentally complicated. Thus, requiring a minimum lepton momentum is inevitable. We measure the hadronic mass moments for different selection criteria on the minimum lepton momentum between $p^*_\ell \geq 0.8\,\mathrm{GeV}/c$ and $p^*_\ell \geq 1.9\,\mathrm{GeV}/c$ calculated in the restframe of the B_{SL} meson.

To ensure an optimal reconstruction of the undetected neutrino originating from the semileptonic B decay, charged tracks and photons need to be reconstructed with sufficient efficiency and quality. Selection criteria are applied to ensure an efficient selection but suppress misreconsted tracks and photons like "ghost tracks", "loopers", and hadronic split-offs. Furthermore, the applied selection criteria are chosen to improve the agreement of data and MC simulations by avoiding regions with data-MC disagreement. See the sections 5.3.1 and 5.3.2 for a discussion of the charged track and photon selection criteria.

The resolution of the reconstructed hadronic system is limited by missing particles that have not been measured due to the limited acceptance and

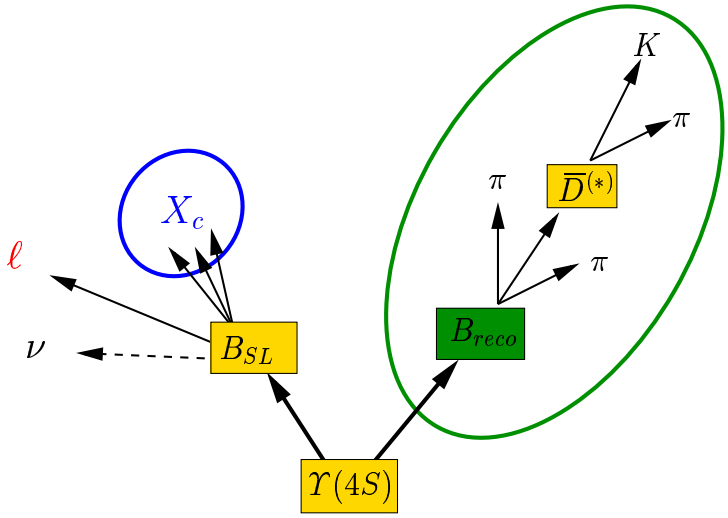

Figure 4.1: Illustration of the studied event structure of decays $\Upsilon(4S) \to B_{reco}B_{SL}(X_c\ell\nu)$. After a fully reconstructed B_{reco} candidate has been selected the semileptonic decay $B_{SL} \to X_c\ell\nu$ is identified by requiring one identified lepton among the tracks not assigned to the B_{reco} candidate. All remaining tracks and photons are assigned to the hadronic system X_c.

resolution of the detector. The missing energy and momentum in the event is calculated by,

$$P_{miss} = P_{\Upsilon(4S)} - P_{B_{reco}} - P_X - P_\ell, \tag{4.1}$$

where $P_{\Upsilon(4S)}$ is the four-momentum of the $\Upsilon(4S)$ produced in the e^+e^- collision, P_ℓ that of the lepton originating from the semileptonic decay, and P_X is the four-momentum of the reconstructed X_c system calculated from the contributing measured particles. The difference of missing energy and momentum, $E_{miss} - |\vec{p}_{miss}|$, is equal to zero within the resolution of the detector if only the neutrino from the semileptonic decay remains unmeasured. To ensure a well reconstructed hadronic system with good resolution the selected events are restricted to the window $|E_{miss} - |\vec{p}_{miss}|| < 0.5\,\text{GeV}$. Starting from a kinematically well defined initial state $e^+e^- \to \Upsilon(4S) \to B\overline{B}$, additional knowledge about the kinematics of the semileptonic final state is exploited in a kinematic fit to improve the overall resolution and reduce the bias of the measured invariant hadronic mass $m_{X,reco}$. The applied event selection criteria and the kinematic fit are described in sections 5.4.1 and 5.4.2, respectively.

By exploiting the observation that the charge of a primary lepton stemming from a semileptonically decaying B meson is correlated with the known flavor of the fully reconstructed B_{reco}, a large fraction of background from subsequent secondary semileptonic decays not originating from $B^0\overline{B}^0$ mix-

ing can be suppressed. Remaining sources of background containing right-charged leptons in the final state and being experimentally indistinguishable from true signal decays are subtracted using MC simulations. The shape and magnitude of combinatorial background stemming from misreconstructed B_{reco} candidates is determined directly on data. The performed background subtraction procedure is described in detail in section 5.6.

Even though the kinematic fit already provides an instrument that allows a reliable measurement of the hadronic system by significantly reducing the average bias of the measured $m_{X,reco}$ distribution, additional corrections have to be applied. For the extraction of moments we utilize a method that "calibrates" the measured and kinematically fitted $m_{X,reco}$ by applying correction factors on an event-by-event basis. The background is subtracted by weighting events according to the fraction of signal events expected in the corresponding part of the $m_{X,reco}$ spectrum. The moments of the invariant hadronic mass distribution $< m_X^n >$ of order $n = 1 \ldots 6$ are determined by calculating the weighted mean,

$$< m_X^n >= \frac{\sum_{i=1}^{N_{evt}} w_i(m_X) m_{X,calib,i}^n}{\sum_i^{N_{evt}} w_i(m_X)} \times \mathcal{C}_{calib} \times \mathcal{C}_{true}. \tag{4.2}$$

The weights $w_i(m_X)$ are the $m_{X,reco}$-dependent background subtraction factors and $m_{X,calib,i}$ is the corrected mass. Additional corrections have to be applied to account for a small remaining bias. Two different bias sources are distinguished:

1. The final extraction of moments suffers from a bias $\mathcal{C}_{calib}$ that is inherent in the applied calibration method itself.

2. The factor $\mathcal{C}_{true}$ corrects for changes in the selection efficiency introduced by the event selection criteria. The $\mathcal{C}_{true}$ also corrects effects introduced by photons emitted in final state radiation.

The moment extration formalism is described in detail in section 5.7. The obtained results are summarized in section 5.8. Systematic studies will be presented in chapter 6.

Chapter 5

Measurement of Hadronic Mass Moments

5.1 Samples of Data and Monte Carlo Simulations

This analysis is based on data recorded between January 2000 and July 2004, Runs 1-4, corresponding to $210.4\,\mathrm{fb}^{-1}$ collected at the $\Upsilon(4S)$ resonance. It comprises a total of $(231.6\pm2.5)\times10^6$ decays of $\Upsilon(4S)\to B\overline{B}$. The number of $B\overline{B}$ pairs is measured by counting hadronic events at the $\Upsilon(4S)$ resonance and subtracting contributions from non-$B\overline{B}$ events using an off-resonance sample recorded 40 MeV below the $\Upsilon(4S)$ resonance [19].

For MC studies three samples of simulated $B\overline{B}$ decays are used:

1. We use a sample of *generator MC* for the determination of residual bias correction factors. Both B mesons decay semileptonically into $B\to X_c\ell\nu$ where the decays in all samples are generated with `EvtGen` [20]. The generator MC does neither incorporate a simulation of the detector response nor the simulation of final state radiation.

2. The *generic MC* is based on a sample of simulated $B\overline{B}$ decays to all possible known final states. A full simulation of the *BABAR* detector based on `GEANT4` [21] is realized. Furthermore it incorporates QED final state radiation simulated with the `PHOTOS` package [22]. The generic MC simulation is used for background studies and the determination of bias correction factors.

3. By contrast to the generator and generic MC samples, in the cocktail MC sample only one of the two B mesons decays generically while the other B decays into one of the hadronic final states $\overline{B}\to D^{(*)+}\pi^-$, $\overline{B}\to D^{(*)+}\rho^-$, and $\overline{B}\to D^{(*)+}a_1^-$. It provides a large sample of clean fully reconstructed B mesons and is used for the construction of the calibration curves. The detector and final state simulation is performed like in the generic MC sample.

Dataset	$N_{B\overline{B}}$
Data	$(231.6 \pm 2.5) \times 10^6$
Generic MC ($B^0\overline{B}^0$)	546.50×10^6
Generic MC (B^+B^-)	544.52×10^6
Cocktail MC ($B^0\overline{B}^0$)	26.49×10^6
Cocktail MC (B^+B^-)	6.28×10^6
Generator MC	23.94×10^6

Table 5.1: Summary of datasets. Given is the overall number of decays $\Upsilon(4S) \to B\overline{B}$.

Approximate numbers of simulated $B^0\overline{B}^0$ and B^+B^- decays are summarized in table 5.1 for all three MC samples.

5.2 Semi-Exclusive Reconstruction of B_{reco}

In the following section the method applied for the full reconstruction of one of the B mesons in the event will be described. It follows a formalism developed and commonly used within the *BABAR* collaboration called "semi-exclusive reconstruction". A more detailed discussion can be found in [23].

5.2.1 Reconstruction Formalism

The semi-exclusive reconstruction implements a procedure to reconstruct hadronic decays $B^0_{reco} \to D^{(*)-}Y^+$ and $B^+_{reco} \to \overline{D}^{(*)0}Y^+$. The hadronic system Y^+ is composed of $\mathrm{n}_\pi\pi^\pm$, $\mathrm{n}_K K^\pm$, $\mathrm{n}_{K^0_S} K^0_S$, and $\mathrm{n}_{\pi^0}\pi^0$ with n_i the number of $\pi^\pm$, $K^\pm$, $K^0_S \to \pi^+\pi^-$, and $\pi^0 \to \gamma\gamma$. Starting from a fully reconstructed $D^{(*)-}$ or $\overline{D}^{(*)0}$ one charged track is added to form a "seed" compatible with the charge of the B_{reco} candidate meant to be reconstructed. Thereupon, the reconstructed seed is combined iteratively with neutral π^0 and K^0_S candidates, as well as pairs of charged tracks $\pi^\pm$ and $K^\pm$ to form a B_{reco} candidate. The final composition of the hadronic system Y^+ is constrained by the following boundary conditions:

$$\begin{aligned} \mathrm{n}_\pi + \mathrm{n}_K &\leq 5, \\ \mathrm{n}_{K^0_S} &\leq 2, \\ \mathrm{n}_{\pi^0} &\leq 2. \end{aligned} \tag{5.1}$$

To suppress combinatorial background and to divide single decay channels into submodes with different purity additional cuts are applied on the invariant mass of the Y^+ system depending on its composition. Table 5.2 summarizes all possible reconstructed combinations adding up to a total number of 52 modes where the definition of the different modes depends also on the reconstructed invariant Y^+ mass.

Decay mode Y^+	N_{Y^+}
h	2
$h\,\pi^0$	4
$3h$	7
$h\,2\pi^0$	4
$3h\,\pi^0$	7
$3h\,2\pi^0$	6
$5h$	6
$5h\,\pi^0$	4
$K_S^0\,h\,(\pi^0)(\pi^0)$	6
$K_S^0\,h\,2\pi^{\pm}\,(\pi^0)$	5
$K_S^0\,K_S^0\,X$	1
total	52

Table 5.2: Summary of reconstructed compositions of the hadronic system Y^+. The first column defines the composition of the hadronic Y^+ system where h stands either for a reconstructed charged $\pi^{\pm}$ or $K^{\pm}$ candidate. The second column gives the number of defined modes. The definition of the different modes depends also on the invariant hadronic Y^+ mass.

Table 5.3 summarizes all reconstructed B_{reco} modes. Depending on the reconstructed mode not all possible Y^+ configurations are considered. For the decays $B^0_{reco} \to D^- Y^+$ all modes $Y^+ = 5h\,\pi^0$ and $3h\,2\pi^0$ are left out of consideration. The D^{*-} meson is reconstructed in the channel $D^{*-} \to \overline{D}^0\pi^-$. Nevertheless, a large fraction of the decays $D^{*-} \to D^-\pi^+$ contained in the reconstructed decays $D^- \to K^+\pi^-\pi^-\pi^0$ and $D^- \to K^0_S\pi^-\pi^0$ can be recovered by requiring that the difference between the invariant masses of the $D^-\pi^0$ system and the D^- system are compatible with a D^{*-} decay, e.g. $0.1366 < \Delta m \equiv m(K^+\pi^-\pi^-\pi^0) - m(K^+\pi^-\pi^-) < 0.1446\,\mathrm{GeV}/c^2$.

5.2.2 Kinematic Variables

Fully reconstructed B_{reco} decays will be described throughout this document using two kinematic variables, the energy difference ΔE and the energy-substituted mass m_{ES}. Both variables are constructed to be minimally correlated. The energy difference is

$$\Delta E = E^*_{B_{reco}} - E^*_{beam}, \tag{5.2}$$

with $E^*_{B_{reco}}$ the energy of the reconstructed B_{reco} candidate and E^*_{beam} the beam energy. Both quantities are calculated in the restframe of the e^+e^- beams. Measured values of ΔE are expected to be close to zero within detector resolution for well reconstructed B_{reco} mesons.

B_{reco} decay mode		N_{modes}
$B^0_{reco} \to D^{*-}Y^+$	$D^{*-} \to \overline{D}^0\pi^-$, $\overline{D}^0 \to K^+\pi^-$	52
	$D^{*-} \to \overline{D}^0\pi^-$, $\overline{D}^0 \to K^+\pi^-\pi^0$	52
	$D^{*-} \to \overline{D}^0\pi^-$, $\overline{D}^0 \to K^+\pi^-\pi^+\pi^-$	52
	$D^{*-} \to \overline{D}^0\pi^-$, $\overline{D}^0 \to K^0_S\pi^-\pi^+$	52
$B^+_{reco} \to \overline{D}^{*0}Y^+$	$\overline{D}^{*0} \to \overline{D}^0\pi^0$, $\overline{D}^0 \to K^+\pi^-$	52
	$\overline{D}^{*0} \to \overline{D}^0\pi^-$, $\overline{D}^0 \to K^+\pi^-\pi^0$	52
	$\overline{D}^{*0} \to \overline{D}^0\pi^-$, $\overline{D}^0 \to K^+\pi^-\pi^+\pi^-$	52
	$\overline{D}^{*0} \to \overline{D}^0\pi^-$, $\overline{D}^0 \to K^0_S\pi^-\pi^+$	52
	$\overline{D}^{*0} \to \overline{D}^0\gamma$, $\overline{D}^0 \to K^+\pi^-$	52
	$\overline{D}^{*0} \to \overline{D}^0\gamma$, $\overline{D}^0 \to K^+\pi^-\pi^0$	52
	$\overline{D}^{*0} \to \overline{D}^0\gamma$, $\overline{D}^0 \to K^+\pi^-\pi^+\pi^-$	52
	$\overline{D}^{*0} \to \overline{D}^0\gamma$, $\overline{D}^0 \to K^0_S\pi^-\pi^+$	52
$B^0_{reco} \to D^-Y^+$	$D^- \to K^+\pi^-\pi^-$	42
	$D^- \to K^0_S\pi^-$	42
	$D^- \to K^0_S\pi^-\pi^0$	43
	$D^- \to K^+\pi^-\pi^-\pi^0$	43
	$D^- \to K^0_S\pi^-\pi^+\pi^-$	42
$B^+_{reco} \to \overline{D}^0Y^+$	$\overline{D}^0 \to K^+\pi^-$	52
	$\overline{D}^0 \to K^+\pi^-\pi^0$	52
	$\overline{D}^0 \to K^+\pi^-\pi^+\pi^-$	52
	$\overline{D}^0 \to K^0_S\pi^-\pi^+$	52
total		1044

Table 5.3: Summary of modes considered in the semi-exclusive B_{reco} reconstruction.

The energy-substituted mass,

$$m_{\mathrm{ES}} = \sqrt{\left(E^*_{beam}\right)^2 - \vec{p}^{*2}_{B_{reco}}}, \tag{5.3}$$

defines the invariant mass of the reconstructed B_{reco} candidate constraining the energy difference ΔE to 0 MeV. It is calculated in the restframe of the beams from the beam energy and the momentum $\vec{p}^{*2}_{B_{reco}}$ of the B_{reco} candidate. Measured values of m_{ES} are expected to correspond with the true B meson mass within detector and storage-ring energy resolution.

As outlined in [24], calculating m_{ES} using beam energies as reported by PEP-II leads to fluctuating mean B meson masses in the m_{ES} peak. This implies an imprecise E_{beam} measurement. Corrections to the PEP-II energies have been computed for different run ranges [25,26]. Applying those corrections shifts the m_{ES} peak to the nominal B meson mass [12].

5.2.3 Selection of the Best B_{reco} Candidate

Reconstructed B_{reco} candidates are preselected by applying cuts on ΔE depending on the composition of the hadronic Y^+ system. The following ΔE windows are chosen,

$$\begin{aligned}
-45 < \Delta E < 30\,\mathrm{MeV} \quad & \text{for } 3h, \\
|\Delta E| < 45\,\mathrm{MeV} \quad & \text{for } h \text{ and } K^0_S\, h, \\
|\Delta E| < 48\,\mathrm{MeV} \quad & \text{for } 5h \text{ and } K^0_S\, 3h, \\
|\Delta E| < 50\,\mathrm{MeV} \quad & \text{for } K^0_S\, K^0_S\, X, \\
-90 < \Delta E < 60\,\mathrm{MeV} \quad & \text{for all remaining modes including a } \pi^0,
\end{aligned} \tag{5.4}$$

corresponding to 3 standard deviations of the ΔE distribution specific to the selected mode. The mode specific resolutions are determined prior to the B_{reco} candidate selection by fitting the ΔE distributions with a linear background and a Gaussian signal functions for modes without π^0 in the final state. To avoid biasing the ΔE distribution towards small values a common window for all modes containing at least one π^0 is determined from the cleanest modes. Reconstructed B_{reco} candidates are preselected by requiring $m_{\mathrm{ES}} > 5.20\,\mathrm{GeV}/c^2$.

All possible channels are ranked according to their purity,

$$\mathcal{P} = \frac{N_{signal}}{N_{signal} + N_{bg}}, \tag{5.5}$$

with N_{signal} the number of signal and N_{bg} the number of misreconstructed B_{reco} candidates. After the application of the preselection cuts on ΔE and m_{ES} the B_{reco} candidate with the highest purity is retained.

Figure 5.1 shows the number of reconstructed B_{reco} candidates per event after the application of the preselection criteria on ΔE and m_{ES}. The left

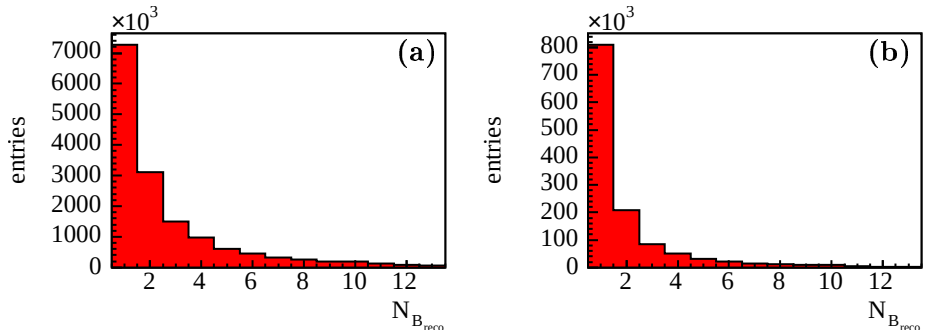

Figure 5.1: Number of B_{reco} candidates per event, $N_{B_{reco}}$, after the application of preselection criteria. Plot (a) shows the $N_{B_{reco}}$ distribution for all B_{reco} mode. Plot (b) shows the $N_{B_{reco}}$ for a subset of modes with $\mathcal{P} > 28\%$ for each individual mode corresponding to a sample with a total purity of 60% as it will be selected in final event selection.

plot in figure 5.1 shows the $N_{B_{reco}}$ distribution for all reconstructed B_{reco} modes. About 47% of all events contain only one reconstructed candidate. In 20% of all events we find a second reconstructed B_{reco} candidate. If the selection of candidates is restricted to modes with $\mathcal{P} > 28\%$ for each individual mode corresponding to a sample with a total purity of 60% as it will be selected in final event selection, we find 64% and 17% of all events with one and two B_{reco} candidates, respectively. Figure 5.1b shows the corresponding $N_{B_{reco}}$ distribution.

Having chosen the best B_{reco} candidate a kinematic fit is performed [27]. Thereby, masses of intermediate states $D^{(*)}$, K^0_S, π^0 are constrained to their nominal masses [12]. By performing the kinematic fit the four-vector of the reconstructed B_{reco} candidate is changed, which is why also the values of the corresponding kinematic variables ΔE and m_{ES} are changed and have to be recalculated.

The m_{ES} distribution for the selected B_{reco} candidates is shown in figure 5.2 for different subsets of B_{reco} modes. Figure 5.2a shows the m_{ES} distribution for all possible modes with an overall purity of 28%. Restricting the selected modes to those with $\mathcal{P} > 7\%$ (figure 5.2b) and $\mathcal{P} > 28\%$ (figure 5.2c) results in overall purities of 40% and 60%, respectively. The selection criteria leading to an overal purity of 60% corresponds to that used in the final event selection. Requiring a selected lepton among the tracks not associated to the B_{reco} candidate improves the purity of the selected sample since semileptonic decays are usually characterized by lower track and photon multiplicities than hadronic decays reducing the number of random combinations. We find an overall purity of 78% as depicted in figure 5.2d.

Figure 5.3 shows the ΔE distributions for the selected B_{reco} candidates for different subsets of B_{reco} modes. While figure 5.3a shows the distribution

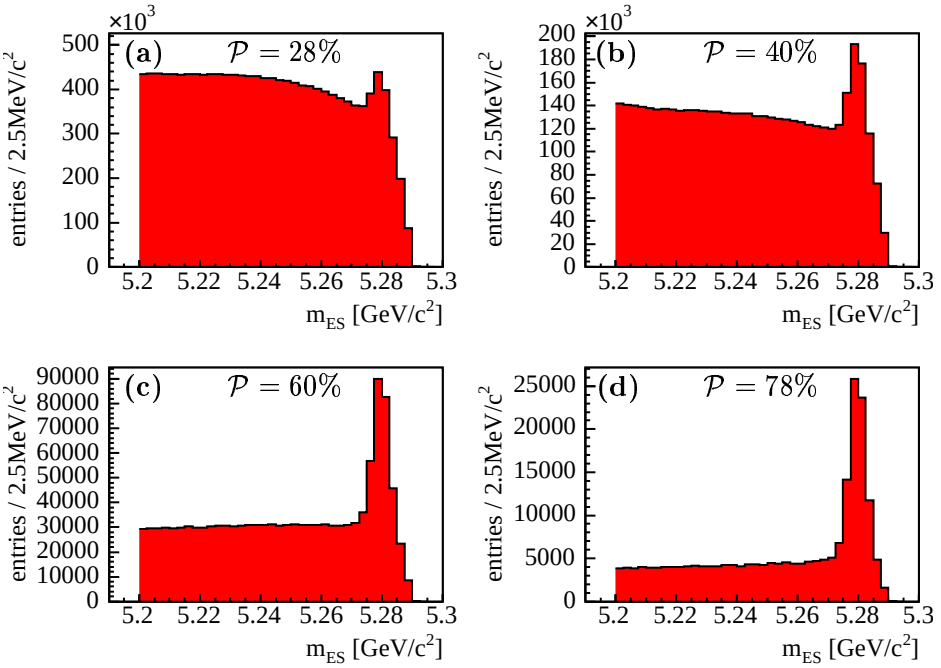

Figure 5.2: Distributions of m_{ES} for the best B_{reco} candidate and different criteria on the purity of the selected modes: all modes (a), a subset of modes with $\mathcal{P} > 7\%$ (b), a subset of modes with $\mathcal{P} > 28\%$ (c), and a subset of modes with $\mathcal{P} > 28\%$ and a selected lepton among the tracks not associated to the B_{reco} candidate (d).

for all reconstructed modes, only a subset of modes with $\mathcal{P} > 28\%$ and a lepton among the tracks not associated to the B_{reco} candidate is selected in figure 5.3b. The edges in both distributions are caused by the preselection cuts on ΔE.

5.3 Particle Selection for the Signal B Meson

After a fully reconstructed B_{reco} candidate has been selected all remaining charged tracks and neutral candidates are assigned to the decay of the second B_{SL} meson in the event. Among those a subset is selected applying selection criteria that have been developed to improve the agreement of data and MC simulations by avoiding regions with large data-MC differences while retaining a sufficient selection efficiency [28, 29]. Charged track selection criteria are summarized in table 5.4 while table 5.5 summarizes all photon selection criteria.

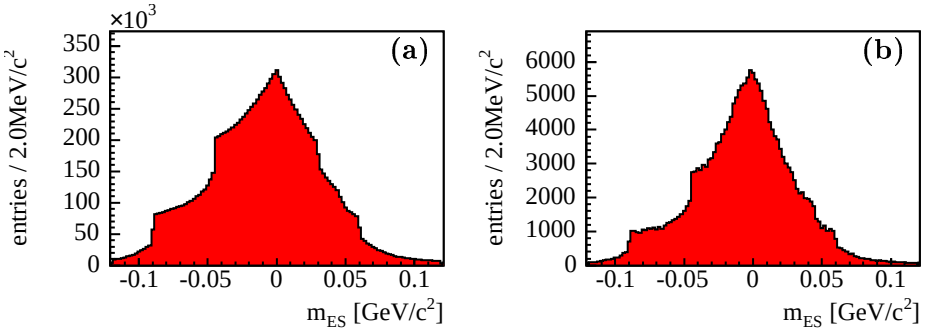

Figure 5.3: Distributions of ΔE for the best B_{reco} candidate and different criteria on the purity of the selected modes: all modes (a) and a subset of modes with $\mathcal{P} > 28\%$ and a selected lepton among the tracks not associated to the B_{reco} candidate (b).

5.3.1 Charged Track Selection

Charged tracks are reconstructed using combined information obtained from the two *BABAR* tracking systems: the DCH and SVT. Therebye, the applied track selection follows two principal guidelines. To ensure an optimal reconstruction of the unmeasured neutrino originating from the semileptonic B decay, tracks need to be reconstructed with sufficient efficiency and quality. At the same time it is desirable to suppress misreconstructed "additional" tracks like ghosts and loopers that result from misfeatures of the tracking algorithm. Reconstructed tracks have to fulfill the following requirements:

1. $0.41 \leq \theta \leq 2.54$, with θ the track's polar angle in the laboratory. Since a reliable particle identification relies on information provided by the EMC, tracks are restricted to its acceptance.

2. $p < 10\,\mathrm{GeV}/c$ removes tracks with momenta p not compatible with the beam energies.

3. $|d_{xy}| < 1.5\,\mathrm{cm}$ and $|d_z| < 5\,\mathrm{cm}$, where d_{xy} and d_z refer to the distance of closest approach to the primary vertex in the plane perpendicular and along the beam axis, respectively. Both cuts aim at a discrimination against tracks not originating from beam-beam interactions.

4. $p_t > 60\,\mathrm{MeV}/c$, with p_t the component of the momentum vector transverse to the beam axis. This cut ensures a minimum transverse momentum required for a reliable measurement.

5. $p_t < 200\,\mathrm{MeV}/c$. This cut is only applied to SVT-only tracks, that is to tracks that have not been measured with the DCH.

6. Charged particles with transverse momenta $p_t \lesssim 360\,\mathrm{MeV}/c$ that do not reach the EMC can loop within the tracking system of the *BABAR* detector. The helix of the corresponding track is usually reconstructed by the tracking algorithm as several smaller segments, one for every half-turn of the loop. Half of the reconstructed segments are identified as positively charged the other half as negatively charged particles. Looper candidates are identified by selecting pairs of charged tracks with $p_t^i < 250\,\mathrm{MeV}/c$, $\cos\theta^i < 0.2$, and $|\Delta p_t| \equiv |p_t^i - p_t^j| < 120\,\mathrm{MeV}/c$, where p_t^i and p_t^j are the transverse momenta of the first and second looper candidate, respectively. Two cases have to be distinguished. First, if the particle loops one time the tracking algorithm will reconstruct two charged particles with opposite charge, $q^i q^j < 0$, going back-to-back. Second, if the particle loops a second time the second loop will be reconstructed as a particle with the same charge, $q^i q^j > 0$, and same angles Θ and ϕ.

   Looper candidates are selected by applying the following cuts:

$$\begin{aligned}
&|\Delta\phi| < 0.1 && \text{if } q^i q^j > 0,\\
&|\pi - \Delta\phi| < 0.1 && \text{if } q^i q^j < 0,\ \Delta\phi > \frac{\pi}{2},\\
&|\pi + \Delta\phi| < 0.1 && \text{if } q^i q^j < 0,\ \Delta\phi < -\frac{\pi}{2},\\
&|\Delta\Theta| < 0.1 && \text{if } q^i q^j > 0,\\
&|\pi - \Delta\Theta| < 0.1 && \text{if } q^i q^j < 0,
\end{aligned}$$

   where q^i and q^j are the charges of the first and second looper candidates, respectively. Finally, the candidate with the smallest impact parameter d_z is retained while the other looper candidates are rejected.

7. If the tracking algorithm reconstructs two tracks from a single physical particle we call one of them a ghost track. The tracking algorithm splits the DCH hits of the physical particle into two separate tracks both following the same trajectory. Ghost candidates are selected by applying the following cuts on pairs of charged particles:

$$\begin{aligned}
&p_t^i < 350\,\mathrm{MeV}/c,\\
&|\Delta p_t| < 150\,\mathrm{MeV}/c,\\
&|\Delta\phi| < 0.1,\\
&|\Delta\Theta| < 0.1,\\
&N^1_{\mathrm{DCH}} < 45 - N^2_{\mathrm{DCH}},
\end{aligned}$$

   where N^1_{DCH} is the number of hits in the DCH. Track 1 is taken to have the greater number of DCH hits. From selected pairs of charged ghost track candidates the one with the greater number of hits in the DCH is retained while the second track is rejected.

Polar angle	$0.41 \leq \theta \leq 2.54$
Momentum	$p < 10\,\mathrm{GeV}/c$
Impact parameter	$\lvert d_{xy}\rvert < 1.5\,\mathrm{cm}$, $\lvert d_z\rvert < 5\,\mathrm{cm}$
Transverse momentum	$p_t > 60\,\mathrm{MeV}/c$
	$p_t < 200\,\mathrm{MeV}/c$ for SVT-only tracks
Looper rejection	$p_t^i < 250\,\mathrm{MeV}/c$
	$\cos\theta^i < 0.2$
	$\lvert\Delta p_t\rvert < 120\,\mathrm{MeV}/c$
	$\lvert\Delta\phi\rvert < 0.1$ if $q^i q^j > 0$
	$\lvert\pi - \Delta\phi\rvert < 0.1$ if $q^i q^j < 0$, $\Delta\phi > \frac{\pi}{2}$
	$\lvert\pi + \Delta\phi\rvert < 0.1$ if $q^i q^j < 0$, $\Delta\phi < -\frac{\pi}{2}$
	$\lvert\Delta\Theta\rvert < 0.1$ if $q^i q^j > 0$
	$\lvert\pi - \lvert\Delta\Theta\rvert\rvert < 0.1$ if $q^i q^j < 0$
	retain candidate with the smallest d_z
Ghost rejection	$p_t^i < 350\,\mathrm{MeV}/c$
	$\lvert\Delta p_t\rvert < 150\,\mathrm{MeV}/c$
	$\lvert\Delta\phi\rvert < 0.1$
	$\lvert\Delta\Theta\rvert < 0.1$
	$N^1_{\mathrm{DCH}} < 45 - N^2_{\mathrm{DCH}}$
	Track 1 with the greater number of DCH hist is retained

Table 5.4: Summary of track selection criteria. A detailed discussion can be found in section 5.3.1.

5.3.2 Neutral Candidate Selection Criteria

Photons are measured as clusters in the EMC that comply with the following criteria:

1. $N_{\text{crys}} > 2$, with N_{crys} the number of crystals in the cluster.

2. $E_{\text{clus}} > 50\,\text{MeV}$, where E_{clus} is the deposited energy in the EMC cluster.

3. LAT < 0.6. The variable LAT is the lateral moment of EMC cluster, defined as

$$\text{LAT} = \frac{\sum_{i=3}^{N_{\text{crys}}} E_{\text{crys},i} r_i^2}{E_{\text{crys},1} r_0^2 + E_{\text{crys},2} r_0^2 + \sum_{i=3}^{N_{\text{crys}}} E_{\text{crys},i} r_i^2}, \tag{5.6}$$

   with $E_{\text{crys},i}$ the energy of crystal i. Energies are ordered starting from the highest energetic crystals $E_{\text{crys},1}$ and $E_{\text{crys},2}$ such that $E_1 > E_2 > \ldots > E_{N_{\text{crys}}}$. The parameter r_i defines the distance of crystal i to the center of the cluster while r_0 is defined as the average distance of two adjacent crystals, approximately 5 cm for the EMC of the *BABAR* detector.

   The variable LAT describes the lateral energy distribution of the cluster and varies between 0 and 1. Electromagnetic showers like those produced by electrons or photons are characterized by small values of LAT, i.e. energies are mostly concentrated in few central crystals. In contrast hadronic showers give large values of LAT.

4. $0.32 < \theta_{\text{clus}} < 2.44$, where θ_{clus} is the polar angle of the cluster's centroid. This selection criteria ensures that the whole cluster is entirely located inside the EMC.

5. $\Delta\alpha \equiv \arccos\left[\cos\theta_{\text{clus}}\cos\theta_{\text{trk}} + \sin\theta_{\text{clus}}\sin\theta_{\text{trk}}\cos(\phi_{\text{clus}} - \phi_{\text{trk}})\right] > 0.08$ is calculated as angular difference between the angles θ_{clus} and ϕ_{clus} of a measured cluster and the angles θ_{trk} and ϕ_{trk} of the impact point of the nearest track at the surface of the EMC. This selection criteria aims at the suppression of split-off clusters that are separated from the points of impact of their associated track and thus remain erroneously unassigned. If the nearest track is identified as an electron no photon selection based on $\Delta\alpha$ is performed.

5.3.3 Particle Identification

In order to distinguish between different particle types combined information obtained from the different *BABAR* subdetectors SVT, DCH, DIRC, EMC, and IFR is used. Each charged track is assigned a specific particle type chosen among $e^{\pm}$, $\mu^{\pm}$, $K^{\pm}$, $\overset{(-)}{p}$, and $\pi^{\pm}$. The mass of the specific particle is

Number of crystals	$N_{\text{crys}} > 2$
Cluster energy	$E_{\text{clus}} > 50\,\text{MeV}$
Lateral energy moment	$\text{LAT} < 0.6$
Polar angle	$0.32 < \theta_{\text{clus}} < 2.44$
Difference of angle to nearest track	$\Delta\alpha > 0.08$

Table 5.5: Summary of neutral candidate selection criteria. A detailed discussion can be found in section 5.3.2.

chosen accordingly. For the particle type assignment different selectors are utilized.

1. A likelihood based selector is used for the identification of electrons ("`PidLHElectrons`") [30] that combines information from EMC, DCH, and DIRC. Discriminating variables are the deposited energy in the EMC E_{dep}/p, the lateral shower shape LAT as defined in equation 5.6, the longitudinal EMC shower shape, the Čerenkov angle θ_C measured in the DIRC, and the energy loss per unit distance $\mathrm{d}E/\mathrm{d}x$ in the DCH. Overall a selection efficiency above 90% is achieved for electron momenta above $p = 0.8\,\text{GeV}/c$ in the laboratory. The misidentification probabilities in this momentum region are below 2‰ and 5‰ for π and K, respectively.

2. We utilize a neural net based selector for the identification of muons ("`muNNTight`") [31] mainly based on information obtained from the IFR. The achieved muon identification efficiency is found to be between 65% and 80% for momenta above $p = 1.5\,\text{GeV}/c$ and drops to only 50% for momenta at $p = 0.9\,\text{GeV}/c$. Misidentifaction probabilities lie between 2% and 4% for π and between 0.5% and 1% for K.

3. Kaons are identified using a neural net based kaon selector ("`KLHTight`") [32] with an overall selection efficiencies between 80% and 90% for momenta between $0.5\,\text{GeV}/c$ and $3\,\text{GeV}/c$. The probability to misidentify a π as a K is below 2% in the aforementioned momentum region.

4. Protons are identified utilizing a standard *BABAR* likelihood based selector ("`pLHTight`"). Overall, selection efficiencies above 85% are achieved with a maximum efficiency near 100% for $p = 600\,\text{MeV}/c$. Pions and kaons are misidentified as protons with probabilities between 1% and 2% for momenta above $1.2\,\text{GeV}/c$ and well below 1% for momenta below $1\,\text{GeV}/c$.

Tracks not identified as leptons, kaons, or protons are assumed to be pions.

5.4 Reconstruction of the Hadronic System

The selected charged tracks and photons recoiling against the fully reconstructed B_{reco} are associated to the decay of the second B meson in the event referred to as B_{SL}. The hadronic system X_c of the semileptonic signal decay $B \to X_c \ell \nu$ is reconstructed from those particles that have not been identified as lepton, e or μ, by calculating its four-momentum,

$$P_X = \sum_{i=1}^{N_{trk,X}} P_{i,trk} + \sum_{j=1}^{N_{\gamma,X}} P_{j,\gamma}, \tag{5.7}$$

where N_{trk} and N_γ are the number of tracks and photons not associated with the B_{reco} candidate or identified as lepton. The four-momentum of the unmeasured neutrino is estimated by calculating the missing four-momentum in the event,

$$P_{miss} = P_{\Upsilon(4S)} - P_{B_{reco}} - P_X - P_\ell, \tag{5.8}$$

with $P_{\Upsilon(4S)}$ the four-momentum of the $\Upsilon(4S)$ produced in the e^+e^- collision and P_ℓ the four-momentum of the lepton originating from the semileptonic decay.

The four-momentum of the B_{SL} is calculated from $P_{B_{SL}} = P_{\Upsilon(4S)} - P_{B_{reco}}$ and will be used in the following to calculate kinematic quantities in the restframe of the recoiling B_{SL}.

In the following sections further steps in the reconstruction of the hadronic X_c system will be discussed. In section 5.4.1 event based selection criteria will be discussed followed by a description of the kinematic fit in section 5.4.2 used to improve the resolution and reduce the bias of the X_c reconstruction. A summary of all event based selection criteria can be found in table 5.6.

5.4.1 Event Selection Criteria

We apply the following event based selection criteria to improve the selection of well reconstructed semileptonic signal decays and suppress background.

1. $\mathcal{P}_{int} > 60\%$, where $\mathcal{P}_{int}$ is the integrated purity of the B_{reco} candidate. The integrated purity of a given B_{reco} mode j is defined as the overall purity of all individual modes i with greater or equal purity, $\mathcal{P}_i \geq \mathcal{P}_j$,

$$\mathcal{P}_{int,j} = \frac{\sum_{i,\mathcal{P}_i \geq \mathcal{P}_j} N_{signal,i}}{\sum_{i,\mathcal{P}_i \geq \mathcal{P}_j} N_{signal,i} + \sum_{i,\mathcal{P}_i \geq \mathcal{P}_j} N_{bg,i}}, \tag{5.9}$$

   where $N_{signal,i}$ and $N_{signal,i}$ are the number of signal and background events of mode i, respectively. As described in section 5.2.3 all B_{reco} reconstruction modes are ranked according to their purity. Starting from the decay mode with the highest purity and adding modes one after another with decreasing purity the purity of the resulting sample is called integrated purity.

2. $|\Delta E| < 90\,\text{MeV}$, where ΔE is the energy difference of the fully reconstructed B_{reco} candidate as defined in equation 5.2. The 90 MeV window corresponds to about three standard deviations of the ΔE distribution.

3. $m_{\text{ES}} > 5.27\,\text{GeV}/c^2$, with m_{ES} the energy substituted mass of the B_{reco} candidate as defined in equation 5.3. The cut defines the signal region of the m_{ES} distribution and is efficient in suppressing background comprising of misreconstructed B_{reco} candidates. Remaining combinatorial background present in the signal region will be subtracted using the sideband of the distribution. A detailed discussion of the applied procedure can be found in section 5.6.1.

4. We require that exactly one lepton, either an electron or muon, is identified among the tracks not associated with the B_{reco} candidate. By requiring exactly one lepton additional unmeasured neutrinos stemming from secondary semileptonic decays are suppressed which would otherwise contribute to the missing momentum and energy in the event.

5. $q_{b_{reco}} q_\ell < 0$. The charge of the single reconstructed lepton is required to be compatible with that of a primary lepton emerging from a semileptonic B decay. In this context we exploit the observation that the primary lepton's charge and the flavor of the B_{reco} meson are correlated. The expression $q_{b_{reco}} q_\ell < 0$ is fulfilled for "right-charged" primary leptons, with $q_{b_{reco}}$ the charge of the b or $\overline{b}$ quark in the B_{reco} meson and q_ℓ the charge of the lepton. Apart from that originating from $B^0\overline{B}^0$ osciallations, a large amount of residual background stemming from subsequent decays of the B_{SL} is suppressed by rejecting events with "wrong-charged" leptons, $q_{b_{reco}} q_\ell > 0$.

6. $p^*_\ell \geq p^*_{\ell,cut}\,\text{GeV}/c$. The analysis is performed for several cuts on the lepton momentum between $p^*_{\ell,cut} = 0.8\,\text{GeV}/c$ and $p^*_{\ell,cut} = 1.9\,\text{GeV}/c$. The lepton's momentum is calculated in the restframe of the B_{SL} meson [1]. The smallest accepted lepton momentum $p^*_{\ell,cut} = 0.8\,\text{GeV}/c$ is chosen to avoid regions of the phase space in which the used particle type selectors are characterized by higher probabilities to misidentify a hadron as a lepton.

7. $|E_{miss} - |\vec{p}_{miss}|| < 0.5\,\text{GeV}$, $E_{miss} > 0.5\,\text{GeV}$, and $|\vec{p}_{miss}| > 0.5\,\text{GeV}/c$. The difference of missing energy and momentum, $|E_{miss} - |\vec{p}_{miss}||$, is equal to zero within the resolution of the detector if only the neutrino from the semileptonic decay remains unmeasured. If there are unmeasured tracks or photons in the event positive values of $|E_{miss} - |\vec{p}_{miss}||$ are expected while additionally measured particles lead to negative

[1] In the following all kinematic quantities accented with $*$ will be calculated in the restframe of the B_{SL}

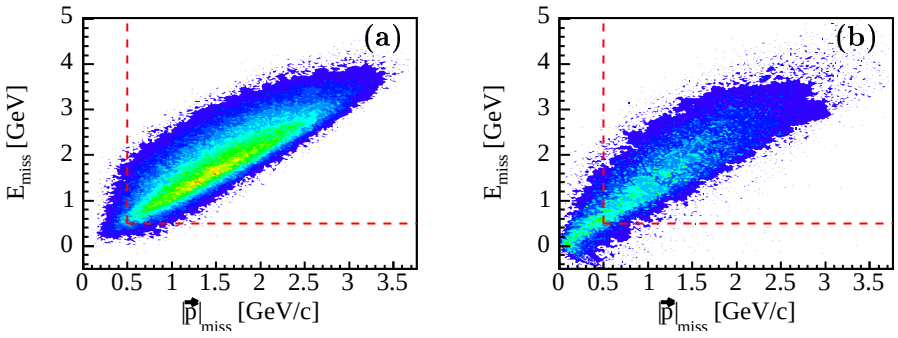

Figure 5.4: Distributions of E_{miss} versus $|\vec{p}_{miss}|$ for simulated signal (a) and background decays (b). The dashed red lines indicate the applied selection criteria of $E_{miss} > 0.5\,\text{GeV}$ and $|\vec{p}_{miss}| > 0.5\,\text{GeV}/c$.

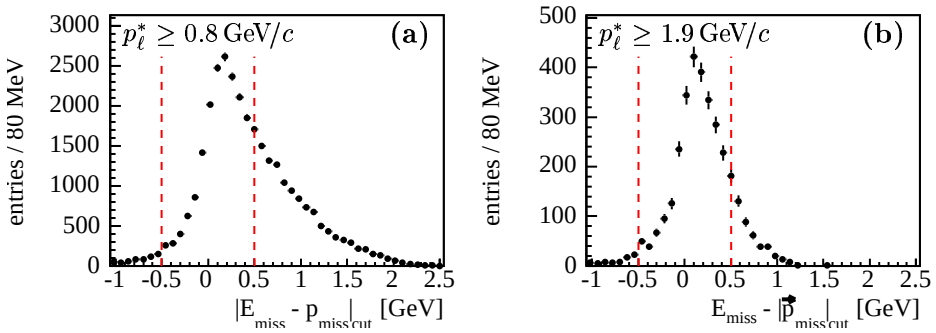

Figure 5.5: Distributions of $E_{miss} - |\vec{p}_{miss}|$ in data for different cuts $p^*_\ell \geq 0.8\,\text{GeV}/c$ (a) and $p^*_\ell \geq 1.9\,\text{GeV}/c$ (b). The dashed lines indicate the applied selection criteria of $|E_{miss} - |\vec{p}_{miss}|| < 0.5\,\text{GeV}$.

values of $|E_{miss} - |\vec{p}_{miss}||$. If all particles except the neutrino are measured, E_{miss} and $|\vec{p}_{miss}|$ are positive quantities. Figure 5.4 illustrates the situation showing the distributions of E_{miss} versus $|\vec{p}_{miss}|$ for simulated signal and background decays. Figure 5.5 illustrates the applied selection criteria on $E_{miss} - |\vec{p}_{miss}|$.

8. $N_{trk,X} \geq 1$, with $N_{trk,X}$ the number of charged track in the X_c system.

9. $|q_{tot}| \equiv |q_{B_{reco}} + q_\ell + q_X| \leq 1$. The quantity q_{tot} is the total reconstructed charge in the event. A small charge imbalance is tolerated to account for unmeasured low momentum tracks that influence the quality of the X_c reconstruction only slightly. In case only one track is found, $N_{trk,X} = 1$, we require charge conservation, $|q_{tot}| = 0$.

Integrated purity	$\mathcal{P}_{int} > 60\%$
B_{reco} energy difference	$\lvert\Delta E\rvert < 90\,\mathrm{MeV}$
B_{reco} energy substituted mass	$m_{\mathrm{ES}} > 5.27\,\mathrm{GeV}/c^2$
Lepton measurement	Exactly one recoiling lepton
Lepton charge correlation	$q_{b_{reco}} q_\ell < 0$
Lepton momentum	$p^*_\ell \geq 0.8 \ldots 1.9\,\mathrm{GeV}/c$
Missing energy and momentum	$E_{miss} > 0.5\,\mathrm{GeV}$
	$\lvert\vec{p}_{miss}\rvert > 0.5\,\mathrm{GeV}/c$
	$\lvert E_{miss} - \lvert\vec{p}_{miss}\rvert\rvert < 0.5\,\mathrm{GeV}$
Number of tracks	$N_{trk,X} \geq 1$
Total charge	$\lvert q_{tot}\rvert \leq 1$ if $N_{trk,X} \geq 2$
	$\lvert q_{tot}\rvert = 0$ if $N_{trk,X} = 1$

Table 5.6: Summary of event selection criteria. A detailed discussion can be found in section 5.4.1.

5.4.2 Kinematic Fit

Starting from a kinematically well defined initial state $e^+e^- \to \Upsilon(4S) \to B\overline{B}$ additional knowledge about the kinematics of the hypothetical semileptonic final state can be exploited to improve the overall resolution and reduce the bias of the measured hadronic system. The applied procedure called "method of least squares" determines corrections to the four-vectors of the measured particles on the basis of kinematic constraints.

A detailed discussion of the applied mathematical procedure described in the following sections 5.4.2.1 to 5.4.2.3 can be found in [33]. Section 5.4.2.4 discusses the application to the given problem utilizing a general purpose kinematic fitter package implemented in `C++`. It is documented in [34].

5.4.2.1 Method of Least Squares with Constraints

We start our considerations with a general problem consisting of n measured quantities $\vec{y}$ and p unmeasured parameters $\vec{a}$. The true underlying quantities $\bar{\vec{y}}$ and $\bar{\vec{a}}$ comply with the model,

$$\begin{aligned} f_1(\bar{a}_1, \bar{a}_2, \ldots, \bar{a}_p, \bar{y}_1, \bar{y}_2, \ldots, \bar{y}_n) &= 0, \\ f_2(\bar{a}_1, \bar{a}_2, \ldots, \bar{a}_p, \bar{y}_1, \bar{y}_2, \ldots, \bar{y}_n) &= 0, \\ &\vdots \\ f_m(\bar{a}_1, \bar{a}_2, \ldots, \bar{a}_p, \bar{y}_1, \bar{y}_2, \ldots, \bar{y}_n) &= 0, \end{aligned} \tag{5.10}$$

defined by m equations. Due to uncertainties in the measurement the quantities $\vec{y}$ will in general not fulfill these conditions. The equations 5.10 provide additional information that allow to improve the knowledge of the measured quantities by determining corrections $\Delta\vec{y}$ so that the corrected quantities

$\vec{y}' = \vec{y} + \Delta\vec{y}$ will comply with all constraints. Furthermore, the unmeasured parameters can be determined with the help of the equations f_i. The corrections are determined by minimizing the squared sum,

$$S(\vec{y}) = \Delta\vec{y}^T \mathcal{V}^{-1} \Delta\vec{y}, \tag{5.11}$$

with $\mathcal{V}$ being the covariance matrix of the measured parameters.

A general approach to determine local extrema of functions with multiple variables and constraints is the method of "Langrange Multipliers". It introduces m additional parameters λ_k, the Lagrange Multipliers, one for each constraint. A solution of the problem can be found by searching for extrema of the function,

$$L(\vec{y}, \vec{a}, \vec{\lambda}) = S(\vec{y}) + 2\sum_{k=1}^{m} \lambda_k f_k(\vec{y}, \vec{a}), \tag{5.12}$$

with respect to all parameters $\vec{y}$, $\vec{a}$, and $\vec{\lambda}$. It is equivalent to the condition for a local minimum of $S(\vec{y})$ under the constraint $f_k(\vec{y}, \vec{a}) = 0$.

If the constraints f_k are linear the solution can be found in one step. Otherwise it has to be found iteratively linearizing the problem in every iteration.

5.4.2.2 Linearization

A linearized form of the constraints as defined in equation 5.10 can be written as,

$$f_k(\vec{y}', \vec{a}') \approx f(\vec{y}^*, \vec{a}^*) + \sum_{j=1}^{p} \frac{\partial f_k}{\partial a_j} \cdot (\Delta a_j - \Delta a_j^*) + \sum_{i=1}^{n} \frac{\partial f_k}{\partial y_i} \cdot (\Delta y_i - \Delta y_i^*) \approx 0, \tag{5.13}$$

where $\vec{y}$ ($\vec{a}$) contains the start values of the measured (unmeasured) parameters, $\vec{y}^*$ ($\vec{a}^*$) contains the values of the measured (unmeasured) parameters after the previous iteration, and $\vec{y}'$ ($\vec{a}'$) contains the values of the measured (unmeasured) parameters of the next iteration. All functional values and derivatives are calculated at $\vec{y}^* = \vec{y} + \Delta\vec{y}^*$ and $\vec{a}^* = \vec{a} + \Delta\vec{a}^*$. The difference of start values and the next iteration is given by $\vec{y}' = \vec{y} + \Delta\vec{y}$ and $\vec{a}' = \vec{a} + \Delta\vec{a}$.

Rewriting equation 5.13 in matrix notation results in

$$\vec{f}^* + \mathcal{A}(\Delta\vec{a} - \Delta\vec{a}^*) + \mathcal{B}(\Delta\vec{y} - \Delta\vec{y}^*) \approx 0 \tag{5.14}$$

or

$$\mathcal{A}\Delta\vec{a} + \mathcal{B}\Delta\vec{y} - \vec{c} = 0 \qquad \text{with} \qquad \vec{c} = \mathcal{A}\Delta\vec{a}^* + \mathcal{B}\Delta\vec{y}^* - \vec{f}^*. \tag{5.15}$$

The constant vector $\vec{c}$ in equation 5.15 for iteration n depends only on quantities of the previous iteration $n-1$. The matrices $\mathcal{A}$ and $\mathcal{B}$ appearing in both equations 5.14 and 5.15 are defined as,

$$\mathcal{A} = \frac{\partial \vec{f}}{\partial \vec{a}} \qquad \text{and} \qquad \mathcal{B} = \frac{\partial \vec{f}}{\partial \vec{y}}. \tag{5.16}$$

For illustration we give the components of the matrices:

$$\mathcal{A} = \begin{pmatrix} \partial f_1/\partial a_1 & \partial f_1/\partial a_2 & \dots & \partial f_1/\partial a_p \\ \partial f_2/\partial a_1 & \partial f_2/\partial a_2 & \dots & \partial f_2/\partial a_p \\ \vdots & & & \\ \partial f_m/\partial a_1 & \partial f_m/\partial a_2 & \dots & \partial f_m/\partial a_p \end{pmatrix} \tag{5.17}$$

$$\mathcal{B} = \begin{pmatrix} \partial f_1/\partial y_1 & \partial f_1/\partial y_2 & \dots & \partial f_1/\partial y_n \\ \partial f_2/\partial y_1 & \partial f_2/\partial y_2 & \dots & \partial f_2/\partial y_n \\ \vdots & & & \\ \partial f_m/\partial y_1 & \partial f_m/\partial y_2 & \dots & \partial f_m/\partial y_n \end{pmatrix} \tag{5.18}$$

$$\vec{f}^{\,*} = \begin{pmatrix} f_1(\vec{a}^{\,*}, \vec{y}^{\,*}) \\ f_2(\vec{a}^{\,*}, \vec{y}^{\,*}) \\ \vdots \\ f_m(\vec{a}^{\,*}, \vec{y}^{\,*}) \end{pmatrix} \tag{5.19}$$

The function L that has to be minimized with respect to the parameters $\Delta\vec{y}$, $\Delta\vec{a}$, and $\vec{\lambda}$ can now be written as,

$$L = \Delta\vec{y}^{\,T}\mathcal{V}^{-1}\Delta\vec{y} + 2\lambda^T(\mathcal{A}\Delta\vec{a} + \mathcal{B}\Delta\vec{y} - \vec{c}). \tag{5.20}$$

The condition for an extremum of L is obtained by differentiation,

$$\begin{aligned} \mathcal{V}^{-1}\Delta\vec{y} + \mathcal{B}^T\vec{\lambda} &= 0, \\ \mathcal{A}^T\vec{\lambda} &= 0, \\ \mathcal{B}\Delta\vec{y} + \mathcal{A}\Delta\vec{a} &= \vec{c}, \end{aligned} \tag{5.21}$$

resulting in a coupled system of $n+p+m$ differential equations that need to be solved for the unknown values of $\Delta\vec{y}$, $\Delta\vec{a}$, and $\vec{\lambda}$.

5.4.2.3 Solution

The system of coupled differential equations defined in equation 5.21 can be written in only one equation with partitioned matrices:

$$\begin{pmatrix} \mathcal{V}^{-1} & 0 & \mathcal{B}^T \\ 0 & 0 & \mathcal{A}^T \\ \mathcal{B} & \mathcal{A} & 0 \end{pmatrix} \begin{pmatrix} \Delta\vec{y} \\ \Delta\vec{a} \\ \lambda \end{pmatrix} = \begin{pmatrix} 0 \\ 0 \\ c \end{pmatrix}. \tag{5.22}$$

In order to find a solution the inverse of the matrix given in equation 5.22 has to be calculated. Writing its inverse matrix in a partitioned form,

$$\begin{pmatrix} \mathcal{V}^{-1} & 0 & \mathcal{B}^T \\ 0 & 0 & \mathcal{A}^T \\ \mathcal{B} & \mathcal{A} & 0 \end{pmatrix}^{-1} = \begin{pmatrix} \mathcal{C}_{11} & \mathcal{C}_{21}^T & \mathcal{C}_{31}^T \\ \mathcal{C}_{21} & \mathcal{C}_{22}^T & \mathcal{C}_{32}^T \\ \mathcal{C}_{31} & \mathcal{C}_{32} & \mathcal{C}_{33} \end{pmatrix}, \tag{5.23}$$

and using the abbreviations

$$\mathcal{V}_\mathcal{B} = \left(\mathcal{B}\mathcal{V}\mathcal{B}^T\right)^{-1} \qquad \text{and} \qquad \mathcal{V}_\mathcal{A} = \left(\mathcal{A}^T\mathcal{V}_\mathcal{B}\mathcal{A}\right) \tag{5.24}$$

gives

$$\begin{aligned} \mathcal{C}_{11} &= \mathcal{V} - \mathcal{V}\mathcal{B}^T\mathcal{V}_\mathcal{B}\mathcal{B}\mathcal{V} \\ &\quad + \mathcal{V}\mathcal{B}^T\mathcal{V}_\mathcal{B}\mathcal{A}{\mathcal{V}_\mathcal{A}}^{-1}\mathcal{A}^T\mathcal{V}_\mathcal{B}\mathcal{B}\mathcal{V} \\ \mathcal{C}_{21} &= -{\mathcal{V}_\mathcal{A}}^{-1}\mathcal{A}^T\mathcal{V}_\mathcal{B}\mathcal{B}\mathcal{V} \\ \mathcal{C}_{22} &= {\mathcal{V}_\mathcal{A}}^{-1} \\ \mathcal{C}_{31} &= \mathcal{V}_\mathcal{B}\mathcal{B}\mathcal{V} - \mathcal{V}_\mathcal{B}\mathcal{A}{\mathcal{V}_\mathcal{A}}^{-1}\mathcal{A}^T\mathcal{V}_\mathcal{B}\mathcal{B}\mathcal{V} \\ \mathcal{C}_{32} &= \mathcal{V}_\mathcal{B}\mathcal{A}{\mathcal{V}_\mathcal{A}}^{-1} \\ \mathcal{C}_{33} &= -\mathcal{V}_\mathcal{B} + \mathcal{V}_\mathcal{B}\mathcal{A}{\mathcal{V}_\mathcal{A}}^{-1}\mathcal{A}^T\mathcal{V}_\mathcal{B} \end{aligned} \tag{5.25}$$

The corrections $\Delta\vec{y}$ and $\Delta\vec{a}$ as well as the Lagrange Multipliers $\vec{\lambda}$ are calculated by multiplication,

$$\begin{aligned} \Delta\vec{y} = \mathcal{C}_{31}^T\vec{c} &= \left(\mathcal{V}\mathcal{B}^T\mathcal{V}_\mathcal{B} - \mathcal{V}\mathcal{B}^T\mathcal{V}_\mathcal{B}\mathcal{A}{\mathcal{V}_\mathcal{A}}^{-1}\mathcal{A}^T\mathcal{V}_\mathcal{B}\right)\vec{c}, \\ \Delta\vec{a} = \mathcal{C}_{32}^T\vec{c} &= \left({\mathcal{V}_\mathcal{A}}^{-1}\mathcal{A}^T\mathcal{V}_\mathcal{B}\right)\vec{c}, \\ \vec{\lambda} = \mathcal{C}_{33}\vec{c} &= \left(-\mathcal{V}_\mathcal{B} + \mathcal{V}_\mathcal{B}\mathcal{A}{\mathcal{V}_\mathcal{A}}^{-1}\mathcal{A}^T\mathcal{V}_\mathcal{B}\right)\vec{c}. \end{aligned} \tag{5.26}$$

The iteration is repeated until certain convergence criteria are met guaranteeing that the squared sum S has reached a minimum and all constraints are fulfilled. Therefore, we define convergence criteria,

$$\frac{S(n-1) - S(n)}{ndf} < \epsilon_S \qquad \text{and} \qquad \sum_{k=1}^{m} f_k^{(n)}(\vec{y}, \vec{a}) < \epsilon_F, \tag{5.27}$$

where n denotes the number of iterations and ndf defines the number of degrees of freedom which is given by difference of the number of constraints and the number of unmeasured parameters, $ndf = m - p$. The parameter ϵ_S defines the size of the allowed change of S from one iteration to the next. The precision by which the constraints have to be fulfilled is defined by the parameter ϵ_F.

5.4.2.4 Application to Semileptonic Decays

After having discussed the general approach of the kinematic fit we will now describe its application to the signal decay $\Upsilon(4S) \to B_{reco}B_{SL}(X_c\ell\nu)$. We consider the following 11 measured parameters:

- Eight measured parameters for the eight components of the B_{reco} and X_c four vectors in cartesian coordinates, $E_{B_{reco}}$, $\vec{p}_{B_{reco}}$, E_{X_c}, and $\vec{p}_{X_c}$.
- Three measured parameters for the three independent components of the ℓ four vector, $\vec{p}_\ell$. The energy of the lepton is constrained by its mass [12] with $E_\ell = \sqrt{m_\ell^2 + \vec{p}_\ell^{\,2}}$.

Furthermore, three parameters have to be considered for the unmeasured neutrino momentum, $\vec{p}_\nu$, constraining its mass to $m_\nu = 0\,\mathrm{GeV}/c^2$.

The covariance matrix utilized in the kinematic fit is comprised of the different covariance matrices of the measured particles. For the lepton the covariance obtained by the track fit is used. For the fully reconstructed B_{reco} candidate the covariance matrix obtained from the final kinematic fit described in section 5.2.3 is used. The situation is more complicated for the covariance of the hadronic X_c system. Due to the limited acceptance of the *BABAR* detector the precision of the X_c measurement is dominated by particles that have not been measured. Therefore, we identify the average covariances of the X_c four vector components with their resolutions $E_{X_c}(meas.) - E_{X_c}(true)$ and $\vec{p}_{X_c}(meas.) - \vec{p}(true)$ calculated as difference of measured and true quantities and determined in simulated signal decays. A diagonal covariance matrix is assumed.

The studied resolutions vary with the X_c multiplicity and polar angle of the X_c momentum Θ_{X_c}. Therefore, they are determined in bins of theses quantities. We choose five bins in Mult_{X_c}, $[1, 4, 7, 10, 13, 21]$, as well as five bins in Θ_{X_c}, $[0, 0.52, 1.05, 1.57, 2.09, \pi]$.

Figure 5.6 shows examples of the extracted energy resolutions. While for high-multiplicity events the resolution distributions are similar to those of Gauss functions, long tails to negative values are observed for low multiplicity events.

However, the least squares approach used in the kinematic fit is the optimal estimator only for Gaussian distributed input parameters. Several different parameterizations of the input four-vectors like spherical coordinates have been studied but did not result in significant improvements of the observed shapes. Nevertheless, even with the non-Gaussian distributed input for some of the X_c covariances the performed fit behaves sufficiently well. We estimate the widths of the extracted resolution distributions by performing fits with Gauss functions. Figure 5.7 summarizes all extracted widths.

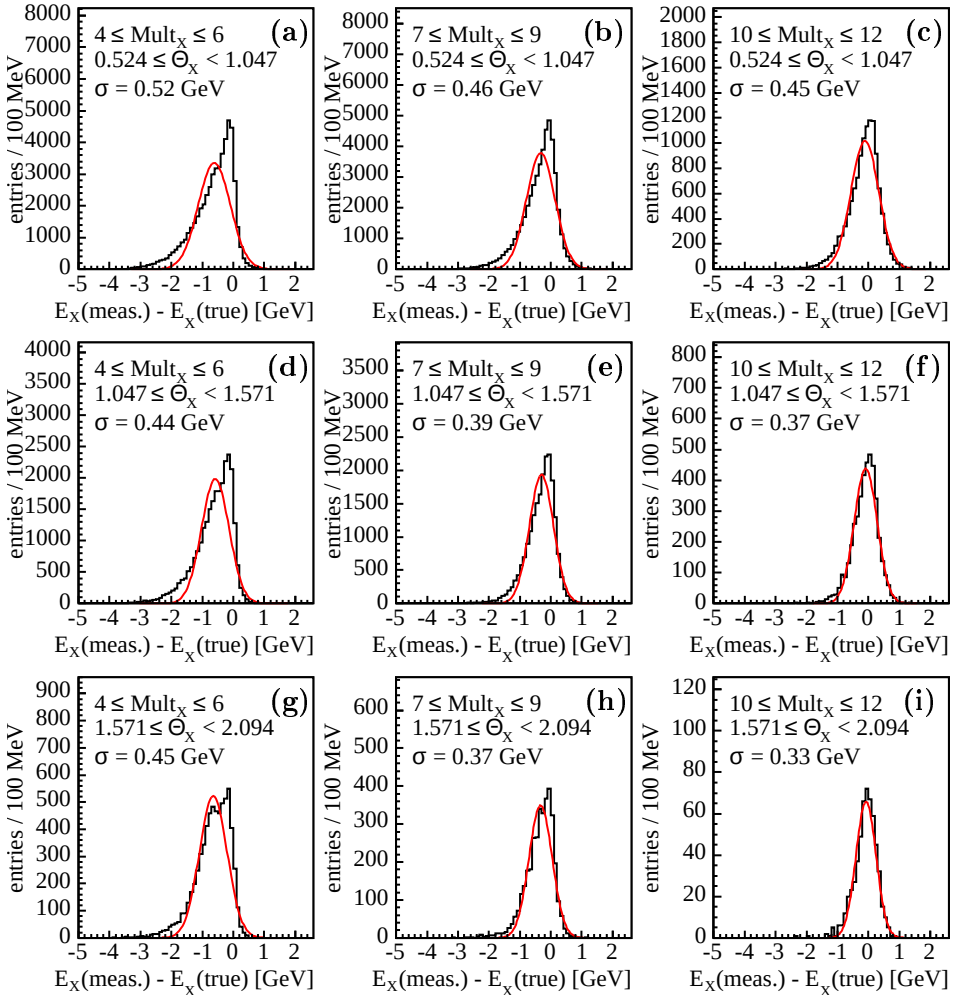

Figure 5.6: Examples of energy resolutions of the hadronic X_c system for different bins of Θ_{X_c} and Mult_{X_c} (histograms a-i). The resolutions are estimated by fitting the distributions with Gauss functions (red lines).

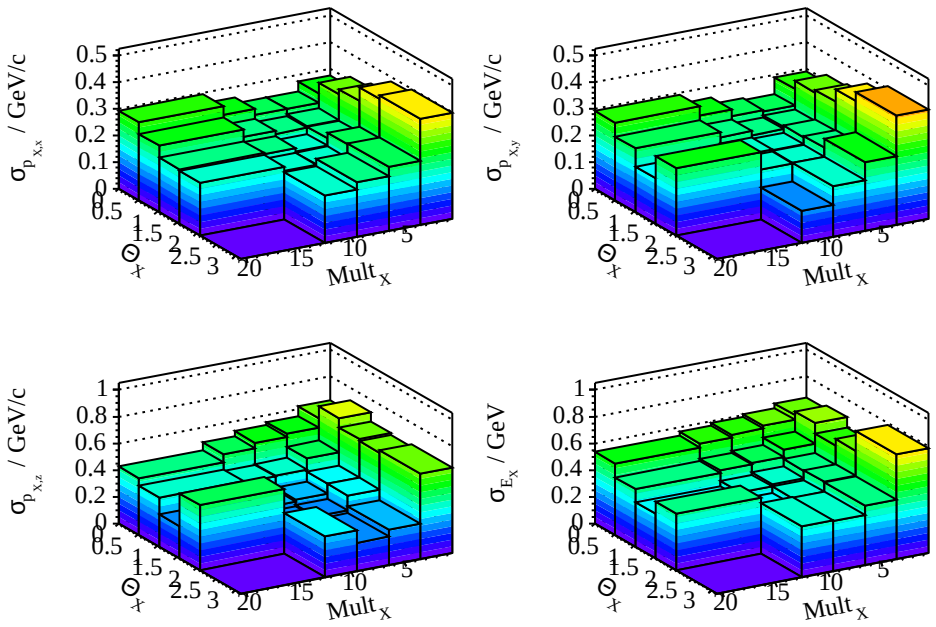

Figure 5.7: Energy and momentum resolution of the measured X_c four vector in bins of Θ_{X_c} and Mult_{X_c}.

The kinematics of the signal decay is constrained by the following relations:

$$\begin{aligned} f_1 &= E_{B_{reco}} + E_{X_c} + E_\ell + E_\nu - E_{\Upsilon(4S)} = 0, \\ f_{2,3,4} &= \vec{p}_{B_{reco}} + \vec{p}_{X_c} + \vec{p}_\ell + \vec{p}_\nu - \vec{p}_{\Upsilon(4S)} = 0, \\ f_5 &= m_{B_{reco}} - m_{B_{SL}} \\ &= \left[E^2_{B_{reco}} - \vec{p}^{\,2}_{B_{reco}}\right] - \left[(E_{X_c} + E_\ell + E_\nu)^2 - (\vec{p}_{X_c} + \vec{p}_\ell + \vec{p}_\nu)^2\right] = 0. \end{aligned} \tag{5.28}$$

The first four constraints ensure energy and momentum conservation in the event. The fifths constraint demands mass equality of the reconstrcuted B_{reco} and B_{SL} mesons. As a consequence the missing mass, $m^2_{miss} = E^2_{miss} - \vec{p}^{\,2}_{miss}$, of the event is constraint to zero. By requiring equal masses rather than fixing both masses to their nominal values avoids small inconsitencies introduced by imprecise beam energy measurements.

The performance of the kinematic fit is depicted in figure 5.8. Presented is the resolution of the hadronic mass $m_X - m_{X,true}$ before and after the kinematic fit in left plot. A significant reduction of the overall bias, $-254\,\mathrm{MeV}/c^2$ before and $-96\,\mathrm{MeV}/c^2$ after the fit, as well as improvement of the resolution, $425\,\mathrm{MeV}/c^2$ before and $355\,\mathrm{MeV}/c^2$ after the fit, is observed.

Figure 5.9 illustrates the effect of the kinematic fit on resolution and bias of the m_X measurement in bins of $E_{miss} - |\vec{p}_{miss}|$ and the hadronic final state

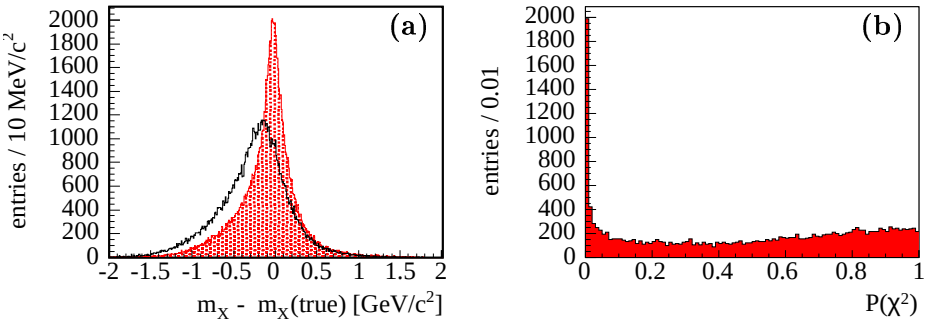

Figure 5.8: (a) Resolution of measured (□) and fitted m_X (■). (b) Probability of χ^2 for the final fit performed on data.

X_c. In both cases, a significant reduction of the bias is observed. Improvements of the resolution are observed for all hadronic final states. Studying the resolution as function of $E_{miss} - |\vec{p}_{miss}|$, improvements are achieved predominantly for positive values where most of the measured decays are accumulated. For negative values of $E_{miss} - |\vec{p}_{miss}|$ a slight degradation of the m_X resolution is observed.

The overall χ^2 probability $\mathcal{P}(\chi^2)$ of the final fit performed on data in shown in the right plot in figure 5.8. While the overall distribution is reasonably flat and only slightly raising toward $\mathcal{P}(\chi^2) = 1$ a peak in the first bin that contains about 10% of the events is visible. It is caused by the imperfect modelling of X_c energy and momentum covariances. Since rejecting these events does not result in an improved background rejection rate and the overall $\mathcal{P}(\chi^2)$ distribution is well modelled in MC simulations we decide to keep them in the analysis.

5.5 Comparison of Data and MC Simulations

In the following, the agreement of different kinematic variables in data and MC simulations relevant for the presented measurement will be discussed. Figure 5.10 compares the distributions of missing energy and momentum $E_{miss} - |\vec{p}_{miss}|$, E_{miss}, and $|\vec{p}_{miss}|$. We scale the extracted MC distributions according to the ratio of the number of fully reconstructed B_{reco} in data and MC. While the positive tails of the $E_{miss} - |\vec{p}_{miss}|$ distributions agree very well, discrepancies are observed in the negative part of the distributions. In the mentioned region an excess of MC events is observed indicating an excess of additionally measured particles with respect to data. The distributions of E_{miss} and $|\vec{p}_{miss}|$ show a good agreement of data and MC simulated distributions.

Comparing the distributions of charged track $N_{trk,X}$ and photon multiplicity $N_{\gamma,X}$ of the X_c system (cf. fig. 5.11) shows that the simulated $N_{\gamma,X}$

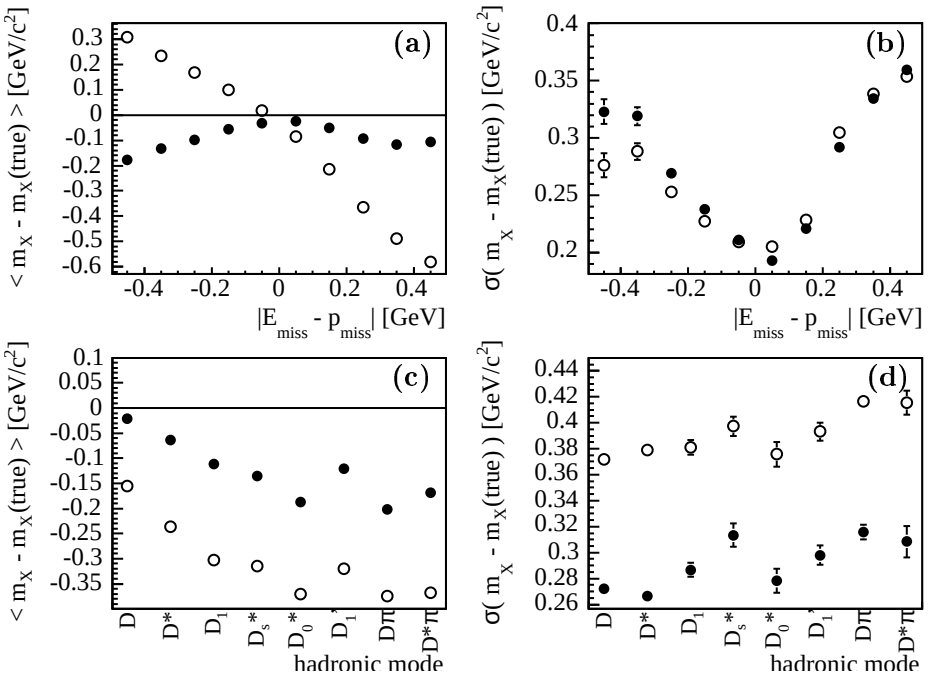

Figure 5.9: Bias $< m_X - m_{X,true} >$ (left column) and resolution $\sigma(m_X - m_{X,true})$ (right column) of m_X in bins of $E_{miss} - |\vec{p}_{miss}|$ (a,b) and the hadronic decay mode (c,d). Shown are bias and resolution before (○) and after (●) the kinematic is performed.

distribution is shifted to higher values with respect to the corresponding distribution in data. The simulation contains on average 0.3 additional photons per event. By contrast the charged track multiplicities agree reasonably well in data and MC simulation.

Figure 5.12 compares the distributions of the energies of all individual photons, E_γ, and the total neutral energy of the hadronic system, $E_{\gamma,X_c} = \sum_{j=1}^{N_{\gamma,X}} E_{j,\gamma}$. As mentioned before, the MC simulation contains additional photons not present in data. These photons appear in the simulation as a significant excess of low-energetic photons with $E_\gamma < 100\,\mathrm{MeV}$ or $E_{\gamma,X_c} < 300\,\mathrm{MeV}$.

Even though discrepancies between data and MC simulations are observed especially in the modelling of low-energetic photons, their overall agreement is generally good. The influence of the observed disagreement on the extracted results will be subject to detailed systematic studies described in section 6.

5.6 Background Subtraction

In the following section procedures applied for the subtraction of background are discussed. Two sources of background are distinguished:

1. Combinatorial background stemming from misreconstructed B_{reco} candidates. The shape and magnitude of this background is determined directly on data utilizing the m_{ES} sideband.

2. Residual background in the reconstruction and selection of the recoiling hadronic system that does not originate from $B \to X_c \ell \nu$ decays. This background peaks in the m_{ES} signal region and is subtracted utilizing MC simulations.

5.6.1 Combinatorial B_{reco} Background

Combinatorial background originates from B_{reco} candidates that are reconstructed in decay modes different from their true underlying modes. Such misreconstruction results from random combination and exchange of tracks and photons. The region under the m_{ES} signal peak is contaminated with combinatorial background which needs to be subtracted. Since the m_{ES} sideband region is signal free and contains pure combinatorial background we use it to determine the shape of the combinatorial background distribution assuming that it agrees with the combinatorial background shape under the signal peak. This procedure holds the advantage that it does not rely on MC simulations. We define the m_{ES} signal and sideband regions as follows:

$$\begin{aligned} 5.27 \leq & m_{\mathrm{ES,signal}} \leq 5.289\,\mathrm{GeV}/c^2 \\ 5.21 \leq & m_{\mathrm{ES,sb}} \leq 5.255\,\mathrm{GeV}/c^2 \end{aligned} \tag{5.29}$$

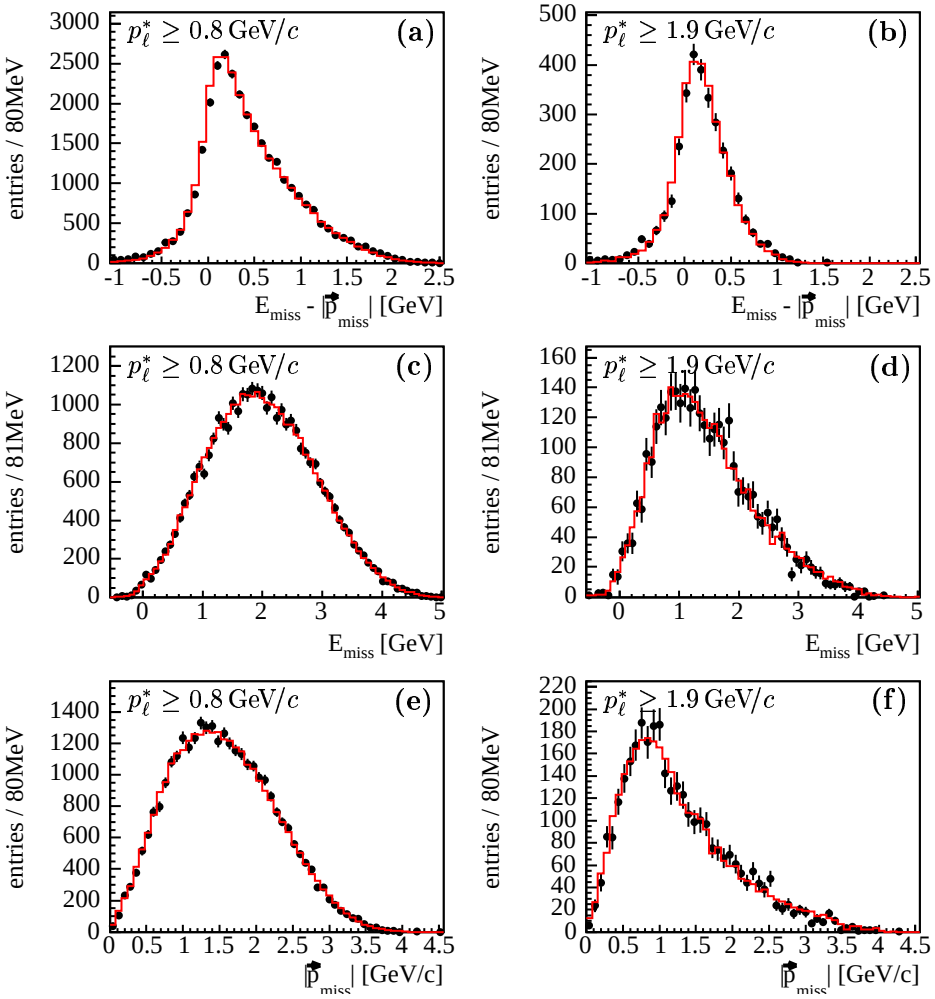

Figure 5.10: Comparison of data (•) and MC simulated distributions (red histogram) for $E_{miss} - |\vec{p}_{miss}|$ (a,b), E_{miss} (c,d), and $|\vec{p}_{miss}|$ (e,f) for different cuts on the minimum lepton momenta, $p_\ell^* \geq 0.8\,\mathrm{GeV}/c$ (left column) and $p_\ell^* \geq 1.9\,\mathrm{GeV}/c$ (right column).

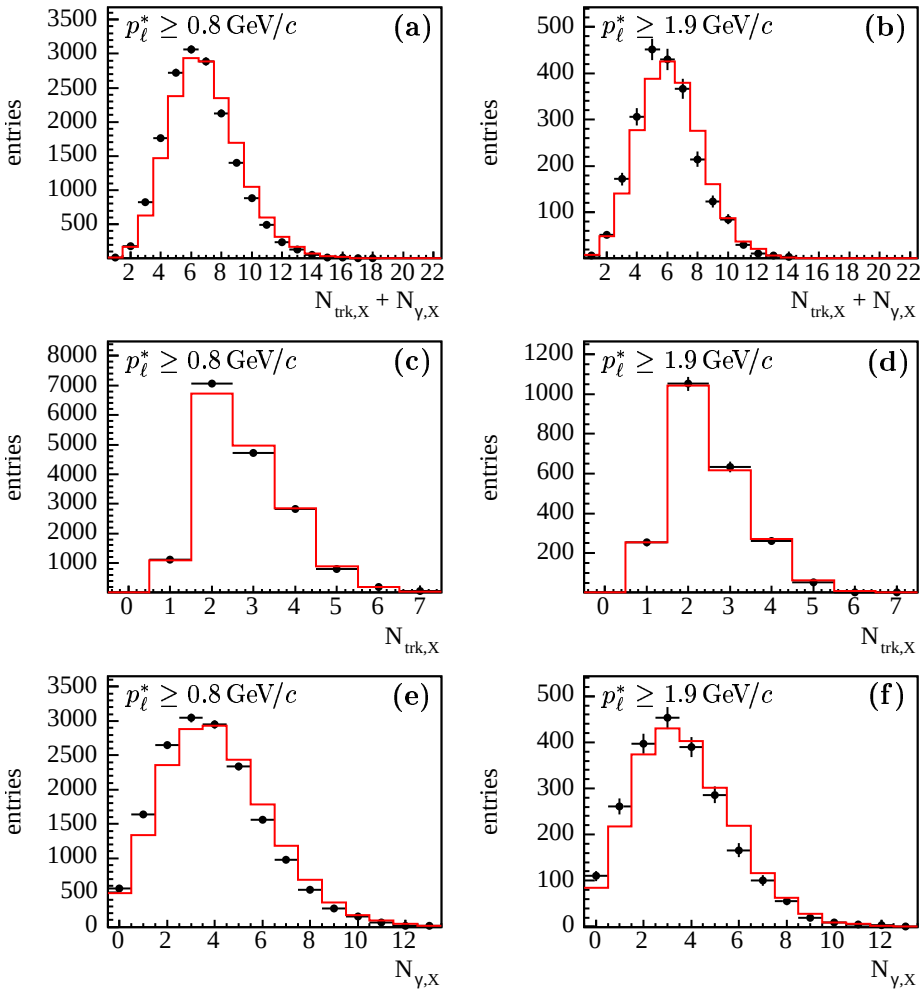

Figure 5.11: Comparison of data (•) and MC simulated distributions (red histogram) for $N_{trk,X} + N_{\gamma,X}$ (a,b), $N_{trk,X}$ (c,d), and $N_{\gamma,X}$ (e,f) for different cuts on the minimum lepton momenta, $p_\ell^* \geq 0.8\,\mathrm{GeV}/c$ (left column) and $p_\ell^* \geq 1.9\,\mathrm{GeV}/c$ (right column).

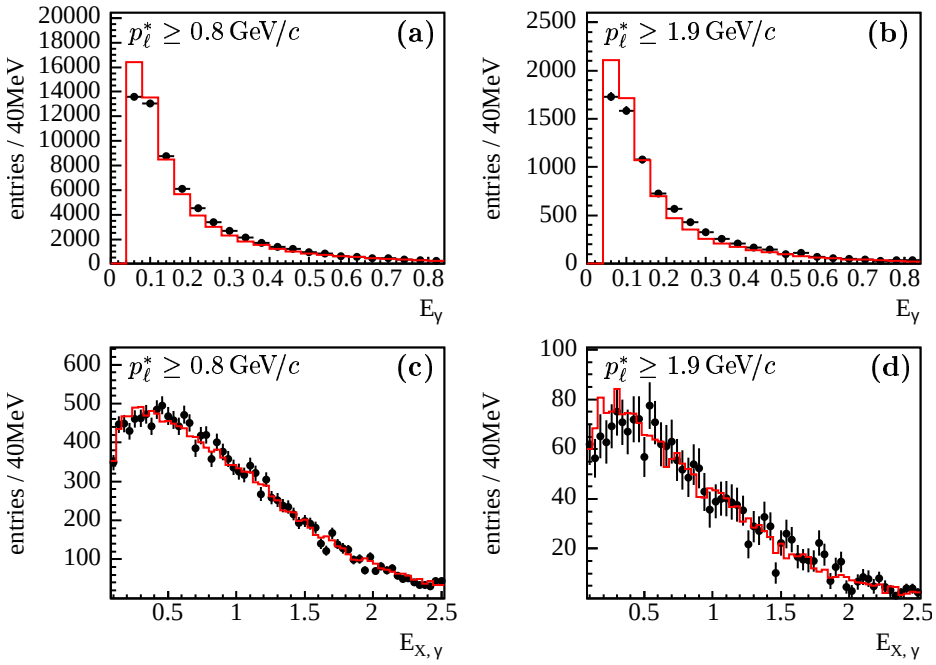

Figure 5.12: Comparison of data (•) and MC simulated distributions (red histogram) of the energies of individual photons E_γ (a,b) and the total neutral energy of the hadronic system E_{γ,X_c} (c,d) for different cuts on the minimum lepton momenta, $p_\ell^* \geq 0.8\,\mathrm{GeV}/c$ (left column) and $p_\ell^* \geq 1.9\,\mathrm{GeV}/c$ (right column).

Thereby, signal and sideband region are separated by $15\,\mathrm{MeV}/c^2$ to avoid leakage of signal events from the signal region into the sideband region.

To quantify the amount of combinatorial background under the m_{ES} signal peak we parametrize the m_{ES} distribution utilizing the sum of an ARGUS [35] and Crystal Ball [36] function. The ARGUS function describes the shape of the combinatorial background. It is defined as

$$f_{ARGUS}(m_{\mathrm{ES}}; N, \chi, m_{\mathrm{ES,max}}) = N m_{\mathrm{ES}} \sqrt{1 - (\frac{m_{\mathrm{ES}}}{m_{\mathrm{ES,max}}})^2} e^{-\chi(1-(\frac{m_{\mathrm{ES}}}{m_{\mathrm{ES,max}}})^2)}, \tag{5.30}$$

where N determines its overall normalization and the parameter χ defines its curvature. The mass $m_{\mathrm{ES,max}}$ describes the kinematic endpoint constrained by the beam energies and is fixed to $m_{\mathrm{ES,max}} = 5.289\,\mathrm{GeV}/c^2$. The signal shape is described by a Crystal Ball function:

$$f_{CB}(m_{\mathrm{ES}}; N, m_0, \sigma, \alpha, n) = N\sigma \cdot \begin{cases} e^{-\left(\frac{m_{\mathrm{ES}}-m_0}{2\sigma}\right)^2} & \\ & \text{if } m_{\mathrm{ES}} > m_0 - \alpha\sigma, \\ \left(1 - \frac{\alpha^2}{n} - \frac{\alpha}{n}\frac{(m_{\mathrm{ES}}-m_0)}{\sigma}\right)^{-n} \cdot e^{-\frac{\alpha^2}{2}} & \\ & \text{if } m_{\mathrm{ES}} \leq m_0 - \alpha\sigma. \end{cases} \tag{5.31}$$

f_{CB} is constituted of a central Gaussian with mean m_0 and width σ and a power law tail to low energies of order n continously joined to the Gaussian at $m_0 - \alpha\sigma$, with $\alpha > 0$. The power law tail is needed to model energy losses in the EMC on the reconstruction of π^0 mesons.

The relative size of the combinatorial background in the signal region with respect to the sideband region can be determined by fitting over the full m_{ES} range, $5.21 \leq m_{\mathrm{ES}} \leq 5.289\,\mathrm{GeV}/c^2$. It is given by the ratio of the two integrals,

$$\zeta_{sb} = \frac{\int_{signal} f_{ARGUS}(m_{\mathrm{ES}})\mathrm{d}m_{\mathrm{ES}}}{\int_{sb} f_{ARGUS}(m_{\mathrm{ES}})\mathrm{d}m_{\mathrm{ES}}}. \tag{5.32}$$

The number of well reconstructed B_{reco} candidates is given by

$$N_{B_{reco}} = N_{signal} - \zeta_{sb} N_{sb}, \tag{5.33}$$

with N_{signal} the total number of events in the signal region and N_{sb} the number of events in the sideband region.

Studies reveal a dependence of the scaling factor ζ_{sb} on the reconstructed hadronic mass m_X resulting from different momentum and multiplicity configurations with regard to different regions in the m_X phase space. Therefore, the fits are performed in bins of m_X (see Fig. 5.13 and 5.14). For the m_X dependent rescaling of the combinatorial background shape, measured separately for every $p^*_{\ell,cut}$, the extracted ζ_{sb} are interpolated with a cubic spline [37]. For the cut $p^*_\ell \geq 0.8\,\mathrm{GeV}/c$ we find scaling factors ranging between 0.61 ± 0.12, $0.40 \leq m_X < 1.44\,\mathrm{GeV}/c^2$, and 0.24 ± 0.03,

$2.40 \leq m_X < 2.72\,\mathrm{GeV}/c^2$. Only a small variation of the extracted ζ_{sb} is found for the cut $p^*_\ell \geq 1.9\,\mathrm{GeV}/c$. The extracted ζ_{sb} are 0.57 ± 0.14m for $0.24 \leq m_X < 1.60\,\mathrm{GeV}/c^2$. and 0.71 ± 0.16m for $0.24 \leq m_X < 2.52\,\mathrm{GeV}/c^2$. Fig. 5.15 shows the extracted scaling factors (left) together with the corresponding combinatorial background distributions (right). For comparison the background distributions scaled with a single factor determined from a fit over the full m_X range are superimposed (red histogram).

5.6.2 Residual Background

We call background that originates from the selection of decays other that $B \to X_c \ell \nu$ residual background. While combinatorial background stemming from misreconstructed B_{reco} can be studied directly in data the subtraction of residual background requires studies with MC simulations.

Residual background shapes are extracted from MC. Combinatorial background is subtracted like in data following the procedure described in the previous section 5.6.1. The extracted spectra are normalized to the number of signal B_{reco} candidates in data, $N_{B_{reco},data} = N_{B_{reco},MC}$.

To improve the quality of the MC simulation we rescale the simulated spectra to match branching fraction measurements of the corresponding processes. Table 5.7 summarizes all applied MC scaling factors.

Fig. 5.16 shows a breakdown of all residual background contributions for different cuts on p^*_ℓ. In the following, dominant sources of residual background will be described and current branching fraction measurements will be summarized.

5.6.2.1 Flavor Anticorrelated D and D_s^+ Decays

While the B mesons decay dominantly via $\bar{b} \to \bar{c} W^{*+}$ into a flavor correlated $\bar{c}$ quark, the production of flavor anticorrelated c quarks is also possible through the decay of the virtual W^{*+}. Fig. 5.17 shows the Feynman graphs of the involved dominant Cabibbo-allowed processes where the W^{*+} fragments into a $c\bar{s}$ quark pair producing $D_s^{(*)+}$, $D^{(*)0}K^+$, and $D^{(*)+}K^0$ mesons in the final state. The charmed mesons can subsequently decay semileptonically into right-charged leptons which cannot be distiguished experimentally from semileptonic B decays.

- The branching fractions of flavor anticorrelated $B \to D^+ X$ and $B \to D^0 X$ decays have been measured recently by the *BABAR* collaboration [38]:

$$\begin{aligned} \mathcal{B}(B^0 \to D^0 X) &= (8.1 \pm 1.5)\%, \\ \mathcal{B}(B^+ \to D^0 X) &= (8.6 \pm 0.7)\%, \\ \mathcal{B}(B^0 \to D^+ X) &= (2.3 \pm 1.1)\%, \\ \mathcal{B}(B^+ \to D^+ X) &= (2.5 \pm 0.5)\%. \end{aligned} \tag{5.34}$$

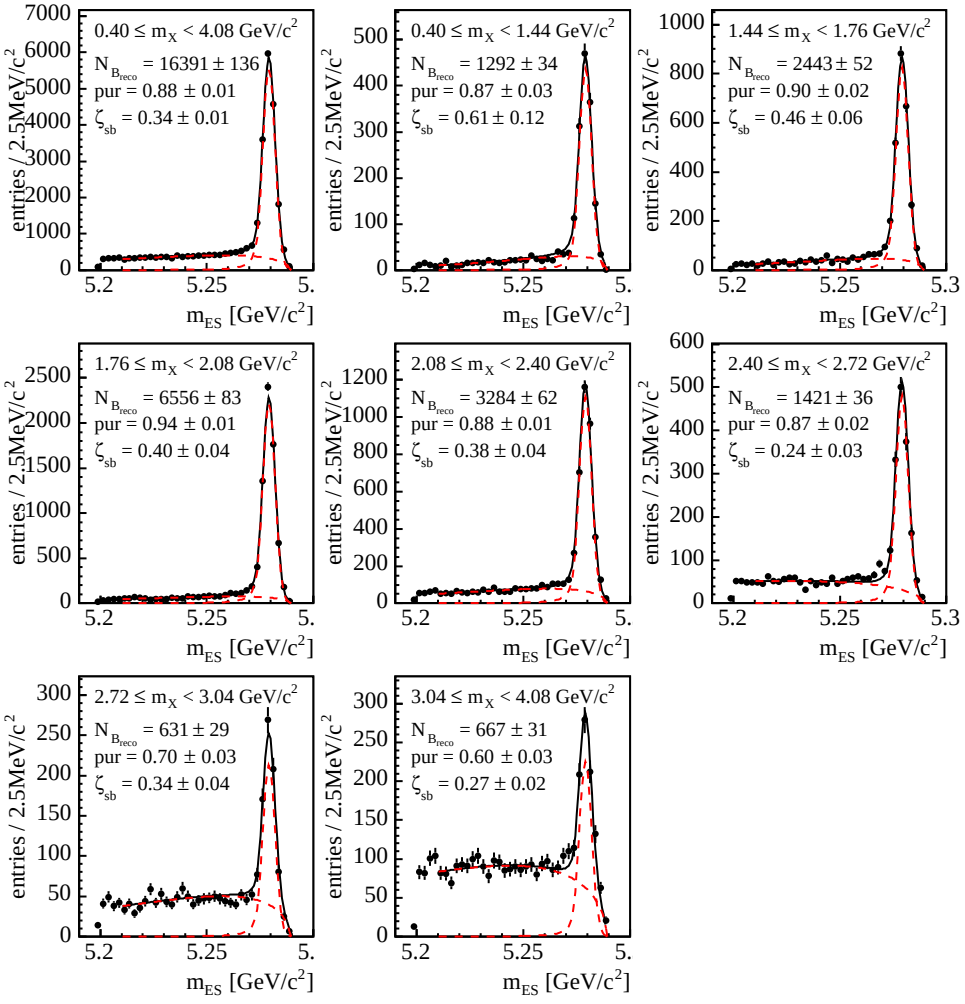

Figure 5.13: Fits of m_{ES} distributions in data (•) for $p^*_\ell \geq 0.8\,\mathrm{GeV}/c$ over the full m_X range (upper left plot) and in bins of m_X (other plots). The fit is performed using a function constituted of an ARGUS and a Crystal Ball function. The fit results are shown (black line) together with their signal and and background shapes (red dashed lines).

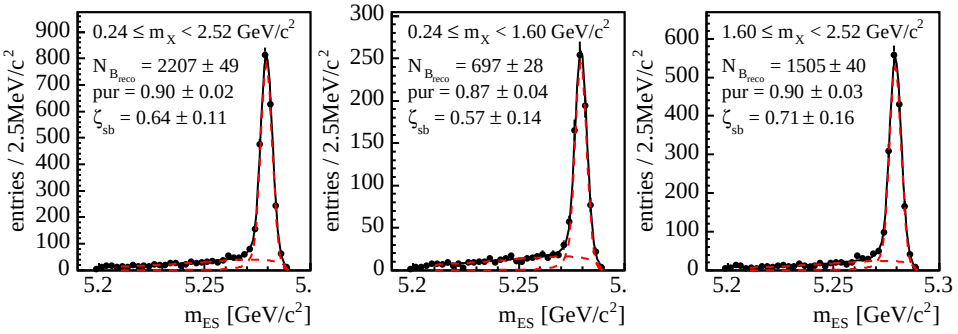

Figure 5.14: Fits of m_{ES} distributions in data (•) for $p^*_\ell \geq 1.9\,\mathrm{GeV}/c$ over the full m_X range (upper left plot) and in bins of m_X (other plots). The fit is performed using a function constituted of an ARGUS and a Crystal Ball function. The fit results are shown (black line) together with their signal and and background shapes (red dashed lines).

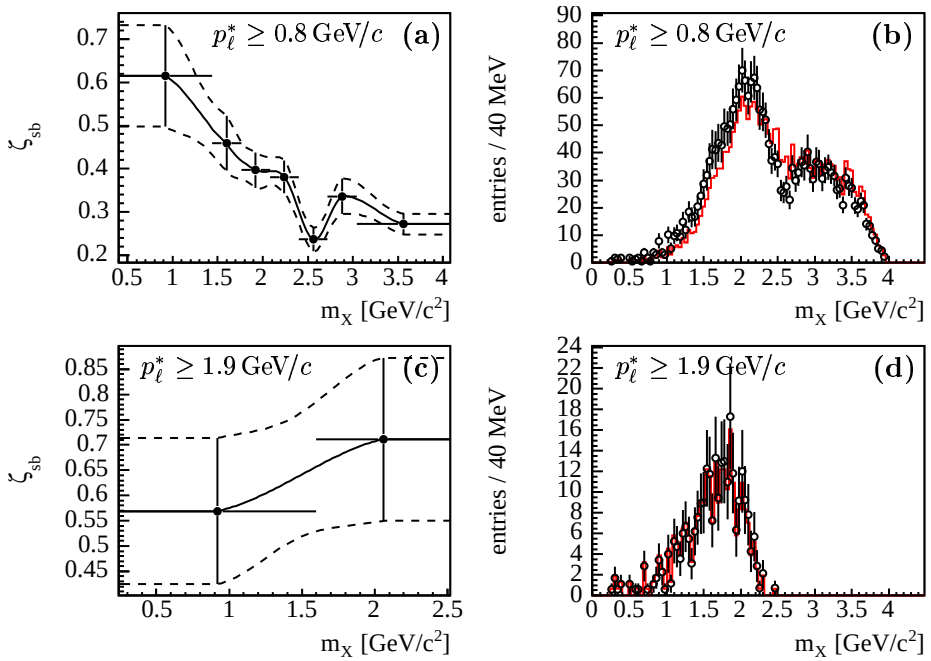

Figure 5.15: Sideband scaling factors ζ_{sb} extracted from m_{ES} fits in bins of m_X for different cuts $p^*_\ell \geq 0.8\,\mathrm{GeV}/c$ (a) and $p^*_\ell \geq 1.9\,\mathrm{GeV}/c$ (c). The ζ_{sb} are interpolated utilizing a cubic spline. The corresponding rescaled combinatorial background distributions are shown in (b,d) (○). Distributions scaled with a single scaling factor extracted over the full m_X range are overlaid (red line).

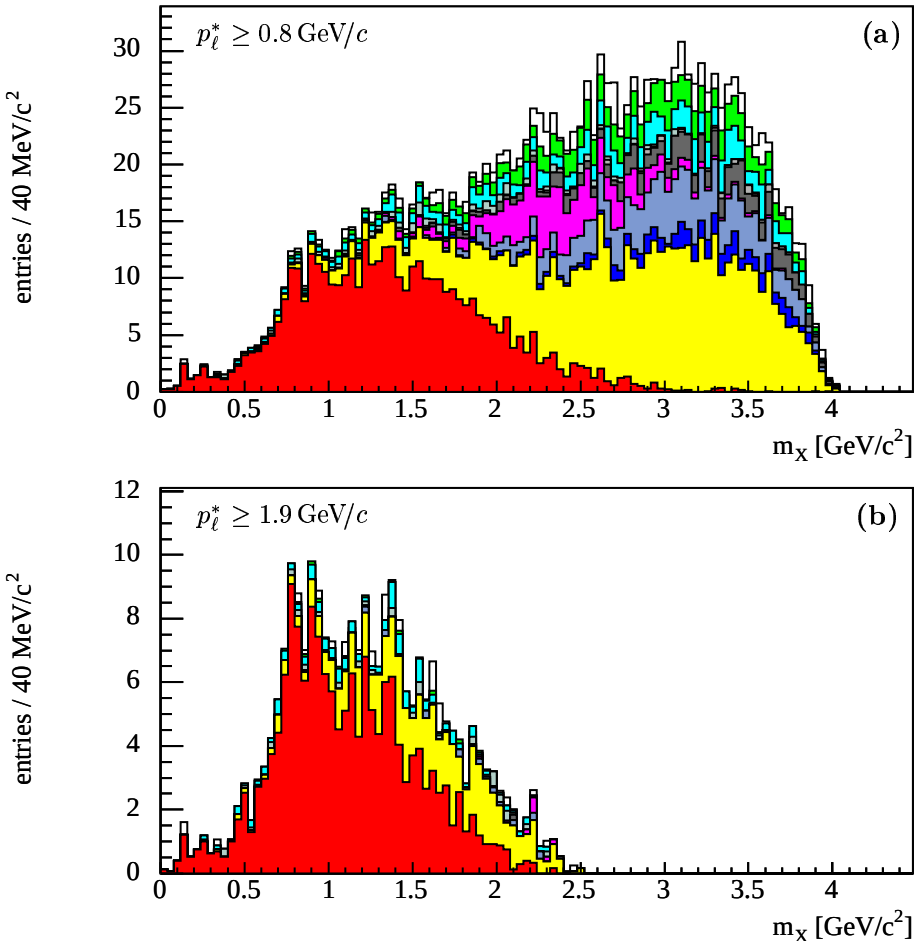

Figure 5.16: Residual background distributions for $p_\ell^* \geq 0.8\,\mathrm{GeV}/c$ (a) and $p_\ell^* \geq 1.9\,\mathrm{GeV}/c$ (b). The background contributions are $B \to X_u \ell\nu$ (■), misidentified hadrons (■), $B^{+,0} \to D^{+,0} X \to Y\ell^+\nu$ (■), $B^{+,0} \to D_s^+ X \to Y\ell^+\nu$ (■), $B^{+,0}(\to D_s^+) \to \tau^+ \to \ell^+$ (■), photon conversions $\gamma \to \ell^+\ell^-$ (■), Dalitz decays $\pi^0 \to \gamma\ell^+\ell^-$ (■), $B \to J/\psi, \psi(2S) \to \ell^+\ell^-$ (■), other (■), $B^0\overline{B}^0$ Mixing (■), and mis tagged events (□).

Decay	$\mathcal{B}_{\mathrm{MC}}[\%]$	$\mathcal{B}_{\mathrm{data}}[\%]$	S
$B^+ \to D^+ X \to Y\ell^+\nu$	0.56	0.40 ± 0.08 [38, 39]	0.719 ± 0.145
$B^0 \to D^+ X \to Y\ell^+\nu$	0.53	0.37 ± 0.18 [38, 39]	0.706 ± 0.338
$B^+ \to D^0 X \to Y\ell^+\nu$	0.51	0.56 ± 0.05 [38, 39]	1.086 ± 0.095
$B^0 \to D^0 X \to Y\ell^+\nu$	0.60	0.52 ± 0.10 [38, 39]	0.871 ± 0.164
$B^+ \to \overline{D}^0, D^- X \to Y\ell^-\nu$	6.60	7.60 ± 0.47 [38, 39, 40]	1.151 ± 0.071
$B^0 \to \overline{D}^0, D^- X \to Y\ell^-\nu$	8.90	7.13 ± 0.52 [38, 39, 40]	$0.801^{+0.058}_{-0.055}$
$B^+ \to D_s^+ X \to Y\ell^+\nu$	0.81	$0.61^{+0.12}_{-0.10}$ [38, 41, 12]	$0.753^{+0.146}_{-0.118}$
$B^0 \to D_s^+ X \to Y\ell^+\nu$	0.77	$0.79^{+0.16}_{-0.14}$ [38, 41, 12]	$1.035^{+0.215}_{-0.185}$
$B^+ \to \tau^+ \to \ell^+$	0.52	0.47 ± 0.05 [12, 26, 42]	0.905 ± 0.098
$B^0 \to \tau^+ \to \ell^+$	0.52	0.43 ± 0.05 [12, 26, 42]	0.834 ± 0.092
$B^+ \to D_s^+ \to \tau^+ \to \ell^+$	0.17	$0.09^{+0.03}_{-0.02}$ [12, 26, 42]	$0.524^{+0.158}_{-0.146}$
$B^0 \to D_s^+ \to \tau^+ \to \ell^+$	0.16	$0.12^{+0.04}_{-0.03}$ [12, 26, 42]	$0.721^{+0.224}_{-0.211}$
$B \to J/\psi \to \ell^+\ell^-$	6.06×10^{-2}	$(6.46 \pm 0.20) \times 10^{-2}$ [12]	1.066 ± 0.034
$B \to \psi(2S) \to \ell^+\ell^-$	0.23×10^{-2}	$(0.226 \pm 0.017) \times 10^{-2}$ [12]	0.982 ± 0.088
$B \to X_u \ell\nu$	0.210	0.222 ± 0.033 [42]	1.057 ± 0.157

Table 5.7: Summary of scaling factors S used to correct braching fractions of background processes in MC $\mathcal{B}_{\mathrm{MC}}$ to measured branching fractions $\mathcal{B}_{\mathrm{data}}$ as discussed on pages 66 - 74.

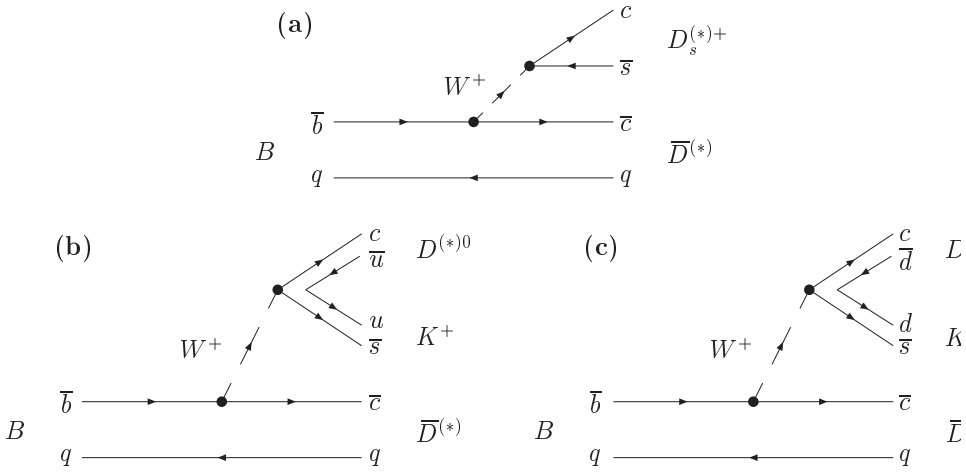

Figure 5.17: Dominant Feynman graphs of right-charged D and D_s^+ Decays, $B \to D_s^+ X \to Y\ell^+\nu$ (a), $B \to D^+ X \to Y\ell^+\nu$ (b), $B \to D^0 X \to Y\ell^+\nu$ (c).

The CLEO collaboration measured the absolute semileptonic D-meson branching fractions [39],

$$\begin{aligned} \mathcal{B}(D^0 \to X\ell^+\nu) &= (6.46 \pm 0.21)\%, \\ \mathcal{B}(D^+ \to X\ell^+\nu) &= (16.13 \pm 0.39)\%, \end{aligned} \tag{5.35}$$

resulting in

$$\begin{aligned} \mathcal{B}(B^+ \to D^+X \to Y\ell^+\nu) &= (0.40 \pm 0.08)\%, \\ \mathcal{B}(B^0 \to D^+X \to Y\ell^+\nu) &= (0.37 \pm 0.18)\%, \\ \mathcal{B}(B^+ \to D^0X \to Y\ell^+\nu) &= (0.56 \pm 0.05)\%, \\ \mathcal{B}(B^0 \to D^0X \to Y\ell^+\nu) &= (0.52 \pm 0.10)\%. \end{aligned} \tag{5.36}$$

- The branching fractions of flavor anticorrelated $B^0 \to D_s^+X$ and $B^+ \to D_s^+X$ decays have been measured in [38] resulting in

$$\begin{aligned} \mathcal{B}(B^+ \to D_s^+X) &= 7.9^{+1.5}_{-1.2}\%, \\ \mathcal{B}(B^0 \to D_s^+X) &= 10.3^{+2.1}_{-1.8}\%. \end{aligned} \tag{5.37}$$

  Since the actual size of the total semileptonic D_s^+-meson branching fraction is unmeasured we estimate it by using the lifetime ratio $\tau_D/\tau_{D_s^+}$. Assuming equal semileptonic decay rates of D and D_s^+ mesons [41] one obtains the following expression

$$\mathcal{B}(D_s^+ \to X\ell^+\nu) = \mathcal{B}(D \to X\ell^+\nu)\frac{\tau_D}{\tau_{D_s^+}}. \tag{5.38}$$

  Using the measured lifetimes $\tau_{D^0} = (410.3 \pm 1.5)$ fs and $\tau_{D_s^+} = (490 \pm 9)$ fs [12] we obtain

$$\mathcal{B}(D_s^+ \to X\ell^+\nu) = (7.71 \pm 0.29)\%. \tag{5.39}$$

  Combining both measurements the total branching fractions are quantified as

$$\begin{aligned} \mathcal{B}(B^+ \to D_s^+X \to Y\ell^+\nu) &= (0.61^{+0.12}_{-0.10})\%, \\ \mathcal{B}(B^0 \to D_s^+X \to Y\ell^+\nu) &= (0.79^{+0.16}_{-0.14})\%. \end{aligned} \tag{5.40}$$

5.6.2.2 τ Decays

There are two relevant sources of background from τ decays which have to be accounted for:

- Semileptonic B decays into τ leptons that subsequently decays into right-charged leptons produce irreducible background that has to be subtracted using MC simulated decays. Since there are no measurements of the semileptonic branching fractions of B mesons $\mathcal{B}(B^0 \to$

$X\tau^+\nu_\tau$) and $\mathcal{B}(B^+ \to X\tau^+\nu_\tau)$ available we utilize the measurement of inclusive semileptonic branching fraction in the admixture of B, B_s, and Λ_b to calculate both branching fractions following the discussion in [26, p. 48]. This branching fraction was measured by the LEP experiments to be $\mathcal{B}(X_{\bar{b}} \to X_{\bar{c}}\tau^+\nu_\tau) = (2.48 \pm 0.26)\%$ [12] where $\mathcal{B}(X_{\bar{b}} \to X_{\bar{c}}\tau^+\nu_\tau)$ is composed of

$$\begin{aligned}\mathcal{B}(X_{\bar{b}} \to X_{\bar{c}}\tau^+\nu_\tau) =& f_{u,d}\mathcal{B}(B^0 \to X\tau^+\nu_\tau) + f_{u,d}\mathcal{B}(B^+ \to X\tau^+\nu_\tau) + \\ & f_s\mathcal{B}(B_s \to X\tau^+\nu_\tau) + f_{\Lambda_b}\mathcal{B}(\Lambda_b \to X\tau^+\nu_\tau).\end{aligned} \tag{5.41}$$

$f_{u,d} = (39.8 \pm 1)\%$, $f_s = (10.4 \pm 1.4)\%$, and $f_{\Lambda_b} = (9.9 \pm 1.7)\%$ [42] are the production fractions. Equal fractions for B^0 and B^+ decays are assumed. Implying equal semileptonic decay rates Γ_{SL} for all hadrons contributing to $X_{\bar{b}}$ eq. 5.41 can be rewritten as

$$\begin{aligned}\mathcal{B}(B^0 \to X\tau^+\nu_\tau) &= \frac{\mathcal{B}(X_{\bar{b}} \to X_{\bar{c}}\tau^+\nu_\tau)}{\left(f_{u,d}(1 + \frac{\tau_{B^+}}{\tau_{B^0}}) + f_s\frac{\tau_{B_s}}{\tau_{B^0}} + f_{\Lambda_b}\frac{\tau_{\Lambda_b}}{\tau_{B^0}}\right)}, \\ \mathcal{B}(B^+ \to X\tau^+\nu_\tau) &= \frac{\mathcal{B}(X_{\bar{b}} \to X_{\bar{c}}\tau^+\nu_\tau)}{\left(f_{u,d}(1 + \frac{\tau_{B^0}}{\tau_{B^+}}) + f_s\frac{\tau_{B_s}}{\tau_{B^+}} + f_{\Lambda_b}\frac{\tau_{\Lambda_b}}{\tau_{B^+}}\right)}.\end{aligned} \tag{5.42}$$

Using $\tau_{B^+} = (1.643 \pm 0.010)$ ps, $\tau_{B^0} = (1.527 \pm 0.008)$ ps, $\tau_{B_s} = 1.454 \pm 0.040)$ ps, and $\tau_{\Lambda_b} = (1.288 \pm 0.065)$ ps [42] we get

$$\begin{aligned}\mathcal{B}(B^0 \to X\tau^+\nu_\tau) &= (2.46 \pm 0.27)\%, \\ \mathcal{B}(B^+ \to X\tau^+\nu_\tau) &= (2.67 \pm 0.29)\%.\end{aligned} \tag{5.43}$$

Combining with the average branching fraction [12]

$$\mathcal{B}(\tau^+ \to \ell^+\overline{\nu}_\tau\overline{\nu}) = (17.60 \pm 0.04)\% \tag{5.44}$$

results in

$$\begin{aligned}\mathcal{B}(B^0 \to X\tau^+\nu_\tau \to \ell^+\overline{\nu}_\tau\overline{\nu}) &= (0.43 \pm 0.05)\%, \\ \mathcal{B}(B^+ \to X\tau^+\nu_\tau \to \ell^+\overline{\nu}_\tau\overline{\nu}) &= (0.47 \pm 0.05)\%.\end{aligned} \tag{5.45}$$

- D_s^+ mesons decaying leptonically into a right-charged τ^+ contribute an additional source of background. The average branching fraction of this decay is known to be $\mathcal{B}(D_s^+ \to \tau^+\nu_\tau) = (6.4 \pm 1.5)\%$ [12]. Combining with eq. 5.37 and 5.44 results in

$$\begin{aligned}\mathcal{B}(B^+ \to D_s^+ \to \tau^+ \to \ell^+) &= (0.09^{+0.03}_{-0.02})\% \\ \mathcal{B}(B^0 \to D_s^+ \to \tau^+ \to \ell^+) &= (0.12^{+0.04}_{-0.03})\%.\end{aligned} \tag{5.46}$$

5.6.2.3 J/ψ and $\psi(2S)$ Decays

J/ψ and $\psi(2S)$ Decays

J/ψ and $\psi(2S)$ decaying into two leptons of which only the right-charged lepton is measured contribute to the background. The average branching fractions are $\mathcal{B}(J/\psi \to \ell^+\ell^-) = (5.91 \pm 0.07)\%$ and $\mathcal{B}(\psi(2S) \to \ell^+\ell^-) = (0.736 \pm 0.042)\%$ [12]. Combining with $\mathcal{B}(B \to J/\psi X) = (1.094 \pm 0.032)\%$ and $\mathcal{B}(B \to \psi(2S)X) = (0.307 \pm 0.021)\%$ [12] results in

$$\begin{aligned} \mathcal{B}(B \to J/\psi \to \ell^+\ell^-) &= (6.46 \pm 0.20) \times 10^{-4} \text{ and} \\ \mathcal{B}(B \to \psi(2S) \to \ell^+\ell^-) &= (0.226 \pm 0.017) \times 10^{-4}, \end{aligned} \tag{5.47}$$

respectively.

5.6.2.4 $B^0\overline{B}^0$ Mixing

After subtraction of all background sources described so far there is still background remaining from $B^0\overline{B}^0$ oscillations. These oscillations result in events with two equally flavored B mesons.

B^0 mesons stemming from $B^0\overline{B}^0$ events are dominantly selected via wrong-charged leptons from $B^0 \to (\overline{D}^0, D^-)X \to Y\ell^-\nu$ cascades. The size of the total flavor-correlated charm production has been measured in [38] to be $\mathcal{B}(B^0 \to (\overline{D}^0, D^-)X) = (84.30^{+4.41}_{-4.18})\%$. Subtracting contributions from semileptonic decays, $\mathcal{B}(B \to X_c\ell\nu) = (10.611 \pm 0.175)\%$ [40], leads to

$$\mathcal{B}(B^0 \to (\overline{D}^0, D^-)X) = (63.08^{+4.42}_{-4.19})\%. \tag{5.48}$$

In combination with the average semileptonic D meson branching fraction [39],

$$\mathcal{B}(D^{+,0} \to X\ell^+\nu) = (11.30 \pm 0.22)\%. \tag{5.49}$$

we estimate

$$\mathcal{B}(B^0 \to (\overline{D}^0, D^-)X \to Y\ell^-\nu) = (7.13^{+0.52}_{-0.49})\%. \tag{5.50}$$

The time-integrated mixing probability χ_d of B^0 mesons oscillating into $\overline{B}^0$ mesons and vice versa has been measured to be $\chi_{d,data} = 0.188 \pm 0.002$ [42]. The MC simulation implements an oscillation probability of $\chi_{d,MC} = 0.181$ resulting in a small scaling factor of $\chi_{d,data}/\chi_{d,MC} = 1.038 \pm 0.017$. Since this scaling factor and its uncertainty are negligible small compared to the effect observed in the rescaling of the branching fraction $\mathcal{B}(B^0 \to (\overline{D}^0, D^-)X \to Y\ell^-\nu)$ we stick to the original MC value and do not perform a rescaling of χ_d.

5.6.2.5 Mis Tagged Events

We call events with B_{reco} candidates that are reconstructed in decay modes different from the underlying true decay modes mis tagged events. Even

though most of the mistagging background is subtracted as combinatorial background there is still a small contribution of "quasi well reconstructed" B_{reco} candidates remaining. Those events occure mainly by exchange of slow charged or neutral pions. MC studies show that true neutral B_{reco} candidates are reconstructed with a probability of about 17.8% as a charged B_{reco} candidate while only 4.84% of all charged B_{reco} candidates are reconstructed as neutral candidates.

Only a small fraction of those events results in a reversal of the charge correlation between lepton and B_{reco} flavor, i.e. when a true B^0 is reconstructed as a $\overline{B}^0$ or B^-. The probabilities to reconstruct true neutral or charged B mesons as B_{reco} candidates with different b quark flavor are 1.9% and 1.8%, respectively. This type of mis tagged events is dominantly selected via wrong-charged leptons from $B^{+,0} \to (\overline{D}^0, D^-)X \to Y\ell^-\nu$ cascades. The branching fraction $\mathcal{B}(B^0 \to (\overline{D}^0, D^-)X \to Y\ell^-\nu)$ is calculated in sec. 5.6.2.4. Accordingly, we get

$$\mathcal{B}(B^+ \to (\overline{D}^0, D^-)X \to Y\ell^-\nu) = (7.60 \pm 0.47)\%, \tag{5.51}$$

using $\mathcal{B}(B^+ \to (\overline{D}^0, D^-)X) = (67.28 \pm 3.91)\%$ [38]. After subtraction of combionatorial background only a small but significant fraction of those events is retained.

5.6.2.6 Misidentified Hadrons

Background stemming from hadrons like π, K, and p that have been misidentified as electrons or muons is estimated from MC simulations corrected for efficiency and misidentification rate differences in data and MC. The correction factors are estimated from pure data control samples [30,31] and applied using the so called "tweaking" method [43].

5.6.2.7 Semileptonic $B \to X_u\ell\nu$ Decays

Semileptonic B meson decays $B \to X_u\ell\nu$ into charmless hadronic final states contribute to the background. The current world average [42],

$$\mathcal{B}(B \to X_u\ell\nu) = (2.22 \pm 0.33) \cdot 10^{-3}, \tag{5.52}$$

has been calculated within the BLNP framework [44]. It uses Heavy Quark parameter input from a global fit to $B \to X_c\ell\nu$ and $B \to X_s\gamma$ moments [11] in the Kinetic Scheme [14].

5.6.3 Summary of Background Subtraction

5.6.3.1 Normalization of Background Distributions

As described above, the overall normalization for combinatorial B_{reco} background is extracted from a fit to the $m_{\rm ES}$ distribution while the residual

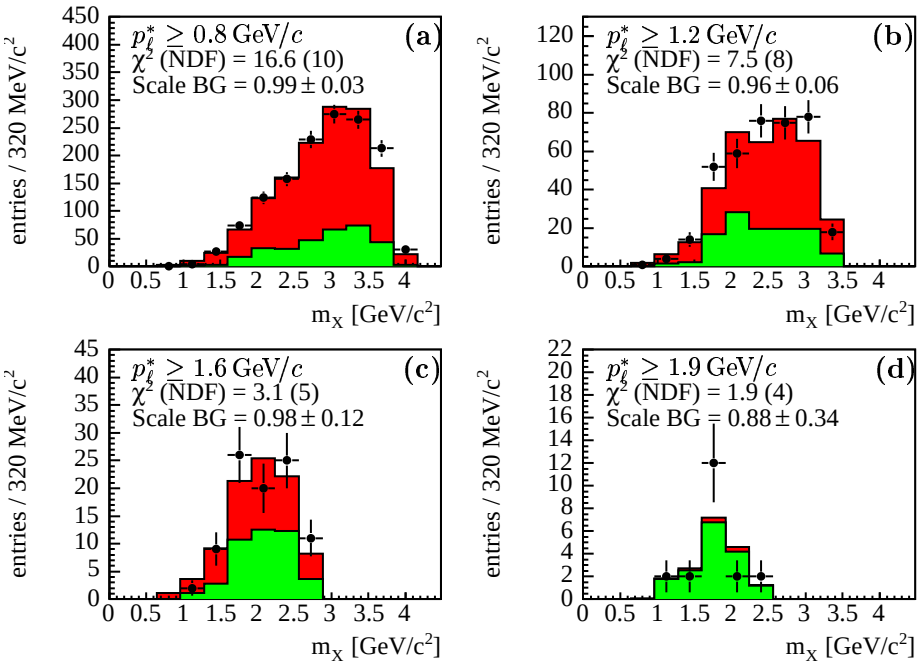

Figure 5.18: Spectra of wrong-charged events in a sample of charged B_{reco} candidates. The overall normalization of the background histograms is determined in a fit to the observed spectrum in data. The histograms are: observed spectrum in data (•), combinatorial background (■), and residual background (■).

background extracted from MC is normalized to the number of signal B_{reco} candidates, $N_{B_{reco}}$, in data.

We check the normalization utilizing a control sample with inverted lepton charge correlation. Since we aim for a sample containing only background events we consider only charged $B^{\pm}_{reco}$ candidates in the selection. Thereby, we reject events which undergo $B^0\overline{B}^0$ oscillations and hence contain wrong-charged signal leptons. Fig. 5.18 shows a comparison of the extracted m_X spectra with combinatorial background and simulated background distributions for different cuts on p^*_ℓ. The background shapes are fitted with a single free scaling factor to the full spectrum. All fitted scaling factors, as given in the figure, are compatible with unity within errors. Together with the reasonable agreement of the simulated and measured spectra we are confident that these results are transferable to the corresponding right-charged samples.

As an additional cross-check we repeat the same procedure with the corresponding control sample of neutral B_{reco} events. The results are shown in Fig. 5.19. Even though this sample contains a significant contribution of signal events the overall agreement of data and MC distributions is reasonable.

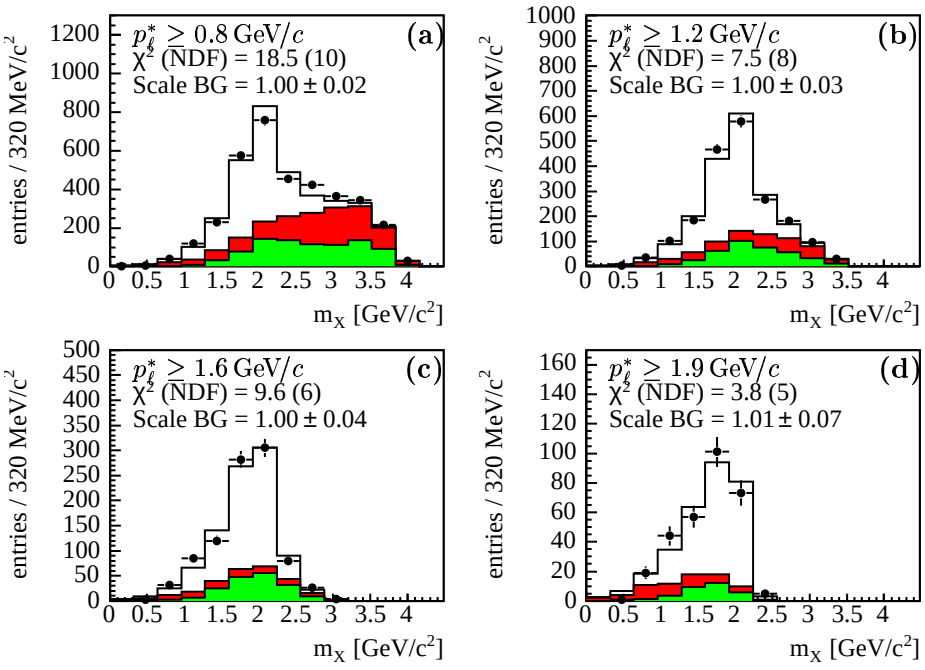

Figure 5.19: Spectra of wrong-charged events in a sample of neutral B_{reco} candidates. The overall normalization of the background histograms is determined in a fit to the observed spectrum in data. The histograms are: observed spectrum in data (•), combinatorial background (■), residual background (■), and signal decays in data (□) using $\chi_d = 0.181$.

$p_{l,cut}$ [GeV/c]	N_{total}	N_{sb}	N_{res}	N_{bg}	N_{signal}
0.8	19212 ± 138	2429 ± 43	1696 ± 19	4126 ± 47	15085 ± 146
0.9	18084 ± 134	2067 ± 39	1443 ± 17	3510 ± 43	14573 ± 141
1.0	16922 ± 130	1835 ± 38	1212 ± 16	3047 ± 41	13874 ± 136
1.1	15637 ± 125	1622 ± 35	1033 ± 15	2655 ± 38	12981 ± 130
1.2	14262 ± 119	1410 ± 33	884 ± 14	2295 ± 36	11966 ± 124
1.3	12764 ± 113	1266 ± 33	763 ± 12	2029 ± 35	10734 ± 118
1.4	11152 ± 105	1081 ± 31	642 ± 11	1724 ± 33	9427 ± 110
1.5	9473 ± 97	918 ± 27	553 ± 10	1471 ± 29	8001 ± 101
1.6	7741 ± 88	766 ± 23	474 ± 10	1240 ± 25	6500 ± 91
1.7	5902 ± 76	604 ± 22	389 ± 9	993 ± 24	4908 ± 80
1.8	4118 ± 64	427 ± 19	310 ± 8	738 ± 21	3379 ± 67
1.9	2527 ± 50	271 ± 17	248 ± 7	520 ± 18	2006 ± 53

Table 5.8: Number of signal and background events for different cuts on p_ℓ^*. Number of total (N_{total}), sideband background (N_{sb}), residual background (N_{res}), total background (N_{bg}), and signal events (N_{signal}).

5.6.3.2 Calculation of Background Subtraction Factors w_i

The left column of Fig. 5.20 shows the measured m_X spectra together with the extracted combinatorial and residual background distributions for different cuts on p_ℓ^*. The corresponding total number of signal and background events are summarized in table 5.8. For each bin in m_X background subtraction factors w_i are determined,

$$w_i(m_X) = \frac{N_{total}(m_X) - N_{bg}(m_X)}{N_{total}(m_X)}. \tag{5.53}$$

The factors w_i define the probability for an event with the invariant hadronic mass m_X to be a signal event. For the final background subtraction we fit the calculated w_i with a polynomial of order 4 (see Fig. 5.20, right column).

5.7 Extraction of Moments

In the following chapter will be described the method utilized to measure the moments of the invariant hadronic mass distribution $< m_X^n >$ with $n = 1 \ldots 6$ as functions of $p_{\ell,cut}^*$. Section 5.7.1 will give an introduction to the applied calibration method. Details of the m_X calibration will be discussed in section 5.7.2. Section 5.7.3 summarizes additional bias corrections that have to be applied. Statistical uncertainties and correlations will be discussed in section 5.7.4. The verification of the overall procedure will be presented in section 5.7.5.

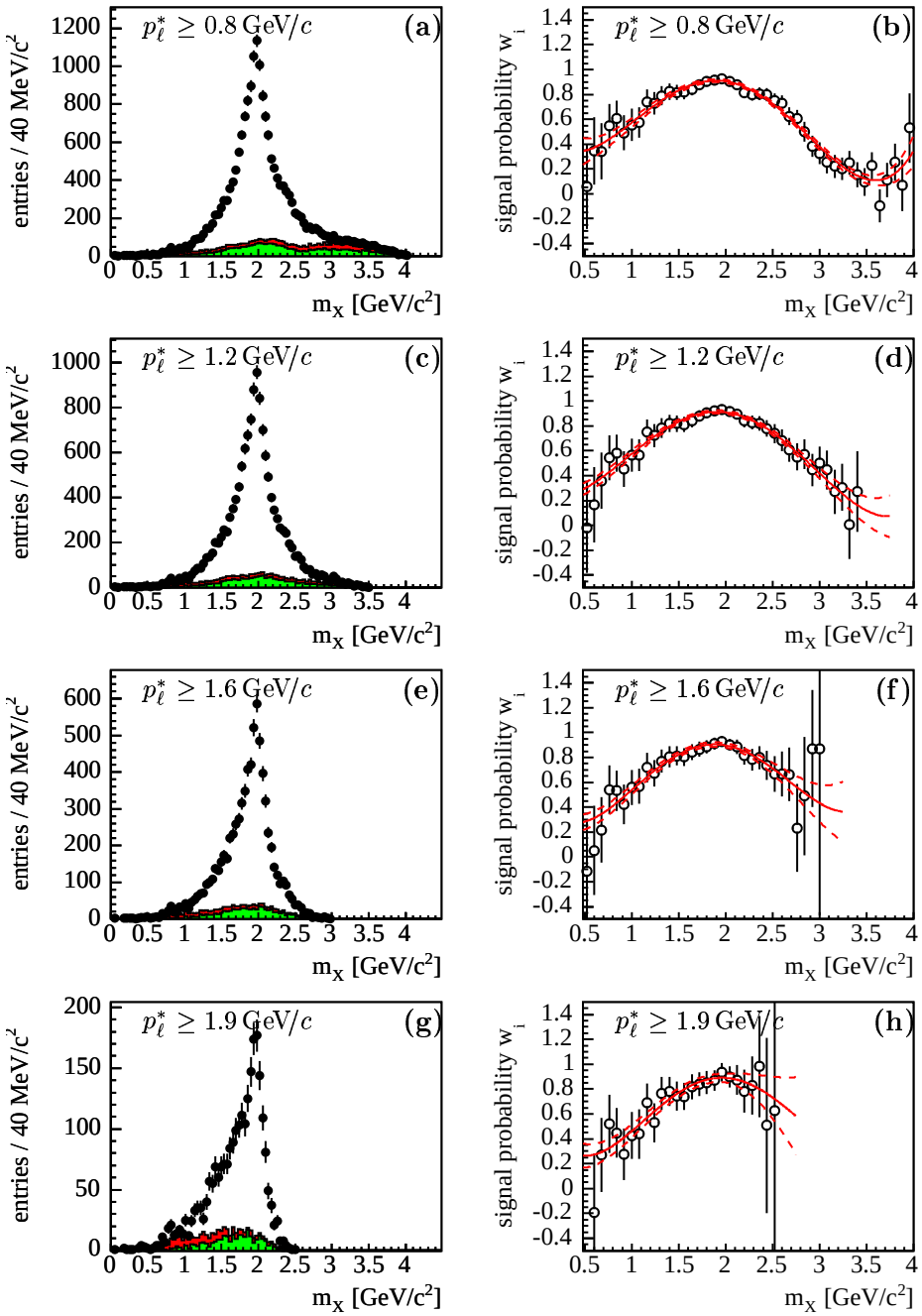

Figure 5.20: The left column shows the measured m_X spectra in data (•) together with the extracted combinatorial (■) and residual (■) background distributions for different cuts on p_ℓ^*. The corresponding background subtraction factors $w_i = \frac{N_{total} - N_{bg}}{N_{total}}$ are shown in the right column together with the fit of a polynomial of 4th order.

5.7.1 Overview

As discussed in section 5.4.2 the kinematic fit already provides an instrument that allows a reliable measurement of the hadronic system in semileptonic decays $B \to X_c \ell \nu$. It significantly reduces the average bias of the measured $m_{X,reco}$ distribution with respect to the true underlying distribution, i.e. the mean of the distribution $m_{X,reco} - m_{X,true}$ is close to zero for all final states. Nevertheless, additional corrections have to be applied to correct remaining effects resulting from the limited acceptance and resolution of the detector. For the extraction of moments we utilize a method that "calibrates" the measured and kinematically fitted $m_{X,reco}$ by applying correction factors on an event-by-event basis. Thereby, the moments $< m_X^n >$ can be calculated directly from the measured $m_{X,reco}$. These factors are chosen in a way that allows the correction of the moments of the measured distribution rather than the deconvolution of the distribution itself.

The background is subtracted by weighting events according to the fraction of signal events expected in the corresponding part of the $m_{X,reco}$ spectrum. The extraction of the background spectrum composed of combinatorial B_{reco} and residual contributions has already been described in the previous chapter 5.6. Fig. 5.20 summarizes the extracted weighting factors $w_i(m_X)$.

We determine the background subtracted moments of order n by calculating the weighted mean,

$$< m_X^n >= \frac{\sum_{i=1}^{N_{evt}} w_i(m_X) m_{X,calib,i}^n}{\sum_i^{N_{evt}} w_i(m_X)} \times \mathcal{C}_{calib} \times \mathcal{C}_{true}, \tag{5.54}$$

with $w_i(m_X)$ the $m_{X,reco}$-dependent background subtraction factors and $m_{X,calib,i}$ the calibrated mass. Nevertheless, additional corrections have to be applied to correct for a remaining small bias after the calibration has been performed. It is distinguished between two categories:

- The factor $\mathcal{C}_{calib}$ corrects for an observed bias of the calibration method.
- The factor $\mathcal{C}_{true}$ corrects for two small principal bias sources: First, for varying selection efficiencies with respect to different exclusive decay channels that can be introduced by the selection cuts. Second, it corrects effects introduced by photons emitted in final state radiation.

5.7.2 Calibration

5.7.2.1 General Construction Principle

The calibration is performed by relating the moments of the measured m_X distribution $< m_{X,reco}^n >$ with the moments of the true underlying mass distribution $< m_{X,true,cut}^n >$ after application of all selection criteria. For the construction of the calibration, decays $B \to X_c \ell \nu$ are selected from the

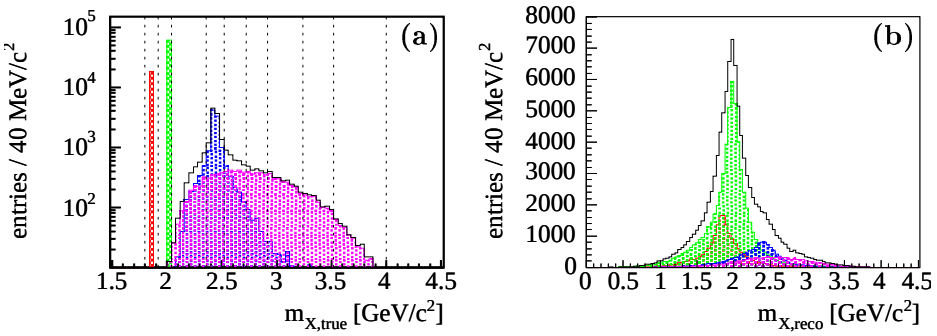

Figure 5.21: Spectra of $m_{X,true}$ (a) and $m_{X,reco}$ (b) with $p^*_\ell \geq 0.8\,\mathrm{GeV}/c$ for different signal decay channels. All selection criteria have been applied. Shown are spectra for the decays $B \to D\ell\nu$ (■), $B \to D^*\ell\nu$ (■), $B \to D^{**}\ell\nu$ (■), $B \to D^{(*)}\pi\ell\nu$ (■), and the sum of all signal decays spectra $B \to X_c\ell\nu$ (□). The dotted lines in (a) indicate the default $m_{X,true}$ binning used in the construction of calibration curves.

sample of cocktail MC simulations. The same subset of events is used for the calculation of $< m^n_{X,true,cut} >$ and $< m^n_{X,reco} >$ dividing the distribution $m^n_{X,true}$ into nine bins. For the first moment $< m_X >$ we choose $[1.8, 1.92, 2.04, 2.36, 2.52, 2.72, 2.92, 3.24, 3.52, 4.0]\,\mathrm{GeV}/c^2$. Fig. 5.21 shows the spectra of true and measured m_X for different signal decay channels together with the chosen binning. The first and the second bin correspond to the decays into true D and D^* mesons, respectively. The remaining bins comprise a mixture of decays $B \to D^{**}\ell\nu$ and $B \to D^{(*)}\pi\ell\nu$. For moments of higher order a corresponding binning is chosen. Bins containing few events, e.g. bins with high m^n_X for high cuts on p^*_ℓ, are merged so that at least 20 events are accumulated in each $m_{X,true}$ bin.

Although the calibration curves are calculated from the cocktail MC simulations that already provide a clean sample of B_{reco} candidates there is still a small amount of combinatorial background existing. The general approach to subtract combinatorial background utilizing a fitting technique has already been discussed. See section 5.6.1 for details. Unfortunately, the small amount of combinatorial background in the cocktail MC sample does not allow to fit the m_{ES} distribution. Therefore, we simply estimate the shape and size of the combinatorial background in the m_{ES} signal region by scaling the combinatorial background spectrum as determined in the m_{ES} sideband region by the relative size of the m_{ES} signal and background regions,

$$\zeta_{sb} = \frac{\int_{signal} \mathrm{d}m_{\mathrm{ES}}}{\int_{sb} \mathrm{d}m_{\mathrm{ES}}}, \tag{5.55}$$

and assume a relative uncertainty of 100% on the scaling factor ζ_{sb}. This sideband subtraction has only a very small effect on the calculated moments.

5.7.2.2 Binning of Calibration

Studies show that the bias of the measured $< m^n_{X,reco} >$ is not constant over the whole phase space but depends on the resolution and multiplicity Mult_{X_c} of the measured hadronic system in the event. The observable $E_{miss} - |\vec{p}_{miss}|$ is closely connected to the resolution of $m_{X,reco}$ since it is a measure for missing (positive values) or additionally measured (negative values) photons and charged particles in the event. Furthermore, we find that the bias of the $< m^n_{X,reco} >$ measurement does also depend on the momentum of the lepton in the semileptonic decay. The p^*_ℓ dependence is clearly evident especially for high p^*_ℓ while its p^*_ℓ dependence is small for low p^*_ℓ. It is indirectly introduced by the observation that the momentum spectrum of the hadronic system varies with different p^*_ℓ and the observed bias and resolution of the $m_{X,reco}$ measurement are functions of the momentum of the hadronic system.

Therefore, the calibration is performed in bins of the mentioned quantities. The following binning is chosen:

1. Twelve bins in p^*_ℓ: eleven bins with widths of $100\,\text{MeV}/c$ between $0.8\,\text{GeV}/c$ and $1.9\,\text{GeV}/c$ and one additional bin with $p^*_\ell \geq 1.9\,\text{GeV}/c$.

2. Three bins in $E_{miss} - |\vec{p}_{miss}|$: $-0.5\,\text{GeV}$ to $0.05\,\text{GeV}$, $0.05\,\text{GeV}$ to $0.2\,\text{GeV}$, and $0.2\,\text{GeV}$ to $0.5\,\text{GeV}$. Due to limited statistics for high p^*_ℓ we do not adopt this binning for $p^*_\ell \geq 1.7\,\text{GeV}/c$.

3. Three bins in Mult_{X_c}: 1 to 5, 6 to 7, and ≥ 8. Like for the $E_{miss} - |\vec{p}_{miss}|$ binning, Mult_{X_c} is not binned for lepton momenta $p^*_\ell \geq 1.7\,\text{GeV}/c$ due to limited MC statistics in that region of the phase space.

Overall the calibration is performed in 75 bins for each moment $< m^n_X >$: 9 for each p^*_ℓ bin below $p^*_\ell = 1.7\,\text{GeV}/c$ and three additional ones for the remaining p^*_ℓ bins.

5.7.2.3 Linear Dependence

Figures 5.22 - 5.25 show the extracted moments $< m^n_{X,reco} >$ vs. $< m^n_{X,true,cut} >$ for $n = 1, 2, 4, 6$ in different bins of $E_{miss} - |\vec{p}_{miss}|$, Mult_{X_c}, and p^*_ℓ. A clear linear dependence between the measured and true quantities is visible. We take advantage of this feature by performing a linear fit that allows to obtain the true moments $< m^n_{X,true,cut} >$ in terms of the reconstructed moments $< m^n_{X,reco} >$.

As shown in figures 5.22 - 5.25 the fitted calibration curves are characterized by comparable slopes but different offsets and follow the linear shape of the calculated moments. A significant deviation from the ideal case of a perfect reconstruction is observed which would imply the equality $< m_{X,reco} >=< m_{X,true,cut} >$ over the full $m_{X,true}$ range.

The observed linear dependence allows to draw some interesting conclusions. The applied method is as far as possible independent of the underlying

physics model as the different decays correspond to different physical processes. By the observed linearity decays to higher masses like $B \to D^{**}\ell\nu$ and $B \to D^{(*)}\pi\ell\nu$ can be described solely from the first two points in the calibration curves which correspond to the decays $B \to D\ell\nu$ and $B \to D^{*}\ell\nu$. This observation supports the assumption that unknown contributions from decays not included in the MC simulation, e.g. $B \to D^{(*)}\pi\pi\ell\nu$, are also properly described by the calibration technique.

In addition the calibration method is independent of the branching fractions of the various contributing decay channels implemented in MC since only the mean values of their m_X^n distributions enter.

5.7.2.4 From the Measured to the Corrected ("Calibrated") Masses

The set of linear calibration curves provide a tool for the correction of the measured $m^n_{X,reco}$. For each event i the calibrated mass $m_{X,calib}$ can be calculated directly from the measured mass by inverting the linear function,

$$m_{X,calib,i} = \frac{m_{X,reco} - A(E_{miss} - |\vec{p}_{miss}|, \mathrm{Mult}_{X_c}, p^*_\ell)}{B(E_{miss} - |\vec{p}_{miss}|, \mathrm{Mult}_{X_c}, p^*_\ell)}, \tag{5.56}$$

with A the offset and B the slope of the corresponding linear calibration curve. Thereby, the measured quantities are on average corrected back to the true masses. The performance of this method is illustrated in figures 5.26 and 5.27 which compare measured, calibrated, and the corresponding true underlying moments with lower cuts on p^*_ℓ and binned in p^*_ℓ, respectively, extracted from the sample of generic MC simulations. Comparing calibrated and measured moments we find an overall correction of the first moment $< m_X >$ between 5% and 16% for moments between $p^*_\ell \geq 0.8\,\mathrm{GeV}/c$ and $p^*_\ell \geq 1.9\,\mathrm{GeV}/c$, respectively. Accordingly, we find relative correction of $8-30\%$ for $< m_X^2 >$, $10-43\%$ for $< m_X^3 >$, $10-54\%$ for $< m_X^4 >$, $10-63\%$ for $< m_X^5 >$, and $21-72\%$ for $< m_X^6 >$. Comparing calibrated and true moments we find a small bias of the size of a few per mille up to 1.5% for all moments. Only for $< m_X^6 >$ the calibration is resulting in larger biases between 3% and 11% for the lowest $p^*_{\ell,cut}$ between $p^*_\ell \geq 0.8\,\mathrm{GeV}/c$ and $p^*_\ell \geq 1.2\,\mathrm{GeV}/c$. The correction of the remaining bias stemming from the calibration will be discussed in section 5.7.3.1.

5.7.3 Bias Corrections

In the following section we discuss sources of small biases that remain after the calibration and need to be corrected. Table 5.9 summarizes all correction factors used in the final moment extraction and their statistical uncertainties. We divide the bias corrections in $\mathcal{C}_{calib}$, as described in the previous section and shown in figures 5.26 and 5.27, and $\mathcal{C}_{true}$, the ratio between true moments before and after analysis cuts.

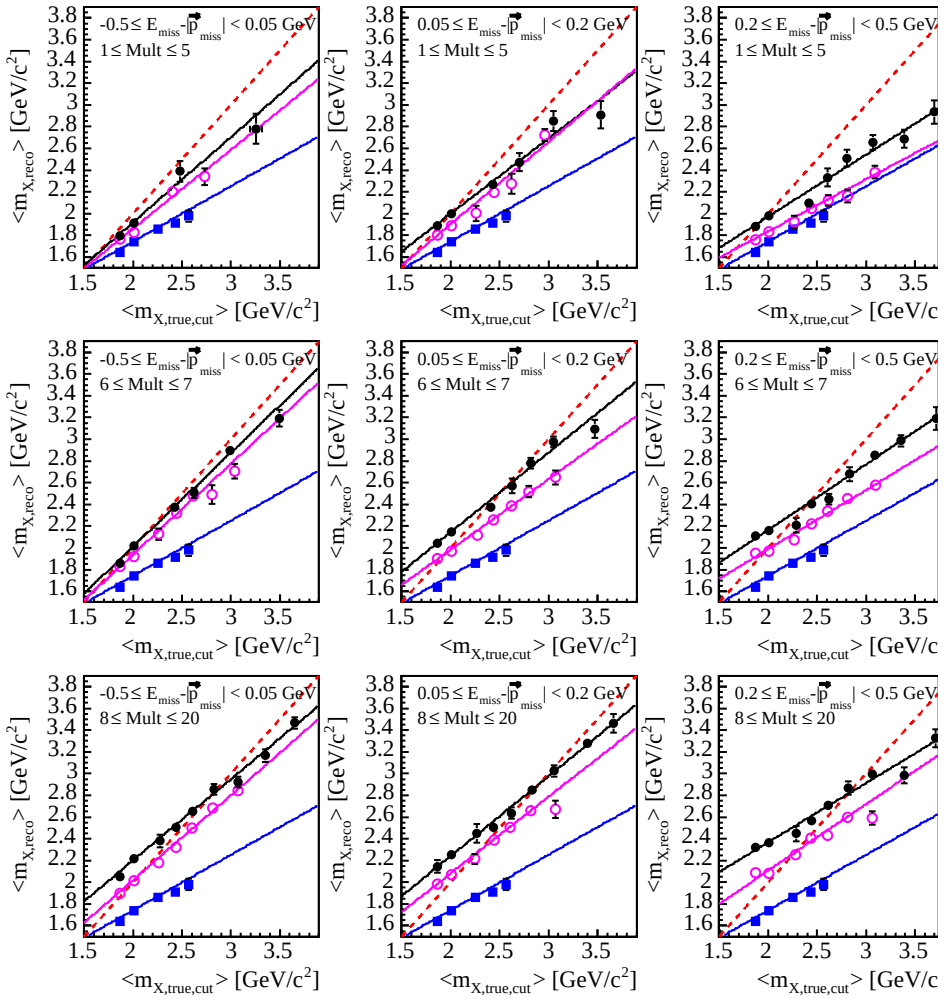

Figure 5.22: Examples of calibration curves for $< m_X >$ in bins of Mult_{X_c}, $E_{miss} - |\vec{p}_{miss}|$ and p^*_ℓ. Shown are the extracted $< m_{X,reco} >$ versus $< m_{X,true,cut} >$ in bins of $m_{X,true}$ for $0.8 \leq p^*_\ell < 0.9\,\mathrm{GeV}/c$ (•), $1.4 \leq p^*_\ell < 1.5\,\mathrm{GeV}/c$ (○), and $p^*_\ell \geq 1.9\,\mathrm{GeV}/c$ (■). The results of fits of linear functions are overlaid as solid lines. A reference line with $< m_{X,reco} >=< m_{X,true,cut} >$ is superimposed as dashed line.

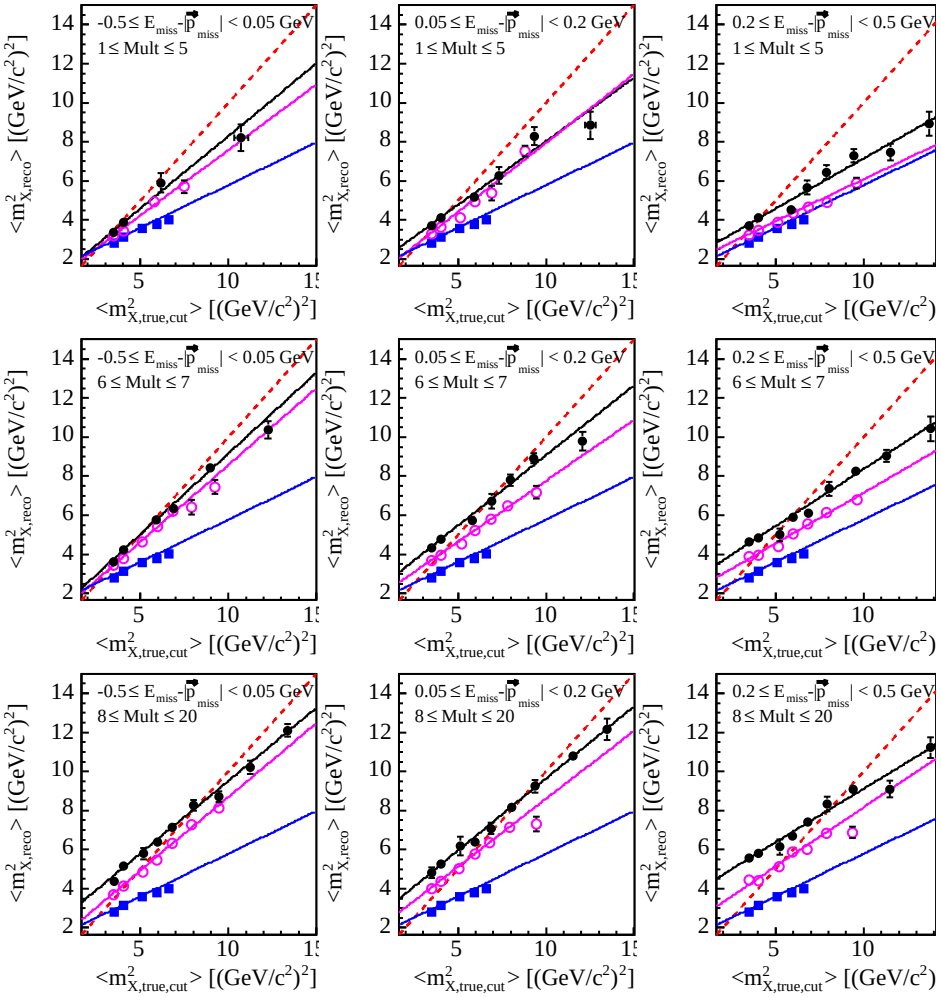

Figure 5.23: Examples of calibration curves for $< m_X^2 >$ in bins of Mult_{X_c}, $E_{miss} - |\vec{p}_{miss}|$ and p_ℓ^*. Shown are the extracted $< m_{X,reco} >$ versus $< m_{X,true,cut} >$ in bins of $m_{X,true}$ for $0.8 \leq p_\ell^* < 0.9\,\mathrm{GeV}/c$ (•), $1.4 \leq p_\ell^* < 1.5\,\mathrm{GeV}/c$ (○), and $p_\ell^* \geq 1.9\,\mathrm{GeV}/c$ (■). The results of fits of linear functions are overlaid as solid lines. A reference line with $< m_{X,reco} >=< m_{X,true,cut} >$ is superimposed as dashed line.

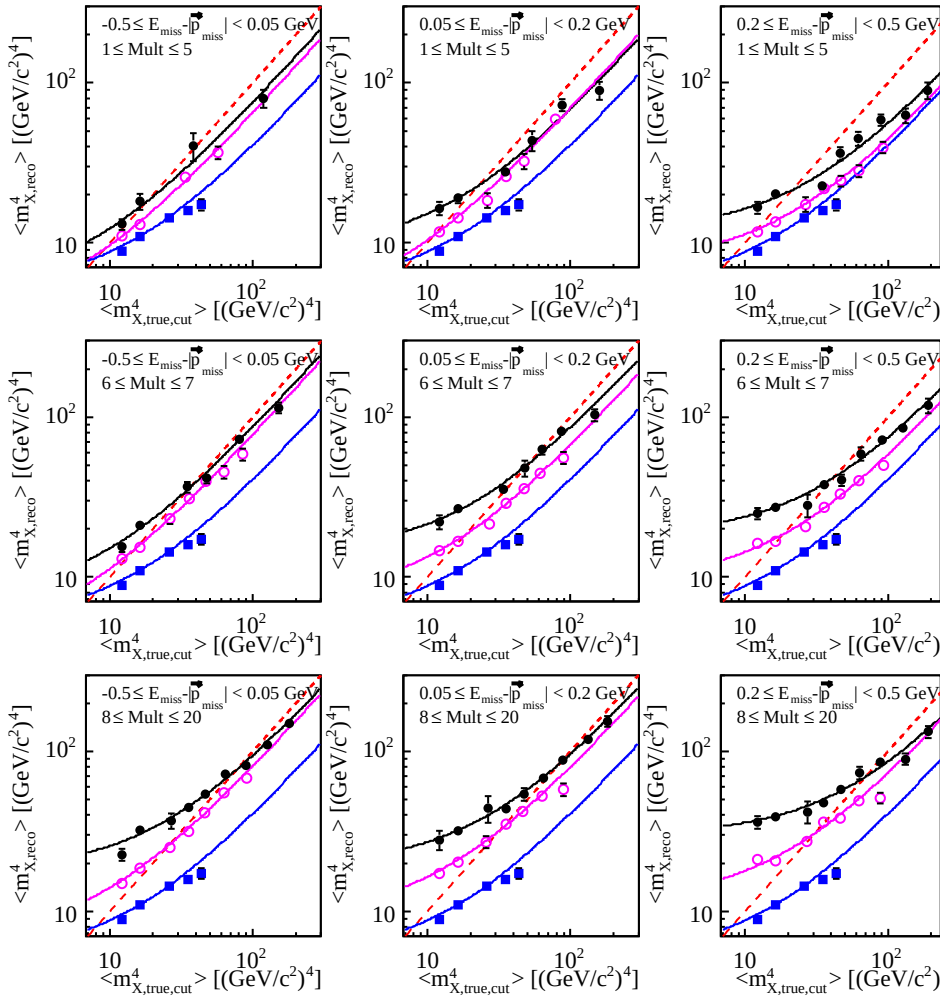

Figure 5.24: Examples of calibration curves for $< m_X^4 >$ in bins of Mult_{X_c}, $E_{miss} - |\vec{p}_{miss}|$ and p_ℓ^*. Shown are the extracted $< m_{X,reco} >$ versus $< m_{X,true,cut} >$ in bins of $m_{X,true}$ for $0.8 \leq p_\ell^* < 0.9\,\mathrm{GeV}/c$ (•), $1.4 \leq p_\ell^* < 1.5\,\mathrm{GeV}/c$ (○), and $p_\ell^* \geq 1.9\,\mathrm{GeV}/c$ (■) on a double logarithmic scale. The results of fits of linear functions are overlaid as solid lines. A reference line with $< m_{X,reco} >=< m_{X,true,cut} >$ is superimposed as dashed line.

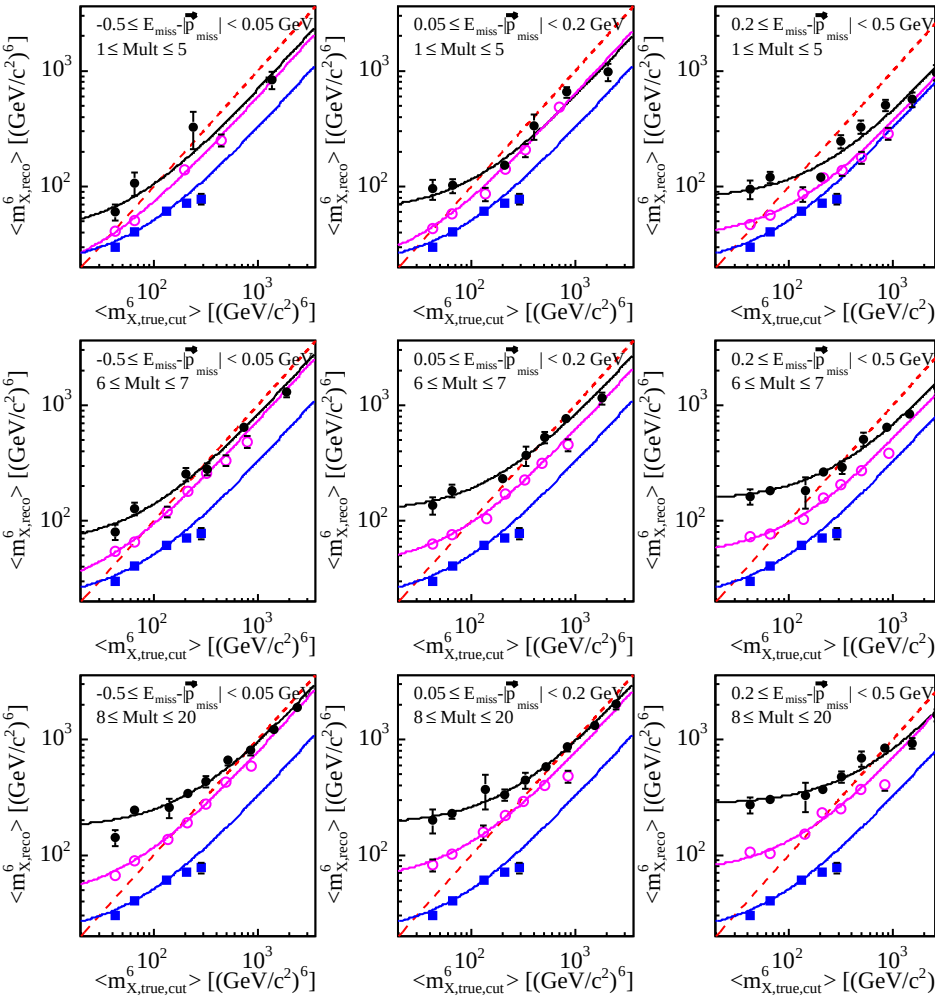

Figure 5.25: Examples of calibration curves for $< m_X^6 >$ in bins of Mult_{X_c}, $E_{miss} - |\vec{p}_{miss}|$ and p_ℓ^*. Shown are the extracted $< m_{X,reco} >$ versus $< m_{X,true,cut} >$ in bins of $m_{X,true}$ for $0.8 \leq p_\ell^* < 0.9\,\mathrm{GeV}/c$ (•), $1.4 \leq p_\ell^* < 1.5\,\mathrm{GeV}/c$ (○), and $p_\ell^* \geq 1.9\,\mathrm{GeV}/c$ (■) on a double logarithmic scale. The results of fits of linear functions are overlaid as solid lines. A reference line with $< m_{X,reco} >=< m_{X,true,cut} >$ is superimposed as dashed line.

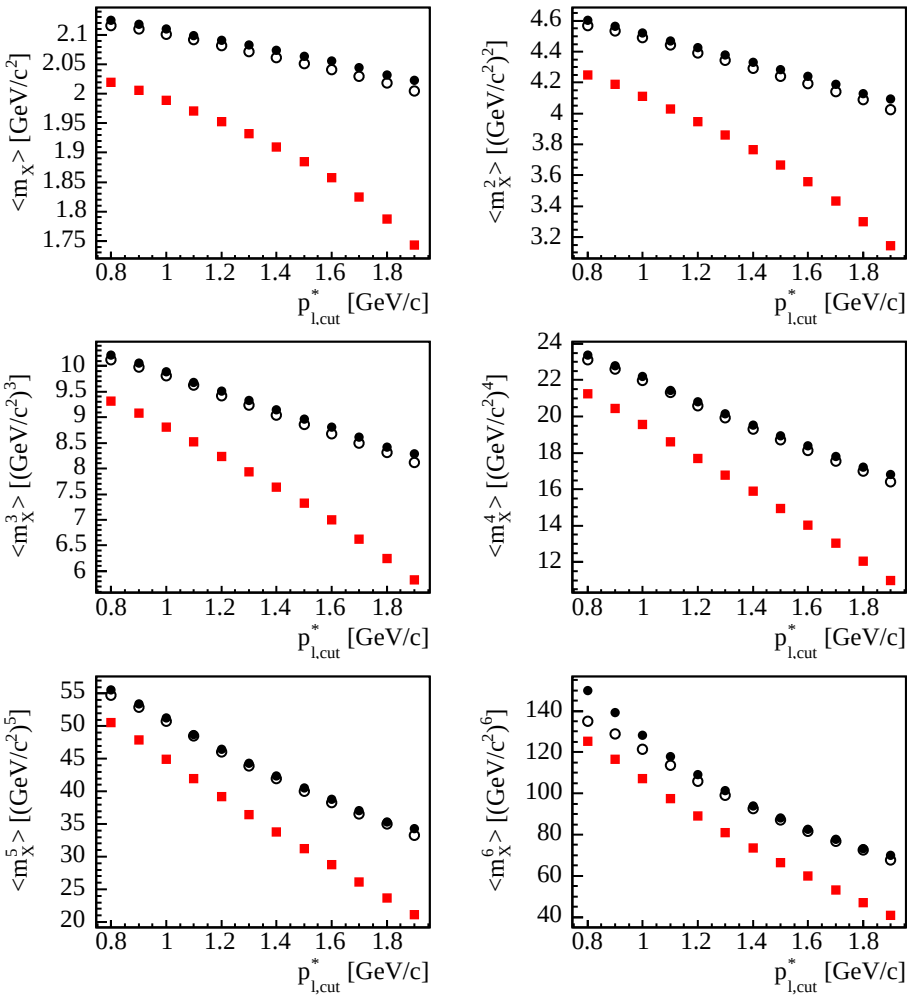

Figure 5.26: Moments calculated in MC simulations for different cuts on p^*_ℓ. The plotted moments are: measured uncalibrated moments (■), calibrated moments (●), and true moments after the application of all analysis cuts (○).

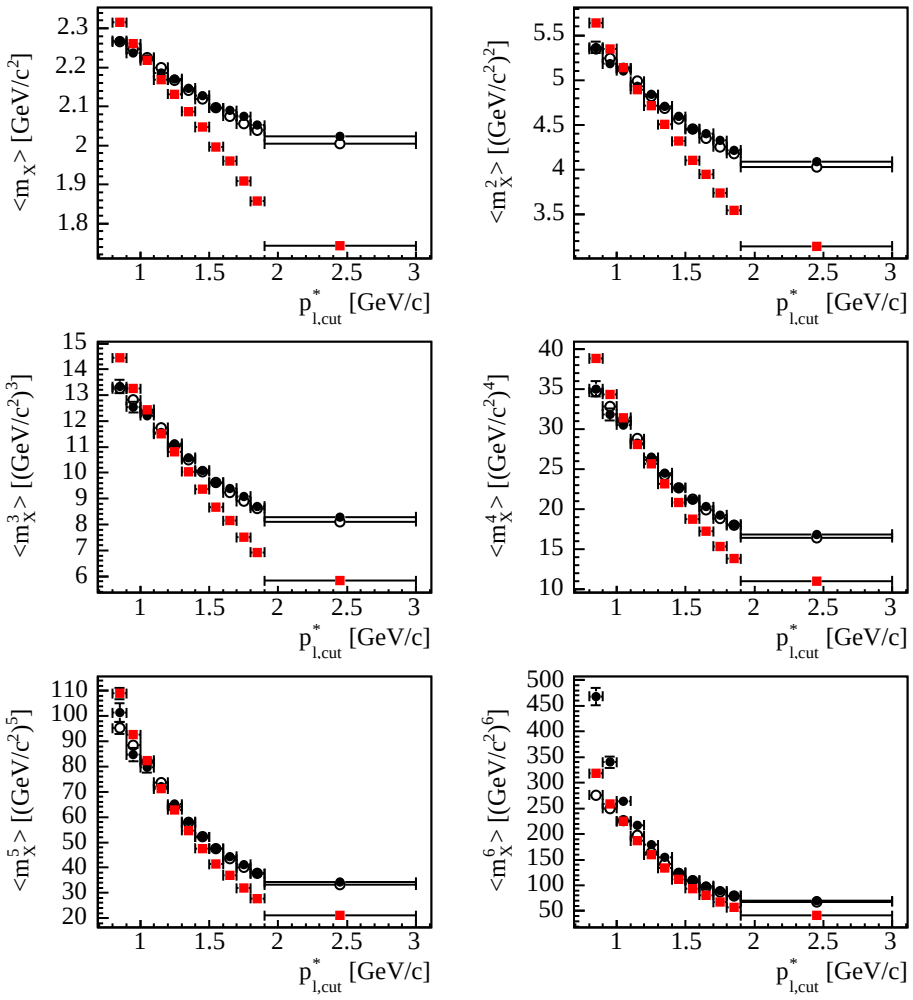

Figure 5.27: Moments calculated in MC simulations in bins of p_ℓ^*. The plotted moments are: measured uncalibrated moments (■), calibrated moments (●), and true moments after the application of all analysis cuts (○).

$p^*_{l,cut}$ [GeV/c]	$< m_X >$ $\mathcal{C}_{calib}$	$\mathcal{C}_{true}$	$\mathcal{C}_{calib} \times \mathcal{C}_{true}$	$< m_X^2 >$ $\mathcal{C}_{calib}$	$\mathcal{C}_{true}$	$\mathcal{C}_{calib} \times \mathcal{C}_{true}$	$< m_X^3 >$ $\mathcal{C}_{calib}$	$\mathcal{C}_{true}$	$\mathcal{C}_{calib} \times \mathcal{C}_{true}$
0.8	0.996 ± 0.001	1.001 ± 0.000	0.997 ± 0.001	0.993 ± 0.002	1.004 ± 0.001	0.997 ± 0.002	0.991 ± 0.004	1.008 ± 0.002	0.999 ± 0.003
0.9	0.996 ± 0.001	1.000 ± 0.000	0.997 ± 0.001	0.994 ± 0.002	1.002 ± 0.001	0.995 ± 0.002	0.992 ± 0.004	1.005 ± 0.002	0.997 ± 0.003
1.0	0.996 ± 0.001	1.000 ± 0.000	0.996 ± 0.001	0.993 ± 0.002	1.001 ± 0.001	0.994 ± 0.002	0.991 ± 0.004	1.003 ± 0.002	0.994 ± 0.003
1.1	0.997 ± 0.001	1.000 ± 0.000	0.996 ± 0.001	0.995 ± 0.002	1.000 ± 0.001	0.995 ± 0.002	0.994 ± 0.004	1.001 ± 0.002	0.995 ± 0.003
1.2	0.995 ± 0.001	0.999 ± 0.000	0.995 ± 0.001	0.993 ± 0.002	0.999 ± 0.001	0.992 ± 0.002	0.991 ± 0.004	1.000 ± 0.002	0.991 ± 0.003
1.3	0.995 ± 0.001	0.999 ± 0.000	0.994 ± 0.001	0.992 ± 0.002	0.998 ± 0.001	0.990 ± 0.002	0.990 ± 0.004	0.998 ± 0.002	0.988 ± 0.003
1.4	0.994 ± 0.001	0.998 ± 0.000	0.993 ± 0.001	0.991 ± 0.002	0.997 ± 0.001	0.988 ± 0.002	0.989 ± 0.004	0.996 ± 0.002	0.986 ± 0.003
1.5	0.994 ± 0.001	0.998 ± 0.000	0.992 ± 0.001	0.990 ± 0.003	0.997 ± 0.001	0.987 ± 0.002	0.989 ± 0.004	0.995 ± 0.002	0.984 ± 0.004
1.6	0.993 ± 0.002	0.998 ± 0.000	0.991 ± 0.001	0.988 ± 0.003	0.997 ± 0.001	0.985 ± 0.003	0.986 ± 0.004	0.996 ± 0.002	0.982 ± 0.004
1.7	0.993 ± 0.002	0.999 ± 0.000	0.991 ± 0.002	0.988 ± 0.003	0.997 ± 0.001	0.986 ± 0.003	0.986 ± 0.005	0.996 ± 0.002	0.983 ± 0.005
1.8	0.993 ± 0.002	0.999 ± 0.000	0.992 ± 0.002	0.990 ± 0.004	0.997 ± 0.001	0.988 ± 0.004	0.989 ± 0.006	0.997 ± 0.002	0.986 ± 0.006
1.9	0.991 ± 0.003	0.999 ± 0.000	0.990 ± 0.003	0.984 ± 0.005	0.998 ± 0.001	0.983 ± 0.005	0.979 ± 0.008	0.998 ± 0.002	0.977 ± 0.008
	$< m_X^4 >$ $\mathcal{C}_{calib}$	$\mathcal{C}_{true}$	$\mathcal{C}_{calib} \times \mathcal{C}_{true}$	$< m_X^5 >$ $\mathcal{C}_{calib}$	$\mathcal{C}_{true}$	$\mathcal{C}_{calib} \times \mathcal{C}_{true}$	$< m_X^6 >$ $\mathcal{C}_{calib}$	$\mathcal{C}_{true}$	$\mathcal{C}_{calib} \times \mathcal{C}_{true}$
0.8	1.011 ± 0.005	0.985 ± 0.003	0.996 ± 0.005	1.015 ± 0.008	0.975 ± 0.004	0.990 ± 0.006	1.111 ± 0.011	0.963 ± 0.006	1.070 ± 0.009
0.9	1.009 ± 0.005	0.991 ± 0.003	1.000 ± 0.004	1.010 ± 0.008	0.984 ± 0.004	0.993 ± 0.006	1.081 ± 0.011	0.974 ± 0.006	1.053 ± 0.008
1.0	1.010 ± 0.005	0.993 ± 0.003	1.003 ± 0.004	1.010 ± 0.007	0.988 ± 0.004	0.998 ± 0.006	1.058 ± 0.010	0.980 ± 0.006	1.037 ± 0.008
1.1	1.006 ± 0.005	0.996 ± 0.003	1.002 ± 0.004	1.005 ± 0.007	0.992 ± 0.004	0.997 ± 0.006	1.037 ± 0.010	0.986 ± 0.005	1.022 ± 0.008
1.2	1.010 ± 0.005	0.997 ± 0.003	1.007 ± 0.004	1.009 ± 0.007	0.993 ± 0.004	1.002 ± 0.006	1.031 ± 0.009	0.987 ± 0.005	1.018 ± 0.008
1.3	1.010 ± 0.005	1.001 ± 0.002	1.011 ± 0.005	1.009 ± 0.007	0.999 ± 0.004	1.008 ± 0.006	1.023 ± 0.009	0.995 ± 0.005	1.018 ± 0.008
1.4	1.011 ± 0.005	1.004 ± 0.002	1.015 ± 0.005	1.010 ± 0.007	1.004 ± 0.003	1.014 ± 0.006	1.013 ± 0.009	1.002 ± 0.005	1.015 ± 0.008
1.5	1.012 ± 0.006	1.006 ± 0.002	1.018 ± 0.005	1.012 ± 0.007	1.006 ± 0.003	1.018 ± 0.006	1.013 ± 0.009	1.006 ± 0.004	1.019 ± 0.008
1.6	1.015 ± 0.006	1.005 ± 0.002	1.020 ± 0.005	1.015 ± 0.008	1.005 ± 0.003	1.020 ± 0.007	1.013 ± 0.009	1.005 ± 0.004	1.019 ± 0.008
1.7	1.015 ± 0.007	1.004 ± 0.002	1.019 ± 0.006	1.014 ± 0.008	1.004 ± 0.003	1.018 ± 0.008	1.012 ± 0.010	1.004 ± 0.004	1.016 ± 0.009
1.8	1.011 ± 0.008	1.004 ± 0.002	1.015 ± 0.008	1.010 ± 0.010	1.004 ± 0.003	1.014 ± 0.010	1.008 ± 0.012	1.004 ± 0.004	1.012 ± 0.011
1.9	1.026 ± 0.010	1.002 ± 0.002	1.029 ± 0.010	1.031 ± 0.013	1.002 ± 0.003	1.032 ± 0.012	1.035 ± 0.015	1.001 ± 0.004	1.036 ± 0.015

Table 5.9: Summary of bias corrections. The bias correction factor $\mathcal{C}_{calib}$ and $\mathcal{C}_{true}$ account for the remaining bias of the calibration method and the residual bias introduced by analysis cuts and final state radiation, respectively. For the definitions of $\mathcal{C}_{calib}$ and $\mathcal{C}_{true}$ see sections 5.7.3.1 and 5.7.3.2.

5.7.3.1 Bias Correction of Calibration

As pointed out in section 5.7.2.4 the final extraction of moments suffers from a bias that is inherent in the applied method itself. Possible sources are the subtraction of combinatorial background and the calibration of moments, i.e. small non-linearities of the calibration curves that are not accounted for in its construction where a linear dependence of measured $< m^n_{X,reco} >$ and true $< m^n_{X,true,cut} >$ quantities is assumed. Although, the observed bias is small compared to the overall size of the calibration it needs to be corrected.

Figure 5.28 shows the difference between the calibrated and true moments together with its statistical uncertainty. We observe a significant deviation from zero for all moments and an uncommonly larger bias for the moments $< m^6_X >$ with lepton momenta cuts below $p^*_\ell \geq 1.2\,\mathrm{GeV}/c$.

The extracted moments are corrected by applying a factor that is calculated from the rate of true and calibrated moments,

$$\mathcal{C}_{calib} = \frac{< m^n_{X,true,cut} >}{< m^n_{X,calib} >}. \tag{5.57}$$

The extracted correction factors $\mathcal{C}_{calib}$ are summarized in table 5.9 and illustrated in figure 5.29. They are typically ranging between 0.4% and 1.5%. For $< m^6_X >$ we observe biases between 3% and 11% for the lowest $p^*_{\ell,cut}$ between $p^*_\ell \geq 0.8\,\mathrm{GeV}/c$ and $p^*_\ell \geq 1.2\,\mathrm{GeV}/c$.

5.7.3.2 Residual Bias Correction

The calibration curves are constructed utilizing the linear dependence of measured $< m^n_{X,reco} >$ and true $< m^n_{X,true,cut} >$ moments where both are calculated for the same events after application of the selection criteria. Thus, applying the calibration procedure, measured moments can only be corrected towards $< m^n_{X,true,cut} >$. Therefore, we have to check, if the moments $< m^n_{X,true,cut} >$ are affected by an intrinsic bias that might be introduced by the applied selection criteria. If the applied selection criteria select different exclusive decay channels with different relative efficiencies the calculated true moments are biased with respect to moments calculated for events that are selected only via their true lepton momenta.

The second effect that needs to be accounted for is caused by photons emitted in final state radiation. Since the theoretical interpretation will be based on calculations that do not take into account final state radiation but it is present in data as well as in the MC simulations, we need to correct this effect.

The residual bias correction factor $\mathcal{C}_{true}$ is calculated from MC simulations alone. It is defined by

$$\mathcal{C}_{true} = \frac{< m^n_{X,true} >}{< m^n_{X,true,cut} >}, \tag{5.58}$$

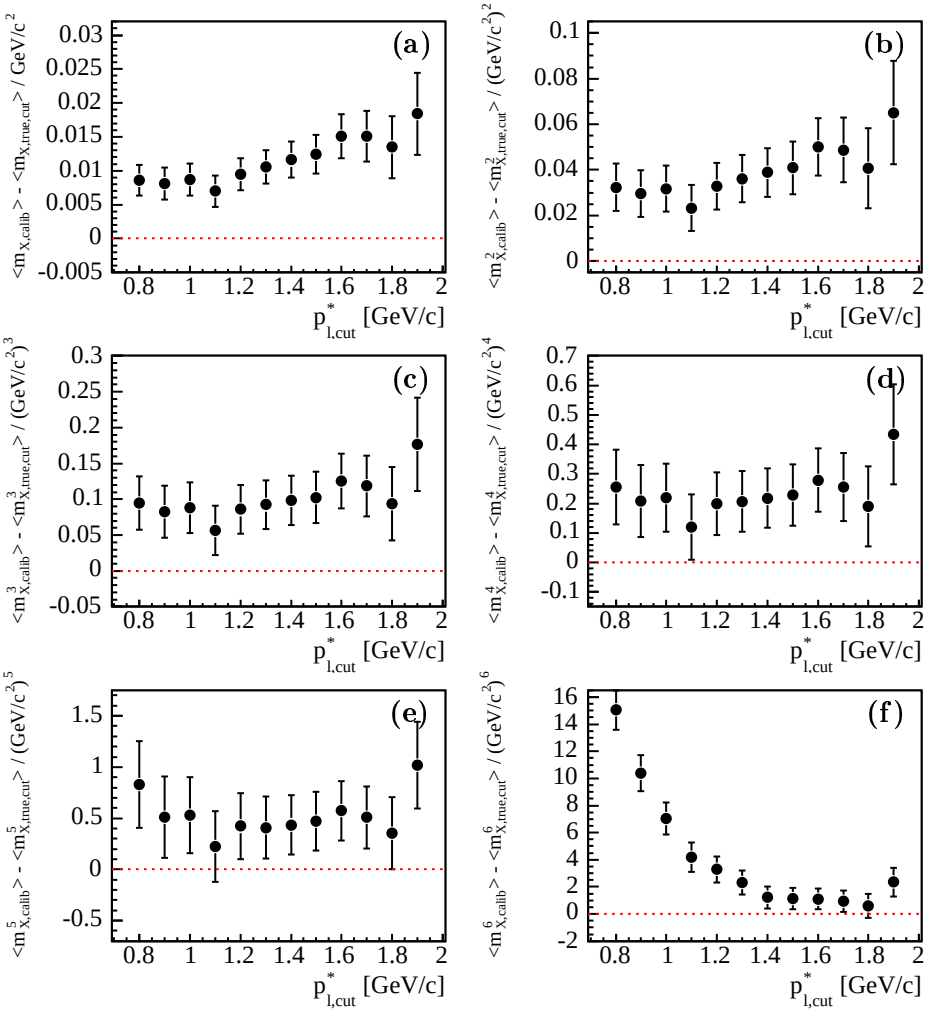

Figure 5.28: Bias after application of the calibration on simulated signal decays.

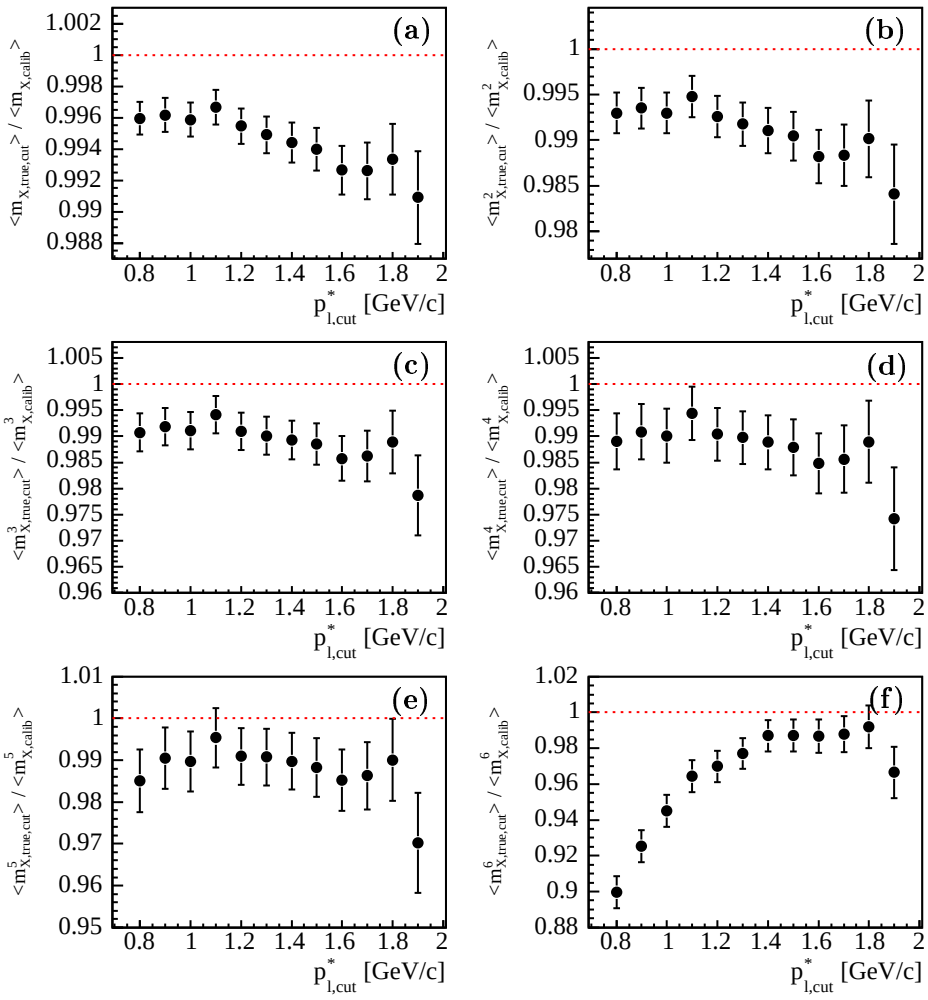

Figure 5.29: Rate of true $< m^n_{X,true,cut} >$ and calibrated moments $< m^n_{X,calib} >$.

with $< m^n_{X,true,cut} >$ the true moment calculated after all selection criteria have been applied whereas $< m^n_{X,true} >$ is the true moment calculated with only the cut on p^*_ℓ applied. The moments $< m^n_{X,true} >$ do not include simulated final state radiation. The extracted correction factors $\mathcal{C}_{true}$ are summarized in table 5.9. Their deviations from unity are typically of the size of a few per mille for all moments.

5.7.4 Statistical Uncertainties and Correlations

Statistical uncertainties stemming from the following sources related to the overall number of signal and background events in data and MC are considered.

1. Moments are extracted from data by calculating the weighted mean,

$$< m^n_X >= \frac{\sum_{i=1}^{N_{evt}} w_i m^n_{X,calib,i}}{\sum_{i=1}^{N_{evt}} w_i},$$

where the weights w_i correspond to the relative amount of signal at the specific location of the m_X spectrum. The sums in the nominator and denominator run over all events. To calculate the variance V of the extracted moments related to the number of observed events, the following expression is used:

$$\begin{aligned} V\left(< m^n_X >\right) &= \mathrm{V}\left(\frac{\sum_{i=1}^{N_{evt}} w_i m^n_{X,calib,i}}{\sum_{i=1}^{N_{evt}} w_i}\right) \\ &= \frac{1}{\left(\sum_{i=1}^{N_{evt}} w_i\right)^2} \mathrm{V}\left(\sum_{i=1}^{N_{evt}} w_i m^n_{X,calib,i}\right) \\ &= \frac{1}{\left(\sum_{i=1}^{N_{evt}} w_i\right)^2} \sum_{i=1}^{N_{evt}} w_i^2 \mathrm{V}\left(m^n_{X,calib,i}\right) \\ &= \frac{\sum_{i=1}^{N_{evt}} w_i^2}{\left(\sum_{i=1}^{N_{evt}} w_i\right)^2} \mathrm{V}\left(m^n_{X,calib}\right). \end{aligned} \tag{5.59}$$

Assuming here that the weights w_i and the calibrated masses $m^n_{X,calib,i}$ do not have uncertainties themselves. It should be noted that the overall statistical variance is given by the variance of the unweighted $m_{X,calib}$ distribution multiplied with the ratio of the sum of squared weights and the squared sum of weights.

2. The statistical uncertainty related to the subtraction of combinatorial and residual background, i.e. the background subtraction factors w_i, is estimated by varying the factors ζ_{sb} used for the rescaling of

background extracted from the m_{ES} sideband randomly within their statistical uncertainties (see sections 5.6.1 and 5.6.2 for details). The ζ_{sb} are varied in data and MC and all moments are extracted based on background distribution changed within their statistical uncertainties. We repeat this procedure 250 times and take the RMS of observed moment variation as measure for the statistical uncertainty related to the background subtraction.

3. The statistical uncertainty related to the extraction of the calibration curves, i.e. the statistical uncertainty in the determination of $m_{X,calib}$, is estimated by varying all calibration curves randomly within their statistical uncertainties resulting in a changed set of curves used for the calibration. We repeat this procedure 250 times and take the RMS of observed moment variation as measure for the statistical uncertainty.

4. Further on we extract additional contributions related to bias corrections factors $\mathcal{C}_{calib}$ and $\mathcal{C}_{true}$. $\mathcal{C}_{calib}$ and $\mathcal{C}_{true}$ are given by fractions of moments (see Eq. 5.57 and 5.58) whose statistical uncertainties are calculated using Eq. 5.59.

All contributions are added in quadrature to form the total statistical uncertainty. The obtained statistical uncertainties are summarized in table 5.10. In total the statistical uncertainties first decrease going to higher cuts on p_ℓ^* and start increasing again. This behaviour can be reasoned directly from equation 5.59. For higher cuts on p_ℓ^* and therefore decreasing number of events the statistical uncertainty is expected to drop since the factor $\sum_{i=1}^{N_{evt}} w_i^2 / \left(\sum_{i=1}^{N_{evt}} w_i\right)^2$ decreases, i.e. the statistical uncertainty is expected to increase for higher cuts on p_ℓ^*. The second effect contributing arises from second term in 5.59, the variance of the measured m_X spetrum. Since the spectrum becomes wider for lower cuts on p_ℓ^* the statistical uncertainty is expected to increase again.

Since all extracted moments share subsets of events among each other they are known to be strong correlated. The overall correlation will be important for the interpretations of the obtained results. We calculate the correlation matrix from first principles. Two arbitrary moments of different orders k and l from different event samples a and c with a being a subset of

c are defined by the weighted means,

$$\begin{aligned} < m_X^k >_a &= \frac{\sum_{i=1}^{N_a} w_i m_{X,calib,i}^k}{\sum_{i=1}^{N_a} w_i}, \\ < m_X^l >_c &= \frac{\sum_{i=1}^{N_c} w_i m_{X,calib,i}^l}{\sum_{i=1}^{N_c} w_i} \\ &= \frac{\sum_{i=1}^{N_a} w_i m_{X,calib,i}^l + \sum_{j=N_a+1}^{N_c} w_i m_{X,calib,i}^l}{\sum_{i=1}^{N_c} w_i} \\ &= \frac{< m_X^l >_a \sum_{i=1}^{N_a} w_i + < m_X^l >_c \sum_{i=N_a+1}^{N_c} w_i}{\sum_{i=1}^{N_c}}. \end{aligned} \tag{5.60}$$

The event sample c is splitted here into two independent subsamples. The covariance of both moments is then given by

$$\begin{aligned} &\mathcal{C}\left(< m_X^k >_a, < m_X^l >_c\right) \\ &= \mathcal{C}\left(< m_X^k >_a, \frac{< m_X^l >_a \sum_{i=1}^{N_a} w_i + < m_X^l >_b \sum_{i=N_a+1}^{N_c} w_i}{\sum_{i=1}^{N_c} w_i} w_i\right) \\ &= \frac{\sum_{i=1}^{N_a} w_i}{\sum_{i=1}^{N_c} w_i} \mathcal{C}\left(< m_X^k >_a, < m_X^l >_a\right) \end{aligned} \tag{5.61}$$

where we make use of the fact that the subsamples a and b are statistically independent by definition. It follows

$$\begin{aligned} &\mathcal{C}\left(< m_X^k >_a, < m_X^l >_c\right) \\ &= \frac{\sum_{i=1}^{N_a} w_i}{\sum_{i=1}^{N_c} w_i} \mathcal{C}\left(\frac{\sum_{i=1}^{N_a} w_i m_{X,calib,i}^k}{\sum_{i=1}^{N_a} w_i}, \frac{\sum_{j=1}^{N_a} w_j m_{X,calib,j}^l}{\sum_{j=1}^{N_a} w_j}\right) \\ &= \frac{1}{\sum_{i=1}^{N_c} w_i \sum_{i=1}^{N_a} w_i} \mathcal{C}\left(\sum_{i=1}^{N_a} w_i m_{X,calib,i}^k \sum_{j=1}^{N_a} w_j m_{X,calib,j}^l\right) \\ &= \frac{1}{\sum_{i=1}^{N_c} w_i \sum_{i=1}^{N_a} w_i} \sum_{i=1}^{N_a} \sum_{j=1}^{N_a} w_i w_j \mathcal{C}\left(m_{X,calib,i}^k, m_{X,calib,j}^l\right) \\ &= \frac{1}{\sum_{i=1}^{N_c} w_i \sum_{i=1}^{N_a} w_i} \sum_{i=1}^{N_a} \sum_{j=1}^{N_a} w_i w_j \delta_{ij} \mathcal{C}\left(m_{X,calib}^k, m_{X,calib}^l\right). \end{aligned} \tag{5.62}$$

The last step follows from the fact that two different $m_{X,calib,i}^k$ and $m_{X,calib,j}^l$ are statistical independent but random samples of the same pdf. Finally, we

arrive at

$$\begin{aligned}
&\mathcal{C}\left(< m_X^k >_a, < m_X^l >_c\right) \\
&= \frac{\sum_{i=1}^{N_a} w_i^2}{\sum_{i=1}^{N_c} w_i \sum_{i=1}^{N_a} w_i} \mathcal{C}\left(m_{X,calib}^k, m_{X,calib}^l\right)_a \\
&= \frac{\sum_{i=1}^{N_a} w_i^2}{\sum_{i=1}^{N_c} w_i \sum_{i=1}^{N_a} w_i} \left\langle \left(m_{X,calib}^k - < m_{X,calib}^k >\right) \left(m_{X,calib}^l - < m_{X,calib}^l >\right) \right\rangle_a \\
&= \frac{\sum_{i=1}^{N_a} w_i^2}{\sum_{i=1}^{N_c} w_i \sum_{i=1}^{N_a} w_i} \left(< m_X^{k+l} >_a - < m_X^k >_a < m_X^l >_a\right).
\end{aligned} \tag{5.63}$$

The corresponding correlations ρ are calculated from the covariance by

$$\begin{aligned}
&\rho\left(< m_X^k >_a, < m_X^l >_c\right) \\
&= \frac{\mathcal{C}\left(< m_X^k >_a, < m_X^l >_c\right)}{\sqrt{\mathrm{V}\left(< m_X^k >_a\right) \mathrm{V}\left(< m_X^l >_c\right)}} \\
&= \sqrt{\frac{\sum_{i=1}^{N_a} w_i^2}{\sum_{i=1}^{N_c} w_i^2}} \cdot \frac{< m_X^{k+l} >_a - < m_X^k >_a < m_X^l >_a}{\sqrt{< m_X^{2k} >_a - < m_X^k >_a^2} \sqrt{< m_X^{2l} >_c - < m_X^l >_c^2}}.
\end{aligned} \tag{5.64}$$

That is, the calculation of the correlation of two moments of orders k and l requires the calculation of the unweighted moments of order k, l, $k+l$, $2k$, and $2l$. The tables A.1 - A.6 summarize all extracted correlation coefficients. They vary between 4% and 99%.

5.7.5 Verification of the Calibration Procedure

In order to verify the method used for the moment extraction, i.e. the calibration and final bias correction, two cross checks are performed.

1. The calibration is checked on simulated exclusive signal final states.
2. A complete check of the entire analysis chain is performed with MC simulation treating a subset of simulated events like data and the remaining events like MC.

The obtained results will be discussed in the following.

5.7.5.1 Calibration of Exclusive Signal Decay Modes

The calibration curves are constructed using the sum of different simulated exclusive final states. As was already shown in section 5.7.2.4 the calibration

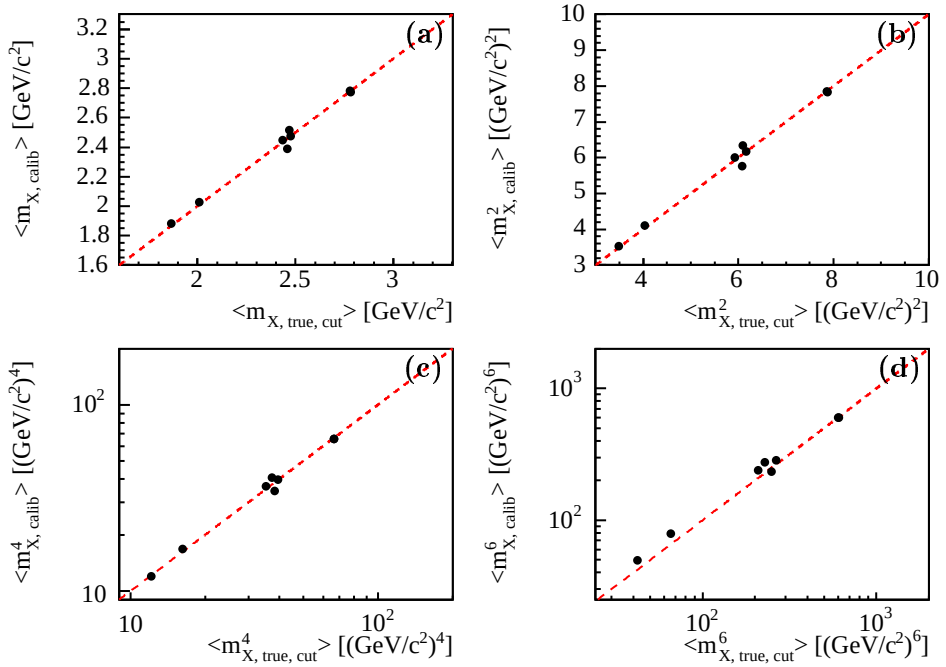

Figure 5.30: Calibration of exclusive decays modes with $p^*_\ell \geq 0.8\,\mathrm{GeV}/c$ for the moments $< m_X >$ (a), $< m_X^2 >$ (b), $< m_X^4 >$ (c), and $< m_X^6 >$ (d). A reference line complying $< m_{X,reco} >=< m_{X,true,cut} >$ is superimposed.

method works reliably, apart from a small remaining bias that needs to be accounted for.

We check whether the calibration is also able to correct exclusive final states back to their true masses by applying the calibration on single signal decay channels. The test is performed for the decays $B \to D\ell\nu$, $B \to D^*\ell\nu$, four resonant decays $B \to D^{**}\ell\nu$, and two non-resonant decays $B \to D^{(*)}\pi\ell\nu$. We use the sample of cocktail MC simulations that is also used for the construction of the calibration curves.

The figures 5.30 and 5.31 show the obtained results for different cuts $p^*_\ell \geq 0.8\,\mathrm{GeV}/c$ and $p^*_\ell \geq 1.9\,\mathrm{GeV}/c$. The dashed line corresponds to $< m_{X,reco} >=< m_{X,true,cut} >$ implying a perfect calibration. As can be seen the calibrated moments line up nicely along this line.

5.7.5.2 Calibration of Generic MC Simulations

We check the procedure applied for the extraction of hadronic mass moments on the sample of generic MC simulations. Thereby, it is split into two even sized subsets which are used for different purposes:

1. The first half is used like data in the final analysis, i.e. only measured quantities and no truth information is used. Moments are calcu-

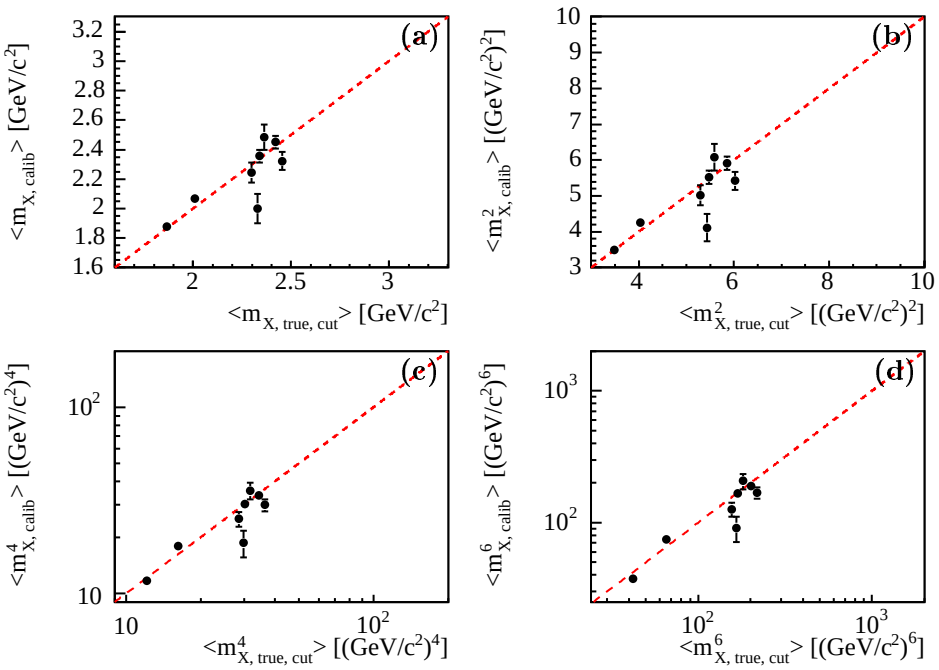

Figure 5.31: Calibration of exclusive decays modes with $p^*_\ell \geq 1.9\,\mathrm{GeV}/c$ for the moments $< m_X >$ (a), $< m_X^2 >$ (b), $< m_X^4 >$ (c), and $< m_X^6 >$ (d). A reference line complying $< m_{X,reco} > = < m_{X,true,cut} >$ is superimposed.

lated by applying the default set of calibration curves constructed on the independent cocktail MC sample and subtraction of combinatorial background.

2. The second half is treated like MC in the final analysis. It is used for the subtraction of residual background and for the determination of bias correction factors.

This test allows to check the performance of the analysis procedure with respect to some important issues:

- It allows to perform a robust test of the extraction formalism. If the true moments are reobtained we can deduce that the overall procedure works reliably stable and delivers self-consistent results.

- Since we utilize a sample of cocktail MC simulations that provide a large quantity of clean B_{reco} candidates for the construction of the calibration curves it has to be checked if systematic effects are introduced in the extraction of moments. If the calibration applied on generic MC is able to extract the true underlying moments it can be concluded that systematic effects stemming from the difference of cocktail and generic MC are small.

Figure 5.32 shows the obtained results for all moments and different lower cuts on p_ℓ^*. Since the different moments are highly correlated we extracted the same quantities also in statistical independent bins of p_ℓ^* as shown in figure 5.33. Applying the analysis procedure the true moments are reobtained within 2σ whereas the moments with higher cuts above $p_\ell^* \geq 1.2\,\mathrm{GeV}/c$ are reobtained within 1σ. All moments extracted in bins of p_ℓ^* match the true underlying moments within 1.5σ. Overall, we conclude that the performed test is able to verify the applied analysis procedure within its statistical uncertainties.

5.8 Results

Figure 5.34 shows the extracted moments $< m_X^n >$ for $n = 1 \ldots 6$ as functions of lower cuts on the lepton momentum p_ℓ^*. The moments are shown together with their statistical and systematic uncertainties. In addition all numerical results are summarized in the table 5.10.

As expected a significant p_ℓ^* dependence is observed manifesting in decreasing moments for higher cuts on p_ℓ^*. It is resulting from a reduced contribution of higher mass final states to the overall m_X spectrum as depicted in Fig. 5.20. For the higher lepton momenta cuts above $p_\ell^* \geq 1.6\,\mathrm{GeV}/c$ a flattening of the measured slope is observed occuring in the region of the phase space where only few higher mass final states with masses above those of the D^* meson contribute.

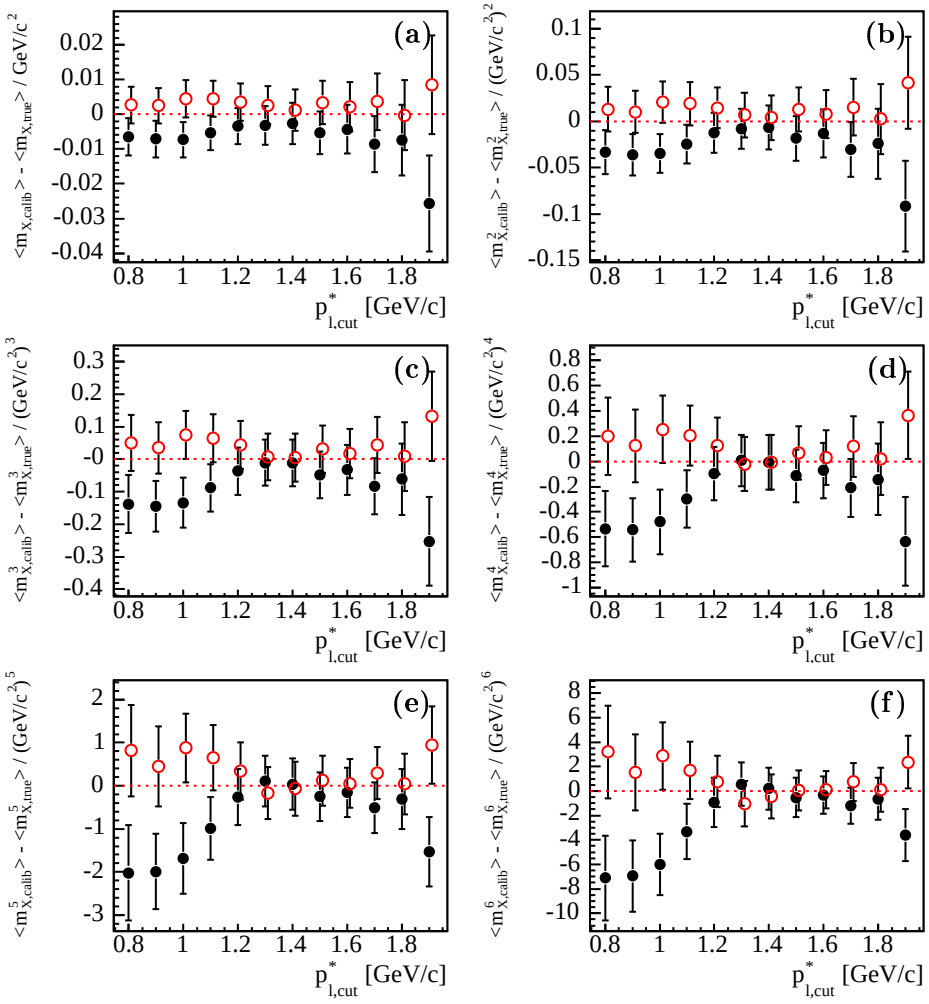

Figure 5.32: Verification of the analysis procedure on MC simulations for all moments and different lower cuts on p^*_ℓ. The moments are calculated on a subset of events while the while the events are used for the subtraction of residual background and calculation of bias correction factors. Two checks are performed with the default subdivision (■) and interchanged samples (●).

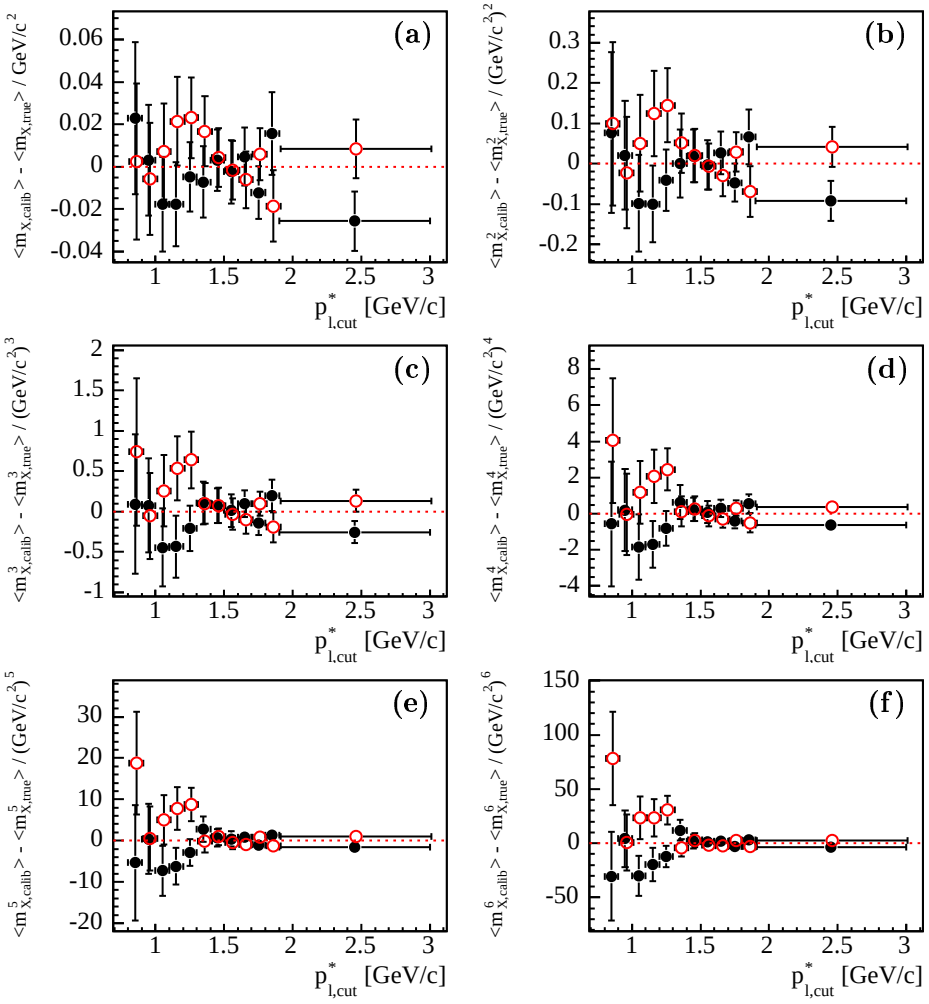

Figure 5.33: Verification of the analysis procedure on MC simulations for all moments in bins of p^*_ℓ. The moments are calculated on a subset of events while the while the events are used for the subtraction of residual background and calculation of bias correction factors. Two checks are performed with the default subdivision (■) and interchanged samples (●).

Correlation coefficients for all moments measured are summarized in tables A.1 - A.6 in the appendix. We obtain correlations ranging between 4% and 99%.

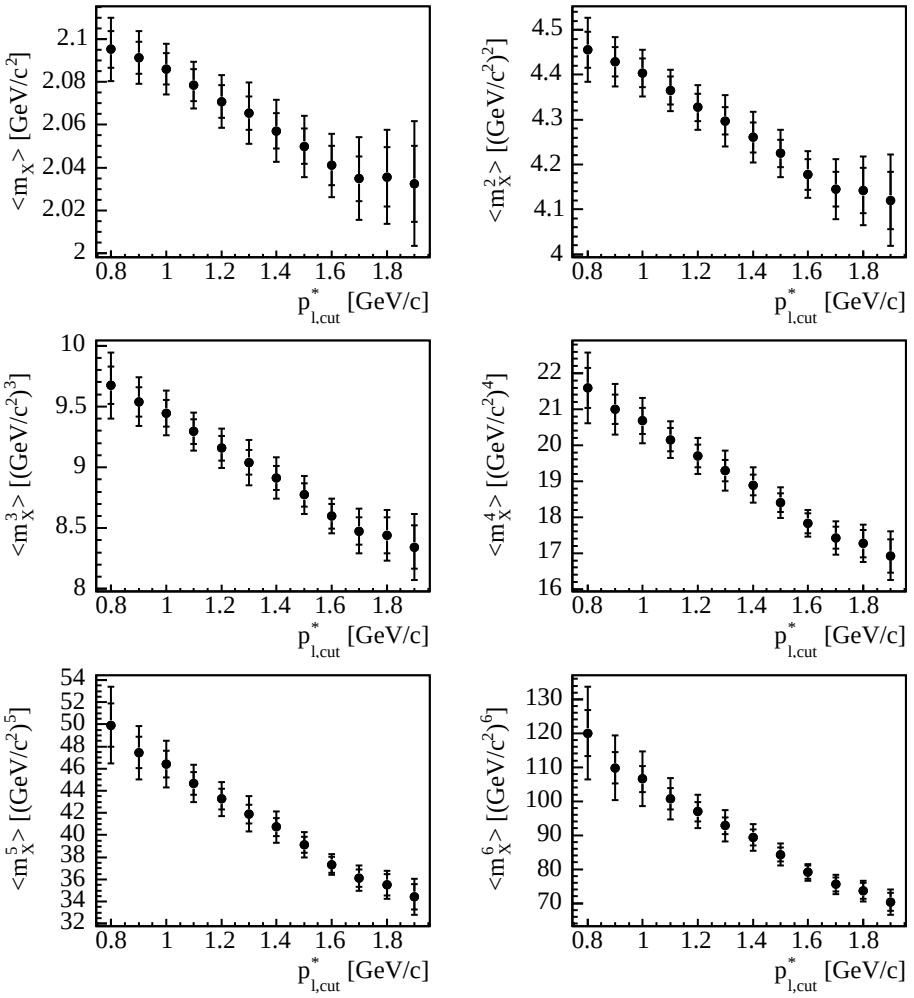

Figure 5.34: Moments calculated for different cuts on p_ℓ^*. The inner error bars correspond to the statistical uncertainties while the full error bars correspond to the square sum of statistical and systematic uncertainties.

$p_{l,cut}$ $[GeV/c]$	$< m_X > [GeV/c^2]$	$< m_X^2 > [(GeV/c^2)^2]$
0.8	$2.0951 \pm 0.0086 \pm 0.0119$	$4.455 \pm 0.041 \pm 0.058$
0.9	$2.0912 \pm 0.0074 \pm 0.0097$	$4.429 \pm 0.035 \pm 0.043$
1.0	$2.0860 \pm 0.0072 \pm 0.0093$	$4.404 \pm 0.032 \pm 0.041$
1.1	$2.0785 \pm 0.0073 \pm 0.0081$	$4.365 \pm 0.031 \pm 0.034$
1.2	$2.0708 \pm 0.0074 \pm 0.0095$	$4.327 \pm 0.031 \pm 0.039$
1.3	$2.0653 \pm 0.0077 \pm 0.0121$	$4.297 \pm 0.031 \pm 0.049$
1.4	$2.0571 \pm 0.0080 \pm 0.0118$	$4.260 \pm 0.032 \pm 0.046$
1.5	$2.0500 \pm 0.0080 \pm 0.0117$	$4.224 \pm 0.031 \pm 0.043$
1.6	$2.0410 \pm 0.0089 \pm 0.0115$	$4.178 \pm 0.034 \pm 0.039$
1.7	$2.0349 \pm 0.0106 \pm 0.0161$	$4.145 \pm 0.039 \pm 0.055$
1.8	$2.0357 \pm 0.0138 \pm 0.0170$	$4.142 \pm 0.050 \pm 0.058$
1.9	$2.0325 \pm 0.0176 \pm 0.0230$	$4.120 \pm 0.064 \pm 0.079$
	$< m_X^3 > [(GeV/c^2)^3]$	$< m_X^4 > [(GeV/c^2)^4]$
0.8	$9.67 \pm 0.15 \pm 0.23$	$21.60 \pm 0.55 \pm 0.81$
0.9	$9.54 \pm 0.12 \pm 0.16$	$21.00 \pm 0.41 \pm 0.56$
1.0	$9.45 \pm 0.11 \pm 0.15$	$20.68 \pm 0.37 \pm 0.51$
1.1	$9.29 \pm 0.10 \pm 0.12$	$20.15 \pm 0.32 \pm 0.40$
1.2	$9.16 \pm 0.10 \pm 0.13$	$19.70 \pm 0.31 \pm 0.40$
1.3	$9.04 \pm 0.10 \pm 0.16$	$19.29 \pm 0.29 \pm 0.47$
1.4	$8.91 \pm 0.10 \pm 0.14$	$18.89 \pm 0.29 \pm 0.40$
1.5	$8.77 \pm 0.09 \pm 0.12$	$18.41 \pm 0.27 \pm 0.33$
1.6	$8.60 \pm 0.10 \pm 0.10$	$17.83 \pm 0.27 \pm 0.25$
1.7	$8.48 \pm 0.11 \pm 0.14$	$17.43 \pm 0.30 \pm 0.35$
1.8	$8.44 \pm 0.15 \pm 0.15$	$17.27 \pm 0.38 \pm 0.36$
1.9	$8.34 \pm 0.18 \pm 0.21$	$16.93 \pm 0.46 \pm 0.50$
	$< m_X^5 > [(GeV/c^2)^5]$	$< m_X^6 > [(GeV/c^2)^6]$
0.8	$49.93 \pm 1.95 \pm 2.87$	$120.04 \pm 6.78 \pm 11.89$
0.9	$47.44 \pm 1.40 \pm 1.97$	$109.85 \pm 4.58 \pm 8.37$
1.0	$46.40 \pm 1.18 \pm 1.75$	$106.58 \pm 3.73 \pm 7.07$
1.1	$44.64 \pm 1.00 \pm 1.34$	$100.73 \pm 3.13 \pm 5.29$
1.2	$43.26 \pm 0.92 \pm 1.22$	$96.95 \pm 2.65 \pm 3.98$
1.3	$41.91 \pm 0.84 \pm 1.37$	$92.83 \pm 2.41 \pm 3.88$
1.4	$40.72 \pm 0.83 \pm 1.14$	$89.38 \pm 2.31 \pm 3.05$
1.5	$39.12 \pm 0.73 \pm 0.89$	$84.32 \pm 1.98 \pm 2.48$
1.6	$37.33 \pm 0.72 \pm 0.59$	$79.06 \pm 1.88 \pm 1.56$
1.7	$36.12 \pm 0.79 \pm 0.83$	$75.53 \pm 2.01 \pm 1.98$
1.8	$35.52 \pm 0.97 \pm 0.83$	$73.58 \pm 2.39 \pm 1.91$
1.9	$34.44 \pm 1.13 \pm 1.14$	$70.37 \pm 2.71 \pm 2.59$

Table 5.10: Summary of extracted moments $< m_X^n >$ as function of $p^*_{\ell,cut}$. The uncertainties given are statistical and systematic.

.

Chapter 6

Systematic Studies

In the following section several potential sources of systematic uncertainties will be discussed. We will focus on studies associated with the calibration procedure, like the bias corrections (6.2) and the chosen calibration curve binning (6.3), the model used for the simulation of signal decays (6.4), residual and combinatorial background subtraction (6.5), effects stemming from mis modeling in MC like track and photon selection efficiencies (6.6, 6.7), hard and soft photon emission (6.8, 6.9), as well as checks testing the stability of the extracted results (6.10). All determined systematic uncertainties are summarized in tables 6.1 - 6.6 at the end of this chapter.

6.1 General Procedure

If not stated otherwise the following procedure is followed in the determination of systematic uncertainties:

1. Starting from the nominal analysis procedure, corrections to MC are applied to the quantities in question.

2. Reapplying the extraction procedure to the changed setup, new moments are calculated.

3. The observed difference with respect to the nominal value is taken as systematic uncertainty.

The described procedure is repeated for every source of systematic uncertainty. The total systematic uncertainty is calculated as the square sum of all of the individual uncertainties

6.2 Bias of Calibration

As discussed in section 5.7.3.1 the calibration method is affected by a small bias. The extracted moments are corrected for this bias. The statistical

uncertainty of the determined bias correction is added to the statistical error. In addition half of the overall bias correction is taken as systematic uncertainty.

6.3 Binning of Calibration Curves

Resolution and bias of the measured hadronic mass $m_{X,reco}$ varies with the multiplicity of the hadronic system and the missing energy and momentum $E_{miss} - |\vec{p}_{miss}|$. This effect is regarded to by the construction of the calibration curves binned in these quantities. Differences in the multiplicity and $E_{miss} - |\vec{p}_{miss}|$ distributions between data and MC might result in the migration of events between bins. To estimate such effects we perform a rebinning of the calibration curves. The nominal calibration curves are binned in multiplicity ($[1, 5, 7, 50]$) and $E_{miss} - |\vec{p}_{miss}|$ ($[-0.5, 0.05, 0.2, 0.5]$ GeV). This default 3×3 binning is changed into a 2×2 binning. We choose $[1, 6, 50]$ for the multiplicity binning and $[-0.5, 0.125, 0.5]$ GeV for the binning in $E_{miss} - |\vec{p}_{miss}|$. We repeat the measurement with the modified calibration curves and take the observed difference as systematic uncertainty.

6.4 Simulation Model of Signal Decays

The analysis technique applied to measure the moments of the invariant hadronic mass distribution relies in important parts on the usage of MC simulations. For the extraction of moments the dependence exists especially with respect to the model utilized to simulate signal decays. Thereby, especially high mass contributions to the full semileptonic decay width apart from $B \to D\ell\nu$ and $B \to D^*\ell\nu$ decays are scarcely known. The simulation contains decays to excited states $B \to D^{**}\ell\nu$ with four exclusive channels and decays into non-resonant $B \to D^{(*)}\pi\ell\nu$ final states with also four exclusive channels. The systematic uncertainty connected with the chosen signal model is evaluated by changing its composition, i.e. dropping one or more exclusive channels. We study the simulation model dependence of the construction of calibration curves and of the residual bias correction.

6.4.1 Simulation Model Dependence of Calibration

The systematic uncertainty of the calibration method with respect to the chosen signal model is checked by applying the following two procedures described below:

1. The compostion of the signal decay distribution is changed by dropping single exclusive modes in the construction of the calibration curves. Thereby, we get eight different sets of calibration curves to be used in the moment extraction.

2. We check the dependence of the calibration method on the simulation of the high mass tail by cutting out events above certain thresholds $m_{X,true} \geq 2.5, 2.7, 2.9, 3.2, 3.5, 4.0\,\mathrm{GeV}/c^2$ corresponding to the highest bins in the calibration curve construction. By doing so the high mass dependence of the calibration curve is changed.

Overall we construct ten different sets of calibration curves with signal decay models deviating from the nominal model. Figure 6.1 shows distributions of moments under variation of the signal model for different cuts $p^*_{\ell,cut}$. The RMS of the observed variations is taken as measure for the systematic uncertainty.

6.4.2 Model Dependence of Residual Bias Correction

The simulation model used in the residual bias correction is changed by simultaneously dropping one or more exclusive modes, $B \to D^{**}\ell\nu$ and $B \to D^{(*)}\pi\ell\nu$, in enumerator and denominator of $\mathcal{C}_{true} = \frac{<m^n_{X,true}>}{<m^n_{X,true,cut}>}$. To keep the total semileptonic branching fraction constant the branching fractions of the remaining high mass channels are scaled up to compensate the dropped modes. The observed variations of the residual bias correction factors are shown in Fig. 6.2. We take the RMS of the observed variations as systematic uncertainties.

6.5 Background Subtraction

6.5.1 Combinatorial Background Subtraction

The shape of the combinatorial background distribution is determined in the m_{ES} sideband region defined as $5.21 \leq m_{\mathrm{ES,sb}} \leq 5.255\,\mathrm{GeV}/c^2$. We vary the upper and lower bounds of the sideband window definition by $\pm 2.5\,\mathrm{MeV}/c^2$ separately and concurrently to study the effect of signal events leaking from the signal region into the sideband region. The size of the performed variation corresponds to the usual σ of the signal peak in the m_{ES} distribution and is chosen to be relatively small to avoid additional statistical fluctuations.

The RMS of the observed variations with respect to the nominal value is taken as measure for possible systematic deviations. Since the observed variation is small and fully covered by the statical uncertainty on the background subtraction we interpret it as a statistical fluctuation and do not consider it as an additional systematic uncertainty.

6.5.2 Residual Background Subtraction

The subtraction of residual background requires the simulation of several decays channels. The branching fractions of those simulated decays are rescaled to meet experimental measurements. The applied procedure is described in

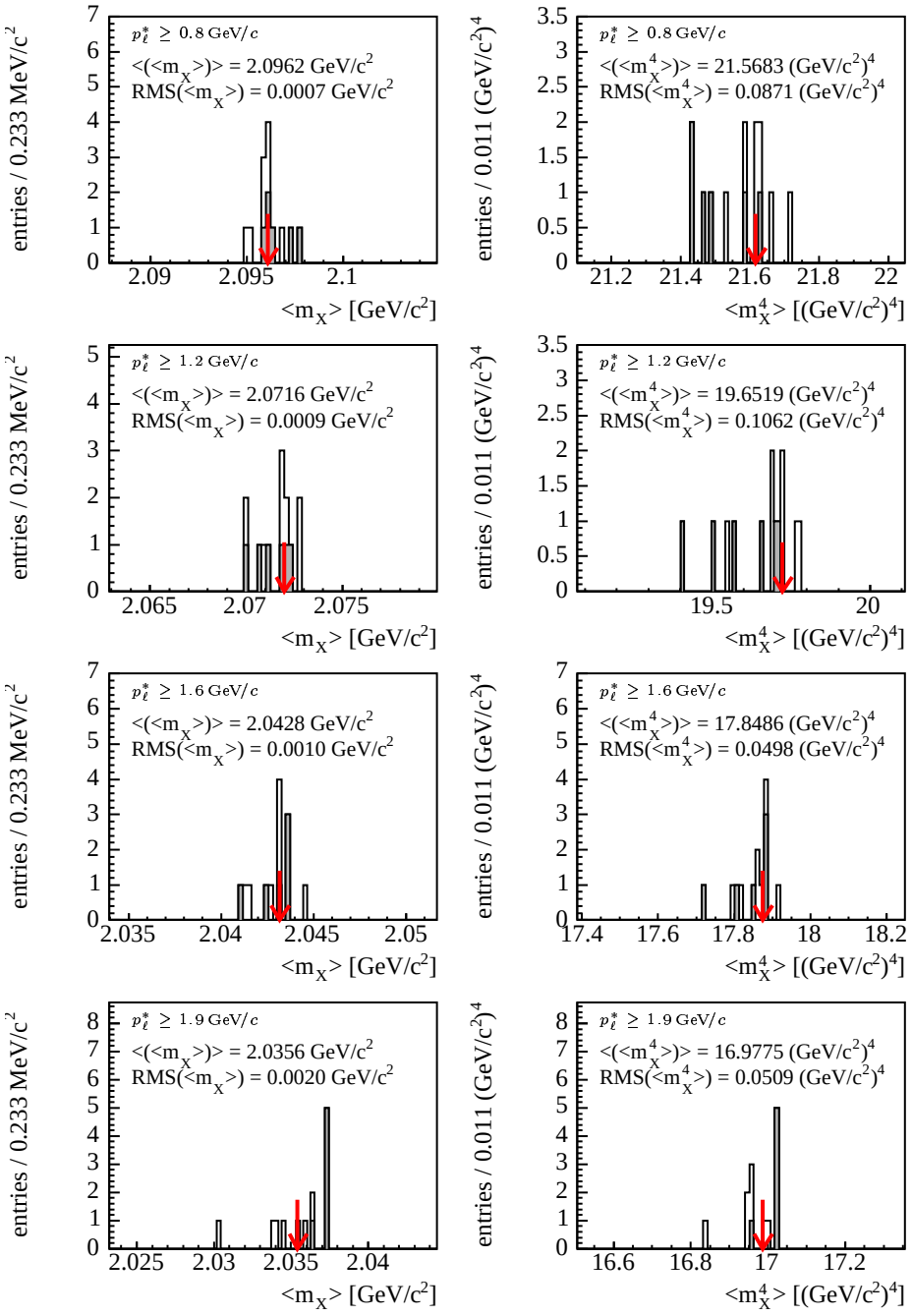

Figure 6.1: Variation of measured moments $< m_X >$ (left column) and $< m_X^4 >$ (right column) under variation of the underlying signal model used to construct the calibration curves. The arrow indicates the nominal result. The histograms are: model changed by dropping single exclusive channels (□), model changed by cutting out the high mass tail (■).

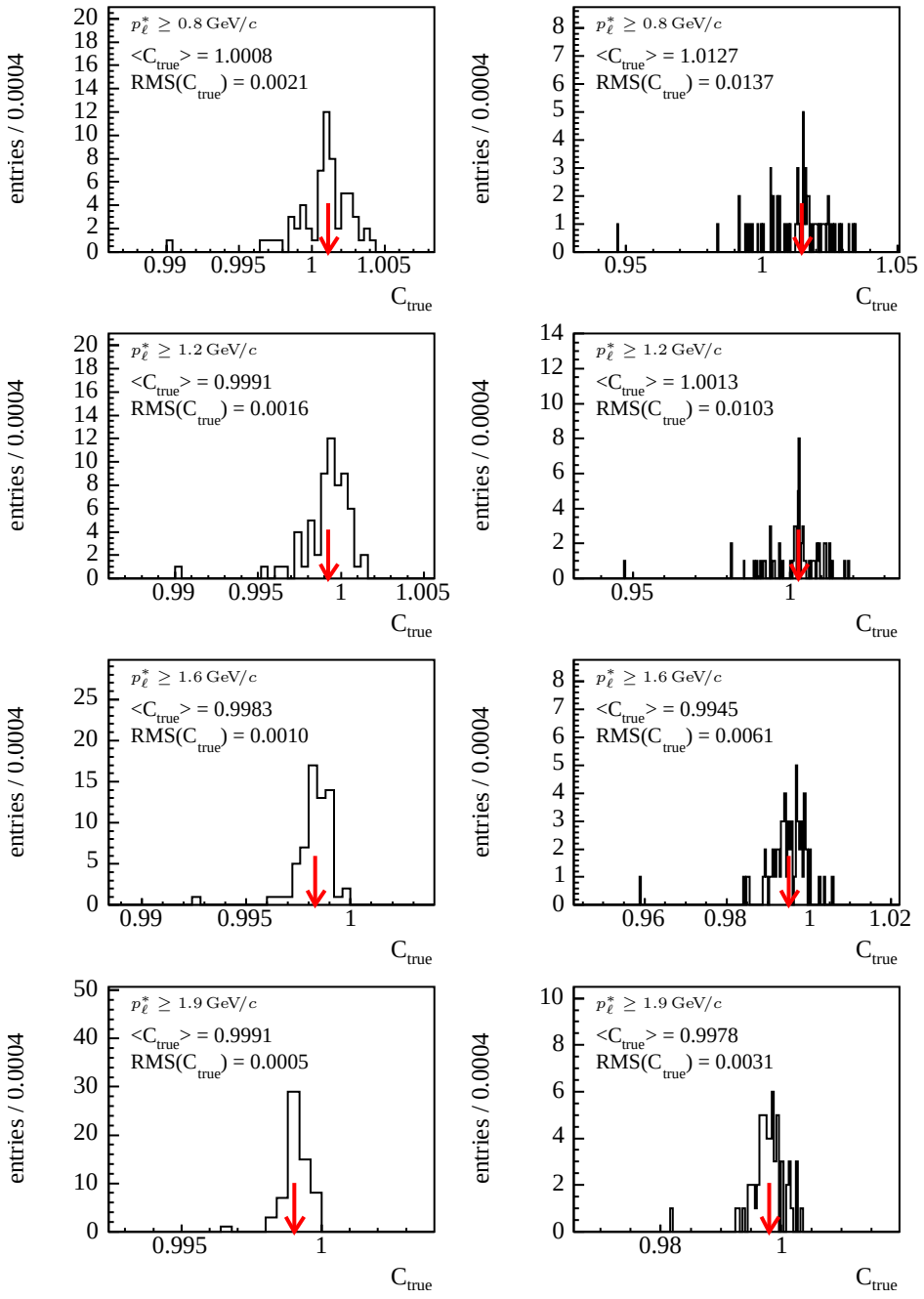

Figure 6.2: Variation of the residual bias correction factor $\mathcal{C}_{true}$ for the measured moments $< m_X >$ (left column) and $< m_X^4 >$ (right column) under variation of the underlying model of $B \to D^{**}\ell\nu$ and $B \to D^{(*)}\pi\ell\nu$ decays. The arrow indicates the nominal result.

detail in section 5.6.2. Table 5.7 summarizes the applied correction factors along with their experimental uncertainties affecting the background estimate. In order to evaluate the resulting systematic uncertainty the MC is adjusted in a way that the branching fraction of the decay type studied matches the measured scaling factor plus or minus its experimental uncertainty. The average deviation from the nominal value is taken as systematic uncertainty.

The errors determined for the several background types are added in quadrature to obtain the full uncertainty on the residual background subtraction. A clear $p^*_{\ell,cut}$ dependence is observed. While for low $p^*_{\ell,cut}$ most of the studied background channels contribute to the systematic uncertainty it is purely dominated by background stemming from $B \to X_u \ell\nu$ decays for high $p^*_{\ell,cut}$. Contributions from J/ψ and $\psi(2S)$ decays are found to be negligible. The full uncertainty stays constant over a large range of $p^*_{\ell,cut}$ and raises slightly for highest cuts on p^*_ℓ.

6.6 Track Selection Efficiency

MC simulations are corrected for differences in the selection efficiency of charged tracks between data and MC. We perform a "flat" correction which weights MC events according to their charged track multiplicity $w_{evt,trk} = (1 - 0.005)^{N_{trk}}$. The correction of $(-0.5 \pm 1.2)\%$ is determined on a sample of $e^+e^- \to \tau^+\tau^-$ decays where one τ decays semileptonically and the other into three charged tracks $\tau^\pm \to h^\pm h^\pm h^\mp \nu_\tau$ [45]. The correction factors are determined for different standard track definition. Since the track selection applied in this analysis does not match one of these standard selections but rather lies "in between" the definitions of "`GoodTracksLoose`" and "`GoodTracksVeryLoose`" we add the difference of the correction factors for both lists, 0.3%, quadratically as additional uncertainty. The total uncertainty is 1.2%. The systematic uncertainty on the tracking efficiency is determined by applying the default tracking efficiency correction plus or minus its uncertainty, $w_{evt,trk} = (1 - 0.005 \pm 0.012)^{N_{trk}}$, and taking the average deviation from the nominal result as systematic uncertainty.

6.7 Photon Selection Efficiency

π^0 selection efficiencies have been studied on samples of $e^+e^- \to \tau^+\tau^-$ decays where one of the τ decays leptonically, $\tau^\pm \to e^\pm \nu_e \overline{\nu}_\tau$ and the other into $\tau^\pm \to \rho^\pm \nu_\tau$ [46]. In the aforementioned study also selection efficiencies and their uncertainties for single photons have been determined. No correction has to be applied to MC with an uncertainty of 1.8%. We determine the systematic uncertainty on the photon selection efficiency by reweighting events in MC according to their photon multiplicity, $w_\gamma = (1 \pm 0.018)^{N_\gamma}$, and taking the average deviation from the nominal result as systematic uncertainty.

6.8 Hard Photon Emission

In the MC simulation final state radiation is modeled utilizing the PHOTOS package [22]. The simulation takes double photon emission of order $\mathcal{O}(\alpha^2)$ into account. Thereby, PHOTOS does not simulate the emission of hard photons by the W boson or quarks in the semileptonic decay. The effect is assumed to be small.

The dependence of the moment measurement on hard photons in the event is checked by rejecting events that contain photons above certain $E^*_{\gamma,max}$, the energy of the highest energetic photon candidate in the event. $E^*_{\gamma,max}$ is measured in the B_{SL} restframe. If a sizable amount of hard photons are present in data the measured moments are expected to vary with different cuts on $E^*_{\gamma,max}$. On the other hand, cutting on $E^*_{\gamma,max}$ might introduce a bias into the measurement by varying selection efficiencies even without hard photon emission in the event. Nevertheless, such a bias will be corrected following the procedure described in sections 5.7.3 resulting in constant moments with varying $E^*_{\gamma,max}$ cuts in MC by construction. Thus, constant moments with varying $E^*_{\gamma,max}$ cut are also expected in data if hard photons are simulated properly.

The study is implemented by performing measurements with several cuts $E^*_{\gamma,max} = \{0.55, 0.60, 0.70, 0.80, 0.90, 1.00, 1.25, 1.50, 2.00\}$ GeV as illustrated in Fig. 6.3. Fig. 6.4 shows the observed variation of the extracted moments. The errors plotted correspond to the statistical errors of the uncorrelated events with respect to the default event sample. As expected the MC shows no variation within statistical uncertainties. In data significant deviations from the nominal moment are observed. The size and direction of those deviations depend strongly on the p^*_ℓ cut applied. While variations to higher moments are observed for low $p^*_{\ell,cut}$, the extracted moments tend to lower moments for high cuts on p^*_ℓ. This behavior is a hint that the observed effect does not stem from hard photon radiation alone but might also be caused by other sources of hard photons, like π^0 decays, and related differences in data and MC. Nevertheless, the observed effect has to be treated as systematic uncertainty. We take the RMS of the observed variation in data as systematic uncertainty. They are depicted as dashed lines in Fig. 6.4.

6.9 Soft Photons

As discussed in section 5.5 even after applying cuts to improve the agreement of data and MC there remains an excess of low energetic photons in the simulation. We study its influence on the moment measurement by applying tighter cuts in the selection of photons, i.e. the cut on the minimal photon energy is raised from $E^*_\gamma > 50\,\text{MeV}$ to $E^*_\gamma > 100\,\text{MeV}$. Since changing the E^*_γ cut does also change the measured E_{miss} and $|\vec{p}_{miss}|$ spectra the selected sample of events is changed and statistical fluctuations are expected. In all

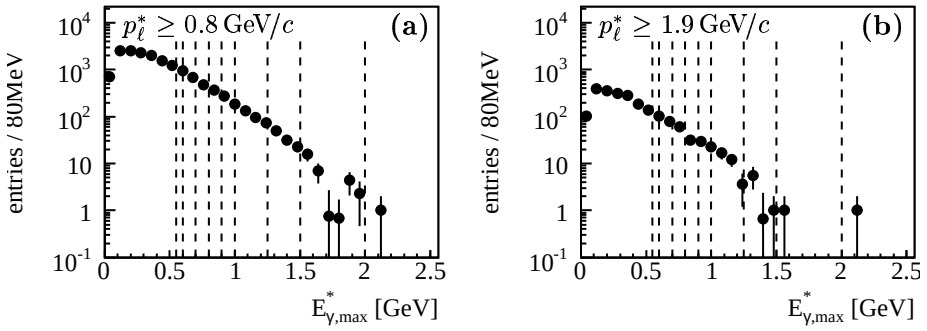

Figure 6.3: Spectra of $E^*_{\gamma,max}$ for cuts $p^*_\ell \geq 0.8\,\mathrm{GeV}/c$ (a) and $p^*_\ell \geq 1.9\,\mathrm{GeV}/c$ (b). The dashed lines correspond to the cuts applied in the study of hard phton emission (see sec. 6.8).

cases the observed shifts are well below the statistical errors. Thus, we do not consider them as additional systematic uncertainty.

6.10 Stability Checks

In order to test the stability of the extracted moments we perform two tests, variations of the applied cuts on $E_{miss} - |\vec{p}_{miss}|$ and moment measurements on disjoined statistical independent data samples.

6.10.1 $E_{miss} - |\vec{p}_{miss}|$ Cut Variation

The stability of the extracted moments as functions of the cut on $E_{miss} - |\vec{p}_{miss}|$ is shown in figure 6.5. The plots show the difference of moments measured with changed cuts on $E_{miss} - |\vec{p}_{miss}|$ and the nominal results. The errors correspond to the statistical uncertainties of the uncorrelated events in the changed and default event samples.

Two different types of cuts are studied, symmetrical cuts of $|E_{miss} - |\vec{p}_{miss}||$ around zero and cuts selecting the negative or positive parts of the $E_{miss} - |\vec{p}_{miss}|$ distribution, respectively. The later cuts are motivated by the fact that the largest differences in the distributions of data and MC are observed for negative values of $E_{miss} - |\vec{p}_{miss}|$.

As shown, significant deviations from the nominal moment values are observed. The scans versus $E_{miss} - |\vec{p}_{miss}|$ cuts are sensitive to mis modeling of the simulation. The following systematic effects stemming from sources that have been discussed so far are expected to contribute to observed variation:

1. Different cuts on $E_{miss} - |\vec{p}_{miss}|$ result in changed calibration curves. The bias associated with the calibration and its systematic uncertainty has been discussed in section 5.7.3.1 and 6.2. This systematic effect does also contribute to the observed variation.

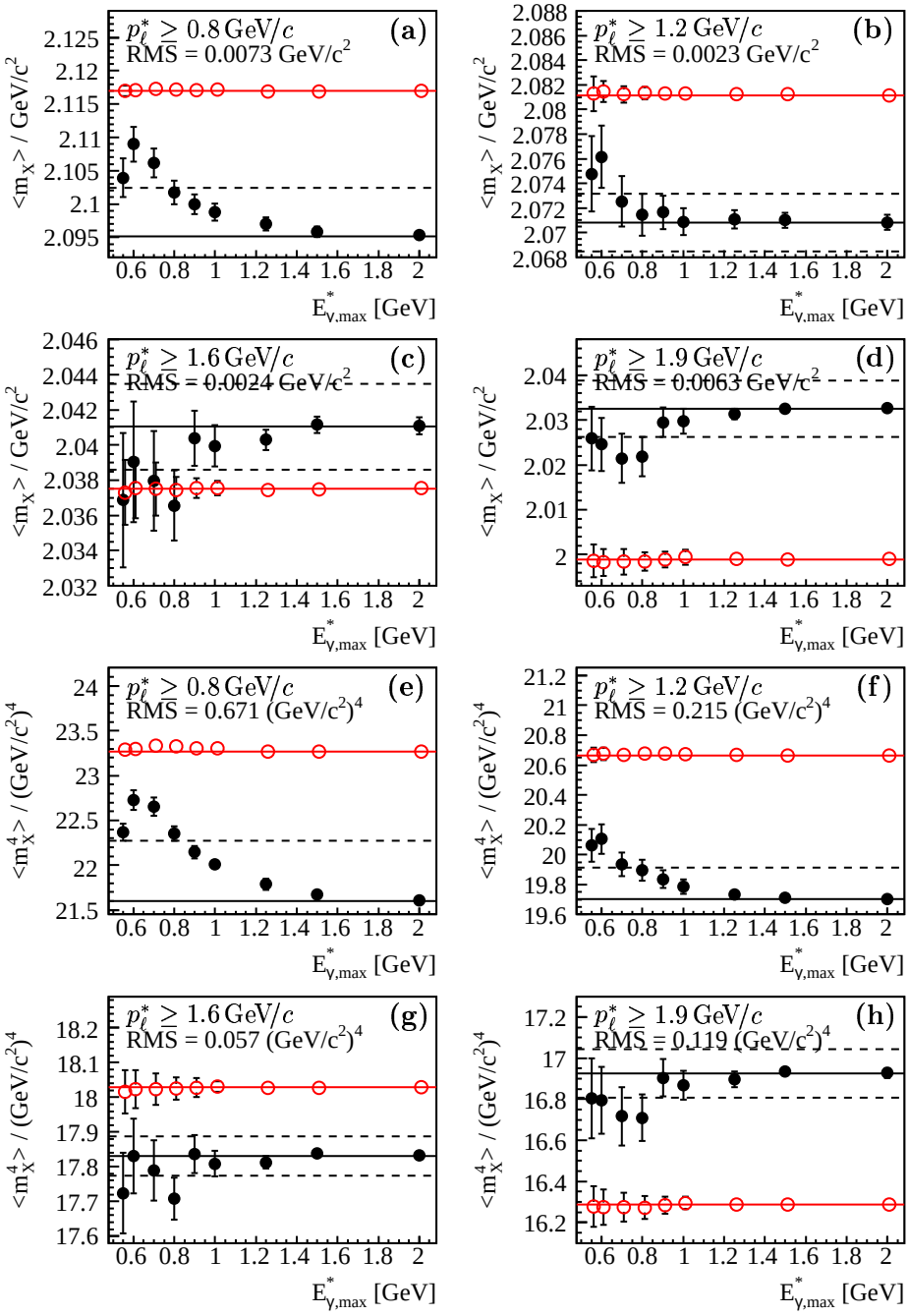

Figure 6.4: Variation of the moments $< m_X >$ (left column) and $< m_X^4 >$ (right column) under variation of $E^*_{\gamma,max}$ for data (•) and MC (○) together with the extracted nominal results (solid lines). The observed RMS in data is indicated by the dashed line.

2. Systematic effects stemming from mis modeling in the track and photon selection efficiencies are expected to contribute.

3. To measure a moment with changed $E_{miss} - |\vec{p}_{miss}|$ cut a new set of calibration curves with changed binning adapted to the new cut has to be constructed. Associated to the chosen binning is a systematic uncertainty as discussed in 6.3.

The square sum of those systematic uncertainties is overlaid as dotted line in Fig. 6.5. In cases where the observed variation exceeds the expected variation additional systematic effects contribute that need to be addressed by an extra contribution to the systematic uncertainty. Its size is estimated from the square difference of the observed RMS, indicated by a dashed line, and the total systematic uncertainty stemming from the source discussed above.

6.10.2 Measurements on Disjoined Data Samples

The stability of the extracted invariant hadronic mass moments is checked by performing the measurement on statistical independent subsamples. The following subsamples are considered:

1. Measurements on datasets of different *BABAR* run periods (Run 1-3 and Run4) are performed.

2. The measurement is repeated with cuts on $E_{miss} - |\vec{p}_{miss}|$ that select the negative tail ($-0.5 \leq E_{miss} - |\vec{p}_{miss}| < 0\,\text{GeV}$) and positive part of the distribution ($0 \leq E_{miss} - |\vec{p}_{miss}| \leq 0.5\,\text{GeV}$), respectively.

3. In order to study effects associated with the charge of the B_{reco} candidate, i.e. different sources of background and $B^0\overline{B}^0$ oscillations, two samples with charged and neutral candidates are selected.

4. We split the total dataset into two statistical independent samples containing events with selected electrons and muons. Thereby, effects stemming from different selection efficiencies and misidentification rates are studied.

Fig. 6.6 shows moments measured on these subsamples for different cuts on p^*_ℓ. The extracted moments are compatible with each other within statistical precision. Only for the measurements on samples of charged and neutral B_{reco} tags a deviation of 2.5σ is observed. It is resulting from a fluctuation in a distinct region of the p^*_ℓ spectrum, $1.5 \leq p^*_\ell < 1.6\,\text{GeV}/c$, as illustrated in Fig. 6.7. Since all other moments measured in different bins of p^*_ℓ show no significant deviation, no additional systematic uncertainty is considered.

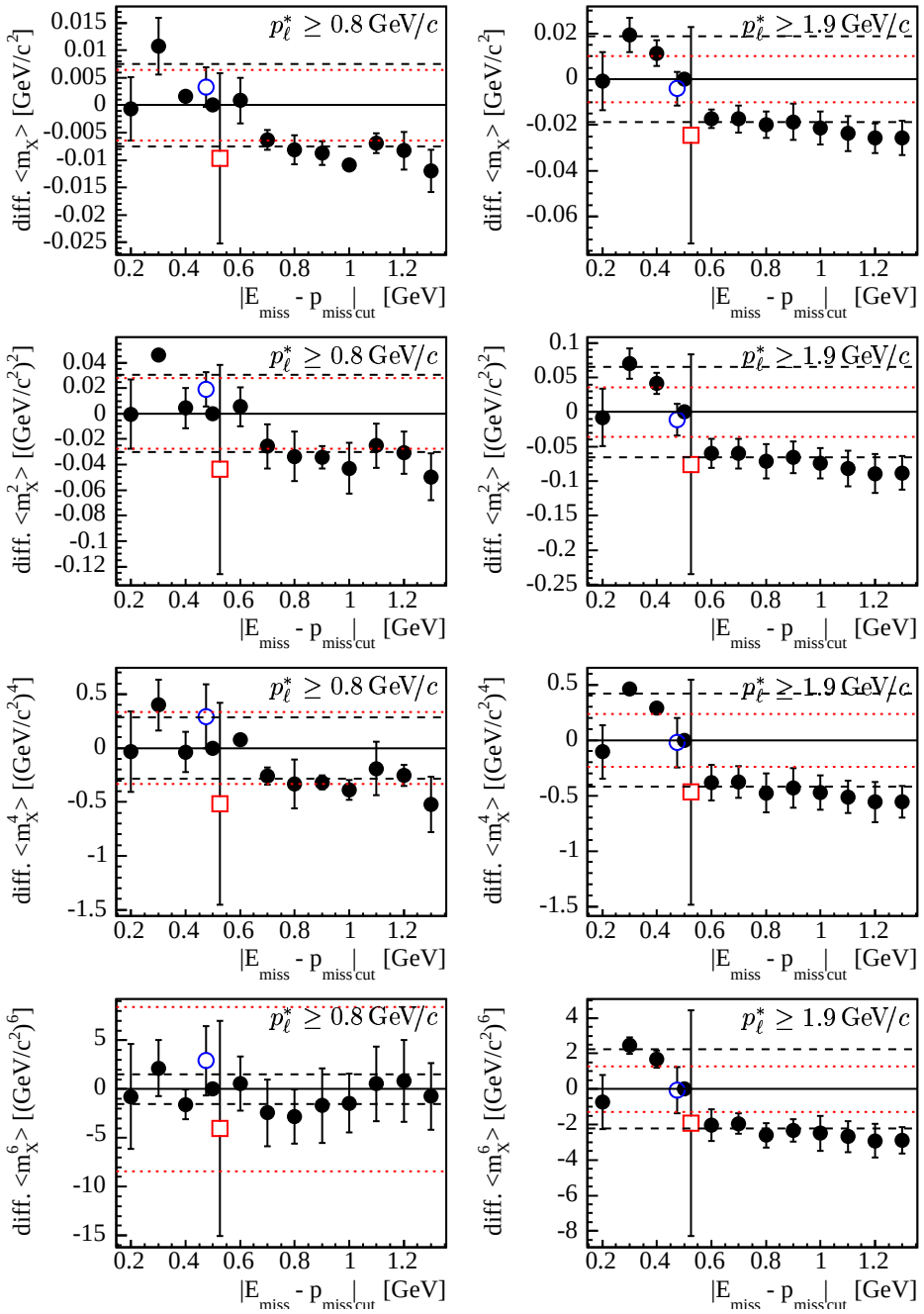

Figure 6.5: Variation of the measured moments as a function of the cut on $E_{miss} - |\vec{p}_{miss}|$ for different lepton momenta cuts $p_\ell^* \geq 0.9\,\mathrm{GeV}/c$ (left column) and $p_\ell^* \geq 1.5\,\mathrm{GeV}/c$ (right column). Shown is the difference between measurements with changed and nominal cuts. $|E_{miss} - |\vec{p}_{miss}|| \leq |E_{miss} - |\vec{p}_{miss}||_{cut}$ (•) , $-0.5 \leq E_{miss} - |\vec{p}_{miss}| < 0\,\mathrm{GeV}$ (○), $0 \leq E_{miss} - |\vec{p}_{miss}| \leq 0.5\,\mathrm{GeV}$ (□). Contributing systematic effects as discussed in section 6.10.1 are indicated by the dottedlines. The dashed line shows the oberved RMS wrt. the nominal result.

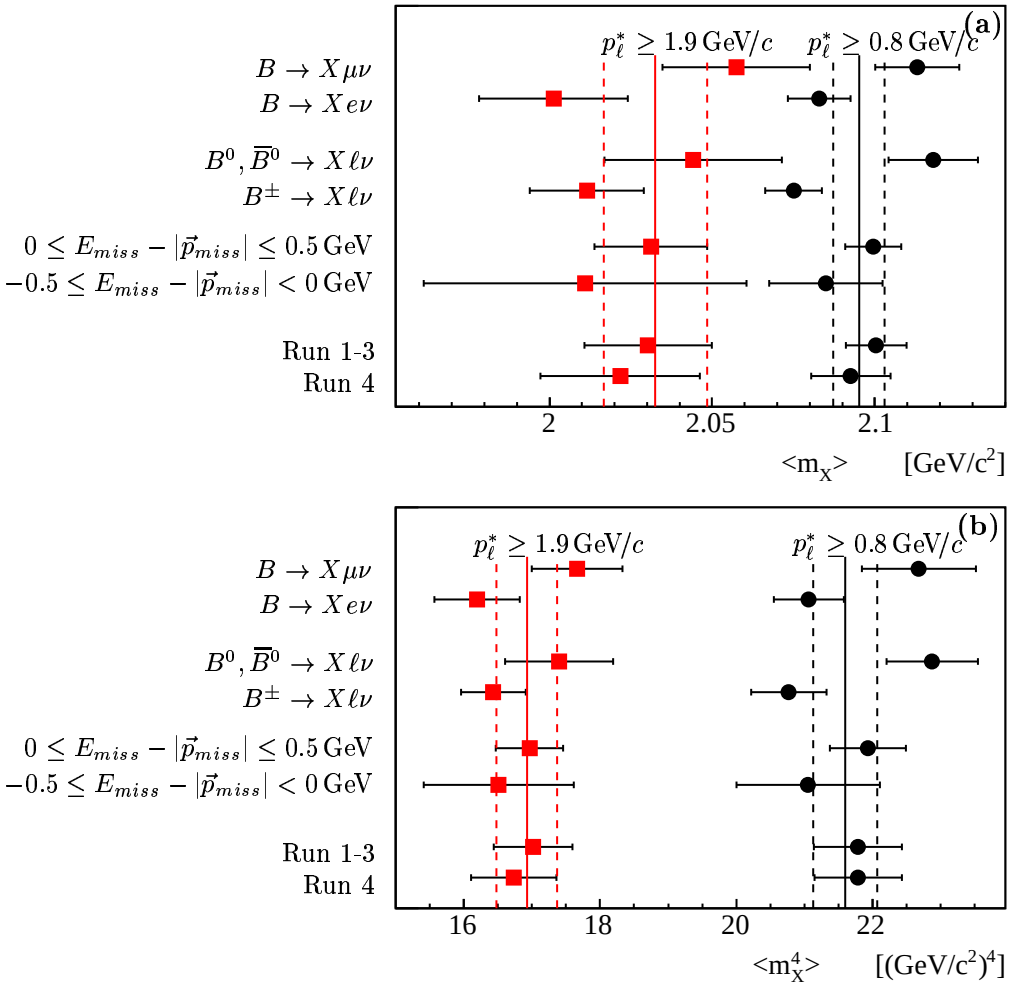

Figure 6.6: Comparison of moments $< m_X^1 >$ (a) and $< m_X^4 >$ (b) measured on statistical independent subsamples of data. Shown are results for different cuts on the lepton momentum $p_\ell^* \geq 0.8\,\mathrm{GeV}/c$ (○) and $p_\ell^* \geq 1.9\,\mathrm{GeV}/c$ (□) together with the default measurement (black and red lines).

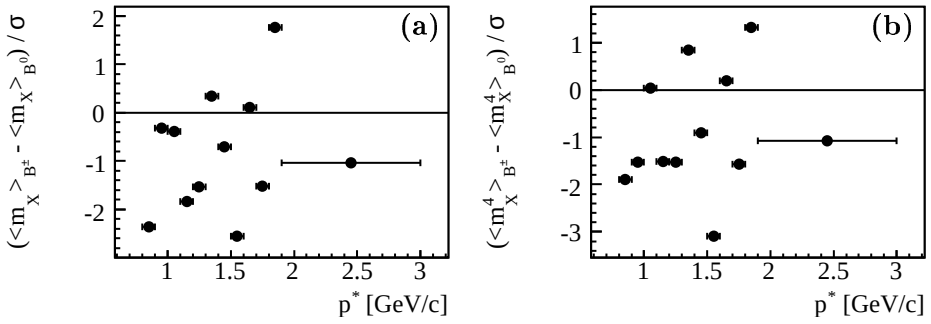

Figure 6.7: Comparison of moments $< m_X^1 >$ (a) and $< m_X^4 >$ (b) measured on disjoined samples of charged and neutral B_{reco} candidates in bins of p_ℓ^*. Plotted is the relative difference between moments extracted on both samples.

6.11 Summary of Systematic Uncertainties

Tables 6.1 - 6.6 summarize the results of all systematic studies discussed. Dominating uncertainties are connected to the bias correction of the calibrated moments, the residual background subtraction, and the stability of the extracted results under variation of the $E_{miss} - |\vec{p}_{miss}|$ cut as well as the emission of hard photons. For the residual background subtraction especially uncertainties stemming from $B \to X_u \ell \nu$ decays give large contributions also for high $p^*_{\ell,cut}$. In most cases we find systematic uncertainties that exceed the statistical uncertainty by a factor of 1.5. For higher moments and $p^*_{\ell,cut}$ systematical and statistical uncertainties are of comparable size.

$p_{l,cut}[GeV/c]$	0.8	0.9	1.0	1.1	1.2	1.3	1.4	1.5	1.6	1.7	1.8	1.9
Moment $< m_X >$	**2.0951**	**2.0912**	**2.0860**	**2.0785**	**2.0708**	**2.0653**	**2.0571**	**2.0500**	**2.0410**	**2.0349**	**2.0357**	**2.0325**
Stat. error (data)	0.0059	0.0057	0.0057	0.0057	0.0059	0.0061	0.0065	0.0071	0.0080	0.0094	0.0119	0.0158
Stat. error (calibration)	0.0013	0.0013	0.0013	0.0014	0.0015	0.0015	0.0016	0.0017	0.0018	0.0019	0.0026	0.0036
Stat. error (bg. subtr)	0.0061	0.0045	0.0042	0.0043	0.0043	0.0044	0.0043	0.0032	0.0035	0.0045	0.0064	0.0068
Stat. error (total)	**0.0086**	**0.0074**	**0.0072**	**0.0073**	**0.0074**	**0.0077**	**0.0080**	**0.0080**	**0.0089**	**0.0106**	**0.0138**	**0.0176**
MC model calibration	0.0007	0.0006	0.0007	0.0008	0.0009	0.0009	0.0009	0.0010	0.0010	0.0012	0.0015	0.0020
MC model res. bias corr.	0.0020	0.0015	0.0013	0.0012	0.0012	0.0009	0.0007	0.0006	0.0006	0.0007	0.0005	0.0006
Bias correction calibr.	0.0042	0.0040	0.0043	0.0035	0.0047	0.0053	0.0058	0.0062	0.0075	0.0075	0.0068	0.0092
Track selection eff.	0.0029	0.0027	0.0026	0.0023	0.0024	0.0024	0.0024	0.0025	0.0026	0.0028	0.0030	0.0036
Photon selection eff.	0.0063	0.0054	0.0048	0.0044	0.0042	0.0043	0.0043	0.0047	0.0051	0.0066	0.0072	0.0080
$B \to X_u e\nu$	0.0038	0.0038	0.0039	0.0040	0.0042	0.0044	0.0048	0.0053	0.0060	0.0072	0.0089	0.0118
$B^{(+,0)} \to D^0 \to e^+$	0.0003	0.0002	0.0001	0.0001	0.0000	0.0000	0.0000	0.0000	0.0000	0.0000	0.0000	0.0000
$B^{(+,0)} \to \bar{D}^0, D^- \to e^-$	0.0005	0.0003	0.0002	0.0001	0.0000	0.0000	0.0000	0.0000	0.0000	0.0000	0.0000	0.0000
$B^{(+,0)} \to D^+ \to e^+$	0.0004	0.0003	0.0002	0.0001	0.0000	0.0000	0.0000	0.0000	0.0000	0.0000	0.0000	0.0000
$B^{(+,0)} \to D_s^+ \to e^+$	0.0021	0.0014	0.0010	0.0007	0.0005	0.0004	0.0002	0.0001	0.0001	0.0001	0.0001	0.0001
$B^{(+,0)} \to \tau^+ \to e^+$	0.0002	0.0002	0.0002	0.0002	0.0001	0.0002	0.0001	0.0001	0.0001	0.0001	0.0000	0.0000
$B^{(+,0)} \to D_s^+ \to \tau^+ \to e^+$	0.0004	0.0003	0.0003	0.0002	0.0002	0.0001	0.0001	0.0000	0.0000	0.0000	0.0000	0.0000
$B(\to X) \to J/\Psi \to e^+e^-$	0.0000	0.0000	0.0000	0.0000	0.0000	0.0000	0.0000	0.0000	0.0000	0.0000	0.0000	0.0000
$B(\to X) \to \Psi(2S) \to e^+e^-$	0.0000	0.0000	0.0000	0.0000	0.0000	0.0000	0.0000	0.0000	0.0000	0.0000	0.0000	0.0000
Res. background total	0.0044	0.0041	0.0040	0.0041	0.0042	0.0045	0.0048	0.0053	0.0060	0.0072	0.0089	0.0118
Calib. curve binning	0.0014	0.0009	0.0008	0.0010	0.0013	0.0009	0.0003	0.0006	0.0009			
Hard photon emission	0.0072	0.0041	0.0036	0.0024	0.0022	0.0022	0.0008	0.0025	0.0024	0.0035	0.0035	0.0061
$E_{miss} - \lvert\vec{p}_{miss}\rvert_{cut}$ stability	0.0000	0.0024	0.0025	0.0021	0.0043	0.0082	0.0076	0.0059	0.0000	0.0092	0.0094	0.0137
Sys. error total	**0.0119**	**0.0097**	**0.0093**	**0.0081**	**0.0095**	**0.0121**	**0.0118**	**0.0117**	**0.0115**	**0.0161**	**0.0170**	**0.0230**
Error total	**0.0147**	**0.0122**	**0.0118**	**0.0109**	**0.0121**	**0.0144**	**0.0143**	**0.0142**	**0.0146**	**0.0193**	**0.0219**	**0.0290**
m_{ES} sideband definition	0.0020	0.0014	0.0015	0.0014	0.0012	0.0011	0.0021	0.0022	0.0031	0.0037	0.0034	0.0020
Soft photons	0.0023	0.0013	0.0000	0.0008	0.0011	0.0044	0.0073	0.0084	0.0138	0.0147	0.0235	0.0164

Table 6.1: Summary of systematic uncertainties for the measurement of $< m_X >$. All quantitites are given in units of GeV/c^2. For the sake of completeness the two systematic studies "m_{ES} sideband definition" and "Soft photons" are listed but not included in the total systematic uncertainty. Details can be found in the sections 6.5.1 and 6.9, respectively.

$p_{l,cut}[GeV/c]$	0.8	0.9	1.0	1.1	1.2	1.3	1.4	1.5	1.6	1.7	1.8	1.9
Moment $< m_X^2 >$	**4.455**	**4.429**	**4.404**	**4.365**	**4.327**	**4.297**	**4.260**	**4.224**	**4.178**	**4.145**	**4.142**	**4.120**
Stat. error (data)	0.027	0.026	0.025	0.024	0.024	0.025	0.026	0.028	0.030	0.035	0.043	0.057
Stat. error (calibration)	0.006	0.006	0.006	0.006	0.006	0.006	0.007	0.007	0.007	0.007	0.009	0.013
Stat. error (bg. subtr)	0.030	0.022	0.020	0.019	0.018	0.018	0.018	0.012	0.013	0.017	0.023	0.027
Stat. error (total)	**0.041**	**0.035**	**0.032**	**0.031**	**0.031**	**0.031**	**0.032**	**0.031**	**0.034**	**0.039**	**0.050**	**0.064**
MC model calibration	0.003	0.004	0.005	0.006	0.006	0.005	0.005	0.005	0.004	0.004	0.006	0.007
MC model res. bias corr.	0.011	0.008	0.007	0.006	0.007	0.004	0.003	0.002	0.003	0.003	0.002	0.003
Bias correction calibr.	0.016	0.014	0.015	0.011	0.016	0.018	0.019	0.020	0.025	0.024	0.020	0.033
Track selection eff.	0.013	0.011	0.010	0.009	0.009	0.009	0.009	0.009	0.009	0.010	0.011	0.013
Photon selection eff.	0.029	0.023	0.020	0.018	0.017	0.016	0.016	0.017	0.019	0.023	0.025	0.028
$B \to X_u e\nu$	0.013	0.013	0.013	0.014	0.014	0.015	0.016	0.017	0.020	0.024	0.029	0.039
$B^{(+,0)} \to D^0 \to e^+$	0.002	0.001	0.000	0.000	0.000	0.000	0.000	0.000	0.000	0.000	0.000	0.000
$B^{(+,0)} \to \bar{D}^0, D^- \to e^-$	0.003	0.002	0.001	0.000	0.000	0.000	0.000	0.000	0.000	0.000	0.000	0.000
$B^{(+,0)} \to D^+ \to e^+$	0.002	0.001	0.001	0.001	0.000	0.000	0.000	0.000	0.000	0.000	0.000	0.000
$B^{(+,0)} \to D_s^+ \to e^+$	0.011	0.007	0.005	0.004	0.002	0.002	0.001	0.001	0.000	0.000	0.000	0.000
$B^{(+,0)} \to \tau^+ \to e^+$	0.001	0.001	0.001	0.001	0.001	0.001	0.001	0.000	0.000	0.000	0.000	0.000
$B^{(+,0)} \to D_s^+ \to \tau^+ \to e^+$	0.002	0.002	0.001	0.001	0.001	0.001	0.000	0.000	0.000	0.000	0.000	0.000
$B(\to X) \to J/\Psi \to e^+e^-$	0.000	0.000	0.000	0.000	0.000	0.000	0.000	0.000	0.000	0.000	0.000	0.000
$B(\to X) \to \Psi(2S) \to e^+e^-$	0.000	0.000	0.000	0.000	0.000	0.000	0.000	0.000	0.000	0.000	0.000	0.000
Res. background total	0.018	0.015	0.014	0.014	0.014	0.015	0.016	0.017	0.020	0.024	0.029	0.039
Calib. curve binning	0.005	0.003	0.003	0.004	0.005	0.004	0.002	0.001	0.003			
Hard photon emission	0.041	0.025	0.023	0.016	0.013	0.013	0.004	0.008	0.008	0.012	0.012	0.020
$E_{miss} - \lvert\vec{p}_{miss}\rvert_{cut}$ stability	0.000	0.007	0.012	0.009	0.020	0.036	0.033	0.025	0.000	0.032	0.033	0.047
Sys. error total	**0.058**	**0.043**	**0.041**	**0.034**	**0.039**	**0.049**	**0.046**	**0.043**	**0.039**	**0.055**	**0.058**	**0.079**
Error total	**0.071**	**0.055**	**0.052**	**0.046**	**0.050**	**0.058**	**0.056**	**0.053**	**0.052**	**0.067**	**0.076**	**0.102**
m_{ES} sideband definition	0.011	0.006	0.007	0.005	0.004	0.004	0.008	0.008	0.011	0.013	0.012	0.007
Soft photons	0.003	0.001	0.003	0.006	0.006	0.020	0.032	0.037	0.056	0.060	0.092	0.065

Table 6.2: Summary of systematic uncertainties for the measurement of $< m_X^2 >$. All quantitites are given in units of $(\,\mathrm{GeV}/c^2)^2$. For the sake of completeness the two systematic studies "m_{ES} sideband definition" and "Soft photons" are listed but not included in the total systematic uncertainty. Details can be found in the sections 6.5.1 and 6.9, respectively.

$p_{l,cut}[GeV/c]$	0.8	0.9	1.0	1.1	1.2	1.3	1.4	1.5	1.6	1.7	1.8	1.9
Moment $< m_X^3 >$	**9.67**	**9.54**	**9.45**	**9.29**	**9.16**	**9.04**	**8.91**	**8.77**	**8.60**	**8.48**	**8.44**	**8.34**
Stat. error (data)	0.10	0.09	0.09	0.08	0.08	0.08	0.08	0.08	0.09	0.10	0.12	0.16
Stat. error (calibration)	0.02	0.02	0.02	0.02	0.02	0.02	0.02	0.02	0.02	0.02	0.02	0.03
Stat. error (bg. subtr)	0.10	0.07	0.07	0.06	0.06	0.05	0.05	0.04	0.04	0.05	0.08	0.08
Stat. error (total)	**0.15**	**0.12**	**0.11**	**0.10**	**0.10**	**0.10**	**0.10**	**0.09**	**0.10**	**0.11**	**0.15**	**0.18**
MC model calibration	0.01	0.02	0.03	0.03	0.03	0.02	0.02	0.02	0.01	0.01	0.02	0.02
MC model res. bias corr.	0.05	0.03	0.03	0.02	0.03	0.02	0.01	0.01	0.01	0.01	0.01	0.01
Bias correction calibr.	0.04	0.04	0.04	0.03	0.04	0.04	0.05	0.05	0.06	0.06	0.05	0.09
Track selection eff.	0.05	0.04	0.03	0.03	0.03	0.03	0.03	0.03	0.03	0.03	0.03	0.03
Photon selection eff.	0.11	0.08	0.07	0.06	0.05	0.05	0.05	0.05	0.05	0.06	0.07	0.07
$B \to X_u e \nu$	0.04	0.04	0.04	0.04	0.04	0.04	0.04	0.04	0.05	0.06	0.07	0.10
$B^{(+,0)} \to D^0 \to e^+$	0.01	0.00	0.00	0.00	0.00	0.00	0.00	0.00	0.00	0.00	0.00	0.00
$B^{(+,0)} \to \bar{D}^0, D^- \to e^-$	0.01	0.01	0.00	0.00	0.00	0.00	0.00	0.00	0.00	0.00	0.00	0.00
$B^{(+,0)} \to D^+ \to e^+$	0.01	0.01	0.00	0.00	0.00	0.00	0.00	0.00	0.00	0.00	0.00	0.00
$B^{(+,0)} \to D_s^+ \to e^+$	0.04	0.03	0.02	0.01	0.01	0.01	0.00	0.00	0.00	0.00	0.00	0.00
$B^{(+,0)} \to \tau^+ \to e^+$	0.00	0.00	0.00	0.00	0.00	0.00	0.00	0.00	0.00	0.00	0.00	0.00
$B^{(+,0)} \to D_s^+ \to \tau^+ \to e^+$	0.01	0.01	0.00	0.00	0.00	0.00	0.00	0.00	0.00	0.00	0.00	0.00
$B(\to X) \to J/\Psi \to e^+e^-$	0.00	0.00	0.00	0.00	0.00	0.00	0.00	0.00	0.00	0.00	0.00	0.00
$B(\to X) \to \Psi(2S) \to e^+e^-$	0.00	0.00	0.00	0.00	0.00	0.00	0.00	0.00	0.00	0.00	0.00	0.00
Res. background total	0.06	0.05	0.04	0.04	0.04	0.04	0.04	0.04	0.05	0.06	0.07	0.10
Calib. curve binning	0.01	0.01	0.01	0.01	0.02	0.01	0.01	0.00	0.01			
Hard photon emission	0.17	0.11	0.10	0.07	0.06	0.06	0.02	0.02	0.02	0.03	0.03	0.05
$E_{miss} - \lvert\vec{p}_{miss}\rvert_{cut}$ stability	0.00	0.00	0.04	0.03	0.07	0.12	0.11	0.08	0.00	0.09	0.09	0.12
Sys. error total	**0.23**	**0.16**	**0.15**	**0.12**	**0.13**	**0.16**	**0.14**	**0.12**	**0.10**	**0.14**	**0.15**	**0.21**
Error total	**0.27**	**0.20**	**0.18**	**0.16**	**0.16**	**0.18**	**0.17**	**0.15**	**0.14**	**0.18**	**0.21**	**0.27**
m_{ES} sideband definition	0.04	0.02	0.02	0.02	0.01	0.01	0.02	0.02	0.03	0.04	0.03	0.02
Soft photons	0.01	0.01	0.02	0.03	0.02	0.07	0.10	0.12	0.17	0.18	0.27	0.19

Table 6.3: Summary of systematic uncertainties for the measurement of $< m_X^3 >$. All quantitites are given in units of $(\,\mathrm{GeV}/c^2)^3$. For the sake of completeness the two systematic studies "m_{ES} sideband definition" and "Soft photons" are listed but not included in the total systematic uncertainty. Details can be found in the sections 6.5.1 and 6.9, respectively.

$p_{l,cut}[GeV/c]$	0.8	0.9	1.0	1.1	1.2	1.3	1.4	1.5	1.6	1.7	1.8	1.9
Moment $< m_X^4 >$	**21.60**	**21.00**	**20.68**	**20.15**	**19.70**	**19.29**	**18.89**	**18.41**	**17.83**	**17.43**	**17.27**	**16.93**
Stat. error (data)	0.38	0.32	0.29	0.26	0.25	0.23	0.23	0.23	0.24	0.27	0.33	0.41
Stat. error (calibration)	0.06	0.05	0.05	0.05	0.05	0.06	0.05	0.05	0.05	0.04	0.06	0.08
Stat. error (bg. subtr)	0.40	0.25	0.22	0.19	0.18	0.16	0.16	0.12	0.11	0.13	0.18	0.20
Stat. error (total)	**0.55**	**0.41**	**0.37**	**0.32**	**0.31**	**0.29**	**0.29**	**0.27**	**0.27**	**0.30**	**0.38**	**0.46**
MC model calibration	0.09	0.11	0.13	0.12	0.11	0.09	0.08	0.07	0.05	0.04	0.04	0.05
MC model res. bias corr.	0.16	0.12	0.10	0.08	0.09	0.05	0.03	0.03	0.04	0.04	0.02	0.02
Bias correction calibr.	0.12	0.10	0.10	0.06	0.09	0.10	0.11	0.11	0.14	0.13	0.10	0.22
Track selection eff.	0.15	0.12	0.10	0.08	0.08	0.08	0.07	0.07	0.07	0.07	0.07	0.08
Photon selection eff.	0.36	0.27	0.21	0.17	0.15	0.14	0.13	0.13	0.14	0.17	0.17	0.18
$B \to X_u e\nu$	0.10	0.09	0.09	0.09	0.09	0.09	0.10	0.11	0.12	0.14	0.17	0.23
$B^{(+,0)} \to D^0 \to e^+$	0.02	0.02	0.01	0.00	0.00	0.00	0.00	0.00	0.00	0.00	0.00	0.00
$B^{(+,0)} \to \bar{D}^0, D^- \to e^-$	0.04	0.02	0.01	0.00	0.00	0.00	0.00	0.00	0.00	0.00	0.00	0.00
$B^{(+,0)} \to D^+ \to e^+$	0.04	0.02	0.02	0.01	0.00	0.00	0.00	0.00	0.00	0.00	0.00	0.00
$B^{(+,0)} \to D_s^+ \to e^+$	0.17	0.11	0.07	0.05	0.03	0.02	0.01	0.01	0.00	0.00	0.00	0.00
$B^{(+,0)} \to \tau^+ \to e^+$	0.01	0.01	0.01	0.01	0.01	0.01	0.00	0.00	0.00	0.00	0.00	0.00
$B^{(+,0)} \to D_s^+ \to \tau^+ \to e^+$	0.02	0.02	0.02	0.01	0.01	0.01	0.00	0.00	0.00	0.00	0.00	0.00
$B(\to X) \to J/\Psi \to e^+e^-$	0.00	0.00	0.00	0.00	0.00	0.00	0.00	0.00	0.00	0.00	0.00	0.00
$B(\to X) \to \Psi(2S) \to e^+e^-$	0.00	0.00	0.00	0.00	0.00	0.00	0.00	0.00	0.00	0.00	0.00	0.00
Res. background total	0.21	0.15	0.12	0.11	0.10	0.10	0.10	0.11	0.12	0.14	0.17	0.23
Calib. curve binning	0.03	0.01	0.01	0.03	0.04	0.02	0.03	0.01	0.01			
Hard photon emission	0.64	0.42	0.39	0.28	0.21	0.20	0.09	0.05	0.05	0.07	0.08	0.11
$E_{miss} - \lvert\vec{p}_{miss}\rvert_{cut}$ stability	0.00	0.00	0.09	0.08	0.21	0.35	0.32	0.24	0.00	0.21	0.21	0.30
Sys. error total	**0.81**	**0.56**	**0.51**	**0.40**	**0.40**	**0.47**	**0.40**	**0.33**	**0.25**	**0.35**	**0.36**	**0.50**
Error total	**0.98**	**0.70**	**0.63**	**0.51**	**0.50**	**0.55**	**0.49**	**0.43**	**0.37**	**0.46**	**0.52**	**0.68**
m_{ES} sideband definition	0.17	0.08	0.07	0.05	0.04	0.04	0.06	0.06	0.09	0.09	0.07	0.05
Soft photons	0.14	0.08	0.07	0.10	0.07	0.22	0.31	0.33	0.46	0.50	0.73	0.52

Table 6.4: Summary of systematic uncertainties for the measurement of $< m_X^4 >$. All quantitites are given in units of $(\,\mathrm{GeV}/c^2)^4$. For the sake of completeness the two systematic studies "m_{ES} sideband definition" and "Soft photons" are listed but not included in the total systematic uncertainty. Details can be found in the sections 6.5.1 and 6.9, respectively.

$p_{l,cut}[GeV/c]$	0.8	0.9	1.0	1.1	1.2	1.3	1.4	1.5	1.6	1.7	1.8	1.9
Moment $< m_X^5 >$	**49.93**	**47.44**	**46.40**	**44.64**	**43.26**	**41.91**	**40.72**	**39.12**	**37.33**	**36.12**	**35.52**	**34.44**
Stat. error (data)	1.37	1.11	0.94	0.82	0.75	0.69	0.67	0.65	0.64	0.70	0.83	1.00
Stat. error (calibration)	0.23	0.19	0.18	0.17	0.15	0.15	0.14	0.14	0.13	0.11	0.15	0.21
Stat. error (bg. subtr)	1.37	0.84	0.68	0.54	0.51	0.44	0.47	0.31	0.30	0.36	0.48	0.49
Stat. error (total)	**1.95**	**1.40**	**1.18**	**1.00**	**0.92**	**0.84**	**0.83**	**0.73**	**0.72**	**0.79**	**0.97**	**1.13**
MC model calibration	0.42	0.49	0.53	0.48	0.40	0.32	0.30	0.23	0.15	0.11	0.11	0.12
MC model res. bias corr.	0.56	0.39	0.33	0.26	0.30	0.17	0.09	0.09	0.12	0.13	0.07	0.05
Bias correction calibr.	0.37	0.23	0.24	0.10	0.20	0.19	0.21	0.23	0.28	0.25	0.18	0.51
Track selection eff.	0.50	0.36	0.28	0.24	0.22	0.20	0.18	0.18	0.17	0.17	0.18	0.19
Photon selection eff.	1.24	0.85	0.63	0.50	0.42	0.37	0.33	0.34	0.34	0.41	0.42	0.43
$B \to X_u e\nu$	0.29	0.24	0.23	0.23	0.22	0.22	0.23	0.24	0.27	0.31	0.39	0.52
$B^{(+,0)} \to D^0 \to e^+$	0.09	0.06	0.02	0.01	0.01	0.00	0.00	0.00	0.00	0.00	0.00	0.00
$B^{(+,0)} \to \bar{D}^0, D^- \to e^-$	0.16	0.09	0.04	0.02	0.01	0.01	0.00	0.00	0.00	0.00	0.00	0.00
$B^{(+,0)} \to D^+ \to e^+$	0.14	0.07	0.05	0.03	0.01	0.00	0.00	0.00	0.00	0.00	0.00	0.00
$B^{(+,0)} \to D_s^+ \to e^+$	0.61	0.37	0.23	0.17	0.09	0.07	0.03	0.02	0.01	0.01	0.01	0.01
$B^{(+,0)} \to \tau^+ \to e^+$	0.02	0.03	0.03	0.03	0.02	0.02	0.01	0.01	0.01	0.01	0.00	0.00
$B^{(+,0)} \to D_s^+ \to \tau^+ \to e^+$	0.08	0.07	0.05	0.04	0.03	0.02	0.01	0.00	0.00	0.00	0.00	0.00
$B(\to X) \to J/\Psi \to e^+e^-$	0.00	0.01	0.00	0.00	0.00	0.00	0.00	0.00	0.00	0.00	0.00	0.00
$B(\to X) \to \Psi(2S) \to e^+e^-$	0.00	0.00	0.00	0.00	0.00	0.00	0.00	0.00	0.00	0.00	0.00	0.00
Res. background total	0.71	0.46	0.34	0.29	0.24	0.23	0.23	0.24	0.27	0.31	0.39	0.52
Calib. curve binning	0.02	0.00	0.03	0.05	0.08	0.05	0.08	0.04	0.02			
Hard photon emission	2.31	1.54	1.41	1.02	0.72	0.65	0.31	0.12	0.13	0.17	0.21	0.24
$E_{miss} - \lvert\vec{p}_{miss}\rvert_{cut}$ stability	0.00	0.00	0.23	0.22	0.63	1.02	0.92	0.68	0.00	0.52	0.49	0.68
Sys. error total	**2.87**	**1.97**	**1.75**	**1.34**	**1.22**	**1.37**	**1.14**	**0.89**	**0.59**	**0.83**	**0.83**	**1.14**
Error total	**3.47**	**2.42**	**2.11**	**1.67**	**1.53**	**1.61**	**1.41**	**1.15**	**0.93**	**1.15**	**1.28**	**1.61**
m_{ES} sideband definition	0.61	0.30	0.25	0.15	0.11	0.12	0.14	0.17	0.22	0.21	0.17	0.11
Soft photons	0.76	0.37	0.26	0.36	0.22	0.67	0.89	0.92	1.21	1.30	1.88	1.31

Table 6.5: Summary of systematic uncertainties for the measurement of $< m_X^5 >$. All quantitites are given in units of $(\,\mathrm{GeV}/c^2)^5$. For the sake of completeness the two systematic studies "m_{ES} sideband definition" and "Soft photons" are listed but not included in the total systematic uncertainty. Details can be found in the sections 6.5.1 and 6.9, respectively.

$p_{l,cut}[GeV/c]$	0.8	0.9	1.0	1.1	1.2	1.3	1.4	1.5	1.6	1.7	1.8	1.9
Moment $< m_X^6 >$	**120.04**	**109.85**	**106.58**	**100.73**	**96.95**	**92.83**	**89.38**	**84.32**	**79.06**	**75.53**	**73.58**	**70.37**
Stat. error (data)	4.71	3.67	3.04	2.56	2.26	2.02	1.90	1.77	1.69	1.78	2.07	2.41
Stat. error (calibration)	0.89	0.69	0.62	0.58	0.58	0.56	0.52	0.48	0.37	0.28	0.34	0.44
Stat. error (bg. subtr)	4.79	2.66	2.07	1.69	1.27	1.18	1.21	0.73	0.72	0.88	1.14	1.17
Stat. error (total)	**6.78**	**4.58**	**3.73**	**3.13**	**2.65**	**2.41**	**2.31**	**1.98**	**1.88**	**2.01**	**2.39**	**2.71**
MC model calibration	3.09	3.09	3.10	2.59	2.07	1.60	1.18	0.87	0.50	0.32	0.30	0.33
MC model res. bias corr.	1.83	1.22	0.96	0.77	0.96	0.55	0.29	0.29	0.37	0.40	0.21	0.14
Bias correction calibr.	6.02	4.10	2.92	1.79	1.46	1.06	0.58	0.54	0.52	0.46	0.30	1.18
Track selection eff.	1.51	1.03	0.76	0.65	0.58	0.52	0.47	0.43	0.42	0.41	0.41	0.44
Photon selection eff.	4.13	2.70	1.89	1.45	1.15	0.95	0.83	0.86	0.83	0.98	0.99	0.99
$B \to X_u e \nu$	0.76	0.56	0.53	0.52	0.48	0.49	0.52	0.54	0.60	0.70	0.87	1.15
$B^{(+,0)} \to D^0 \to e^+$	0.31	0.20	0.07	0.04	0.02	0.00	0.00	0.00	0.00	0.00	0.00	0.00
$B^{(+,0)} \to \bar{D}^0, D^- \to e^-$	0.54	0.29	0.13	0.05	0.05	0.02	0.01	0.01	0.00	0.00	0.00	0.00
$B^{(+,0)} \to D^+ \to e^+$	0.49	0.24	0.18	0.09	0.04	0.01	0.00	0.01	0.00	0.00	0.00	0.00
$B^{(+,0)} \to D_s^+ \to e^+$	2.04	1.21	0.75	0.53	0.30	0.21	0.10	0.05	0.04	0.02	0.03	0.01
$B^{(+,0)} \to \tau^+ \to e^+$	0.04	0.10	0.08	0.07	0.04	0.06	0.03	0.03	0.03	0.02	0.01	0.00
$B^{(+,0)} \to D_s^+ \to \tau^+ \to e^+$	0.24	0.20	0.16	0.13	0.08	0.07	0.02	0.01	0.01	0.00	0.00	0.00
$B(\to X) \to J/\Psi \to e^+e^-$	0.01	0.02	0.00	0.01	0.01	0.01	0.00	0.00	0.00	0.00	0.00	0.00
$B(\to X) \to \Psi(2S) \to e^+e^-$	0.00	0.00	0.00	0.00	0.00	0.00	0.00	0.00	0.00	0.00	0.00	0.00
Res. background total	2.33	1.42	0.96	0.77	0.58	0.54	0.53	0.55	0.60	0.70	0.87	1.15
Calib. curve binning	0.13	0.10	0.10	0.11	0.08	0.01	0.07	0.05	0.03			
Hard photon emission	8.22	5.64	5.08	3.79	2.43	2.09	1.03	0.36	0.35	0.40	0.51	0.52
$E_{miss} - \lvert\vec{p}_{miss}\rvert_{cut}$ stability	0.00	0.00	0.00	0.00	0.75	2.29	2.29	1.91	0.66	1.29	1.13	1.56
Sys. error total	**11.89**	**8.37**	**7.07**	**5.29**	**3.98**	**3.88**	**3.05**	**2.48**	**1.56**	**1.98**	**1.91**	**2.59**
Error total	**13.69**	**9.55**	**7.99**	**6.15**	**4.78**	**4.57**	**3.83**	**3.17**	**2.44**	**2.82**	**3.06**	**3.75**
m_{ES} sideband definition	2.04	1.01	0.77	0.46	0.34	0.42	0.39	0.43	0.54	0.49	0.36	0.27
Soft photons	4.97	2.46	1.29	1.30	0.63	1.83	2.40	2.42	3.10	3.30	4.71	3.25

Table 6.6: Summary of systematic uncertainties for the measurement of $< m_X^6 >$. All quantitites are given in units of $(\text{GeV}/c^2)^6$. For the sake of completeness the two systematic studies "m_{ES} sideband definition" and "Soft photons" are listed but not included in the total systematic uncertainty. Details can be found in the sections 6.5.1 and 6.9, respectively.

Chapter 7

Interpretation of Results and Extraction of $|V_{cb}|$

In the following section the obtained results will be interpreted in the context of the *Heavy Quark Expansion* (HQE) in the kinetic scheme. An introduction to the HQE in the kinetic scheme can be found in section 2.5.2. We extract results for the CKM-Matrix element $|V_{cb}|$, the quark masses m_b and m_c, the total semileptonic branching fraction $\mathcal{B}(B \to X_c \ell \nu)$, as well as the four non-perturbative HQE parameters μ_π^2, μ_G^2, ρ_{LS}^3, and ρ_D^3 in a global fit combining the presented results with additional measurements of moments of the lepton energy spectrum, $< E_\ell^n >$, in decays $B \to X_c \ell \nu$ and moments of the photon energy spectrum, $< E_\gamma^n >$, in decays $B \to X_s \gamma$. The performed fit is closely related to the work presented in [11]. It is repeated by replacing the previous *BABAR* measurement of invariant hadronic mass moments [47] with the moments extracted in this analysis.

The implemented fitting procedure will be described in section 7.1. Section 7.2 will summarize the experimental input used in the combined fit followed by a discussion of the obtained results as well as a comparison with other measurements in section 7.3.

7.1 Extraction Formalism

The utilized extraction formalism is based on a χ^2 minimization technique,

$$\chi^2 = \left(\vec{M}_{exp} - \vec{M}_{HQE}\right)^T \left(\mathcal{C}_{exp} + \mathcal{C}_{HQE}\right)^{-1} \left(\vec{M}_{exp} - \vec{M}_{HQE}\right), \tag{7.1}$$

to determine the best fit of the HQE predictions to the measurements. The vectors $\vec{M}_{exp}$ and $\vec{M}_{HQE}$ contain the measured moments included in the fit and the corresponding predicted moments, respectively. Furthermore, the expression in equation 7.1 contains the sum of the experimental, $\mathcal{C}_{exp}$, and theoretical, $\mathcal{C}_{HQE}$, covariance matrices.

The total semileptonic branching fraction, $\mathcal{B}(B \to X_c \ell\nu)$, is extracted in the fit by extrapolating measured partial branching-fractions, $\mathcal{B}_{p^*_{\ell,cut}}(B \to X_c \ell\nu)$, with $p^*_\ell \geq p^*_{\ell,cut}\,\mathrm{GeV}/c$ to the full lepton energy spectrum. Using HQE predictions of the relative decay fraction

$$R_{p^*_{\ell,cut}} = \frac{\int_{p^*_{\ell,cut}} \frac{\mathrm{d}\Gamma_{SL}}{\mathrm{d}E^*_\ell}\mathrm{d}E^*_\ell}{\int_0 \frac{\mathrm{d}\Gamma_{SL}}{\mathrm{d}E^*_\ell}\mathrm{d}E^*_\ell}, \tag{7.2}$$

the total branching fraction can be introduced as a free parameter in the fit. It is given by

$$\mathcal{B}(B \to X_c \ell\nu) = \frac{\mathcal{B}_{p^*_{\ell,cut}}(B \to X_c \ell\nu)}{R_{p^*_{\ell,cut}}}. \tag{7.3}$$

The total branching fraction can be used together with the average B meson lifetime τ_B to calculate the total semileptonic rate,

$$\Gamma_{SL} = \frac{\mathcal{B}(B \to X_c \ell\nu)}{\tau_B} \propto |V_{cb}|^2, \tag{7.4}$$

propotional to $|V_{cb}|^2$. Finally, $|V_{cb}|$ can be extracted by means of a HQE prediction for the total semileptonic rate and introducing an additional free parameter to the fit.

The non-perturbative parameters μ_G^2 and ρ_{LS}^3 are estimated from B-B^* mass splitting and heavy-quark sum rules to be $\mu_G^2 = (0.35 \pm 0.07)\,\mathrm{GeV}^2$ and $\rho_{LS}^3 = (-0.15 \pm 0.10)\,\mathrm{GeV}^3$ [11], respectively. Both parameters are restricted in the fit by imposing Gaussian error constraints.

As discussed in [11] and specified in [14] the following theoretical uncertainties are taken into account:

1. The uncertainty related to the uncalculated perturbative corrections to the Wilson coefficients of nonperturbative operators is assumed to be 20% due to μ_π^2 and μ_G^2 and 30% due to ρ_D^3 and ρ_{LS}^3. It is estimated by varying the corresponding parameters accordingly around theor theoretically expected values $\mu_\pi^2 = 0.4\,\mathrm{GeV}^2$, $\mu_G^2 = 0.35\,\mathrm{GeV}^2$, $\rho_D^3 = 0.2\,\mathrm{GeV}^3$, and $\rho_{LS}^3 = -0.15\,\mathrm{GeV}^3$.

2. Theoretical uncertainties for the perturbative corrections are estimated by varying α_s by 0.1 for the hadronic mass moments and by 0.04 for the lepton energy moments around its nominal value $\alpha_s = 0.22$.

3. Theoretical uncertainties in the perturbative corrections of the quark m_b and m_c are addressed by varying both by $20\,\mathrm{MeV}/c^2$ around their nominal values of $4.6\,\mathrm{GeV}/c^2$ and $1.18\,\mathrm{GeV}/c^2$, respectively.

4. For the extracted value of $|V_{cb}|$ and additional theoretical error of 1.4% is added for the uncertainty in the expansion of the semileptonic rate

Γ_{SL} [15, 48]. It accounts for remaining uncertainties in the perturbative corrections to the leading operator $\bar{b}b$, uncalculated perturbative corrections to the chromomagnetic and Darwin operator, higher order power corrections, and possible nonperturbative effects in the operators with charm fields. This uncertainty will not be included into the theoretical covariance matrix $\mathcal{C}_{HQE}$ but will be added separately to the final fit result of $|V_{cb}|$.

5. For the predicted photon energy moments $< E_\gamma^n >$, additional theoretical uncertainties are taken into account. As outlined in [16] additional uncertainties of 30% of the applied bias correction as well as half the difference in the moments derived from two different distribution-function ansätze have to be considered.

The theoretical covariance matrix $\mathcal{C}_{HQE}$ is constructed by assuming fully correlated theoretical uncertainties for a given moment with different lepton momentum or photon energy cutoff and assuming uncorrelated theoretical uncertainties for moments of different orders and types.

Theoretical expressions for predictions of hadronic mass, lepton energy, and photon energy moments in the kinetic scheme are calculated in [14, 16]. Calculations for the total semileptonic rate can be found in [15]. A discussion of perturbative corrections to the hadronic mass moments can be found in [49, 13, 50].

7.2 Experimental Input

The performed global fit combines measurements of moments of the invariant hadronic mass, $< m_X^n >$, and lepton energy distribution, $< E_\ell^n >$, in decays $B \to X\ell\nu$ as well as moments of the photon energy spectrum, $< E_\gamma^n >$, in decays $B \to X_s\gamma$ of different order n and for different cuts on the minimum lepton momentum, $p^*_{\ell,cut}$, and photon energy $E_{\gamma,cut}$. Beside the measurement presented in this analysis, currently available experimental moment measurements that are used in the combined fit are in detail:

1. The *BABAR* collaboration measures zeroth to third order moments of lepton energy distribution in decays $B \to X_c\ell\nu$ [51] for different cuts on the lepton momentum starting from $p^*_\ell \geq 0.6\,\mathrm{GeV}/c$. The first and second moments of the photon energy distribution in decays $B \to X_s\gamma$ are measured utilizing two different experimental methods. First, by measuring the photon energy spectrum from a sum of exclusive final states [52] and second with a fully inclusive approach [53].

2. The BELLE collaboration performed inclusive measurements of the first and second photon energy moments [54, 55].

3. The CDF collaboration measures invariant hadronic mass moments with a minimum lepton momentum $p^*_\ell \geq 0.7\,\mathrm{GeV}/c$ [56].

4. The CLEO collaboration provides measurements of the second and fourth hadronic mass moments [57] as well as the first photon energy moments [58] with different cuts on the lepton momentum and the photon energy, respectively.

5. Moments of the invariant hadronic mass spectrum and the lepton energy spectrum [59] without restrictions on the lepton momentum are provided by the DELPHI collaboration.

6. In addition we use the world average of partial branching fraction $\mathcal{B}_{p_\ell^* \geq 0.6\,\mathrm{GeV}/c}(B \to X_c \ell \nu)$ measurements provided by the Heavy Flavor Averaging Group (HFAG) [42, 11]. The average does not include measurements already used in the fit.

Only a subset of all measurements available with correlations below 95% is considered. The inclusion of highly correlated measurements does not contribute additional information to the fit but results in an uninvertible covariance matrix. The hadronic mass moments $< m_X >$ and $< m_X^3 >$ are not considered in the fit since the accuracy of the theoretical expansion of those moments is believed to be reduced. Table 7.1 summarizes all measurements used as experimental input for the combined fit.

In addition to the experimental input of measured moments the average B meson lifetime, $\tau_B = (1.585 \pm 0.007)\,\mathrm{ps}$ [42], is used for the calculation of the total semileptonic rate Γ_{SL}.

7.3 Fit Results and Comparison With Other Measurements

A comparison of the HQE predictions obtained from the best fit and the hadronic mass moment measurement is shown in figure 7.1. The green band corresponds to the experimental uncertainties obtained by translating the uncertainties of the extracted fit parameters into uncertainties for the individual moments. The total error calculated as squared sum of theoretical and experimental uncertainties is depicted as yellow band. Moments with filled markers are included in the fit while moments with open markers are not included in the fit.

The theoretical prediction is in good agreement with all measured moments. This is also reflected by the excellent minimal χ^2 found to be $\chi^2 = 24\,(ndf = 38)$ and corresponding to a χ^2 probability of $\mathcal{P}(\chi^2) = 96\%$. In particular, the prediction that is obtained from a fit to the measured moments $< m_X^2 >$ and $< (m_X^2 - < m_X^2 >)^2 >$ is also in good agreement with the measured moments $< m_X >$ and $< m_X^3 >$ that are not included in the fit.

The HQE approach is expected to break down for moments calculated with high cuts on the lepton momentum. This behaviour is indicated by

Experiment	Hadronic mass moments $< m_X^n >$	Lepton energy moments $< E_\ell^n >$	Photon energy moments $< E_\gamma^n >$
This analysis	$n = 2$, $p^*_{\ell,cut} = 0.9, 1.1, 1.3, 1.5\,\mathrm{GeV}/c$		
	$n = 4$, $p^*_{\ell,cut} = 0.8, 1.0, 1.2, 1.4\,\mathrm{GeV}/c$		
BABAR		$n = 0$, $p^*_{\ell,cut} = 0.6, 1.2, 1.5\,\mathrm{GeV}$	
[51,52,53]		$n = 1$, $p^*_{\ell,cut} = 0.6, 0.8, 1.0, 1.2, 1.5\,\mathrm{GeV}$	$n = 1$, $E_{\gamma,cut} = 1.9, 2.0\,\mathrm{GeV}$
		$n = 2$, $p^*_{\ell,cut} = 0.6, 1.0, 1.5\,\mathrm{GeV}$	$n = 2$, $E_{\gamma,cut} = 1.9\,\mathrm{GeV}$
		$n = 3$, $p^*_{\ell,cut} = 0.8, 1.2\,\mathrm{GeV}$	
BELLE			$n = 1$, $E_{\gamma,cut} = 1.8, 1.9\,\mathrm{GeV}$
[54,55]			$n = 2$, $E_{\gamma,cut} = 1.8, 2.0\,\mathrm{GeV}$
CDF	$n = 2$, $p^*_{\ell,cut} = 0.7\,\mathrm{GeV}/c$		
[56]	$n = 4$, $p^*_{\ell,cut} = 0.7\,\mathrm{GeV}/c$		
CLEO	$n = 2$, $p^*_{\ell,cut} = 1.0, 1.5\,\mathrm{GeV}/c$		$n = 1$, $E_{\gamma,cut} = 2.0\,\mathrm{GeV}$
[57,58]	$n = 4$, $p^*_{\ell,cut} = 1.0, 1.5\,\mathrm{GeV}/c$		
DELPHI	$n = 2$, $p^*_{\ell,cut} = 0\,\mathrm{GeV}/c$	$n = 1$, $p^*_{\ell,cut} = 0\,\mathrm{GeV}$	
[59]	$n = 4$, $p^*_{\ell,cut} = 0\,\mathrm{GeV}/c$	$n = 2$, $p^*_{\ell,cut} = 0\,\mathrm{GeV}$	
	$n = 6$, $p^*_{\ell,cut} = 0\,\mathrm{GeV}/c$	$n = 3$, $p^*_{\ell,cut} = 0\,\mathrm{GeV}$	
HFAG average [42,11]		$n = 0$, $p^*_{\ell,cut} = 0.6\,\mathrm{GeV}$	

Table 7.1: Summary of measurements used as experimental input for the combined fit. The table lists the different hadronic mass moments $< m_X^n >$, lepton energy moments $< E_\ell^n >$, and photon energy moments $< E_\gamma^n >$ together with their order n and the applied minimum lepton momentum, $p^*_{\ell,cut}$, as well as minimum photon energy, $E_{\gamma,cut}$, cuts. The Heavy Flavor Averaging Group (HFAG) averages several measurements of partial branching fraction not including measurements already used in the fit.

the measurement for moments above $p^*_\ell \geq 1.6\,\mathrm{GeV}/c$ corresponding to the region in which the measured $p^*_{\ell,cut}$ dependence changes and flattens out with respect to that measured for moments below the mentioned $p^*_{\ell,cut}$. In contrast the theoretical prediction is not expected to show this behaviour in the mentioned region of the phase space. However, the measurement cannot confirm a break down of the HQE approach with the experimental accuracy available.

As can be seen from figure 7.1, the measured moments presented in this work are in good agreement with other measurements. Comparing this measurement to a previous measurement performed by the *BABAR* collaboration [47], we find an agreement within one experimental standard deviation but with reduced experimental uncertainty in this measurement. While both analyses obtain the same $p^*_{\ell,cut}$ dependency for the measured moments, the measurement presented here is offset to higher values. In general the agreement of both measurements improves for higher moments reaching perfect agreement for the fourth central moments $< (m_X^2 - < m_X^2 >)^2 >$ (cf. figure 7.1d).

Figure 7.2 presents a comparison of the results obtained in the combined fit (black line) with those obtained from a fit to all hadronic mass and lepton energy moments in decays $B \to X\ell\nu$ (red green line) and a fit combining information of this measurement and the other *BABAR* measurements of lepton energy and photon energy moments (red line) in the μ_π^2-m_b plane. The obtained results agree for all fits. As can bee seen the inclusion of the photon energy moments significantly improves the sensitivity to extract the b-quark mass m_b. The same conclusion can be drawn comparing the $\Delta\chi^2 = 1$ contours of the mentioned fits in the $|V_{cb}|$-m_b plane. While the results of the fits are in good agreement it can be seen that the inclusion of the photon energy moments adds additional sensitivity to the extracted b-quark mass.

Table 7.2 summarizes the fit results together with the experimental (Δexp), theoretical (ΔHQE), and combined ($\Delta total$) uncertainties. For the extracted value of $|V_{cb}|$ an additional theoretical error, $\Delta\Gamma_{SL}$, of 1.4% is added for the uncertainty in the expansion of the semileptonic rate Γ_{SL}. We find,

$$|V_{cb}| \times 10^{-3} = (42.06 \pm 0.21_{exp} \pm 0.35_{HQE} \pm 0.59_{\Gamma_{SL}}) \times 10^{-3}. \qquad (7.5)$$

obtaining an overall precision of 1.7% dominated by theoretical uncertainties. The obtained result is in good agreement with previous measurements:

- A global analysis of inclusive measurements is performed by Buchmüller and Flächer. They find: $|V_{cb}| = (41.96 \pm 0.23_{exp} \pm 0.35_{HQE} \pm 0.6_{\Gamma_{SL}}) \times 10^{-3}$ [11]. The presented fit is very similar to the one presented here but instead of using this measurement of hadronic mass moments a previous measurement by the *BABAR* collaboration is included [40]. While theoretical uncertainties are found to be identical in both fits, we observe a slight improvement in the experimental uncertainty of the extracted value for $|V_{cb}|$.

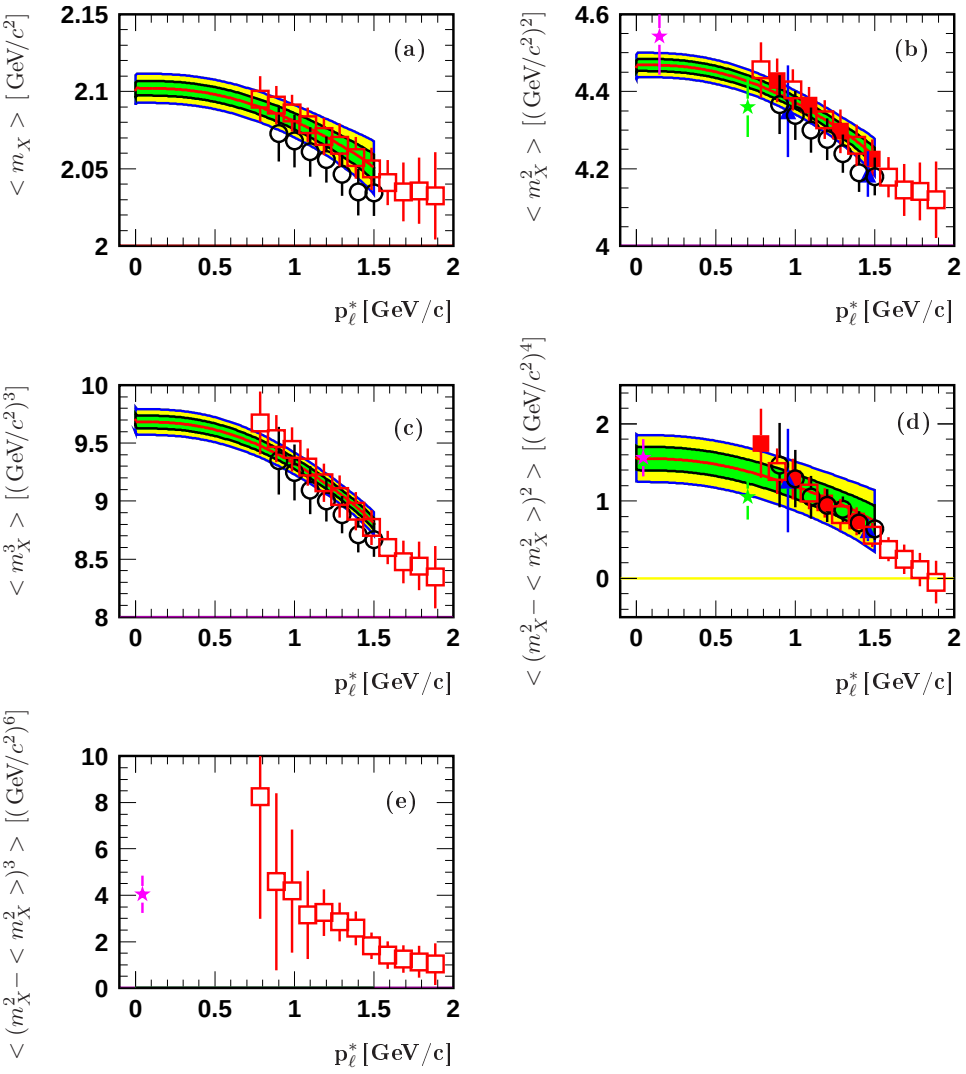

Figure 7.1: Comparison of measurements (markers) and HQE predictions (red line) for the best fit. The yellow band corresponds to the squared sum of theoretical and experimental uncertainties. The green band corresponds to the experimental uncertainties only. Moments with filled markers are included in the fit while moments with open markers are not included. The measurements are in detail: this analysis (■/□), *BABAR* collaboration [47] (○), CDF collaboration [56] (★), CLEO collaboration [57] (▲/△), and DELPHI collaboration [59] (★).

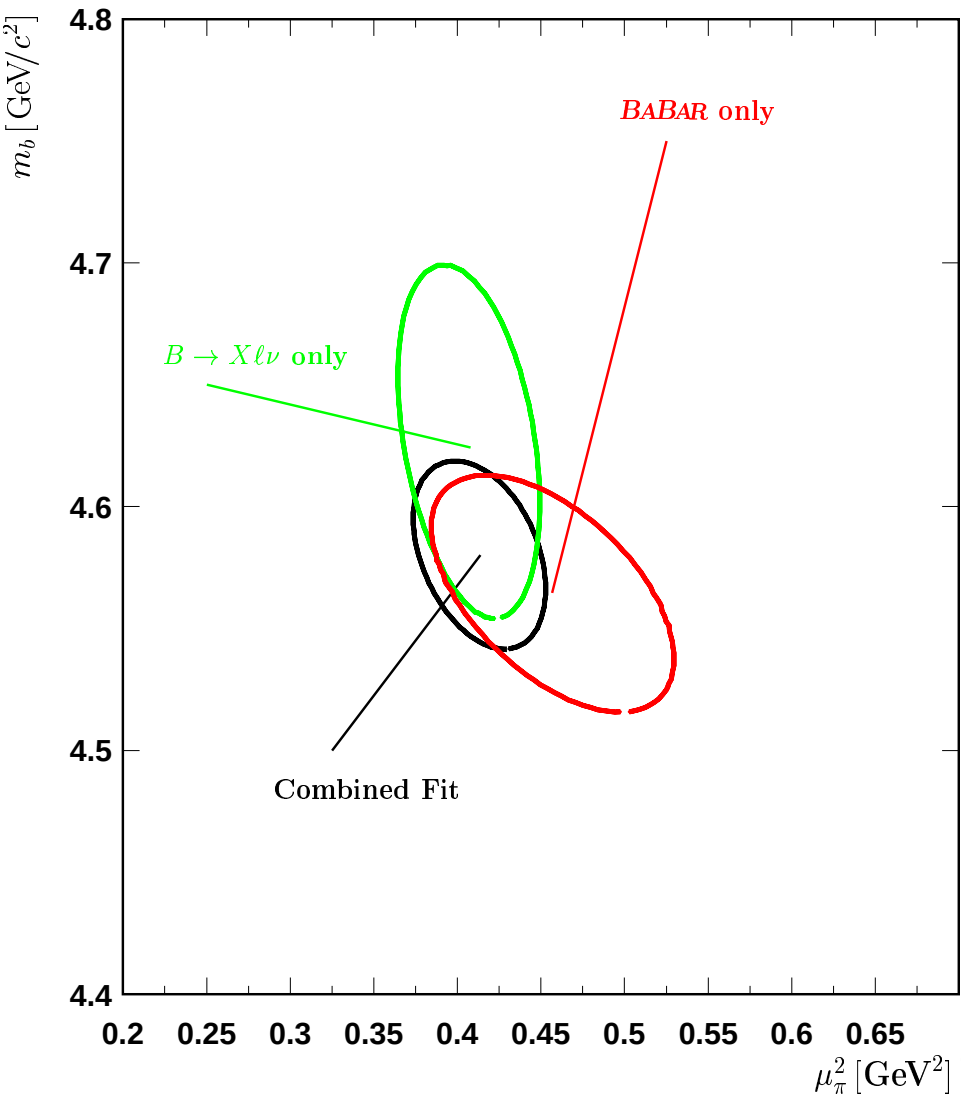

Figure 7.2: Comparison of fits to different subsets of moments in the μ_π^2-m_b plane. Shown are the $\Delta\chi^2 = 1$ contours for the combined fit to all moments (black line), a fit to all hadronic mass and lepton energy moments in decays $B \to X\ell\nu$ only (green line), and a fit to moments measured in this analysis combined with measurements of the lepton energy and photon energy spectrum performed by the *BABAR* collaboration.

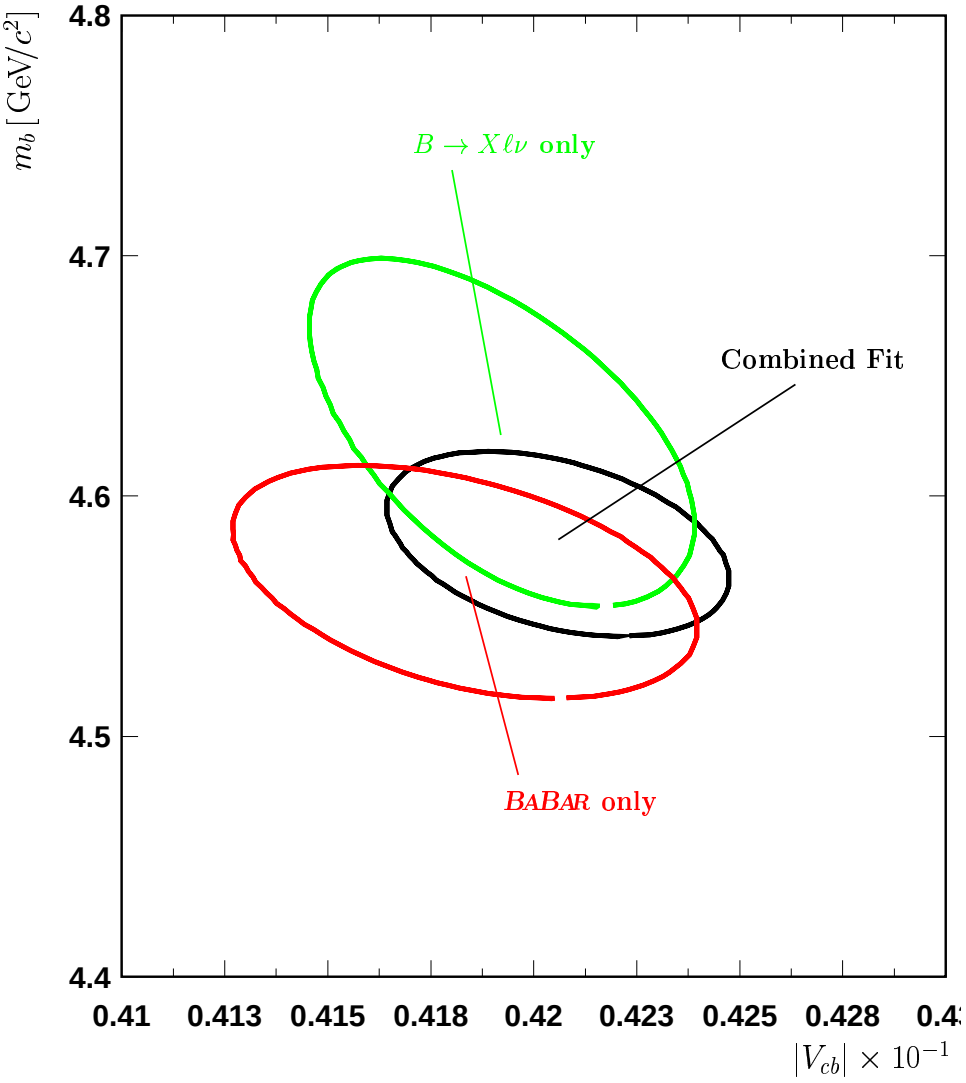

Figure 7.3: Comparison of fits to different subsets of moments in the $|V_{cb}|$-m_b plane. Shown are the $\Delta\chi^2 = 1$ contours for the combined fit to all moments (black line), a fit to all hadronic mass and lepton energy moments in decays $B \to X\ell\nu$ only (green line), and a fit to moments measured in this analysis combined with measurements of the lepton energy and photon energy spectrum performed by the *BABAR* collaboration.

Parameter	Value	Δexp	ΔHQE	$\Delta\Gamma_{SL}$	$\Delta total$
$\lvert V_{cb}\rvert \times 10^{-3}$	42.06	0.21	0.35	0.59	0.72
$m_b\,[\mathrm{GeV}/c^2]$	4.580	0.025	0.030		0.039
$m_c\,[\mathrm{GeV}/c^2]$	1.131	0.037	0.045		0.058
$\mathcal{B}(B \to X_c\ell\nu)\,[\%]$	10.71	0.10	0.08		0.13
$\mu_\pi^2\,[\mathrm{GeV}^2]$	0.414	0.019	0.035		0.040
$\mu_G^2\,[\mathrm{GeV}^2]$	0.293	0.024	0.046		0.052
$\rho_D^3\,[\mathrm{GeV}^3]$	0.077	0.009	0.022		0.024
$\rho_{LS}^3\,[\mathrm{GeV}^3]$	−0.165	0.054	0.071		0.089

Table 7.2: Summary of fit results obtained from a combined fit of HQE predictions to measurements of moments of the invariant hadronic mass distribution and moments of the lepton energy spectrum in decays $B \to X_c\ell\nu$ as well as moments of the photon energy spectrum in decays $B \to X_s\gamma$ (cf. table 7.1). All quantities are given in the kinematic scheme with $\mu = 1\,\mathrm{GeV}$. The given uncertainties are experimental (Δexp), theoretical (ΔHQE), and the combined experimental and theoretical ($\Delta total$). For $|V_{cb}|$ an additional theoretical error, $\Delta\Gamma_{SL}$, of 1.4% is added for the uncertainty in the expansion of Γ_{SL}.

- The Heavy Flavor Averaging Group (HFAG) averages several measurements of $|V_{cb}|$ obtained from exclusive analyses of decays $B \to D^*\ell\nu$ and performed by the collaborations ALEPH, *BABAR*, BELLE, CLEO, DELPHI, and OPAL. They find: $|V_{cb}| = (41.3 \pm 1.0_{exp} \pm 1.8_{theo}) \times 10^{-3}$ [42].

- The DELPHI collaboration performed an inclusive measurement of hadronic mass and lepton energy moments in semileptonic decays $B \to X\ell\nu$ without applying restrictions on the lepton momentum, $p^*_{\ell,cut} = 0$. In a combined fit in the kinetic HQE scheme they extract: $|V_{cb}| = (42.1 \pm 0.6_{exp} \pm 0.6_{fit} \pm 0.6_{theo}) \times 10^{-3}$ [59].

- Bauer et al. perform a combined fit in a different HQE scheme, namely the 1S scheme, to measurements by *BABAR*, BELLE, CDF, CLEO, and DELPHI. They obtain: $|V_{cb}| = (41.4 \pm 0.6 \pm 0.1_{\tau_B}) \times 10^{-3}$ [60],

- A combined fit in the kinetic HQE scheme to previous inclusive BABAR measurements of hadronic mass and lepton energy moments obtains the result: $|V_{cb}| = (41.4 \pm 0.4_{exp} \pm 0.4_{HQE} \pm 0.6_{\Gamma_{SL}}) \times 10^{-3}$ [40],

Figure 7.4 compares this measurement of $|V_{cb}|$ with those described above.

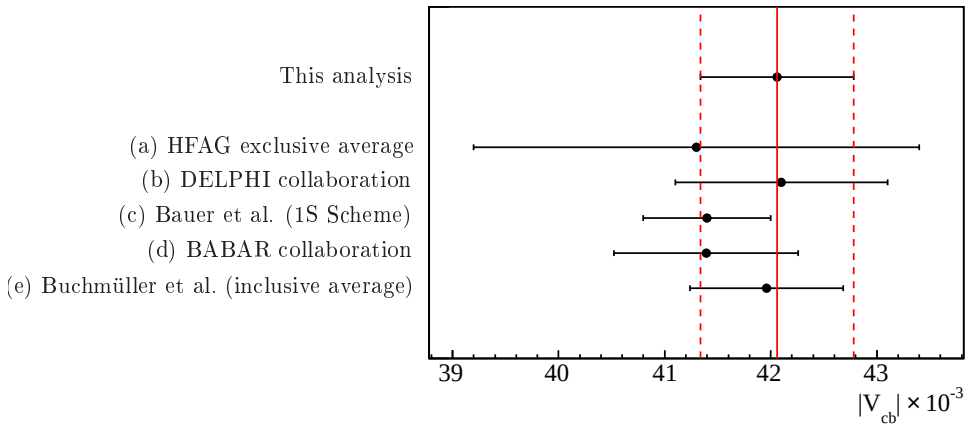

Figure 7.4: Comparison of extracted $|V_{cb}|$ with other measurements: (a) Heavy Flavor Averaging Group (HFAG) average of exclusive $B \to D^*\ell\nu$ decays ($|V_{cb}| = (41.3 \pm 1.0_{exp} \pm 1.8_{theo}) \times 10^{-3}$) [42], (b) DELPHI collaboration inclusive analysis of $B \to X\ell\nu$ decays ($|V_{cb}| = (42.1 \pm 0.6_{exp} \pm 0.6_{fit} \pm 0.6_{theo}) \times 10^{-3}$) [59], (c) combined fit in the 1S scheme by Bauer at al. ($|V_{cb}| = (41.4 \pm 0.6 \pm 0.1_{\tau_B}) \times 10^{-3}$) [60], (d) *BABAR* collaboration inclusive analysis of $B \to X\ell\nu$ decays ($|V_{cb}| = (41.4 \pm 0.4_{exp} \pm 0.4_{HQE} \pm 0.6_{theo}) \times 10^{-3}$) [40], (e) Global analysis of inclusive measurements by Buchmüller and Flächer ($|V_{cb}| = (41.96 \pm 0.23_{exp} \pm 0.35_{HQE} \pm 0.6_{\Gamma_{SL}}) \times 10^{-3}$) [11].

Appendix A

Correlation Matrix

		$< m_X > [GeV/c^2]$												$< m_X^2 > [(GeV/c^2)^2]$											
$p_{l,cut}[GeV/c]$		0.8	0.9	1.0	1.1	1.2	1.3	1.4	1.5	1.6	1.7	1.8	1.9	0.8	0.9	1.0	1.1	1.2	1.3	1.4	1.5	1.6	1.7	1.8	1.9
$< m_X >$	0.8	1.00	0.94	0.88	0.83	0.79	0.74	0.69	0.64	0.58	0.52	0.45	0.36	0.96	0.86	0.77	0.70	0.64	0.58	0.54	0.48	0.42	0.36	0.31	0.23
	0.9		1.00	0.94	0.88	0.84	0.79	0.74	0.68	0.62	0.55	0.48	0.38	0.86	0.96	0.86	0.78	0.72	0.65	0.60	0.54	0.47	0.41	0.34	0.26
	1.0			1.00	0.94	0.90	0.84	0.79	0.73	0.66	0.59	0.51	0.41	0.77	0.86	0.96	0.87	0.80	0.73	0.67	0.60	0.53	0.45	0.38	0.29
	1.1				1.00	0.95	0.88	0.83	0.77	0.70	0.62	0.54	0.43	0.70	0.78	0.87	0.96	0.88	0.79	0.73	0.66	0.58	0.50	0.42	0.32
	1.2					1.00	0.93	0.88	0.81	0.74	0.66	0.57	0.45	0.64	0.72	0.80	0.88	0.96	0.87	0.80	0.71	0.63	0.54	0.46	0.35
	1.3						1.00	0.94	0.87	0.79	0.70	0.61	0.48	0.58	0.65	0.73	0.80	0.87	0.96	0.87	0.78	0.69	0.59	0.50	0.38
	1.4							1.00	0.93	0.84	0.75	0.65	0.52	0.54	0.60	0.67	0.73	0.80	0.87	0.96	0.86	0.75	0.65	0.55	0.42
	1.5								1.00	0.91	0.81	0.70	0.56	0.48	0.54	0.60	0.65	0.71	0.78	0.86	0.96	0.84	0.72	0.61	0.47
	1.6									1.00	0.89	0.78	0.61	0.42	0.47	0.53	0.58	0.63	0.69	0.75	0.84	0.95	0.82	0.69	0.53
	1.7										1.00	0.87	0.69	0.36	0.41	0.45	0.49	0.54	0.59	0.65	0.72	0.82	0.95	0.80	0.62
	1.8											1.00	0.79	0.31	0.34	0.38	0.42	0.46	0.50	0.55	0.61	0.70	0.81	0.95	0.73
	1.9												1.00	0.23	0.26	0.29	0.32	0.35	0.38	0.42	0.47	0.53	0.62	0.73	0.95
$< m_X^2 >$	0.8													1.00	0.89	0.80	0.73	0.67	0.61	0.56	0.50	0.44	0.38	0.32	0.25
	0.9														1.00	0.90	0.82	0.75	0.68	0.63	0.56	0.49	0.43	0.36	0.28
	1.0															1.00	0.91	0.84	0.76	0.70	0.63	0.55	0.47	0.40	0.31
	1.1																1.00	0.92	0.83	0.77	0.69	0.61	0.52	0.44	0.34
	1.2																	1.00	0.91	0.83	0.75	0.66	0.57	0.48	0.37
	1.3																		1.00	0.91	0.82	0.72	0.62	0.52	0.40
	1.4																			1.00	0.90	0.79	0.68	0.57	0.44
	1.5																				1.00	0.88	0.76	0.64	0.49
	1.6																					1.00	0.86	0.73	0.56
	1.7																						1.00	0.85	0.65
	1.8																							1.00	0.76
	1.9																								1.00

Table A.1: Correlation matrix of the moments $< m_X >$ and $< m_X^2 >$.

		$< m_X^3 > [(GeV/c^2)^3]$												$< m_X^4 > [(GeV/c^2)^4]$											
$p_{l,cut}[GeV/c]$		0.8	0.9	1.0	1.1	1.2	1.3	1.4	1.5	1.6	1.7	1.8	1.9	0.8	0.9	1.0	1.1	1.2	1.3	1.4	1.5	1.6	1.7	1.8	1.9
$< m_X^3 >$	0.8	1.00	0.85	0.73	0.64	0.58	0.51	0.46	0.40	0.34	0.29	0.23	0.18	0.99	0.80	0.66	0.56	0.49	0.43	0.38	0.31	0.25	0.21	0.17	0.12
	0.9		1.00	0.86	0.76	0.68	0.60	0.54	0.47	0.40	0.34	0.28	0.21	0.80	0.99	0.81	0.69	0.60	0.52	0.46	0.38	0.31	0.26	0.21	0.15
	1.0			1.00	0.88	0.79	0.70	0.63	0.54	0.46	0.39	0.32	0.24	0.66	0.81	0.99	0.84	0.74	0.64	0.56	0.47	0.38	0.31	0.26	0.18
	1.1				1.00	0.89	0.79	0.71	0.62	0.53	0.44	0.37	0.27	0.56	0.69	0.84	0.98	0.86	0.74	0.66	0.55	0.45	0.37	0.30	0.22
	1.2					1.00	0.89	0.80	0.69	0.59	0.49	0.41	0.31	0.49	0.60	0.74	0.86	0.98	0.85	0.75	0.63	0.51	0.42	0.34	0.25
	1.3						1.00	0.89	0.77	0.65	0.55	0.45	0.34	0.43	0.52	0.64	0.74	0.85	0.98	0.86	0.72	0.58	0.48	0.39	0.28
	1.4							1.00	0.87	0.74	0.62	0.51	0.38	0.38	0.46	0.56	0.66	0.75	0.86	0.98	0.82	0.66	0.55	0.45	0.32
	1.5								1.00	0.85	0.72	0.60	0.44	0.31	0.38	0.47	0.55	0.63	0.72	0.82	0.99	0.81	0.66	0.54	0.39
	1.6									1.00	0.83	0.70	0.52	0.26	0.31	0.38	0.45	0.51	0.58	0.67	0.81	0.99	0.80	0.66	0.48
	1.7										1.00	0.83	0.62	0.21	0.26	0.31	0.37	0.42	0.48	0.55	0.66	0.79	0.99	0.81	0.58
	1.8											1.00	0.74	0.17	0.21	0.26	0.30	0.34	0.39	0.45	0.55	0.66	0.82	0.99	0.71
	1.9												1.00	0.12	0.15	0.18	0.22	0.25	0.28	0.32	0.39	0.47	0.59	0.71	0.99
$< m_X^4 >$	0.8													1.00	0.81	0.67	0.57	0.50	0.43	0.38	0.32	0.26	0.21	0.17	0.12
	0.9														1.00	0.82	0.70	0.61	0.53	0.47	0.39	0.32	0.26	0.21	0.15
	1.0															1.00	0.86	0.75	0.65	0.57	0.47	0.38	0.32	0.26	0.19
	1.1																1.00	0.87	0.75	0.67	0.55	0.45	0.37	0.30	0.22
	1.2																	1.00	0.86	0.77	0.63	0.52	0.42	0.35	0.25
	1.3																		1.00	0.88	0.72	0.58	0.48	0.39	0.28
	1.4																			1.00	0.83	0.67	0.55	0.45	0.33
	1.5																				1.00	0.82	0.67	0.55	0.40
	1.6																					1.00	0.80	0.67	0.48
	1.7																						1.00	0.82	0.59
	1.8																							1.00	0.71
	1.9																								1.00

Table A.2: Correlation matrix of the moments $< m_X^3 >$ and $< m_X^4 >$.

		$< m_X^5 > [(GeV/c^2)^3]$												$< m_X^6 > [(GeV/c^2)^4]$										
$p_{l,cut}[GeV/c]$		0.8	0.9	1.0	1.1	1.2	1.3	1.4	1.5	1.6	1.7	1.8	1.9	0.8	0.9	1.0	1.1	1.2	1.3	1.4	1.5	1.6	1.7	1.8	1.9
$< m_X^5 >$	0.8	1.00	0.78	0.61	0.51	0.43	0.37	0.32	0.25	0.19	0.15	0.12	0.09	0.99	0.73	0.54	0.45	0.38	0.32	0.27	0.20	0.15	0.11	0.09	0.06
	0.9		1.00	0.78	0.65	0.56	0.48	0.42	0.32	0.25	0.20	0.16	0.11	0.73	0.98	0.73	0.60	0.51	0.43	0.37	0.27	0.20	0.15	0.12	0.08
	1.0			1.00	0.84	0.71	0.61	0.53	0.41	0.32	0.25	0.20	0.14	0.55	0.74	0.99	0.81	0.68	0.57	0.50	0.36	0.26	0.20	0.16	0.11
	1.1				1.00	0.85	0.73	0.63	0.50	0.38	0.31	0.25	0.17	0.45	0.60	0.80	0.99	0.83	0.70	0.60	0.44	0.33	0.25	0.20	0.13
	1.2					1.00	0.85	0.74	0.58	0.45	0.36	0.29	0.20	0.37	0.50	0.67	0.83	0.99	0.83	0.72	0.53	0.39	0.29	0.23	0.16
	1.3						1.00	0.87	0.68	0.51	0.41	0.33	0.23	0.32	0.43	0.57	0.70	0.83	0.99	0.85	0.62	0.45	0.34	0.27	0.18
	1.4							1.00	0.78	0.61	0.48	0.39	0.27	0.27	0.36	0.49	0.60	0.72	0.85	0.98	0.72	0.53	0.40	0.32	0.21
	1.5								1.00	0.78	0.62	0.50	0.35	0.20	0.26	0.35	0.44	0.52	0.62	0.72	0.99	0.74	0.55	0.45	0.30
	1.6									1.00	0.77	0.64	0.44	0.14	0.19	0.25	0.32	0.38	0.45	0.53	0.73	0.99	0.73	0.60	0.40
	1.7										1.00	0.82	0.56	0.11	0.15	0.20	0.24	0.29	0.34	0.40	0.55	0.73	0.99	0.80	0.53
	1.8											1.00	0.69	0.09	0.12	0.15	0.19	0.23	0.27	0.32	0.45	0.60	0.81	0.99	0.66
	1.9												1.00	0.06	0.08	0.10	0.13	0.16	0.18	0.22	0.30	0.40	0.54	0.65	0.99
$< m_X^6 >$	0.8													1.00	0.74	0.55	0.45	0.38	0.32	0.28	0.20	0.14	0.11	0.09	0.06
	0.9														1.00	0.75	0.61	0.51	0.43	0.37	0.27	0.19	0.15	0.11	0.08
	1.0															1.00	0.82	0.69	0.58	0.50	0.36	0.26	0.20	0.15	0.10
	1.1																1.00	0.84	0.71	0.61	0.44	0.32	0.24	0.19	0.13
	1.2																	1.00	0.84	0.73	0.53	0.39	0.29	0.23	0.16
	1.3																		1.00	0.86	0.63	0.45	0.34	0.27	0.18
	1.4																			1.00	0.73	0.54	0.40	0.32	0.22
	1.5																				1.00	0.74	0.56	0.45	0.30
	1.6																					1.00	0.74	0.61	0.40
	1.7																						1.00	0.81	0.54
	1.8																							1.00	0.66
	1.9																								1.00

Table A.3: Correlation matrix of the moments $< m_X^5 >$ and $< m_X^6 >$.

		$< m_X^3 > [(GeV/c^2)^3]$												$< m_X^4 > [(GeV/c^2)^4]$											
$p_{l,cut}[GeV/c]$		0.8	0.9	1.0	1.1	1.2	1.3	1.4	1.5	1.6	1.7	1.8	1.9	0.8	0.9	1.0	1.1	1.2	1.3	1.4	1.5	1.6	1.7	1.8	1.9
$< m_X >$	0.8	0.89	0.76	0.65	0.58	0.51	0.46	0.41	0.36	0.30	0.26	0.21	0.16	0.82	0.67	0.55	0.46	0.40	0.35	0.31	0.26	0.21	0.18	0.14	0.10
	0.9	0.76	0.89	0.77	0.68	0.60	0.53	0.48	0.42	0.36	0.30	0.25	0.19	0.66	0.82	0.67	0.57	0.50	0.43	0.38	0.32	0.26	0.22	0.18	0.13
	1.0	0.65	0.77	0.89	0.79	0.70	0.62	0.56	0.49	0.41	0.35	0.29	0.22	0.55	0.67	0.82	0.70	0.61	0.52	0.46	0.39	0.32	0.26	0.22	0.16
	1.1	0.57	0.67	0.78	0.89	0.79	0.70	0.63	0.55	0.47	0.40	0.33	0.25	0.46	0.57	0.69	0.81	0.70	0.60	0.54	0.45	0.38	0.31	0.25	0.19
	1.2	0.51	0.60	0.70	0.80	0.89	0.79	0.71	0.62	0.53	0.44	0.37	0.28	0.40	0.50	0.60	0.71	0.81	0.70	0.61	0.52	0.43	0.35	0.29	0.21
	1.3	0.46	0.54	0.62	0.70	0.79	0.89	0.80	0.69	0.59	0.50	0.41	0.31	0.35	0.43	0.52	0.61	0.70	0.81	0.71	0.59	0.48	0.41	0.33	0.24
	1.4	0.41	0.48	0.56	0.63	0.71	0.80	0.89	0.77	0.66	0.56	0.46	0.35	0.31	0.38	0.46	0.54	0.61	0.71	0.80	0.68	0.55	0.46	0.38	0.27
	1.5	0.36	0.42	0.49	0.55	0.62	0.69	0.77	0.89	0.76	0.64	0.53	0.40	0.26	0.32	0.39	0.45	0.52	0.60	0.68	0.81	0.67	0.56	0.45	0.33
	1.6	0.31	0.36	0.42	0.47	0.53	0.59	0.66	0.77	0.89	0.75	0.62	0.47	0.22	0.27	0.32	0.38	0.43	0.50	0.57	0.68	0.81	0.67	0.55	0.40
	1.7	0.26	0.30	0.35	0.40	0.44	0.50	0.56	0.64	0.74	0.90	0.74	0.55	0.18	0.22	0.26	0.31	0.35	0.41	0.46	0.55	0.66	0.83	0.67	0.49
	1.8	0.21	0.25	0.29	0.33	0.37	0.41	0.46	0.54	0.63	0.75	0.89	0.67	0.15	0.18	0.22	0.25	0.29	0.33	0.38	0.46	0.55	0.69	0.83	0.60
	1.9	0.16	0.19	0.22	0.25	0.28	0.31	0.35	0.40	0.47	0.56	0.67	0.90	0.11	0.13	0.16	0.19	0.21	0.24	0.28	0.33	0.40	0.50	0.60	0.84
$< m_X^2 >$	0.8	0.98	0.84	0.72	0.63	0.57	0.50	0.45	0.39	0.33	0.28	0.23	0.17	0.94	0.76	0.63	0.53	0.46	0.40	0.35	0.30	0.24	0.20	0.16	0.12
	0.9	0.83	0.98	0.84	0.74	0.67	0.59	0.53	0.46	0.39	0.33	0.27	0.20	0.76	0.94	0.77	0.66	0.57	0.49	0.44	0.36	0.30	0.25	0.20	0.15
	1.0	0.72	0.84	0.98	0.86	0.77	0.68	0.62	0.53	0.45	0.38	0.32	0.24	0.62	0.77	0.94	0.80	0.70	0.60	0.53	0.44	0.36	0.30	0.25	0.18
	1.1	0.63	0.74	0.86	0.98	0.88	0.77	0.70	0.61	0.52	0.43	0.36	0.27	0.53	0.65	0.80	0.93	0.81	0.70	0.62	0.52	0.43	0.35	0.29	0.21
	1.2	0.57	0.66	0.77	0.88	0.98	0.87	0.78	0.68	0.58	0.49	0.40	0.30	0.46	0.57	0.70	0.81	0.93	0.80	0.71	0.59	0.49	0.40	0.33	0.24
	1.3	0.50	0.59	0.69	0.77	0.87	0.98	0.88	0.76	0.64	0.55	0.45	0.34	0.40	0.50	0.60	0.70	0.80	0.93	0.82	0.68	0.55	0.46	0.37	0.27
	1.4	0.45	0.53	0.62	0.70	0.78	0.88	0.98	0.85	0.72	0.61	0.51	0.38	0.35	0.44	0.53	0.62	0.71	0.81	0.93	0.78	0.64	0.53	0.43	0.31
	1.5	0.39	0.46	0.53	0.61	0.68	0.76	0.85	0.98	0.83	0.70	0.58	0.44	0.30	0.37	0.44	0.52	0.59	0.68	0.78	0.94	0.77	0.63	0.52	0.38
	1.6	0.33	0.39	0.46	0.52	0.58	0.65	0.73	0.84	0.98	0.82	0.69	0.51	0.25	0.30	0.37	0.43	0.49	0.56	0.64	0.78	0.94	0.77	0.63	0.46
	1.7	0.28	0.33	0.38	0.43	0.49	0.55	0.61	0.70	0.82	0.98	0.81	0.61	0.20	0.25	0.30	0.35	0.40	0.46	0.53	0.63	0.75	0.94	0.77	0.56
	1.8	0.23	0.27	0.32	0.36	0.41	0.45	0.51	0.59	0.69	0.82	0.98	0.73	0.17	0.20	0.25	0.29	0.33	0.38	0.43	0.52	0.63	0.78	0.94	0.68
	1.9	0.17	0.20	0.24	0.27	0.30	0.34	0.38	0.44	0.51	0.61	0.73	0.99	0.12	0.15	0.18	0.21	0.24	0.27	0.31	0.38	0.45	0.57	0.68	0.95

Table A.4: Correlation matrix of the moments $< m_X >$, $< m_X^2 >$, $< m_X^3 >$, and $< m_X^4 >$.

		$< m_X^5 > [(GeV/c^2)^5]$												$< m_X^6 > [(GeV/c^2)^6]$											
$p_{l,cut}[GeV/c]$		0.8	0.9	1.0	1.1	1.2	1.3	1.4	1.5	1.6	1.7	1.8	1.9	0.8	0.9	1.0	1.1	1.2	1.3	1.4	1.5	1.6	1.7	1.8	1.9
$< m_X >$	0.8	0.75	0.58	0.45	0.37	0.31	0.26	0.23	0.19	0.15	0.12	0.10	0.07	0.68	0.49	0.37	0.30	0.24	0.20	0.17	0.13	0.10	0.08	0.06	0.04
	0.9	0.58	0.74	0.58	0.48	0.41	0.34	0.29	0.24	0.19	0.15	0.12	0.09	0.50	0.67	0.50	0.40	0.33	0.27	0.23	0.18	0.14	0.11	0.08	0.06
	1.0	0.45	0.58	0.74	0.61	0.52	0.43	0.38	0.31	0.24	0.20	0.16	0.11	0.37	0.49	0.66	0.53	0.44	0.36	0.31	0.24	0.18	0.14	0.11	0.08
	1.1	0.37	0.48	0.61	0.73	0.62	0.52	0.45	0.37	0.29	0.24	0.19	0.14	0.29	0.39	0.52	0.64	0.53	0.44	0.37	0.29	0.23	0.18	0.14	0.10
	1.2	0.31	0.41	0.52	0.62	0.72	0.61	0.53	0.43	0.34	0.28	0.22	0.16	0.24	0.32	0.43	0.53	0.64	0.52	0.45	0.35	0.27	0.21	0.17	0.11
	1.3	0.27	0.34	0.44	0.52	0.61	0.72	0.62	0.50	0.39	0.32	0.26	0.18	0.20	0.27	0.36	0.44	0.53	0.63	0.53	0.41	0.31	0.25	0.19	0.13
	1.4	0.23	0.29	0.38	0.45	0.53	0.62	0.71	0.58	0.46	0.37	0.30	0.21	0.17	0.23	0.30	0.37	0.45	0.53	0.61	0.48	0.36	0.29	0.23	0.16
	1.5	0.19	0.24	0.31	0.37	0.43	0.50	0.58	0.73	0.58	0.47	0.38	0.27	0.13	0.18	0.24	0.29	0.35	0.41	0.48	0.65	0.50	0.39	0.31	0.21
	1.6	0.15	0.19	0.25	0.30	0.35	0.40	0.47	0.60	0.74	0.60	0.48	0.34	0.10	0.14	0.18	0.23	0.27	0.32	0.37	0.51	0.67	0.52	0.41	0.29
	1.7	0.12	0.15	0.20	0.24	0.28	0.32	0.37	0.47	0.58	0.76	0.61	0.43	0.08	0.11	0.14	0.18	0.21	0.25	0.29	0.39	0.51	0.70	0.55	0.38
	1.8	0.10	0.13	0.16	0.19	0.23	0.26	0.30	0.39	0.48	0.63	0.76	0.54	0.06	0.09	0.11	0.14	0.17	0.20	0.23	0.32	0.42	0.57	0.69	0.48
	1.9	0.07	0.09	0.11	0.14	0.16	0.19	0.21	0.27	0.34	0.44	0.53	0.78	0.04	0.06	0.08	0.10	0.12	0.14	0.16	0.22	0.29	0.39	0.47	0.72
$< m_X^2 >$	0.8	0.88	0.68	0.53	0.44	0.38	0.32	0.27	0.22	0.17	0.14	0.11	0.08	0.82	0.60	0.45	0.36	0.30	0.25	0.21	0.16	0.12	0.10	0.08	0.05
	0.9	0.68	0.88	0.69	0.57	0.48	0.41	0.35	0.28	0.22	0.18	0.15	0.10	0.60	0.81	0.60	0.49	0.41	0.33	0.29	0.22	0.17	0.13	0.10	0.07
	1.0	0.53	0.69	0.88	0.73	0.62	0.52	0.45	0.36	0.29	0.23	0.19	0.13	0.45	0.60	0.81	0.66	0.54	0.45	0.38	0.29	0.22	0.17	0.14	0.09
	1.1	0.44	0.57	0.72	0.87	0.74	0.62	0.54	0.43	0.35	0.28	0.22	0.16	0.36	0.48	0.64	0.79	0.66	0.54	0.47	0.36	0.28	0.21	0.17	0.12
	1.2	0.38	0.48	0.62	0.74	0.87	0.73	0.63	0.51	0.40	0.32	0.26	0.18	0.30	0.40	0.54	0.66	0.79	0.65	0.56	0.43	0.32	0.25	0.20	0.14
	1.3	0.32	0.41	0.52	0.63	0.73	0.86	0.74	0.59	0.46	0.37	0.30	0.21	0.25	0.33	0.45	0.55	0.65	0.78	0.66	0.50	0.38	0.29	0.23	0.16
	1.4	0.27	0.35	0.45	0.54	0.63	0.74	0.85	0.68	0.54	0.43	0.35	0.25	0.21	0.28	0.38	0.46	0.55	0.66	0.76	0.58	0.44	0.34	0.27	0.19
	1.5	0.22	0.28	0.36	0.43	0.51	0.59	0.69	0.87	0.69	0.55	0.45	0.31	0.16	0.22	0.29	0.36	0.42	0.50	0.58	0.80	0.61	0.47	0.38	0.26
	1.6	0.18	0.23	0.29	0.35	0.41	0.47	0.55	0.70	0.88	0.70	0.57	0.40	0.12	0.17	0.22	0.27	0.33	0.39	0.45	0.62	0.82	0.63	0.51	0.34
	1.7	0.14	0.18	0.23	0.28	0.32	0.38	0.44	0.55	0.68	0.89	0.72	0.51	0.10	0.13	0.17	0.21	0.25	0.30	0.35	0.47	0.62	0.84	0.67	0.46
	1.8	0.11	0.15	0.19	0.23	0.26	0.31	0.36	0.46	0.57	0.74	0.89	0.63	0.08	0.10	0.14	0.17	0.20	0.24	0.28	0.38	0.51	0.69	0.83	0.57
	1.9	0.08	0.10	0.13	0.16	0.18	0.21	0.25	0.32	0.40	0.51	0.62	0.91	0.05	0.07	0.09	0.11	0.14	0.16	0.19	0.26	0.34	0.46	0.56	0.86

Table A.5: Correlation matrix of the moments $< m_X >$, $< m_X^2 >$, $< m_X^5 >$, and $< m_X^6 >$.

		$< m_X^5 > [(GeV/c^2)^5]$												$< m_X^6 > [(GeV/c^2)^6]$											
$p_{l,cut}[GeV/c]$		0.8	0.9	1.0	1.1	1.2	1.3	1.4	1.5	1.6	1.7	1.8	1.9	0.8	0.9	1.0	1.1	1.2	1.3	1.4	1.5	1.6	1.7	1.8	1.9
$< m_X^3 >$	0.8	0.95	0.74	0.58	0.48	0.41	0.35	0.30	0.24	0.18	0.15	0.12	0.08	0.91	0.67	0.50	0.41	0.34	0.28	0.24	0.18	0.13	0.10	0.08	0.06
	0.9	0.74	0.95	0.75	0.62	0.53	0.45	0.39	0.31	0.24	0.19	0.15	0.11	0.67	0.90	0.67	0.55	0.46	0.38	0.32	0.24	0.18	0.14	0.11	0.08
	1.0	0.58	0.75	0.95	0.79	0.67	0.57	0.50	0.39	0.31	0.24	0.20	0.14	0.50	0.67	0.90	0.73	0.61	0.51	0.44	0.33	0.24	0.19	0.15	0.10
	1.1	0.48	0.62	0.79	0.95	0.81	0.68	0.59	0.47	0.37	0.29	0.24	0.17	0.40	0.54	0.72	0.89	0.74	0.62	0.53	0.40	0.30	0.23	0.18	0.12
	1.2	0.41	0.53	0.67	0.81	0.94	0.80	0.69	0.55	0.43	0.34	0.28	0.19	0.33	0.45	0.60	0.74	0.89	0.73	0.63	0.47	0.36	0.27	0.22	0.15
	1.3	0.35	0.45	0.57	0.68	0.80	0.94	0.81	0.64	0.49	0.40	0.32	0.22	0.28	0.38	0.51	0.62	0.74	0.88	0.75	0.56	0.42	0.32	0.25	0.17
	1.4	0.30	0.39	0.50	0.59	0.69	0.81	0.94	0.74	0.58	0.46	0.37	0.26	0.24	0.32	0.43	0.53	0.63	0.75	0.86	0.65	0.49	0.37	0.30	0.20
	1.5	0.24	0.31	0.39	0.47	0.55	0.64	0.74	0.95	0.74	0.59	0.48	0.33	0.18	0.24	0.32	0.39	0.47	0.56	0.65	0.89	0.67	0.51	0.41	0.28
	1.6	0.19	0.24	0.31	0.37	0.44	0.50	0.59	0.75	0.95	0.75	0.61	0.43	0.13	0.18	0.24	0.30	0.36	0.42	0.49	0.68	0.91	0.69	0.56	0.37
	1.7	0.15	0.19	0.25	0.29	0.35	0.40	0.46	0.59	0.73	0.96	0.77	0.54	0.10	0.14	0.19	0.23	0.27	0.32	0.38	0.52	0.68	0.92	0.73	0.49
	1.8	0.12	0.16	0.20	0.24	0.28	0.32	0.38	0.48	0.61	0.79	0.96	0.66	0.08	0.11	0.15	0.18	0.22	0.26	0.30	0.42	0.56	0.75	0.92	0.61
	1.9	0.08	0.11	0.14	0.17	0.19	0.23	0.26	0.34	0.42	0.55	0.66	0.96	0.06	0.07	0.10	0.12	0.15	0.17	0.20	0.28	0.37	0.50	0.61	0.93
$< m_X^4 >$	0.8	0.99	0.77	0.60	0.50	0.43	0.36	0.32	0.25	0.19	0.15	0.12	0.09	0.96	0.71	0.53	0.43	0.36	0.30	0.26	0.19	0.14	0.11	0.09	0.06
	0.9	0.77	0.99	0.77	0.65	0.55	0.47	0.41	0.32	0.25	0.20	0.16	0.11	0.71	0.95	0.71	0.58	0.49	0.41	0.35	0.26	0.19	0.15	0.12	0.08
	1.0	0.60	0.77	0.99	0.83	0.70	0.60	0.52	0.41	0.32	0.25	0.20	0.14	0.53	0.71	0.96	0.78	0.66	0.55	0.47	0.35	0.26	0.20	0.16	0.10
	1.1	0.50	0.65	0.82	0.99	0.84	0.71	0.62	0.49	0.38	0.30	0.25	0.17	0.43	0.58	0.77	0.95	0.80	0.67	0.58	0.43	0.32	0.24	0.19	0.13
	1.2	0.43	0.55	0.70	0.84	0.99	0.84	0.73	0.57	0.45	0.35	0.29	0.20	0.36	0.48	0.65	0.80	0.95	0.79	0.69	0.51	0.38	0.29	0.23	0.15
	1.3	0.36	0.47	0.60	0.72	0.84	0.99	0.85	0.67	0.51	0.41	0.33	0.23	0.30	0.41	0.55	0.67	0.80	0.95	0.81	0.60	0.44	0.34	0.26	0.18
	1.4	0.32	0.41	0.52	0.62	0.73	0.85	0.98	0.77	0.60	0.48	0.39	0.27	0.26	0.35	0.47	0.57	0.68	0.81	0.94	0.69	0.52	0.39	0.31	0.21
	1.5	0.25	0.32	0.41	0.49	0.57	0.67	0.77	0.99	0.77	0.61	0.50	0.34	0.19	0.25	0.34	0.42	0.50	0.60	0.69	0.95	0.72	0.54	0.43	0.29
	1.6	0.19	0.25	0.32	0.38	0.45	0.51	0.60	0.78	0.99	0.77	0.63	0.44	0.14	0.19	0.25	0.31	0.37	0.44	0.52	0.71	0.96	0.72	0.59	0.39
	1.7	0.15	0.20	0.25	0.30	0.36	0.41	0.48	0.61	0.76	0.99	0.80	0.56	0.11	0.14	0.19	0.24	0.29	0.34	0.39	0.54	0.71	0.97	0.78	0.52
	1.8	0.12	0.16	0.20	0.25	0.29	0.33	0.39	0.50	0.63	0.81	0.99	0.68	0.09	0.11	0.15	0.19	0.23	0.27	0.32	0.44	0.59	0.79	0.97	0.64
	1.9	0.09	0.11	0.14	0.17	0.20	0.23	0.27	0.35	0.44	0.56	0.68	0.99	0.06	0.08	0.10	0.13	0.15	0.18	0.21	0.29	0.39	0.52	0.64	0.97

Table A.6: Correlation matrix of the moments $< m_X^3 >$, $< m_X^4 >$, $< m_X^5 >$, and $< m_X^6 >$.

List of Tables

List of Figures

Bibliography

[1] Manohar, A. V. *et al.*, *Heavy Quark Physics*, Cambridge Monogr. Part. Phys. Nucl. Phys. Cosmol. 10(2000):1–191.

[2] Falk, A. F., *The Heavy Quark Expansion of QCD* (1996), hep-ph/9610363.

[3] Falk, A. F., *The CKM Matrix and the Heavy Quark Expansion* (2000), hep-ph/0007339.

[4] Super-Kamiokande, Fukuda, Y. *et al.*, *Evidence for Oscillation of Atmospheric Neutrinos*, Phys. Rev. Lett. 81(1998):1562–1567, hep-ex/9807003.

[5] Higgs, P. W., *Broken Symmetries, Massless Particles and Gauge Fields*, Phys. Lett. 12(1964):132–133.

[6] Higgs, P. W., *Broken Symmetries and the Masses of Gauge Bosons*, Phys. Rev. Lett. 13(1964):508–509.

[7] Higgs, P. W., *Spontaneous Symmetry Breakdown Without Massless Bosons*, Phys. Rev. 145(1966):1156–1163.

[8] Englert, F. *et al.*, *Broken Symmetry and the Mass of Gauge Vector Mesons*, Phys. Rev. Lett. 13(1964):321–322.

[9] Guralnik, G. S., *et al.*, *Global Conservation Laws and Massless Particles*, Phys. Rev. Lett. 13(1964):585–587.

[10] CKMfitter Group, Charles, J. *et al.*, *CP Violation and the CKM Matrix: Assessing the Impact of the Asymmetric B Factories*, Eur. Phys. J. C41(2005):1–131, hep-ph/0406184. Available from: `http://ckmfitter.in2p3.fr/`.

[11] Buchmüller, O. *et al.*, *Fit to Moments of Inclusive $B \to X_c \ell \nu$ and $B \to X_s \gamma$ Decay Distributions using Heavy Quark Expansions in the Kinetic Scheme*, Phys. Rev. D73(2006):073008, hep-ph/0507253.

[12] Particle Data Group (PDG), Eidelman, S. *et al.*, *Review of Particle Physics*, Physics Letters B 592(2004):1+. Available from: http://pdg.lbl.gov.

[13] Trott, M., *Improving Extractions of $|V_{cb}|$ and m_b from the Hadronic Invariant Mass Moments of Semileptonic Inclusive B Decay*, Phys. Rev. D70(2004):073003, hep-ph/0402120.

[14] Gambino, P. *et al.*, *Moments of Semileptonic B Decay Distributions in the $1/m_b$ Expansion*, Eur. Phys. J. C34(2004):181–189, hep-ph/0401063.

[15] Benson, D., *et al.*, *Imprecated, Yet Impeccable: On the Theoretical Evaluation of $\Gamma(B \to X_c \ell \nu)$*, Nucl. Phys. B665(2003):367–401, hep-ph/0302262.

[16] Benson, D., *et al.*, *On the Photon Energy Moments and their 'Bias' Corrections in $B \to X_s \gamma$*, Nucl. Phys. B710(2005):371–401, hep-ph/0410080.

[17] *PEP-II: An Asymmetric B Factory. Conceptual Design Report* (June 1993), sLAC-418.

[18] *BABAR* collaboration, Aubert, B. *et al.*, *The BaBar Detector*, Nucl. Instrum. Meth. A479(2002):1–116, hep-ex/0105044.

[19] *BABAR* collaboration, Hearty, C., *Measurement of the Number of $\Upsilon(4S)$ Mesons Produced in Run 1 (B Counting)* (2001), *BABAR* Analysis Document #134.

[20] Lange, D. J., *The* `EvtGen` *Particle Decay Simulation Package*, Nucl. Instrum. Meth. A462(2001):152–155.

[21] `GEANT4` collaboration, Agostinelli, S. *et al.*, `GEANT4`*: A Simulation Toolkit*, Nucl. Instrum. Meth. A506(2003):250–303.

[22] Richter-Was, E., *QED Bremsstrahlung In Semileptonic B and Leptonic τ Decays*, Phys. Lett. B303(1993):163–169.

[23] *BABAR* collaboration, del Re, D., *Semi-Exclusive B reconstruction* (2001), *BABAR* Analysis Document #271.

[24] *BABAR* collaboration, Ulmer, K., *Correcting COM Beam Energies* (November 24, 2004), presented at Wednesday Physics Meeting. Available from: http://www.slac.stanford.edu/BFROOT/www/Physics/WednesdayMeetings/W112404/Ulmer.pdf.

[25] *BABAR* collaboration, Ulmer, K. (March 29, 2005), hypernews Forum for Conditions Database Management. Available from: http://babar-hn.slac.stanford.edu:5090/HyperNews/get/condmgmt/81/2/1.html.

[26] *BABAR* collaboration, Brandt, T., *Measurement of Inclusive Semileptonic Branching Fractions of Charged and Neutral B Mesons* (2006), *BABAR* Analysis Document #1366.

[27] Hulsbergen, W. D., *Decay Chain Fitting with a Kalman Filter*, Nucl. Instrum. Meth. A552(2005):566–575, physics/0503191.

[28] *BABAR* collaboration, Fortin, D. *et al.*, *Particle Selection Criteria, Optimized for Visible Energy Measurement* (2003), *BABAR* Analysis Document #633.

[29] *BABAR* collaboration, Mazur, M. A. *et al.*, *Study of Exclusive Decays* $B \to D^{(*)}\tau\nu$ (2006), *BABAR* Analysis Document #1111.

[30] *BABAR* collaboration, Brandt, T., *Likelihood Based Electron Identification* (2002), *BABAR* Analysis Document #396.

[31] *BABAR* collaboration, Band, H. *et al.*, *Studies of A Neural Net Based Muon Selector for the BABAR Experiment* (2004), *BABAR* Analysis Document #474.

[32] *BABAR* collaboration, Mancinelli, G. *et al.*, *Kaon Selection at the BABAR Experiment* (2001), *BABAR* Analysis Document #116.

[33] Blobel, V. *et al.*, *Statistische und numerische Methoden der Datenanalyse* (Teubner, 1998).

[34] *BABAR* collaboration, Klose, V. *et al.*, *KinFitter – A Kinematic Fit with Constraints* (2004), *BABAR* Analysis Document #1061.

[35] ARGUS collaboration, Albrecht, H. *et al.*, *Reconstruction Of B Mesons*, Phys. Lett. B 185(1987):218.

[36] Crystal Ball collaboration, Skwarnicki, T., *A Study Of The Radiative Cascade Transitions Between The* $\Upsilon\prime$ *And* Υ *Resonances*, DESY F31-86-02 (1986).

[37] Catmull, E. *et al.*, *A Class Of Local Interpolating Splines*, in Barnhill, R. *et al.* (eds.), *Computer Aided Geometric Design* (Academic Press, 1974) pp. 317–326.

[38] *BABAR* collaboration, Aubert, B. *et al.*, *Study of Inclusive* B^- *and* $\overline{B}^0$ *Decays to Flavor-Tagged D,* D_s^+ *and* Λ_c^+ (2006), hep-ex/0606026.

[39] CLEO collaboration, Adam, N. E. *et al.*, *Absolute Branching Fraction Measurements for* D^+ *and* D^0 *Inclusive Semileptonic Decays* (2006), hep-ex/0604044.

[40] *BABAR* collaboration, Aubert, B. *et al.*, *Determination of the Branching Fraction for $B \to X_c \ell \nu$ Decays and of $|V_{cb}|$ from Hadronic-Mass and Lepton-Energy Moments*, Phys. Rev. Lett. 93(2004):011803, hep-ex/0404017.

[41] ARGUS collaboration, Albrecht, H. *et al.*, *A Model-Independent Determination of the Inclusive Semileptonic Decay Fraction of B Mesons*, Phys. Lett. B 318(1993):397–404.

[42] Heavy Flavor Averaging Group (HFAG), Barberio, E. *et al.*, *Averages of b-hadron Properties at the End of 2005* (Winter 2006), hep-ex/0603003. Available from: http://www.slac.stanford.edu/xorg/hfag.

[43] *BABAR* collaboration, *Performing Particle ID on Monte Carlo* (2006). Available from: http://www.slac.stanford.edu/BFROOT/www/Physics/Tools/Pid/PidOnMc/pidonmc.html.

[44] Lange, B. O., *et al.*, *Theory of Charmless Inclusive B Decays and the Extraction of V_{ub}*, Phys. Rev. D72(2005):073006, hep-ph/0504071.

[45] *BABAR* collaboration, Allmendinger, T. *et al.*, *Tracking Efficiency Studies in Release 12 and 14* (2004), *BABAR* Analysis Document #867.

[46] *BABAR* collaboration, Allen, M. *et al.*, *A Measurement of π^0 Efficiency Using $\tau \to \rho\nu$ and $\tau \to \pi\nu$ Decays* (2004), *BABAR* Analysis Document #870.

[47] *BABAR* collaboration, Aubert, B. *et al.*, *Measurements of Moments of the Hadronic Mass Distribution in Semileptonic B Decays*, Phys. Rev. D69(2004):111103, hep-ex/0403031.

[48] Bigi, I. I., *et al.*, *On the Nonperturbative Charm Effects in Inclusive $B \to X_c \ell \nu$ Decays* (2005), hep-ph/0511158.

[49] Uraltsev, N., *Perturbative Corrections to the Semileptonic b-Ddecay Moments: E^{ℓ}_{cut} Dependence and Running-α_s Effects in the OPE Approach*, Int. J. Mod. Phys. A20(2005):2099–2118, hep-ph/0403166.

[50] Aquila, V., *et al.*, *Perturbative Corrections to Semileptonic b Decay Distributions*, Nucl. Phys. B719(2005):77–102, hep-ph/0503083.

[51] *BABAR* collaboration, Aubert, B. *et al.*, *Measurement of the Electron Energy Spectrum and its Moments in Inclusive $B \to X \ell \nu$ Decays*, Phys. Rev. D69(2004):111104, hep-ex/0403030.

[52] *BABAR* collaboration, Aubert, B. *et al.*, *Measurements of the $B \to X_s \gamma$ Branching Fraction and Photon Spectrum from a Sum of Exclusive Final States*, Phys. Rev. D72(2005):052004, hep-ex/0508004.

[53] *BABAR* collaboration, Aubert, B. *et al.*, *Results from the BABAR Fully Inclusive Measurement of* $B \to X_s\gamma$ (2005), hep-ex/0507001.

[54] BELLE collaboration, Koppenburg, P. *et al.*, *An Inclusive Measurement of the Photon Energy Spectrum in* $b \to s\gamma$ *Decays*, Phys. Rev. Lett. 93(2004):061803, hep-ex/0403004.

[55] BELLE collaboration, Abe, K. *et al.*, *Moments of the Photon Energy Spectrum from BtoXsGamma Decays Measured by BELLE* (2005), hep-ex/0508005.

[56] CDF collaboration, Acosta, D. *et al.*, *Measurement of the Moments of the Hadronic Invariant Mass Distribution in Semileptonic B Decays*, Phys. Rev. D71(2005):051103, hep-ex/0502003.

[57] CLEO collaboration, Csorna, S. E. *et al.*, *Moments of the B Meson Inclusive Semileptonic Decay Rate Using Neutrino Reconstruction*, Phys. Rev. D70(2004):032002, hep-ex/0403052.

[58] CLEO, Chen, S. *et al.*, *Branching Fraction and Photon Energy Spectrum for* $b \to s\gamma$, Phys. Rev. Lett. 87(2001):251807, hep-ex/0108032.

[59] DELPHI collaboration, Abdallah, J. *et al.*, *Determination of Heavy Quark Non-Perturbative Parameters from Spectral Moments in Semileptonic B Decays*, Eur. Phys. J. C45(2006):35–59, hep-ex/0510024.

[60] Bauer, C. W., *et al.*, *Global Analysis of Inclusive B Decays*, Phys. Rev. D70(2004):094017, hep-ph/0408002.

Acknowledgements